# The relationship between obscured AGN and their host galaxies

Cyprian Francis Rangel
Astrophysics Group

Department of Physics
Imperial College London

Thesis submitted for the Degree of Doctor of Philosophy to
Imperial College London

· 2013 ·

# Abstract

This thesis presents an investigation into obscured Active Galactic Nuclei (AGN) activity at high redshift and the interactions they share with their host galaxies. Using a combination of X-ray spectral fitting and X-ray stacking analyses, three studies are undertaken in this work. The first study is a reinvestigation of a specific group of X-ray undetected mid-IR excess galaxies at $z \sim 2$ that have previously been identified as Compton thick AGN candidates through X-ray stacking analysis. The parent sample of optically identified galaxies is found to possess above average obscured AGN activity. The galaxies exhibiting mid-IR excess, however, do not exhibit elevated levels of obscured AGN activity relative to the parent sample. Key to this result is the increased depth of X-ray observations, which resolves hard X-ray sources that had biased earlier stacking analyses.

The second study concerns the nature of AGN residing in massive galaxies at $z \sim 2$. The highlight of this research is the identification of two accretion modes which are dependent upon host galaxy compactness: a “transformative mode for compact galaxies and a “maintenance mode for extended galaxies. AGN in the transformative mode are heavily obscured and X-ray luminous and are thought to rapidly quench star formation in their host galaxies through violent feedback. The AGN in “maintenance mode have lower luminosities and tend to be unobscured, but appear to suppress further star formation in their host galaxies through a gentler feedback process.

The third study is a comparison of colour-excitation (CEx) and mass-excitation (MEx) classification techniques designed to identify Type 2 AGN out to $z \sim 0.8$. The CEx technique is found to identify obscured AGN with a high degree of accuracy, with X-ray stacking revealing many as yet X-ray undetected sources. The MEx technique is adept at identifying X-ray detected AGN but is less accurate at isolating obscured sources.

# Contents

# List of Tables

# List of Figures

# Declaration and Copyright

This thesis is my own work, except where explicitly indicated in the text.

Cyprian Rangel
September 2013

# Acknowledgments

Studying for my PhD has been without doubt the most demanding task I have undertaken and would have been impossible if not for the help and support of so many people. First and foremost I have to thank Paul, my (at times elusive) supervisor. It has been a long and at times difficult journey the last 4 years as progress of the research has ebbed and flowed, but you always seemed to be there to provide much needed direction. You managed to find time in your ever hectic schedule to provide sage advice and even when you may have been at a loss you always knew of someone whose expertise could aid me. I realise I can be a fairly difficult individual to work with at times given my tendency to leave everything until the last minute (thesis submission included!), but you always remained patient with me. Without your contribution it is safe to say there wouldn't be a thesis to attach to these acknowledgements.

Secondly I would like to thank Steve, my 'adopted' supervisor. I was somewhat dropped in your lap when Paul moved to Munich, but you never complained and always been willing to provide me with counsel. You even read through my thesis, a brave undertaking indeed. I am also hugely indebted to Elise Laird and Murray Brightman who showed me the ropes and fielded my constant stream of questions about X-ray astronomy.

I am deeply indebted to my mum and dad. As they have throughout my life they provided unwavering support during my PhD, even though they had no idea what exactly I was studying! Thanks to my brother, Joe, for just being himself. I always have great fun hanging out with you and I'm so lucky to have a brother who I can call my best friend. It's crazy to think you have started a PhD of your own and I wish you every success. I'm lucky enough to have 4 wonderful grandparents and I hope I have made them proud.

My fellow post-graduates at Imperial, past and present, have proved vital in preserving my sanity over the last 4 years. We've all shared hundreds of lunch and tea breaks helped break up the long days and provided more than a few laughs along the way. I will remember Mitesh, Shyam, Dan, Harsit and Jonathan for the many hours of table tennis we played and the banter in the pub afterwards. It has been a pleasure to share this PhD journey with my year mates, Caroline and Laura, I wish you both all the best in the future. I would like to thank the ever bubbly Ashley whose endless supply of cat videos always brought a smile to my face, and Alfredo for adding a bit of class to proceedings (sort of). Cat, Tot, Alex and Justin, you are all awesome and I can only imagine the research you produce is going to blow mine out of the water. Charlotte, I know we have had our differences but I am glad that I can now call you a friend as well as a colleague despite my previous transgressions.

A special mention goes to Simon, our ‘honourary’ post-graduate, whose wanderlust provided the inspiration for unforgettable group road trips across Norway and Spain. Also thanks to Till who got me hooked on climbing providing me with a welcome distraction from thesis writing in the final 6 or so months. Finally, Nathalie, it as been an absolute pleasure (most of the time) working with you over the last 3 years. An outside observer could probably not imagine two more different souls but thanks to your (unhealthy) obsession with UCB and a video of the Cal marching band we managed to hit it off from day one. From that point forward you’ve always been around there to pick me up when I’ve been down and to kick me up the arse when I’ve been lazy. I now consider you one of my dearest friends and my life would have been poorer if not for having met you.

As for those friends beyond Imperial Astrophysics, I’d like to thank Sid and Jordan for the many fine beers and ‘interesting’ conversations we have shared. I love the fact that even when I’m not in astrophysics I can indulge in physics geekery. Thanks to Tom, Phil and Jimmy who have been there for me since my school days. It’s always great to hang out with you and remember that there is a world beyond physics research.

Quite frankly there are too many people to thank individually so if you have not been mentioned by name please do not take this is not a personal sleight. All my friends and family have contributed to this thesis in one way or another and you all mean the world to me.

# Publications

- “Evidence for two modes of black hole accretion in massive galaxies at z $\sim$ 2”
  **Rangel, C.,** Nandra, K., Barro, G., Brightman, M., Hsu, L., Salvato, M., Koekemoer, A. M., Brusa, M., Laird, E. S., Trump, J. R., Croton, D. J., Koo, D. C., Kocevski, D., Donley, J. L., Hathi, N. P., Peth, M., Faber, S. M., Mozena, M., Grogin, N. A., Ferguson, H. C., Lai, K., submitted to MNRAS

- “X-ray properties of BzK-selected galaxies in the deepest X-ray fields”
  **Rangel, C.,** Nandra, K., Laird, E. S., Orange, P., MNRAS, 428, 3089

- “X-Ray Selected AGN Host Galaxies are Similar to Inactive Galaxies out to z = 3: Results from CANDELS/CDF-S”
  Rosario, D. J., Mozena, M., Wuyts, S., Nandra, K., Koekemoer, A., McGrath, E., Hathi, N. P., Dekel, A., Donley, J., Dunlop, J. S., Faber, S. M., Ferguson, H., Giavalisco, M., Grogin, N., Guo, Y., Kocevski, D. D., Koo, D. C., Laird, E., Newman, J., **Rangel, C.,** Somerville, R., ApJ, 763, 59

- “CANDELS: Constraining the AGN-Merger Connection with Host Morphologies at z $\sim$ 2”
  Kocevski, Dale D., Faber, S. M., Mozena, Mark, Koekemoer, Anton M., Nandra, Kirpal, **Rangel, Cyprian,** Laird, Elise S., Brusa, Marcella, Wuyts, Stijn, Trump, Jonathan R., Koo, David C., Somerville, Rachel S., Bell, Eric F., Lotz, Jennifer M., Alexander, David M., Bournaud, Frederic, Conselice, Christopher J., Dahlen, Tomas, Dekel, Avishai, Donley, Jennifer L., Dunlop, James S., Finoguenov, Alexis, Georgakakis, Antonis, Giavalisco, Mauro, Guo, Yicheng, Grogin, Norman A., Hathi, Nimish P., Juneau, Stphanie, Kartaltepe, Jeyhan S., Lucas, Ray A., McGrath, Elizabeth J., McIntosh, Daniel H., Mobasher, Bahram, Robaina, Aday R., Rosario, David, Straughn, Amber N., van der Wel, Arjen, Villforth, Carolin, ApJ, 744, 148

- “A CANDELS WFC3 Grism Study of Emission-line Galaxies at z $\sim$ 2: A Mix of Nuclear Activity and Low-metallicity Star Formation”
  Trump, Jonathan R., Weiner, Benjamin J., Scarlata, Claudia, Kocevski, Dale D., Bell, Eric F., McGrath, Elizabeth J., Koo, David C., Faber, S. M., Laird, Elise S., Mozena, Mark, **Rangel, Cyprian,** Yan, Renbin, Yesuf, Hassen, Atek, Hakim, Dickinson, Mark, Donley, Jennifer L., Dunlop, James S., Ferguson, Henry C., Finkelstein,

Steven L., Grogin, Norman A., Hathi, Nimish P., Juneau, Stphanie, Kartaltepe, Jeyhan S., Koekemoer, Anton M., Nandra, Kirpal, Newman, Jeffrey A., Rodney, Steven A., Straughn, Amber N., Teplitz, Harry I., ApJ, 743, 144

# Foreword

This thesis is based on work carried out at Imperial College London between October 2009, and September 2013.

# Chapter 1

# Introduction

## 1.1 A brief introduction to Active Galactic Nuclei

### 1.1.1 What are Active Galactic Nuclei?

An 'Active Galactic Nucleus' is a nuclear region of a galaxy that exhibits non-stellar emission. Carl Seyfert (1943) was among the first to study Active Galactic Nuclei (AGN) in detail, focusing on a group of galaxies exhibiting high-excitation nuclear emission lines in their optical spectra. The luminosity produced by such a small region points to a compact and highly energetic source, suggesting that AGN are driven by the energy produced by matter accreting onto a supermassive black hole (SMBH) as opposed to starbursts or other compact energetic processes (Rees, 1984). This principally involves emission from the accretion disk, where in-falling matter loses angular momentum and emits electromagnetic radiation. This in turn may interact with dust and gas surrounding the black hole, re-radiating through a variety of secondary emission processes which in concert produce the spectrum of the AGN.

There is a growing consensus that SMBH are present in the centres all bulge dominated galaxies (Kormendy and Richstone, 1995). Strong correlations have been observed between black hole mass ($M_{bh}$) and the velocity dispersion of stars in the bulge (Gebhardt et al., 2000) and the central bulge mass (Kormendy and Gebhardt, 2001; Marconi and Hunt, 2003). All of these SMBH have the potential to be AGN but few are actively accreting at a sufficient rate to be classed as such. The "dormant" SMBH will have accreted most of their mass during the formation and subsequent evolution of the host galaxy. The black hole only becomes "active" when the accretion rate is high enough. For instance Genzel et al. (1996) detected the presence of a central dark mass $2.45 \times 10^6 M_\odot$ at the centre of the Milky Way which is most likely a dormant SMBH. Further studies have shown this SMBH to possess an accretion rate of $\sim 10^{-7} M_\odot yr^{-1}$ (Marrone et al 2007), which is extremely low meaning that this would not be classified - or even detected - as an AGN if present in a distant galaxy.

With a full census of AGN it would be possible to trace the accretion history of the universe (e.g. Maccacaro et al. 1991; Boyle et al. 1993; Ueda et al. 2003; Aird et al. 2010). The observed link between AGN and their host galaxies (e.g. Gebhardt et al. 2000; Kormendy and Gebhardt 2001; Marconi and Hunt 2003) suggests a physical link between the evolution of black holes and galaxies, and a greater understanding of AGN and their host galaxies will better constrain the extent of this relationship. Compiling a full census of AGN over cosmic time, however, is a complex problem.

### 1.1.2 AGN Taxonomy

AGN exhibit a wide variety of characteristics, producing a menagerie of objects exhibiting different emission but thought to share the same ultimate source, an actively accreting SMBH. There have been numerous attempts to classify AGN based on these emission characteristics. AGN observed to have similar properties to those observed by Seyfert (1943), galaxies with a luminous nuclear region and high-excitation emission lines, are known as Seyfert galaxies. In some, strong radio emission has been attributed to jets of particles emitted along the polar axes of AGN. Thus AGN have been classed as radio-loud or radio-quiet, depending on whether strong radio emission from these jets is observed. Among the rarest types of known AGN are “blazars” which are characterised by rapid variations in luminosity and are dominated by their jet emission. Quasi-stellar objects (QSOs) were first identified as AGN by Schmidt (1963), who observed broad Balmer lines of hydrogen, which had been strongly redshifted. QSOs are the brightest and rarest form of AGN. Their high luminosity allows them to be observed at higher redshifts than other AGN, the current record is $z = 7.085$ (Mortlock et al., 2011).

As the “zoo” of AGN has grown, the original classification schemes have been expanded to incorporate additional subspecies. Khachikian and Weedman (1974) observed that the shape of emission lines in Seyfert galaxy spectra was not uniform across the population. Using this information they defined two categories; Seyfert 1 when broad lines were observed in the spectrum, and Seyfert 2 when only narrow lines were observed. These were initially considered to be two unique populations of AGN. As observations continued intermediate Seyfert types were discovered that could not be classified using the existing definitions. These intermediate types of AGN were classified subsequently using the H$\beta$ to [O III] optical emission line ratio (Winkler, 1992), see Table 1.1.

As the field of AGN research has expanded some of the existing classification schemes have become more complex and convoluted, prompting the search for inclusive selection techniques. Unfortunately to date there remains no single classification technique that can identify all types of AGN. Given the sheer diversity of AGN emission characteristics it is doubtful a universal classification will be found, but by using a variety of suitable AGN identification techniques in concert it is possible to obtain a fairly comprehensive census of AGN.

**Table 1.1:** Classification scheme for intermediate type Seyfert galaxies devised by Winkler (1992). Column (1): Seyfert Type identifier; column (2): optical line characteristics corresponding to Seyfert Type.

| Seyfert Type (1) | Optical emission line characteristics (2) |
|---|---|
| 1.0 | H$\beta$/[O III]$>$ 5.0 |
| 1.2 | 2.0$<$H$\beta$/[O III]$<$ 5.0 |
| 1.5 | 0.33$<$H$\beta$/[O III]$<$ 2.0 |
| 1.8 | H$\beta$/[O III]$<$ 0.33 |
| 1.9 | only broad H$\alpha$ |
| 2.0 | no broad component visible |

### 1.1.3 A Unified model for AGN

Despite the wide variation in AGN emission characteristics they are all thought to share the same central engine, an actively accreting SMBH. As such, numerous models for AGN structure have been developed, seeking to unify the emission characteristics of the various types of AGN. One of the most significant breakthroughs in this line of inquiry was the work of Rowan-Robinson (1977) and Lawrence and Elvis (1982), who proposed that Type 1 and 2 AGN were actually the same type of object, where the broad lines in the spectra of Type 2 AGN are obscured by clouds of dust. Following these revelations, interest in a "unified" scheme of AGN intensified following the discovery of sources previously identified as Type 1 AGN that possessed more Type 2 AGN properties upon re-inspection (e.g. Penston and Perez 1984). Conversely, Antonucci and Miller (1985) discovered polarised broad-lines in the spectra of NGC 1068, which had previously been considered a classic example of a Type 2 AGN, using spectropolarimetry. The nuclear polarisation used to isolate the broad lines was attributed to electron scattering (Miller and Antonucci, 1983), leading to the idea that the obscuring material was distributed in a torus surrounding the central source, covering a large solid angle as seen from the nucleus. Predictions were made for the infrared spectra of the dust torus model agreed with the observed IR properties of known Type 2 galaxies (Pier and Krolik, 1992, 1993). Most unification schemes (Antonucci, 1993; Urry and Padovani, 1995) theorised the differences between the Type 1 and Type 2 emission is primarily dependent on the orientation of the AGN relative to the observer. Alternative unification models have also been suggested such as the Galactic Dust Model (GDM; Malkan et al. 1998), where the type of emission observed is dependent on obscuration by large clouds of galactic dust.

The AGN unification paradigm of Antonucci (1993) has been widely accepted as the most comprehensive approximation of AGN structure to date, explaining the majority of observed AGN emission characteristics (see Figure 1.1). The broad lines of Type 1 AGN are thought to originate from rapidly moving clouds of gas in close proximity to the central SMBH, known as the Broad Line Region (BLR). AGN broad lines are typically observed to have undergone doppler broadening of $\sim$5000 km s$^{-1}$, though in some quasars it can

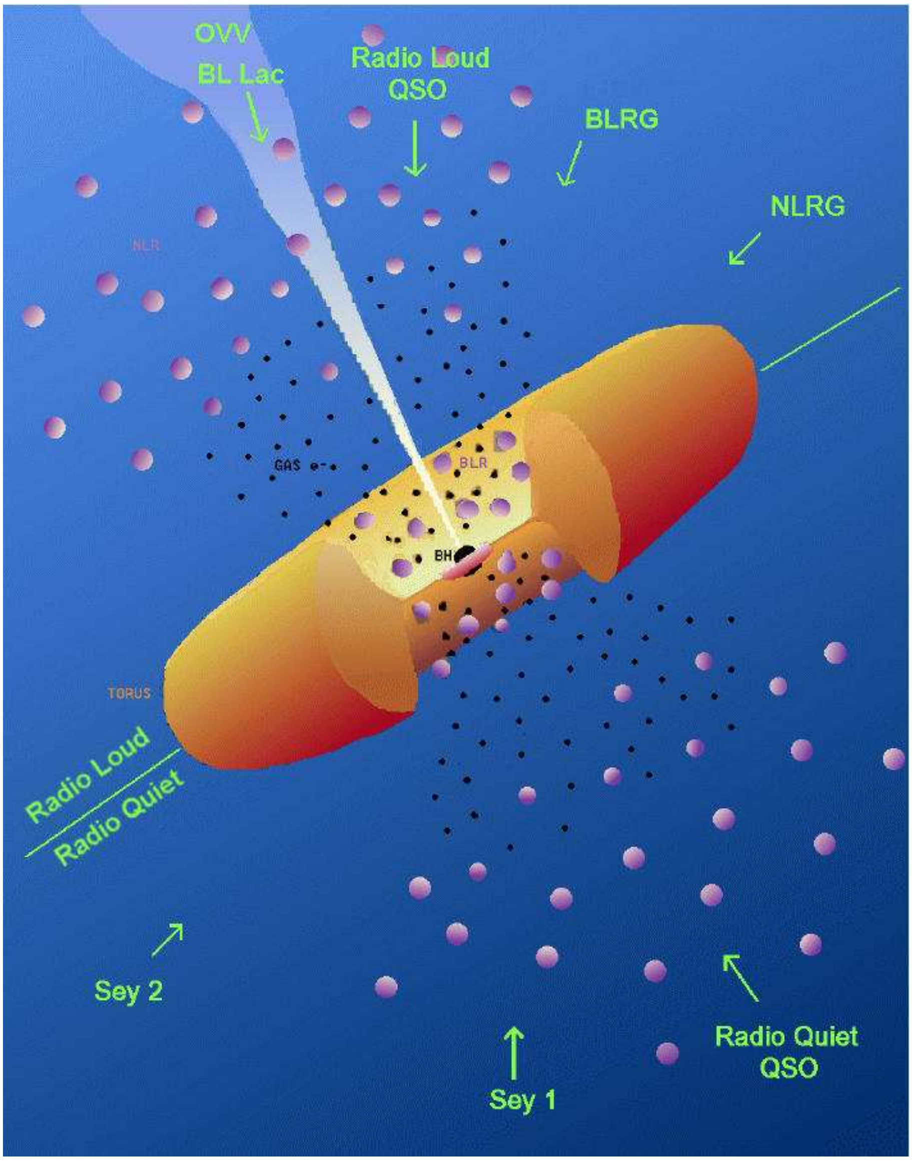

**Figure 1.1:** Simplified 'Unified' AGN structure taken from Urry and Padovani (1995).

reach ~30,000 km $s^{-1}$ (e.g. Elvis 2000). The inner location of the BLR also means the broad line emission is obscured by the dust torus over a large solid angle. The narrow lines are thought to originate from clouds of gas and dust known as the Narrow Line Region (NLR). AGN have been observed to emit permitted and forbidden narrow lines (Rees, 1984), hence the NLR is thought to have low electron densities. The NLR is located much further away from the SMBH than the BLR so the gravitational forces exerted upon it are much less extreme, hence it moves at much lower velocities and less doppler broadening occurs. Being further from the SMBH also means the NLR is not obscured by the dust torus. The orientation of the AGN determines whether or not the broad emission lines are observed, when face on the BLR is visible hence the AGN appears to be Type 1, but when edge on the dust torus obscures the broad lines hence the AGN is seen as Type 2. Some AGN have been observed to possess "ionisation cones", conical regions of photoionisation thought to be illuminated by inonising radiation emitted by the central source (NGC 1068, Pogge 1988; Tadhunter and Tsvetanov 1989). The collimation of ionising radiation is consistent with models of the obscuring torus, and the gas illuminated by the radiation is thought to be the NLR's of AGN. The BLR is thought to exist ~1 parsec from the SMBH and the obscuring torus is thought to exist 10-100 parsecs away; to date neither has been imaged directly.

### 1.1.4 The spectral energy distribution of an AGN

AGN are known to emit strongly over a wide range of wavelengths and their unique spectral energy distributions (SED) can help disentangle them from their host galaxies (Elvis et al., 1994). Quasars for instance exhibit a large bump at UV wavelengths (the "Big Blue Bump"; see Figure 1.2) produced by thermal emission from hot gas in the accretion disk around the SMBH. The 'Big Blue Bump' in quasar SEDs is much stronger than similar UV bumps in normal galaxy SEDs and was one of the first emission characteristics used to detect AGN (UVX; Sandage 1965). Optical and UV wavelength emission from AGN tend to be heavily attenuated when an AGN is obscured. The radio emission from radio-loud quasars is thought to originate from synchrotron radiation produced by electrons spiralling around the magnetic fields produced by quasar jets.

AGN also produce significant amounts of near-IR and mid-IR emission through reprocessing of optical and UV emission from the accretion disk into IR by the dusty molecular torus thought to surround the AGN. This feature can be confused with star formation and has the potential to contaminate star formation rate estimates of the host galaxy. If the star formation of the host galaxy can be correctly estimated, however, then the excess emission at IR wavelengths can serve as an indicator of AGN activity (e.g. Alonso-Herrero et al. 2006; Daddi et al. 2007; Fiore et al. 2008). IR emission encounters very little attenuation due to obscuration, therefore is useful when trying to detect obscured AGN.

AGN also produce a tremendous amount of X-ray emission, and are among the most X-ray luminous extragalactic objects. The X-rays are thought to be produced by the

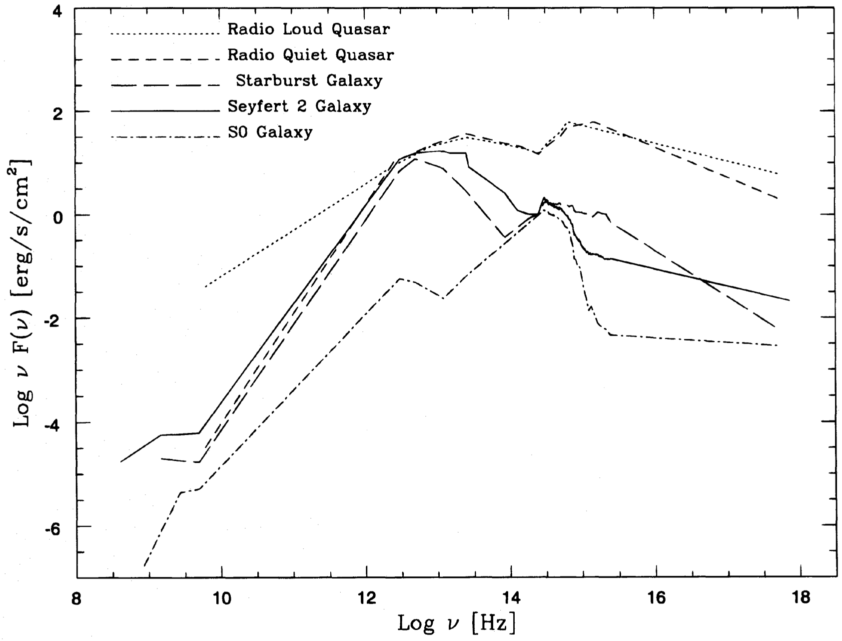

**Figure 1.2:** Measured SEDs of an S0 galaxy (NGC1553), a starburst galaxy (NGC 7714) and a Seyfert 2 galaxy (NGC 1068) with radio-loud and radio-quiet quasar templates (Sanders et al., 1989) overlaid. Figure taken from Kinney et al. (1996).

Compton upscattering of UV photons from the accretion disk by a corona of hot gas (T of order $10^7$K), producing power-law continuum emission. At the highest X-ray energies ($>$ 10keV) a large bump (known as the 'Compton hump') is present in AGN continua. This is thought to be produced by Compton scattering of higher energy photons. Typically it is assumed that objects detected in X-ray surveys with 2-10 keV luminosity $L_X \geq 10^{42}$ ergs $s^{-1}$ are AGN because even the most luminous star-forming galaxies do not exceed this luminosity (Zezas et al., 1998). Recent research has argued this limit can be stretched to $L_X \geq 10^{41}$ ergs $s^{-1}$, with minimal contamination from starburst galaxies (Tozzi et al., 2006; Brightman and Nandra, 2011b). Much like IR emission, X-rays are less heavily attenuated than optical and UV emission and thus prove useful for detecting all but the most heavily obscured AGN.

## 1.2 Observing AGN with X-rays

Using X-ray observations it is possible to study a wide variety of objects on solar, galactic and extragalactic scales. Of particular interest in this work is the utilisation of X-ray surveys to detect AGN. AGN emit strongly over a broad range of wavelengths, but at UV, optical and infrared wavelengths it can be difficult to differentiate their emission from stellar processes. X-ray observations have therefore played a pivotal role in furthering our current understanding of AGN and there role in the universe.

### 1.2.1 The contribution of X-ray surveys

Early methods of space based X-ray detection were primarily rocket-based or balloon borne experiments. Giacconi et al. (1962) were the first to identify X-rays from beyond our solar system from the binary system Sco X-1, and the diffuse glow of the cosmic X-ray background. UHURU (Giacconi et al., 1971) was the first satellite dedicated to X-ray detection, surveying the sky for cosmic X-rays in the range 2-20keV. The observatory was designed to be sensitive to $5 \times 10^{-4}$ times the flux of the crab nebula ($1.5 \times 10^{-11}$ergs cm$^{-2}$ $s^{-1}$), and a positional accuracy of a few arc minutes squared. This instrument was orders of magnitude less accurate than the satellites available today, but it was a vital precursor to modern X-ray astronomy. Results from *UHURU* confirmed the initial findings of Giacconi et al. (1962) and revealed the extragalactic X-rays to have a high degree of isotropy. This was one of the first observations of the extragalactic X-ray background (XRB). The XRB is known to be the aggregate emission of numerous discrete sources, with a dominant contribution provided by AGN (e.g. Setti and Woltjer 1973).

Previous observations of AGN in the X-ray regime demonstrated them to be luminous X-ray emitters (e.g. Tananbaum et al. 1979). Consequently, soft X-ray surveys (0.5-2 keV) have proved vital in identifying large numbers of AGN. Early surveys carried out by *ROSAT* detected an AGN sky density of $\sim 780 - 870$ sources deg$^{-2}$, significantly higher than AGN sky densities produced by AGN selection at other wavelengths (Miyaji et al., 2000). These objects were primarily unobscured AGN. The unobscured AGN identified in these surveys resolved $\sim 80\%$ of the soft X-ray background (Hasinger, 1998). It is thought the remaining unresolved contribution originates from star forming and normal galaxies (Bauer et al., 2002). Surveys of similar depth at hard energies (2-10 keV) are much more difficult to achieve due to the limitations of instrumentation. Hard X-ray observations taken using Gas Imaging Spectrometer (GIS) aboard *ASCA* were confusion limited to sky densities of $\sim 10 - 100$ sources deg$^{-2}$ (e.g. Georgantopoulos et al. 1997; Ueda et al. 1998; Cagnoni et al. 1998; Ishisaki et al. 2001) due to limited angular resolutions. Therefore hard X-ray surveys have resolved a much lower fraction of the hard XRB ($\sim 30\%$; Ueda et al. 1998).

Modern surveys using the current generation of satellites (e.g. *XMM-Newton* and *Chandra*) have resolved a greater fraction of AGN activity and the XRB. The deepest modern survey, the Chandra Deep Field South 4Ms. Observations were taken using the *Chandra* satellite placed the AGN source density at $9800^{+1300}_{-1100}$sources deg$^{-2}$ (Xue et al., 2011) in the regions of deepest exposures. The XRB has also been almost entirely resolved at soft energies and is up to $\sim 60\%$ complete at hard energies (Worsley et al., 2005). They have also improved constraints on X-ray faint AGN populations, such as obscured and Compton thick AGN (e.g. Alexander et al. 2011; Gilli et al. 2011). Greater understanding of the low luminosity AGN population also provides evidence in favour of lowering the commonly accepted AGN X-ray luminosity boundary ($10^{42}$erg s$^{-1}$) to $L_X > 10^{41}$erg s$^{-1}$ (e.g. Tozzi et al. 2006; Brightman and Nandra 2011b). Using X-ray based AGN surveys it is possible to estimate the evolution of the X-ray Luminosity Funciton (XLF) and from this infer the accretion history of the universe (e.g. Maccacaro et al. 1991; Boyle et al. 1993; Ueda et al. 2003; Aird et al. 2010).

While current surveys now have a high level of completeness, the contribution of low luminosity AGN and obscured AGN at higher redshifts remain largely unresolved.

### 1.2.2 X-ray spectra of AGN

X-rays emitted by AGN are thought to be produced by inverse Compton scattering of thermal emission from a "cold" accretion disk off of a hot corona (Haardt and Maraschi, 1993). Inverse Compton scattering occurs when photons collide with 'hot' relativistic free electrons in the corona, exciting the photons to X-ray energies. The observed power-law is a result of Comptonisation of the thermal spectrum of the accretion disk by the hot corona of gas (Sunyaev and Titarchuk, 1980). The model X-ray continuum of an AGN is typically comprised of a power-law defined by the photon index Γ ($F_\gamma(E) \propto E^{-\Gamma}$; where $F_\gamma(E)$ is the photon flux) with a variety of intrinsic emission and absorption features overlaid. The power-law extends from <1 keV to ~100 keV, typically defined by $\Gamma \sim 1.9$ for unobscured AGN, with dispersion $\sigma_p = 0.15$ (Nandra and Pounds, 1994).

Iron line emission is frequently observed in the spectra of AGN. The iron K$\alpha$ fluorescence line from relatively low ionisation states at rest-frame 6.4 keV is the most common, but ionised iron line emission has also been observed. The iron K$\alpha$ line is thought to originate from either the reflection of X-rays off of the accretion disk and the obscuring dust torus or transmission of X-rays through the dust torus. The profile of the line is determined by where in the AGN the fluorescence occurs. For instance a broad iron line is produced by reflection near to the accretion disk due to the strong gravitational redshift effects (Tanaka et al., 1995). Nandra et al. (1997) observed average doppler broadening of $\sim 50,000$ km s$^{-1}$ for the iron lines of 18 Seyfert 1 galaxies. Narrow iron lines are thought to originate from the dust torus because it lies at a greater distance from the SMBH, thus the gravitational effects are less intense and doppler broadening experienced is reduced. AGN also exhibit a Compton reflection hump at energies >20 keV thought to be the result of Compton down scattering (Lightman and White, 1988) of the power-law emission. This feature normally extends from ~ 20 keV to ~ 100 keV, peaking below ~ 60 keV. George and Fabian (1991) attempt to reproduce the X-ray continuum of AGN using models for a "cold" ($\leq 10^6 K$) gas disk irradiated with X-rays. There is a good agreement between this simple model and observations (Pounds et al., 1990; Nandra and Pounds, 1994).

If an AGN is obscured, the majority of X-ray absorption typically occurs in the soft regime (0.5-2 keV) while the hard regime (2-10 keV) typically remains unaffected. Thus a "hard" X-ray spectrum is a robust indicator of X-ray absorption (see Figure 1.3). Obscured AGN spectra also feature a strong reflected emission component, the product of X-ray emission reflecting off of the torus or nearby gas clouds (George and Fabian, 1991). The reflected component can be less attenuated than the transmitted X-ray emission from

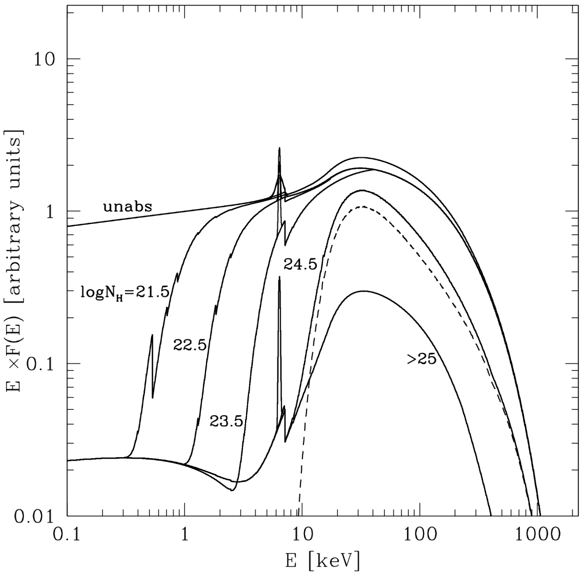

**Figure 1.3:** Model AGN X-ray emission spectra used by Gilli et al. (2007) to model when modelling the XRB. Models for various column densities are represented by solid lines, the attached numbers are $\log_{10}(N_H)$ and the dashed line is the dust torus transmission component of a Compton thick AGN.

the central engine and thus begins to dominate the spectrum of obscured AGN. NGC 6552 is a prime example of an object with a 'Reflection Dominated' spectrum (Reynolds et al., 1994). It is characterised by a flat continuum with a strong 6.4 keV Iron line and other emission line like features that are strong indicators of a fluorescence dominated spectrum, as one would expect to observe in a reflected spectrum (Reynolds et al., 1994). By fitting the X-ray spectrum to a 'warm absorber' model (see Figure 1.4), Reynolds et al. (1994) estimate $N_H = (8.7 \pm 1.8) \times 10^{23}$ cm $^{-2}$, hence NGC 6552 is a heavily obscured AGN. Similar to unobscured AGN, obscured AGN also exhibit a soft excess, the result of either scattered emission or a diffuse thermal component. A thermal excess could be produced by hot gas heated by the AGN or by star-formation within the nuclear region. One of the most significant benefits of observing AGN with X-rays is that it is possible to determine the column density ($N_H$) of obscured AGN by studying soft flux suppression and the reflection component. Spectral fitting provides the best estimates for $N_H$ (Uttley et al., 1999; Guainazzi et al., 2005), but the accuracy of these estimates is dependant on the quality of the spectrum. The variation in the EW of the Iron K$\alpha$ line can be calibrated to estimate the line of sight column density (George and Fabian, 1991). A minor caveat to this is that values of $N_H$ derived from reflected emission represent a lower limit (Maiolino et al., 1998; Risaliti et al., 1999).

Obscured AGN have been observed exhibiting an excess of soft X-ray emission, commonly termed the 'soft excess'. The origins of this soft X-ray emission in local obscured (Seyfert 2) AGN are well understood (e.g. NGC 1068; Kinkhabwala et al. 2002; Brinkman et al. 2002). Their spectra indicate the 'soft excess' feature is produced through a combi-

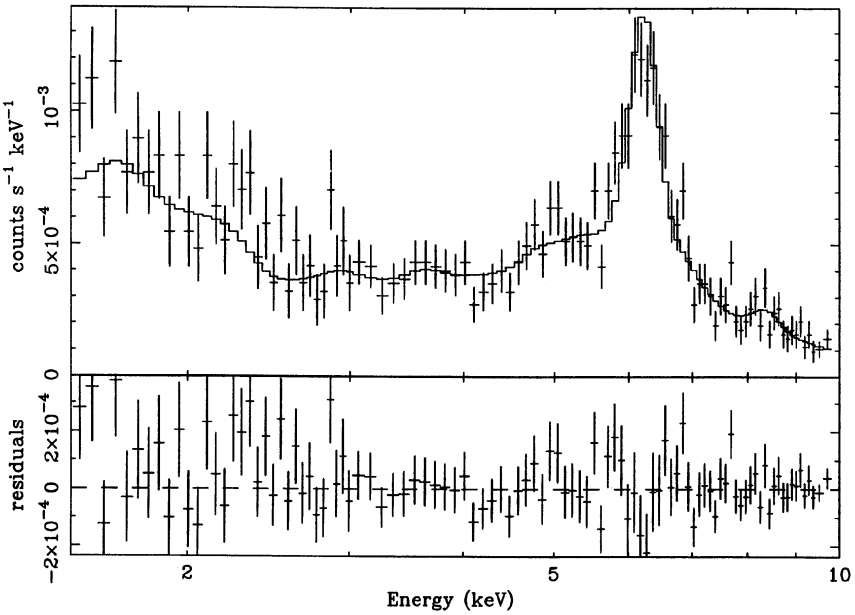

**Figure 1.4:** Reflection Dominated X-ray spectrum of NGC 6552 (Reynolds et al., 1994) with strong K$\alpha$ iron emission line at 6.4 keV, fitted to model spectrum (solid line) with $N_H = (8.7 \pm 1.8) \times 10^{23}$ cm$^{-2}$. Spectrum observed using the GIS on board *ASCA*.

nation of photoionisation and photoexcitation processes. Numerous Radiative Recombination Continua suggest the dominant contribution is from a photoionised plasma (Kinkhabwala et al., 2002). The He-like G ratios observed, however, are atypical of pure recombination, necessitating the presence of an additional component. This additional component is thought to be from photoexcitation as this is the only process which can explain the excess strength of higher order lines, such as He$\gamma$ and He$\delta$ (Kinkhabwala et al., 2002). Using the ratio of photoionisation and photoexcitation processes provides detailed information regarding the geometry of the absorbing/reflecting material. Kinkhabwala et al. (2002) conclude that the absorbing/reemitting material responsible for the 'soft excess' is arranged in a conical geometry. Unobscured AGN also exhibit a 'soft excess'. This feature was first observed by Arnaud et al. (1985), who noticed that the emission in the soft (<2keV) regime is greater than that expected when extrapolating the hard (>2keV) power-law. The origins of the soft excess in unobscured AGN remain a topic of some debate (Gierliński and Done, 2004; Crummy et al., 2006; D'Ammando et al., 2008).

If the column density ($N_H$) is $\gtrsim 10^{24}$ cm$^{-2}$, however, the AGN is "Compton thick" and X-rays in the hard regime also suffer significant attenuation. Above $N_H$=1.5 × $10^{24}$ cm$^{-2}$ the Compton scattering optical depth is greater than one and even the X-ray emission is heavily obscured. In Compton thick AGN almost no X-ray flux from the central source is transmitted through the obscuring medium directly, except for very hard energies (E>10keV). The majority of securely identified Compton thick AGN to date possess reflection dominated spectra. An iron K$\alpha$ line with an unusually large Equivalent Width (EW), associated with this reflection, is another good indicator of Compton thickness

(Krolik and Kallman, 1987). Maiolino et al. (1998) study the spectra of 8 X-ray weak Seyfert 2's, 6 of which are measured to have $N_H > 10^{24}$ cm$^{-2}$ and exhibit prominent K$\alpha$ iron lines (EW > 0.5 keV) and flat continua predicted to be indicative of Compton thick AGN.

## 1.3 The interplay between AGN and their host galaxies

The well documented bulge-mass to black hole mass relations observed in massive bulge galaxies (Kormendy and Richstone, 1995; Faber et al., 1997; Magorrian et al., 1998; Häring and Rix, 2004; Schramm and Silverman, 2013) indicate a physical link between AGN and their host galaxies. There is also a strong coincidence between the epochs of greatest star formation ($z \sim 1-3$; Lilly et al. 1996; Madau et al. 1996; Hopkins et al. 2005) and AGN activity ($z = 2-3$; e.g. Osmer et al. 1994; Hasinger 1998) which many believe to be due to co-eval star formation and black hole growth (e.g. Boyle and Terlevich 1998; Silverman et al. 2008; Aird et al. 2010).

One illustration of the interplay between AGN and their host galaxies is presented by the colour-magnitude diagram (CMD). Galaxies in the local universe are known to produce a bimodal distribution in colour, with early-type quiescent galaxies inhabiting a red parameter space (the "red sequence") while late-type star forming galaxies populate a blue parameter space (the "blue cloud"). In between these major concentrations is an under-dense region of intermediate colour (known as the "green valley"). The red sequence galaxies tend to possess higher masses and higher luminosities than galaxies in the blue cloud and exhibit a strong correlation between mass and colour (metallicity). Galaxies on the red sequence are thought to be much older than the galaxies in the blue cloud. Studies of the evolution of the red sequence since $z \sim 1$ (e.g. Bell et al. 2004; Weiner et al. 2005; Faber et al. 2007) provide clear evidence of a build up of stellar mass in the red sequence. As the majority of these galaxies are quiescent, the build up of stellar mass has instead been attributed to blue cloud galaxies moving onto the red sequence through the quenching of star formation. Overlaying X-ray detected AGN onto the CMD, there is a clear bias towards detecting AGN in galaxies in the red sequence and the green valley (see Nandra et al. (2007a)). These observations predominantly favour a scenario where feedback due to AGN activity is quenching and/or suppressing star formation within the host galaxy (e.g. Hopkins et al. 2006; Croton et al. 2006; Bower et al. 2006). With the AGN preventing the formation of new stars in the host galaxy the average age of the stellar population increases, driving blue cloud galaxies onto the red sequence via the green valley.

### 1.3.1 AGN feedback

It would appear the most direct way in which AGN can interact with their host galaxies is through feedback processes. There is growing observational evidence of AGN feedback processes in the local universe (e.g. Fabian 2012 and references therein), although there is much debate regarding the extent to which these processes can affect the behaviour of host galaxies. At higher redshifts direct observational evidence is lacking but introducing AGN feedback models into galaxy evolution simulations can help reproduce the observed properties such as the luminosity functions. The majority of these feedback models require the AGN to quench star formation activity in the host galaxy (e.g. Fan et al. 2008; Damjanov et al. 2009) to create the old stellar populations observed in massive early-type galaxies in the local universe. These models require high luminosity AGN and are often characterised by violent AGN winds which rapidly quench the star formation. Low luminosity AGN are thought to quench and suppress star formation through more subtle AGN feedback processes (e.g. radio-mode feedback; Croton et al. 2006; Bower et al. 2006).

### 1.3.2 The role of AGN in host galaxy evolution

There are numerous co-evolution models for black-holes and host galaxies. One of the most frequently cited models is that of Hopkins et al. (2005) in which the formation and fuelling of quasars directly influences star formation within the host galaxy. It is assumed that the fuel for AGN formation is provided by the merger of galaxies. When calculating the necessary accretion to produce the luminosities observed in quasars it becomes apparent that the amount of infalling matter should obscure the quasar. When the AGN is "buried" underneath the infalling matter we observe an obscured AGN. Hopkins et al. (2005) propose that the quasar is only visible once feedback - an expulsion of galactic gas by the central source - has occurred. This process blows away the surrounding dust and gas making the quasar visible, but greatly reduces the amount of material available to accrete onto the black hole. Therefore feedback eventually leads to the extinction of the black hole, limiting the time the quasar is visible. The feedback from the AGN also quenches star formation within the host galaxy (Silk and Rees, 1998). This model potentially explains why quasars are scarce as they are only observable during the relatively short intermediate phase between obscuration and extinction, unifying them with lower luminosity AGN. Additionally, violent feedback from luminous AGN could influence the size evolution of its host galaxy (e.g. Fan et al. 2008; Damjanov et al. 2009). Observations of intrinsically X-ray luminous "buried" (ie obscured) AGN at high redshift would go a long way towards corroborate these models, but such observations remain scarce. If such processes are proved to be occurring they could partially explain the disappearance of the massive compact galaxy population observed at $z \sim 2$ (e.g. Daddi et al. 2005; Trujillo et al. 2006; Longhetti et al. 2007; Toft et al. 2007; Zirm et al. 2007; Cassata et al. 2011).

Lower luminosity AGN feedback might also drive the co-evolution of black holes and their host galaxies. The radio-mode feedback mechanism proposed by Croton et al. (2006) is driven by hot gas falling onto the host galaxy, gradually trickling down to the AGN. The infalling hot gas would normally cool and condense, triggering star formation in the host galaxy. The accretion of gas onto the AGN prevents this by producing a gentle feedback that heats the gas, preventing it from cooling and thus suppressing star formation. The galaxies exhibiting this form of AGN feedback are anticipated to be quiescent in their nature and should contain a high fraction of low luminosity AGN. It is unclear whether such feedback processes could drive size evolution in the host galaxies. One of the most recent low luminosity AGN feedback models proposes that the AGN exerts a positive feedback which promotes star formation in the outskirts of the host galaxy (Ishibashi et al., 2013). Several such episodes of this feedback could reproduce the size evolution observed in massive galaxies since $z \sim 2$. Additionally the central regions of the host galaxy would remain quenched, preserving the old stellar cores observed in massive early-type galaxies in the local universe (Heavens et al., 2004; Feulner et al., 2005; Thomas et al., 2005).

## 1.4 The role of obscured AGN

Gilli et al. (2007) postulate the obscured fraction is constant at all times, based on their modelling of the XRB, while the evolution models of Hopkins et al (2005; 2006) imply a greater obscured fraction at earlier times. Either way, obscured AGN play a significant role in the accretion history of the universe and potentially galaxy evolution. The full extent of their contribution can only be verified using a large and representative sample of obscured AGN over a range of redshifts, in particular the elusive Compton thick AGN population.

### 1.4.1 Obscured AGN and the X-ray background

The X-ray Background (XRB) represents the emission of discrete sources summed over all cosmological time, and AGN are thought to be the major contributors to the XRB. The overwhelming majority of the soft XRB has been resolved using emission from unobscured AGN (Hasinger, 1998), with additional contributions from star forming and normal (quiescent) galaxies (Bauer et al., 2002). There is a significant deficit, however, between the hard XRB and the output of discrete X-ray sources. The average spectral slope of unobscured AGN ($\Gamma \sim 1.9$; Nandra and Pounds 1994) over hard energies (ie 2-10keV) is softer than the observed spectral slope of the XRB at similar energies ($\Gamma \sim 1.4$; Comastri et al. 1995). This implies that there is an unresolved hard contribution to the XRB that is flattening the continuum. Worsley et al. (2005) use stacking analysis to resolve the XRB, stacking all observed X-ray sources across a range of energy bands regardless of whether they are detected in that band or not. They resolve 0.5-2 keV and 2-10 keV bands to ~85% and ~80% respectively, but the resolved fraction diminishes in the hard band as energy increases, with only ~60% resolved above 6 keV. It is thought that this hard X-ray deficit (Mushotzky et al., 2000) is a large population of as yet X-ray undetected obscured and Compton thick AGN at high redshifts because they produce flatter, harder continuum emission than unobscured AGN.

Seyfert 2's are known to possess higher average $N_H$ than Type 1's (e.g. Awaki et al.

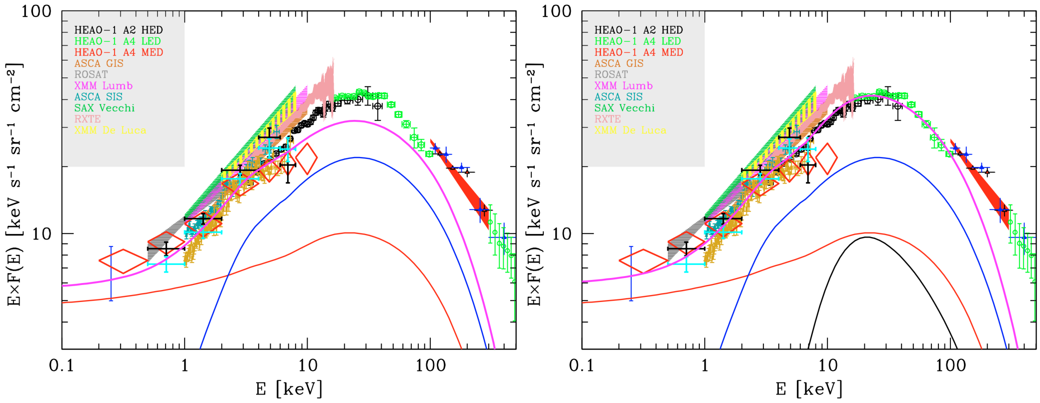

**Figure 1.5:** Synthesised XRB's (magenta curves) of Gilli et al (2007) plotted against observations from literature. The model plotted on the left incorporates the predicted contribution contribution from Compton thin AGN only. The plot on the right incorporates the contribution from Compton thick AGN (black curve).

1991; Smith and Done 1996; Turner et al. 1997; Maiolino et al. 1998). Objects with similarly large $N_H$ at high redshifts could easily go undetected in all but the deepest X-ray surveys. Setti and Woltjer (1989) proposed that unification models predict the existence of dust torus obscured AGN whose emission is heavily absorbed up to 20-30 keV. Their models reproduced the flat spectrum as observed in the XRB energies lower than 20 keV. The emission from these sources could cover the hard X-ray deficit if the number of obscured sources is approximately equal to the number of unobscured sources. Based on their stacking analysis, Worsley et al. (2005) predict a population of heavily obscured AGN, $N_H \sim 10^{23} - 10^{24}$ cm$^{-2}$, at z ∼0.5-1.5 would account for the observed deficit. Gilli et al. (2007) use X-ray surveys studying Compton thin AGN to constrain their contribution to the XRB. They find applying a spread to the range of photon indices about $\langle\Gamma\rangle = 1.9$ partially accounts for the 30 keV XRB deficit, but a Compton thick population is necessary to fully resolve the hard deficit (see Figure 1.5).

Resolving Compton thick AGN at high redshift could have significant implications for the shape of the X-ray Luminosity Functions (e.g. Maccacaro et al. 1991; Boyle et al. 1993; Ueda et al. 2003; Aird et al. 2010). Ueda et al. (2003) use observations of unobscured and obscured sources to synthesise the Hard X-ray Luminosity Function (HXLF) and the $N_H$ distribution between $0 < z < 3$ in order to model the XRB. Their model predicts roughly the same number of Compton thick AGNs with $N_H = 10^{24} - 10^{25}$ cm$^{-2}$ as obscured AGN with $N_H = 10^{23} - 10^{24}$ cm$^{-2}$, which is consistent with current observations in the local universe. Most XRB models are waiting for deep X-ray surveys to confirm their predictions in the hard band regarding heavily obscured and Compton thick AGN.

### 1.4.2 X-ray observations of obscured AGN

Many obscured AGN have been observed in the local universe, with current estimates putting the obscured to unobscured AGN ratio at $\sim 3:1$ (Maiolino and Rieke, 1995). There is strong evidence indicating that the AGN dust torus is the primary obscurer of X-ray emission from AGN in the local universe. For a population of obscured AGN in the local universe, Kirhakos and Steiner (1990) find that ∼90% (25/28) are Type 2 Seyferts. Combining these observation with the torus model proposed by Maiolino and Rieke (1995) indicates that the dust torus is the main obscurer of AGN emission in the local universe. Lawrence (1991) showed the optical depth of a torus varies with luminosity and proposed the probability of a torus existing are reduced as the source power increases. This is known as the "receding torus" model, where more luminous AGN begin to partially sublimate the dust torus, decreasing the solid angle over which the nucleus is obscured. Simpson (2005) uses [O III] emission as an isotropic indicator of source luminosity, because the NLR emission is thought to remain unaffected by the dust torus. They find an increasing fraction of Type 1 AGN as [O III] luminosity increases, which is qualitatively consistent with the receding torus model. Both Ueda et al. (2003) and Gilli et al. (2007) find evidence for a decrease in the obscured fraction of AGN as X-ray luminosity increases, in agreement with the receding torus model.

There are also numerous observations of Compton thick AGN in the local universe. Matt et al. (1996) deduced the Circinus galaxy was Compton thick because its X-ray spectrum was indicative of emission from an invisible nuclear source being reprocessed by cold matter. This produces a flat, 'hard' X-ray spectrum ($\Gamma < 1$) with prominent K$\alpha$ iron line fluorescence (EW about 2 keV). NGC 1068 is one of the most notable and well studied examples of a Compton thick AGN in the local Universe. In addition to possessing the archetypal obscuring torus, Matt et al. (1997) observed a broad reflected iron line feature while the continuum emission was totally obscured at all energies.

While the obscured and Compton thick AGN populations in the Universe are well observed, much less is known about how these populations evolve at high redshifts. The chances of detecting heavily obscured AGN are shown to decrease rapidly with increasing redshift (see Figure 1.6). To date, the overwhelming majority of securely identified Compton thick AGN are limited to the local universe as there are few X-ray surveys that are sufficiently deep to provide high quality X-ray spectra at higher redshifts. Nonetheless, the search for obscured and Compton thick AGN at high redshifts continues in earnest. As stated in Section 1.2.2 the transmitted X-ray emission is often extremely faint but the reflected component is less suppressed by obscuration. This reflected component is typically 2 dex fainter than observed continua of unobscured AGN (Tozzi et al., 2006). The fluorescence of the K$\alpha$ iron line, through either X-ray reflection of the dust torus or accretion disk or X-ray transmission through the dust torus, also remains a strong feature of obscured AGN at high redshift. Some studies have successfully carried out X-ray spectroscopy of high redshift Compton thick AGN (e.g. Georgantopoulos et al. 2009; Comastri

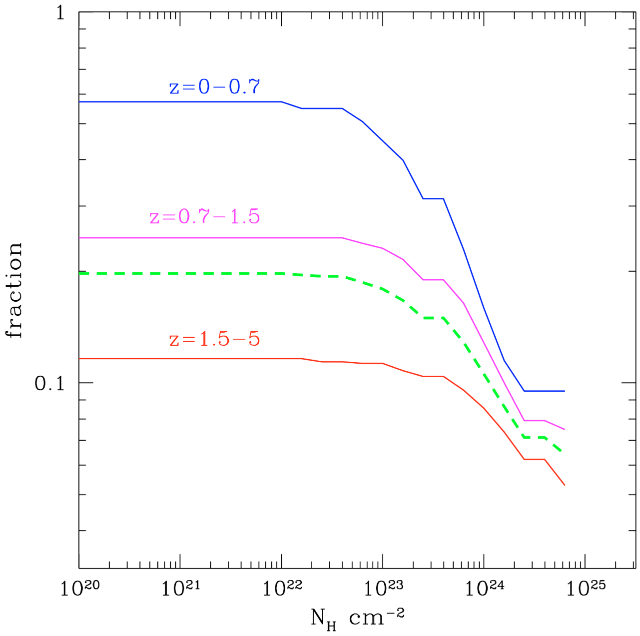

**Figure 1.6:** Fraction of detected AGN with increasing column density (Tozzi et al., 2006), lower detected fraction at higher $z$ as these objects tend to be lower luminosity. Dashed line is the average of all samples depicted.

et al. 2011; Feruglio et al. 2011; Gilli et al. 2011) but these objects only represent a small percentage of the total population. Stacking the X-ray spectra of weakly detected AGN which are thought to be heavily obscured to improve their signal-to-noise ratios has also proved effective (e.g. Alexander et al. 2011). But the large population of Compton thick AGN at high redshift predicted from observations of the XRB hard X-ray deficit is yet to be confirmed observationally.

## 1.5 Identifying obscured AGN without X-rays

One of the main drivers of the research presented in this thesis is the identification of obscured and Compton thick AGN at high redshifts. Such sources can be serendipitously identified in deep X-ray surveys, but the limited coverage of such surveys makes it difficult to constrain the extent of these populations. Additionally the majority of high redshift Compton thick AGN are too X-ray faint and remain completely undetected in typical X-ray surveys (Comastri, 2004). More and more frequently, alternative identification methods using wavelengths (e.g. optical and IR) with wider coverage are implemented to identify obscured AGN candidate sources. The accuracy of these techniques can be checked with follow up X-ray observations through a combination of X-ray spectral fitting and X-ray stacking analyses. If these techniques prove accurate, they may be vital in identifying the large, heavily obscured AGN population predicted from the hard XRB deficit (e.g. Gilli et al. 2007).

### 1.5.1 Mid-IR selection

The majority of the Infrared (IR) emission of AGN is due to thermal emission from dust, hence is observed to be blackbody, or a superposition of many blackbodies. The strongest IR emitters are typically regions of intense star-formation, where high concentrations of gas and dust are in close proximity to young stars, absorbing the UV and optical emission and re-emitting it in the IR. AGN are only a small fraction of all the sources selected in IR surveys, compared to say normal and starburst galaxies, and can be indistinguishable from non-AGN if only a few infrared bands are available (Polletta et al., 2008). But a major benefit of observing in the infrared is that, like X-rays, it experiences far less attenuation than optical and UV when transmitting through gas and dust. This is particularly useful when observing obscured AGN and can in principle reveal AGN in which even the X-ray emission is suppressed. Figure 1.6 illustrates the drop-off in the X-ray detected fraction as $N_H$ increases, with a sharp drop-off as AGN enter moderate-to-heavy obscuration regime ($N_H > 10^{23}$ cm$^{-2}$). Using Infrared emission, which can be less heavily attenuated, techniques for identifying X-ray undetected heavily obscured and Compton thick AGN activity have been developed.

IR emission in Compton thick AGN is thought to be produced by the reprocessing of UV and optical emission from the accretion disk by the dust torus into IR wavelengths. It can be difficult to distinguish between obscured AGN and starbursts without additional characteristic AGN emission features, such as hard X-ray emission or strong radio emission. However, AGN have been observed to possess distinctive mid-infrared colours compared to star-forming galaxies (Lacy et al., 2004; Stern et al., 2005; Hatziminaoglou et al., 2010). Alonso-Herrero et al. (2001) examine the source of non-stellar emission in Seyfert galaxies, typically seen at $\lambda > 3\mu m$ and conclude mid-IR emission can be used as a measure of AGN luminosity. Therefore galaxies exhibiting excessive amounts of mid-IR emission (mid-IR excess) appear likely to contain AGN. This proves especially useful for investigating heavily obscured AGN populations which are faint or undetected in X-ray surveys. LIRG and ULIRG (Sanders and Mirabel, 1996) galaxies are among the most IR luminous objects in the universe, containing vast quantities of molecular dust in their central regions that is ideal for the fuelling of intense starbursts and building/fuelling of AGN. They are likely to be chosen as mid-IR excess galaxies, but it is often unclear whether this is due to an obscured AGN or an obscured starburst.

Fiore et al. (2008) observe that $F(24\mu\mathrm{m})/F(R)$ is tightly correlated to the X-ray to optical flux ratio (itself correlated to X-ray luminosity). They plot this ratio versus the $R-K$ colour, because X-ray obscured AGN tend to have red $R-K$ colours (Brusa et al., 2005), for a sample of X-ray sources. They postulate that sources with $F(24\mu\mathrm{m})/F(R) > 1000$ and $R-K > 4.5$ are powered by highly obscured AGN based on template fitting and stacking analysis. Polletta et al. (2008) select AGN with featureless, red power-law like IR SEDs which exhibit excessive mid-IR emission as obscured candidates, identifying 61 unobscured sources and 120 obscured sources. The 2:1 ratio of obscured to unobscured

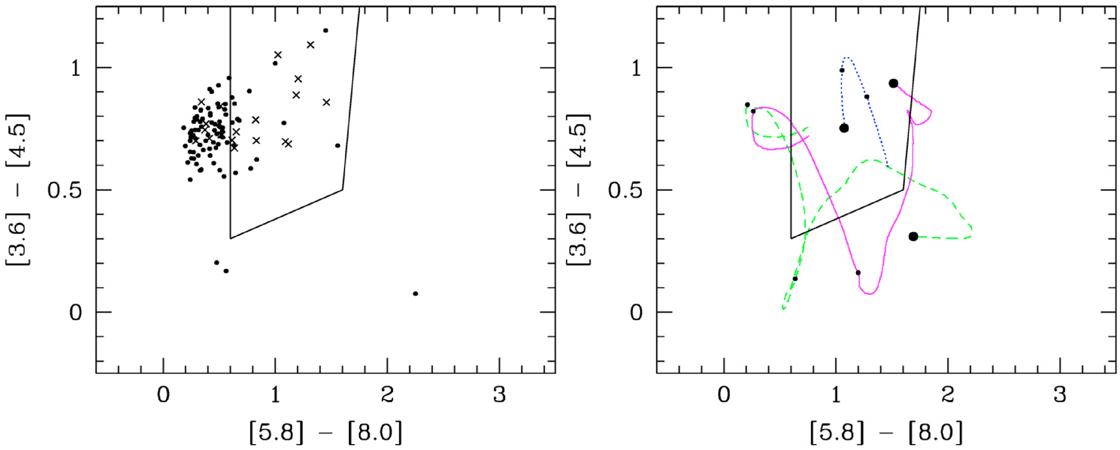

**Figure 1.7:** Stern plots from Georgantopoulos et al. (2008). Left plot depicts distribution of *mid-IR excess* galaxies chosen using the criteria of Fiore et al. (2008). Right plot tracks redshift evolution of for ULIRGs, one of which is a Seyfert 2 (Mrk 273; solid magenta) and the other a starburst (Arp 220; dashed green) for $0 \leq z \leq 3$.

objects is similar to previous studies of a similar nature (e.g. Alonso-Herrero et al. 2006), but is somewhat at odds with the 3:1 ratio which is observed in the local universe and predicted by most XRB models. Using Mid-IR selection, Polletta et al. (2008) estimate a surface density of Compton thick AGN that is 10% of the expected value derived from analysis of the XRB. This suggests that mid-IR excess selection techniques for Compton thick AGN are not as comprehensive as some research has suggested, and any conclusions drawn regarding their contribution to the XRB may require further investigation.

Stacking X-ray undetected mid-IR excess sources may hold the solution to the perceived deficit in obscured AGN activity. Studies in which X-ray undetected mid-IR excess sources are stacked frequently produce hard stacked emission indicative of significant obscured and Compton thick AGN activity (Daddi et al., 2007; Luo et al., 2011). Georgantopoulos et al. (2008) compared the properties of X-ray undetected 24$\mu$m excess (Fiore et al., 2008) and IRAC colour selected AGN using X-ray stacking analysis. They found the Stern wedge selected objects (Stern et al., 2005) exhibit soft X-ray emission suggesting contamination by normal galaxies. The 24$\mu$m excess objects have a much harder stacked continuum indicative of either Compton thick AGN or low luminosity AGN with $N_H \sim 10^{22}$ cm$^{-2}$. Most of these objects lie in a region outside the Stern wedge more commonly associated with star-forming ULIRGs (see Figure 1.7). Donley et al. (2005) look at radio excess relative to 24 $\mu m$ emission for X-ray undetected AGN, finding no Compton thick $N_H$s for X-ray weak AGN, but 6 X-ray undetected sources that could be Compton thick. This corresponds to ∼22% of the sample being Compton thick which is consistent with the lower end of predictions from the XRB. Georgakakis et al. (2010) studied the X-ray luminosity of high IR-optical ratio objects selected by the Fiore et al. (2008) technique and observe many possess low X-ray luminosities ($L_X < 10^{43}$ erg s$^{-1}$). Therefore the Fiore et al. (2008) technique appears to be selecting a significant amount

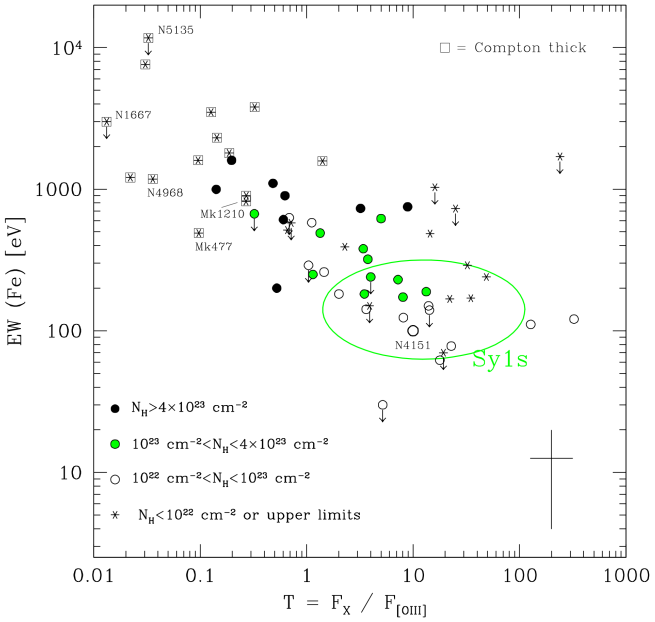

**Figure 1.8:** Plot of K$\alpha$ iron line EW versus T-ratio from Bassani et al (1999). The results presented suggest that sources with T$\leq$0.1 are Compton thick AGN.

of Compton thin AGN, low luminosity AGN and starbursts in addition to Compton thick candidates.

### 1.5.2 Optical emission line diagnostics

The optical emission line diagnostic of Baldwin et al. (1981) and Veilleux and Osterbrock (1987) identify Type 2 AGN with high accuracy out to $z < 0.4$ based on the ratio of optical emission line strengths (e.g. [O III]/H$\beta$ versus [N II]/H$\alpha$). This selection technique (BPT selection) categorises different sources according to the excitation processes using narrow line emission. The AGN are selected based on their dominant [O III] emission, with preferential selection in high metallicity sources. In the case of AGN this emission occurs in narrow line region clouds located away from the central source, therefore suffers less attenuation when the AGN is obscured by the dust torus. The majority of Type 2 AGN in the local universe are obscured (e.g. Kirhakos and Steiner 1990) and contain a high fraction of Compton thick AGN (e.g. Risaliti et al. 1999). Thus the BPT technique can be used to select heavily obscured and Compton thick AGN candidates which remain undetected in X-rays. While the optical window limits the redshifts to which this technique can be implemented in optical spectroscopy ($z < 0.4$), BPT selection can be replicated at higher redshifts using NIR spectroscopy (Trump et al., 2011, 2013). Recent attempts to produce pseudo-BPT diagrams that loosen the redshift constraints to $z \sim 1$ by replacing the longer wavelength emission lines have also proved effective (Weiner et al. 2007; Yan et al. 2011; Juneau et al. 2011; see Chapter 5).

The [OIII] emission line is used as an isotropic indicator of the intrinsic nuclear luminosity of AGN because it is generated by reprocessing of AGN emission in the NLR, which typically remains unobscured in Compton thick AGN. Risaliti et al. (1999) selected an "optimal" sample of Seyfert 2's using observations of the [O III] emission line and found $\sim 50\%$ of the galaxies chosen were Compton thick. The results of Risaliti et al. (1999) also imply the obscuring material is located close to the central source (less than 100 parsecs). Bassani et al. (1999) use the "T-ratio" to identify objects with sufficient column density to be classified as Compton thick. The T-ratio is defined as

$$T = \frac{F(2 - 10keV)}{F([OIII])} \tag{1.1}$$

Comparing the [O III] emission line luminosity to the hard X-ray flux they obtain a probe of the X-ray suppression factor. The full analysis uses a three-dimensional diagnostic (Figure 1.8), plotting the T-ratio against the K$\alpha$ iron line EW for well studied objects with reliable measurements of N$_H$. This diagnostic is a hybrid technique combining the hard spectra and the uniquely broad K$\alpha$ iron line EW associated with reflection dominated AGN to establish definitive identifications. Using this information it is possible to calibrate N$_H$ as a function of $T$, and thus select obscured and Compton thick AGN candidates which are too faint for X-ray spectral fitting. Difficulties in accurately characterising and correcting extinction have been known to reduce the reliability of this technique (Brightman and Nandra, 2011b).

## 1.6 Motivation

Observations of the XRB and local AGN suggest there should be a large population of obscured AGN at high redshifts. To date this population has only been partially uncovered. Greater understanding of this population could also provide further information regarding the nature of AGN feedback processes at high redshift as some of these models require an obscured AGN phase.

In this thesis, promising obscured AGN candidate populations are followed up in deep X-ray surveys to test there efficacy and accuracy. This is done using a combination of X-ray point source detection, X-ray spectral analysis and X-ray stacking analysis. The relationship between AGN properties and those of their host galaxies are also investigated to test for correlations that might enhance our understanding of AGN-host galaxy co-evolution. The first study is a reinvestigation of a mid-IR excess selection at $z \sim 2$ which has shown promise as a method for identifying Compton thick AGN candidates using deeper X-ray data. The second study revolves around the X-ray properties of compact galaxies at $z \sim 2$ that have shown elevated X-ray AGN activity and comparing them to their extended counterparts. The third study is an X-ray followup of optical emission line diagnostic techniques designed to select Type 2 AGN at $0.3 < z < 0.8$, examining the accuracy with which they select obscured AGN.

# Chapter 2

# X-ray data reduction and analysis techniques

## Overview

This chapter outlines the various methods through which X-ray data presented in this thesis have been collected, reduced and interpreted. First a very basic outline of the *Chandra* X-ray observatory is given. Particular attention is paid to the characteristics of the Advanced CCD Imaging Spectrometer and the High Resolution Mirror Array, the two instruments which were used to collect all the X-ray data presented in this thesis. Then the data reduction pipeline used to reduce image data and the associated point source detection software (both developed at Imperial College) are described. The spectral extraction method and the associated spectral fitting techniques used to probe source properties, such as the X-ray luminosity and the obscuring column density, are discussed in detail. Finally the X-ray stacking technique used to probe the average X-ray properties of X-ray undetected sources is described.

## 2.1 *Chandra* X-ray Observatory Instrumentation

In this section the characteristics of the *Chandra* X-ray Observatory, in particular the High Resolution Mirror Array and Advanced CCD Imaging Spectrometer, are discussed. This is to provide context for instrumental effects, such as detector response and PSF widening at high off-axis angles, that need to be accounted for in the data reduction.

### 2.1.1 Mission Overview

Launched on July 23$^{\rm rd}$, 1999, the *Chandra* X-ray Observatory (CXO) is one of NASA's four Great Observatories along with the Hubble Space Telescope (HST), the Spitzer Space Telescope (now running in warm mode) and the Compton Gamma-ray observatory (decommissioned). The CXO follows a highly elliptical (e=0.8) orbit, with an apogee of

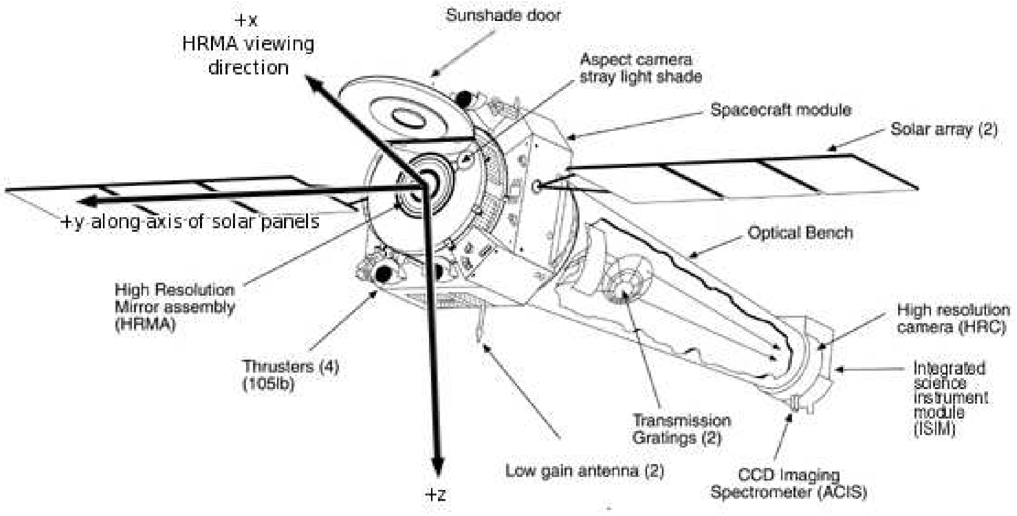

**Figure 2.1:** Diagram of the *Chandra* X-ray Observatory depicting the configuration of the various science instruments on board the satellite. The positioning of the High Resolution Mirror Array and the Advanced CCD Imaging Spectrometer are of particular interest as these are the instruments with which all X-ray data in this thesis have been collected. Figure taken from the *Chandra* Proposers Guide.

140,000 km and a perigee of 10,000 km, around the earth. The orbital period of the satellite is 64.3 hours. This orbital pattern ensures the spacecraft spends upwards of 85% of its orbital period above the belts of charged particles surrounding the earth, allowing for single exposure observations of up to 55 hours in length. The CXO (Figure 2.1) offers order of magnitude advances in spatial and spectral resolution relative to the previous generation of X-ray satellites (e.g. UHURU, ROSAT). X-rays are focused onto the various science instruments using the High Resolution Mirror Array (HRMA), a nested set of Wolter-1 grazing incidence mirrors. The key science instruments are the Advanced CCD Imaging Spectrometer (ACIS) and the High Resolution Camera (HRC). The ACIS instrument is capable of providing imaging and spectroscopy, the latter of which can be enhanced when used in conjunction with the High Energy Transmission Grating. The HRC instrument is designed for wide-field imaging and is sensitive to energies beyond the range of the ACIS instrument, although it does not offer the same level of spectral resolution. More detailed summaries of the *Chandra* X-ray Observatory are provided by the *Chandra* X-ray Observatory website[1] and the *Chandra* Proposers Guide.

### 2.1.2 High Resolution Mirror Array

The X-ray photons are focused onto the ACIS detector using the High Resolution Mirror Assembly (HRMA) (see Figure 2.2). The HRMA offers unparalleled spatial and spectral resolution. Connected to the ACIS instrument by an optical bench, the HRMA consists

---

[1] http://chandra.harvard.edu

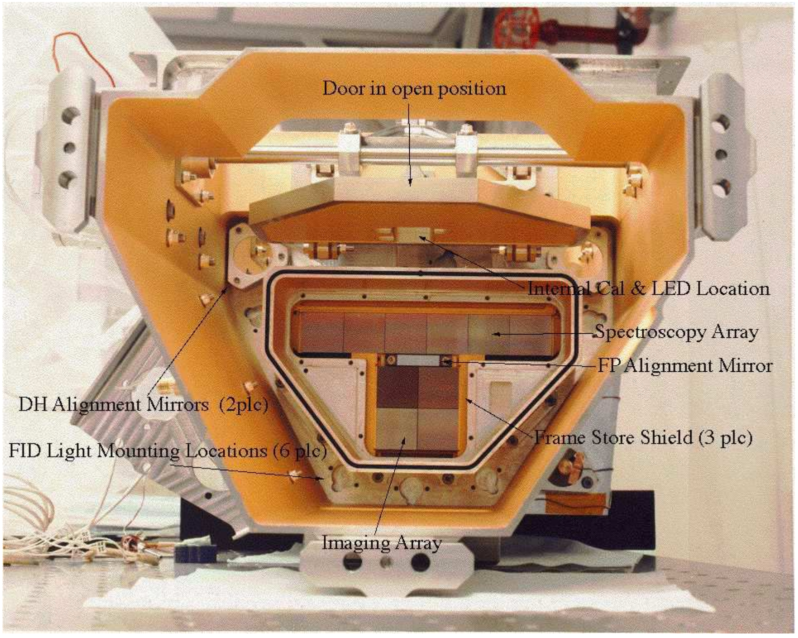

**Figure 2.2:** Photograph of the ACIS viewed as it would be seen looking down the HRMA. Figure taken from the *Chandra* Proposers Guide.

of 4 pairs of concentric nested grazing incidence (Wolter Type-I) mirrors (paraboloids at the front and hyperboloids at the back) with a geometric area of 1145 cm$^2$ (see Figure 2.3; a review of X-ray optics can be found in Aschenbach 1985). The mirror system is held at a constant temperature of 21 °C in order to prevent thermal warping of the mirrors altering the photon optical path. The X-ray reflectivity of the mirrors varies according to both photon energy and photon incidence angle and was measured prior to launch using an X-ray beam from the Brookhaven National Laboratory synchrotron (Graessle et al., 1998, 2004).

The structure of the *Chandra* HRMA plays a key role in determining the PSF of the observed X-ray sources. Source PSFs increase as a function of both off-axis angle (OAA) and photon energy (see Figures 2.4 and 2.5). The PSF is sharpest at the optical aimpoint, widening as the OAA increases due to unavoidable aberrations on the grazing incidence mirror surfaces. The optical aimpoint for the ACIS-I detector is slightly off centre (slightly inset on chip I3; see Figure 2.6) thus the increase in PSF with OAA is not azimuthally symmetric. Wider PSFs at high energies are caused by increased X-ray scattering. The Chandra Ray-Tracing (ChaRT) software package was designed to predict the source PSF/EEF across the ACIS detector after photons had propagated through the HRMA. ChaRT was calibrated using measurements taken at ground based facilities and initial observations taken by *Chandra* just after it was put into orbit.

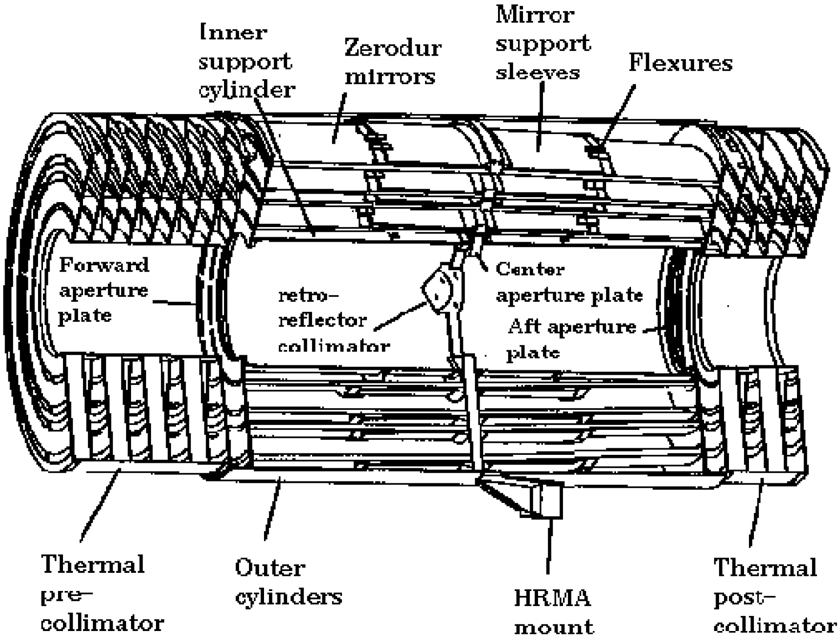

**Figure 2.3:** Schematic of HRMA mirror configuration. Figure taken from the *Chandra* Proposers Guide.

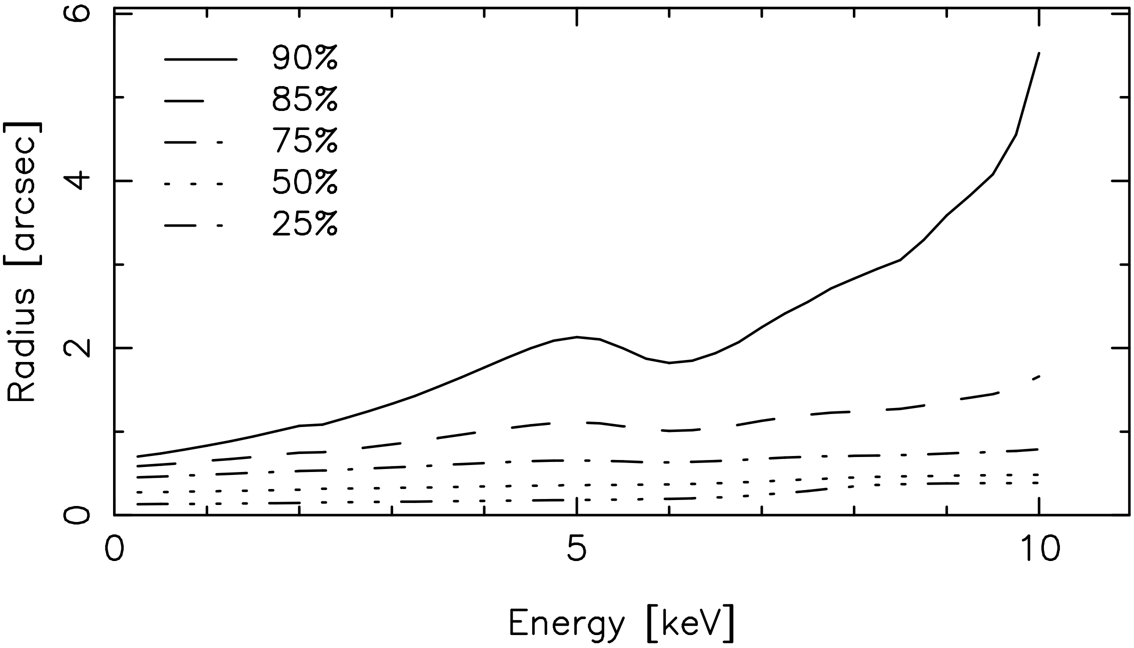

**Figure 2.4:** Variation of the 25, 50 75 85 90% EEFs of an on-axis source as a function of the incident photon energy measured on the ACIS-I instrument. All EEFs have been calculated using a circular profile. Figure taken from the *Chandra* Proposers Guide.

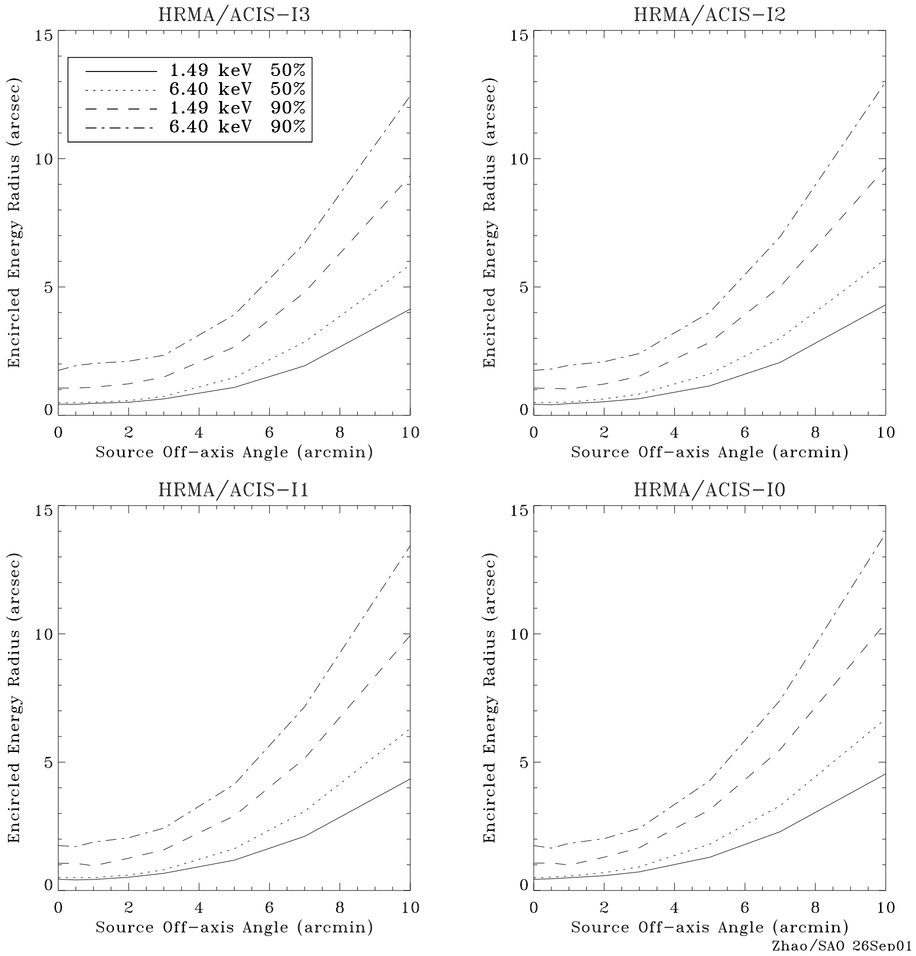

**Figure 2.5:** Variation of the 50 and 90% EEFs as a function of the source OAA calculated for 1.49 keV and 6.40 keV measured on each chip of the ACIS-I instrument. All EEFs have been calculated using a circular profile. The EEFs have been measured for each chip because the nominal aimpoint of the ACIS-I instrument is slightly inset to chip I3. Figure taken from the *Chandra* Proposers Guide.

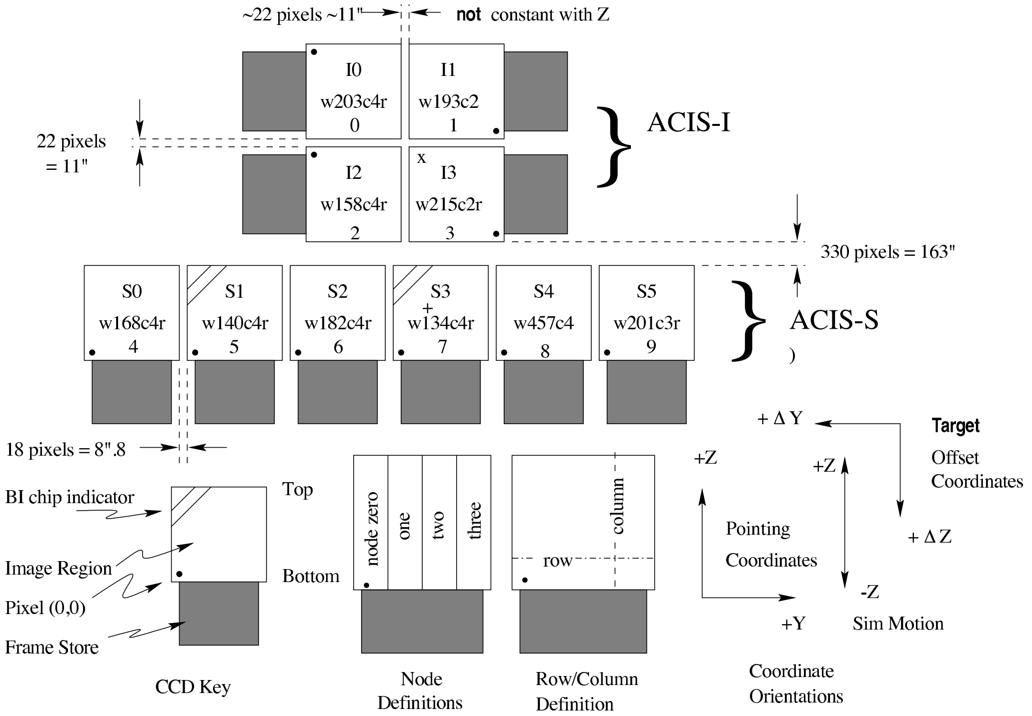

**Figure 2.6:** Sketch diagram of the ACIS focal plane. The nominal aimpoints for the ACIS-I (imaging) and ACIS-S (spectral) arrays are denoted by 'X' and '+' respectively. Figure taken from the *Chandra* Proposers Guide.

### 2.1.3 Advanced CCD Imaging Spectrometer

All X-ray data presented in this thesis was collected using the Advanced CCD Imaging System (ACIS) on board the *Chandra* satellite (see Figure 2.7); this instrument is briefly described here. The ACIS consists of 10 planar 1024x1024 pixel CCDs and is used to acquire high resolution images and moderate resolution spectra of X-ray sources. The 10 CCDs are arranged in two sub-arrays; the 2x2 ACIS-I for imaging and the linear 1x6 ACIS-S for spectroscopy (see Figure 2.6). Up to 6 of the CCDs can be used simultaneously irrespective of the combination, though using more CCDs will obviously increase total count rate and saturate the telemetry more quickly. Two of the CCDs (S1 and S3) are back illuminated (BI) and can probe lower energy ranges than the 8 remaining front illuminated (FI) CCDs. The CCDs are also sensitive down to photons of energy 3.7 eV (optical wavelengths), therefore Optical Blocking Filters (OBF) are placed over the chips to eliminate contamination from UV/Optical photons. Since launch the temperature of the CCDs was lowered until they reached a temperature of $\sim -120\,^{\circ}\mathrm{C}$ on 30$^{\mathrm{th}}$ Jan 2000 and has been held constant ever since.

The spectral resolution of the CCDs is governed by the accuracy with which the charge deposited by an incident photon is measured. Within the detector this can be broken down into two key features; the Quantum Efficiency (QE) and the Charge Transfer Inefficiency (CTI). The QE is the fraction of incident photons that create electron-hole

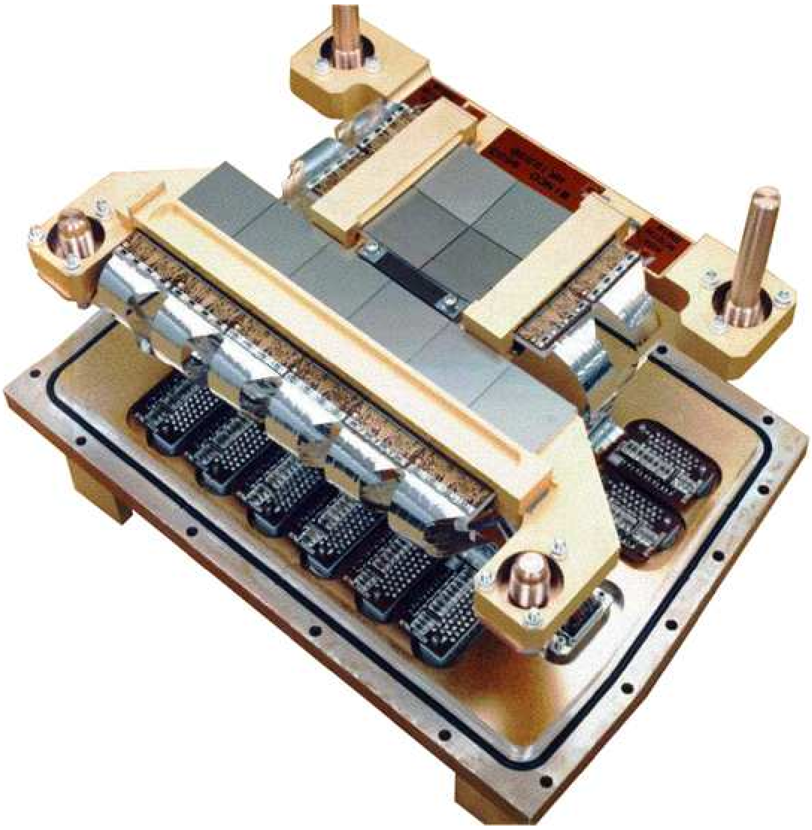

**Figure 2.7:** Photograph of the ACIS prior to installation on the *Chandra* X-ray Observatory. Figure taken from the *Chandra* Proposers Guide.

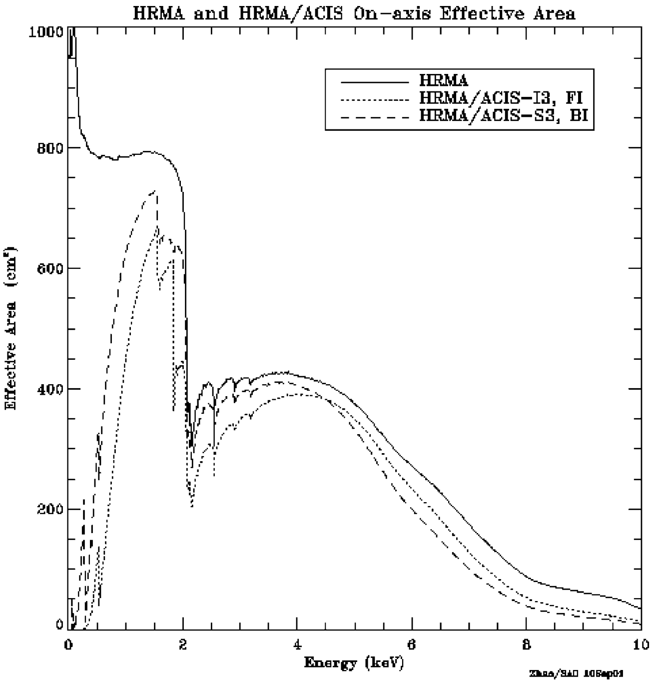

**Figure 2.8:** Variation of the Effective Area of the ACIS instrument as a function of the energy of incident photons taken from Weisskopf et al. (2002). Note the sharp drop-off in effective area at E< 0.5keV.

pairs while the CTI is the fraction of charge lost in pixel-to-pixel transfer. The 'effective area' (EEF) of the ACIS instrument is dependent upon the QE of the detector, the transmission characteristics of the OBF, the reflectivity of the chips and the off-axis pixel vignetting. The on-axis EEF of the ACIS instrument as a function of energy is plotted in Figure 2.8. The ultimate limit on astrometric resolution of $\sim 0.492$ arcseconds is determined by the size of the pixels (24.0$\mu$m). The astrometric resolution increases with off-axis angle due to aberrations in the HRMA (see Section 2.1.2).

Shortly after the satellite's launch the FI CCDs exhibited a distinct increase in the CTI. This is thought to be the result of radiation damage by low-energy protons incurred when the shield for the *Chandra* satellite was left open during radiation belt passages (Townsley et al., 2000). Operational procedures were subsequently changed and no further degradation of the telescope performance in this regard has been noticed. The CTI algorithms were also revised to accommodate for the change in CCD responses. During the satellites operation there has also been a slow and steady deterioration of the energy resolution, reducing the effective area of the instrument. The energy resolution (ie FWHM) varies proportionally to the square root of the energy, thus the degradation is most keenly felt at low energies. This is thought to be the result of molecular contamination of the OBF by outgassed material from *Chandra* itself. Models to account for the change in the instrument response have been periodically released with updates to the *Chandra* calibration database (CALDB), the most recent version having been released with CALDB 4.4.10 (May 30th, 2012). Some of the pixels in the CCD consistently produce spurious or saturated pulse heights during the observations; these are referred to as hot pixels. They are the result of inherent defects within the pixel or due to temporary saturation due to incident cosmic rays. These hot pixels have been mapped and flagged during the telescope's operation and are removed during the data reduction using the acis_remove_hotpix tool (see Section 2.2.2).

Images in the CDFS, CDFN and EGS presented in this thesis were taken using the ACIS-I CCDs (ie chips I0-3). The CDFS 4Ms and CDFN 2Ms are public datasets: the CDFS 4Ms observation program was commissioned as part of the Director's discretionary time, whereas the CDFN 2Ms field is the combination of 500ks of guaranteed time observations and 1.5 Ms of guest observing by W. N. Brandt (Garmire et al., 2003). The EGS 200ks and 800ks observations are proprietary data courtesy of successful proposals by Kirpal Nandra (proposal numbers 06900444 and 09900660 respectively). All spectroscopic data presented herein were extracted from the ACIS-I observations; neither the High Energy Transmission Grating nor the Low Energy Transmission Grating were used. During the observations the spacecraft was dithered using a pattern based on a Lissajous figure. The dithering helps provide exposure in the gaps between the CCDs and smooths out variations in pixel-to-pixel response. The dithering is removed from the data during ground based data processing. The observations presented here were taken in the "Very Faint" mode (VFAINT) where possible; for each incident photon (event) the position, amplitude, arrival time, event grade and pixel values in a 5x5 island were recorded. This mode provides a reduced background making it the optimal observation mode for long exposures. This is only suitable for observations of faint sources/regions ($< 68$counts $\mathrm{s}^{-1}$) otherwise the telemetry will be saturated. For observations where VFAINT mode was unavailable (ie detector temperature $> -120$ degrees C), FAINT mode was used instead (identical to VFAINT except 3x3 pixel islands are measured).

## 2.2 X-ray Image Reduction and Source Detection

### 2.2.1 X-ray Image Reduction Overview

The data reduction pipeline and point source detection procedure used in this thesis was designed by Dr Elise Laird (ESL) during her time at Imperial College London. The most recent description of these procedures can be found in Nandra et al (in prep). This is an updated version of the methodology originally presented in Laird et al (2009)/Nandra et al (2005). The data reduction in CDFS 4Ms and CDFN 2Ms was carried out by myself using CIAO version 4.2 software and CALDB version 4.4.10 calibration libraries. Both EGS 200ks and 800ks data reductions were carried out by ESL using CIAO version 3.4 and 4.2 respectively, the 200ks data having been reduced with an earlier version of the pipeline described in detail in Laird et al 2009. Spectral reduction was carried out using the acis_extract IDL package (Broos et al 2010) following the data reduction recipes of Patrick Broos/given in the manual. All the spectral data presented in this thesis (CDFS 4Ms and EGS) was reduced by myself.

### 2.2.2 X-ray Image Reduction Pipeline

X-ray images are produced using the data reduction pipeline of ESL. Raw data from the Chandra satellite (level 1 event files) is first corrected for known aspect offsets. Hot pixels and cosmic ray afterglows are also removed at this stage using the CIAO acis_run_hotpix task for observations taken in VFAINT mode. In this work the only observations for which this is not the case were those taken to create the EGS-8 field (200ks; Laird et al 2009). These observations were taken in FAINT mode thus the older acis_detect_afterglow routine was used instead. Level 2 event files are produced from the corrected level 1 event files using the acis_process_events routine. This applies the charge-transfer inefficiency (CTI), time-dependent gain corrections and pulse height amplitude (PHA) randomisation. As outlined in Section 2.1.3, the CTI is used to model the potential charge realised upon photons impacting the CCDs and the charge lost as it is shifted from pixel-to-pixel. The loss of charge during readout can result in a change in grade for an 'event' causing some good events to be rejected. PHA randomisation reduces aliasing in the spectra produced from the data. An ACIS particle background cleaning algorithm is applied to all data taken in VFAINT mode to reduce the quiescent background. Each event is also screened according to ASCA grades 0, 2, 3, 4 and 6 (measure of charge dispersion) in order to distinguish between X-ray and charged particle events.

The level 2 event files are screened for background flares by analysing their lightcurves, taken at 50s intervals, using custom software developed by Kirpal Nandra (KN) and Paul O'Neill (Nandra et al 2007b). The algorithm determines the value at which the excess variance of the light curve is equal to zero and designates this as the quiescent background. Time intervals where the count rate exceeds 1.36 times the quiescent level are designated as flares and excluded from further analysis. The flare threshold was empirically derived using ACIS data from the AEGIS-X survey (Laird et al 2009). Sometimes background flares are missed by the algorithm because the rise in count rate is either too gradual or their duration is too brief as demonstrated by Figures 2.9 and 2.10 respectively. Therefore all lightcurves are visually inspected before proceeding with the pipeline. Visual inspection of the lightcurves revealed flares were missed in five CDFS obsIDs (441, 581, 1431, 2405 and 2406) and two CDFN obsIDs (966 and 3389). In these obsIDs the flares were removed manually. Astrometric corrections are also applied to the level 2 event files at this point. These are calculated by comparing obvious X-ray source positions to reference catalogues with superior astrometry. The CIAO *wavdetect* tool is run on each obsID with a threshold probability of $10^{-6}$ to identify bright X-ray sources. These sources should be common to all the obsIDs in a tile and hence ideal for marrying their astrometry. The bright sources are then cross correlated to reference catalogues, recording the offsets between X-

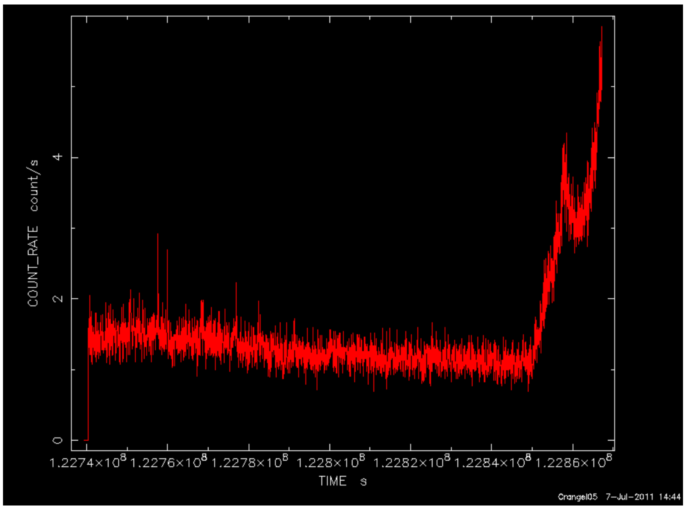

**Figure 2.9:** Unfiltered lightcurve of obsID 3389 in the CDFN field produced by the Imperial X-ray data reduction pipeline. Gradual rise in X-ray activity from $\sim 1.22845 \times 10^8$s until the end of the observation due to flare activity was not detected by the flare removal algorithm and thus had to be removed manually.

ray sources and reference sources. The aspect solutions of the obsIDs are then corrected according to these offsets; squashed, stretched and translated as necessary. In CDFS the reference astrometry was taken from a catalogue of H-band selected galaxies from the GOODS-MUSYC survey (Gawiser et al., 2006). Reference astrometry for the CDFN was taken from an r-band selected catalogue of Capak et al. (2004).

Images of each obsID are now created from the processed level 2 event files following the standard CIAO procedure (merge_all) in four energy bands; 0.5-2.0 keV (soft band), 2.0-7.0 keV (hard band), 4.0-7.0 keV (ultra-hard band) and 0.5-7.0 keV (full band). Photons with energies $<$ 0.5keV and $>$ 7.0keV are omitted from the images because the response of the ACIS-I instrument drops off markedly at these energies (see Figure 2.8; Weisskopf et al 2002). The *merge_all* tool takes into account the gaps between chips, the dithering pattern of the telescope and the instrument efficiencies. Weighted exposure maps are created assuming a $\Gamma = 1.4$ spectrum, a rough approximation to the X-ray background, to model the energy distribution (instrument efficiencies are also a function of energy). Offsets between the obsIDs are calculated with the *align_evt* tool, using a reference catalogue of X-ray sources from the first observation taken in the field. A merged level 2 event file is created for the region using this information. The *reproject_image* tool is then used to create merged exposure maps from the individual exposure maps of each obsID. Finally merged images are produced for each energy band using the merged level 2 event file and corresponding merged exposure map.

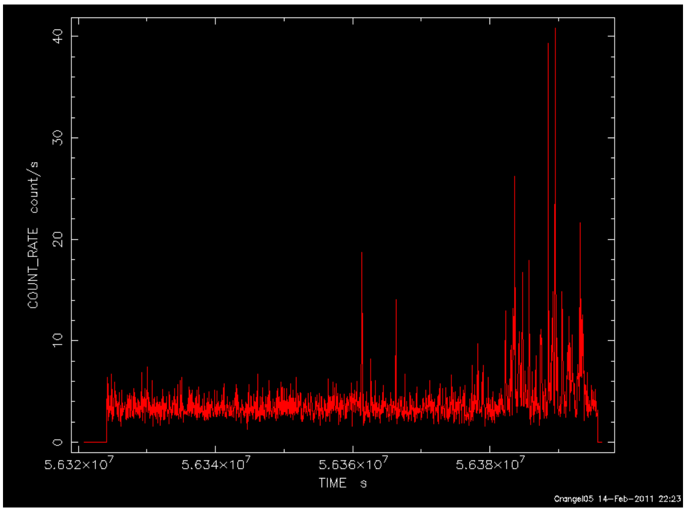

**Figure 2.10:** Unfiltered lightcurve of obsID 581 in the CDFS field produced by the Imperial X-ray data reduction pipeline. Sharp spikes in X-ray activity at $\sim 5.6361 \times 10^7$s and then from $\sim 5.6382 \times 10^7$s until the end of the observation were not detected by the flare removal algorithm and thus had to be removed manually.

### 2.2.3 MARX Point Spread Functions

It is necessary to model potential source PSFs in order to detect X-ray point sources and calculate aperture corrections for the point sources. To this end, PSFs are calculated using a basic version of the Chandra Ray Tracer simulator (ChaRT) HRMA model available within the MARX simulator (Wise et al 2003) software. Elliptical PSFs corresponding to a variety of EEF values (50-95%) across the full extent ACIS-I instrument in a grid (10 pixel intervals). These are stored in a datacube that will be used as a lookup table for X-ray source PSFs to be used in point source detection and photometry calculations (see Section 2.2.4). The final merged image consists of numerous obsIDs with a variety of roll angles and aimpoints, hence the orientation or OAA of a given source will vary over the course of its observation which the final PSF must reflect. To create the final PSF for the merged image to be used in source detection two methods have been employed depending on which version of the pipeline was used to create the point source catalogue. For CDFS 4Ms, CDFN 2Ms and EGS 200ks the PSFs across all obsIDs for a specific source are weighted according to their exposure to produce a single circular PSF. For the EGS 800ks image the elliptical PSFs are combined to make a final elliptical PSF that should more closely resemble the true source profile. The latter method did not provide a significant improvement in either source detection or photometry calculations and for those reasons has not been applied to the other surveys in the interests of time. The same process is repeated in all energy bands.

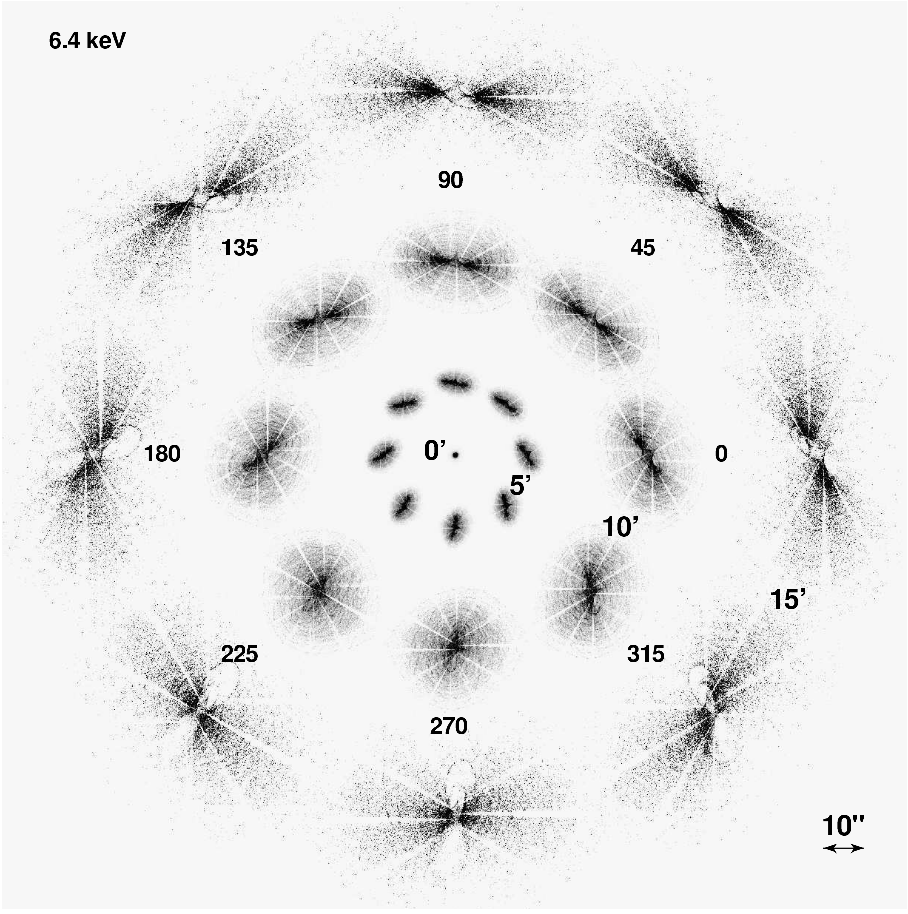

**Figure 2.11:** Simulated Point Spread Functions for 6.4 keV point sources at various OAAs and roll angles. Spokes in the images are due to shadowing by mirror support struts. Figure taken from the *Chandra* Proposers Guide.

### 2.2.4 Source Detection

The source detection is carried out using custom software developed by ESL that employs a variety of CIAO tools. Initially a seed catalogue is produced using the CIAO wavelet detection algorithm *wavdetect*, setting a low significance threshold ($10^{-4}$). This seed catalogue is expected to contain nearly all real sources but will produce numerous spurious sources from background fluctuations. The source counts for all these potential sources are extracted from the 70% EEF of each potential source (using PSFs as defined in the lookup table; see section PSF) as this was empirically determined to be the most efficient aperture for source detection by Laird et al 2009. All potential sources are then masked using their 95% EEFs and individual background estimates for each source using annuli covering regions between the perimeter of 1.5 times the 95% EEF to 100 pixels past this mark. The background counts in these annuli are scaled according to the effective area and exposure within their source extraction regions.

The poisson probability of detecting the observed counts in the source extraction region based on the expected background counts is calculated for all sources. A poisson false-probability threshold of $4 \times 10^{-6}$ is applied to the potential sources (following Nandra et al. 2005), eliminating the majority of spurious sources (and possibly a few legitimate sources). The remaining sources are run through the source detection process a second time so the background fluctuations spuriously identified as sources in the seed catalogue and masked out can now be included in the background calculations. Sources that still satisfy the poisson false probability threshold are now considered genuine.

This source detection process is repeated in all four energy bands separately. It is possible that a source is unique to one of the energy bands but more often they are detected across several. Therefore we merge the source lists from each band to create the final point source catalogue. Covering the widest energy range, the full band is the most likely energy band in which a source would be detected. Thus the sources of soft, hard and ultra-hard bands are first matched to the full band source list. To cross match the sources a nearest neighbour method is adopted with a variable radius equal to 3 times the positional uncertainty of both sources added in quadrature. This is to accommodate the greater positional uncertainties of high OAA sources that might be missed with a fixed radius approach. Sources in which there are multiple possible matches are visually inspected to check that the nearest neighbour assumption is correct. The full band astrometry is thought to be most accurate, therefore the full band position is always adopted if a significant full band detection exists. If not, the positions adopted in descending order are the soft band, then the hard band, and finally the ultra-hard band position. Before finalising the catalogue the sources are visually inspected to ensure they are not the extended regions of other sources. This was the case for 2 sources in the CDFS 4Ms point source catalogue; cdfs4Ms_562 and cdfs4Ms_564. Both sources were soft band only detections, which it transpired were extended regions of full band detected galaxies, and so they were removed.

### 2.2.5 Source Photometry

Once the source detection has run to completion the pipeline computes photometry for the X-ray point sources. The photometry calculations are described in detail in Laird et al (2009); what follows is a brief outline of the method. Photometry calculations are attempted in all four energy bands, regardless of whether they have been detected in all the energy bands. The only exceptions are sources with net source counts $\leq 0$ in an energy band; these sources are assigned an upper flux limit based on the local background. To estimate the source flux, counts are extracted from the 90% EEF while the scaled background counts are calculated in identical fashion to those used in source detection. The scaled background counts are subtracted from the counts within the 90% EEF to give the net source counts. Sources whose 90% EEFs overlap are flagged as their source counts are likely to be contaminated by one another.

Source fluxes are calculated in 4 energy bands commonly used in X-ray analysis; 0.5-10 keV (full band), 0.5-2.0 keV (soft band), 2.0-10.0 keV (hard band) and 4.0-10.0 keV (ultra-hard band). Counts are converted to flux estimates assuming a $\Gamma = 1.4$ power-law spectrum. For the full, hard and ultra-hard bands the spectrum is extrapolated from 7 keV to 10 keV. The Bayesian flux estimation method of Laird et al (2009) is used to correct for Eddington bias (Eddington, 1940).

$$P(S|N,B) \propto L(N|S,B)\pi(S), \tag{2.1}$$

where $P(S|N,B)$ is the posterior distribution function for the source count rate, $\pi(S)$ is the prior distribution function of source count rates and $L(N|S,B)$ is the Poisson likelihood of obtaining the observed data given the source rate and background (see Equation 2.2).

$$L(N|S,B) = \frac{(S+B)^N}{N!} e^{-(S+B)} \tag{2.2}$$

The prior distribution of X-ray fluxes $\pi(S)$ is modelled using a broken power-law (Georgakakis et al., 2008). This compensates for the Eddington bias by modelling the faint source distribution with a shallower slope than bright sources. This Bayesian method is much better at estimating faint source fluxes which can be overestimated by the classical method by up to a factor of 2 (see Laird et al. 2009).

## 2.3 X-ray Spectral Extraction

### 2.3.1 X-ray Spectral Extraction Overview

In this thesis, the nature of X-ray sources is studied in greater depth by fitting models to their X-ray spectra. In particular we use the spectra to study AGN demographics, estimate obscuring column densities and find better estimates for X-ray fluxes and luminosities. Spectral extraction is a non-trivial process as X-ray sources are observed with multiple overlapping obsIDs (with a variety of aim points and roll angles; see Section 2.2.2), with a single source possessing a variety of PSF profiles across the constituent obsIDs. To obtain the most accurate spectra possible the source counts must be extracted from each obsID using the respective PSFs. To facilitate this process, X-ray spectra were extracted using the ACIS EXTRACT IDL package (Broos et al 2010). Developed at Penn State University, the ACIS EXTRACT package is designed to deal with large numbers of sources across multiple overlapping obsIDs. The X-ray data products used as inputs by this package were created using the X-ray data reduction pipeline (see Section 2.2.2). The spectra are extracted directly from the level 2 event files without any binning according to event energy (unlike the reduced image data). Binning is only applied to the spectrum for the purpose of spectral fitting. Spectral extractions of sources in the CDFS 4Ms field were performed by myself, while the spectral extraction of EGS 800ks sources was carried out by Murray Brightman. All spectral fitting of X-ray detected sources in this thesis was carried out by myself.

### 2.3.2 X-ray Spectral Extraction Pipeline

Spectra were extracted following the recipe of Patrick Broos from the ACIS EXTRACT manual. First the *ae_make_catalog* tool uses the MARX ray-tracing tool to generate PSFs for each obsID. For the purposes of spectral extraction the 95% EEF is used to ensure the PSFs enclose and include as many of the source counts as possible (while maintaining a sensible extraction aperture size). The extraction region is iteratively reduced in size if the source is within a crowded region, to avoid contamination of the source counts by neighbouring sources. The PSFs are all created at a “primary” energy of 1.5 keV to minimise variation of PSF size relative to the high-end and low-end of the energy range. PSF ranges are pixelated as opposed to using a simple geometric ellipse to maximise their accuracy. ACIS EXTRACT uses the aspect solution files for each obsID to determine the orientation of the telescope as a function of time to ensure the source dithering is identical to the original observation. The FITS keyword RAND_SKY is read to determine how much blurring ACIS EXTRACT should apply to the PSF images in order to account for pixel randomisation applied to the level 2 event file during the image data reduction (see Section 2.2.2). The *ae_make_catalog* tool also constructs circular masking regions of size 1.1 times the 99% source PSF; these are to be used later in the background extraction.

Next the *ae_standard_extraction* tool is used to extract the spectrum of each source. Using the 90% EEF extraction regions defined by *ae_make_catalog*, source counts are extracted from the level 2 event files of each obsID and subsequently filtered by photon energy to produce the source spectrum (using the dmextract CIAO tool). To calculate the background spectrum, the masking regions calculated by *ae_make_catalog* are applied to the level 2 event file. Annuli are then applied around each source starting at the edge of the masked region and are increased incrementally until a minimum of 150 background counts have been enclosed. The background counts are then scaled according to the size and exposure of the respective source extraction region. This process is repeated for each obsID until every obsID has unique source and background spectra for all sources.

Using source and background spectra in each obsID, composite spectra are created using the *ae_merge_observation* tool. The ACIS-I detector temperature must be identical for all obsIDs that are to be merged to ensure a consistent detector response profile. The source and background spectra extracted from all complementary obsIDs are summed to form the final composite source and background spectrum. The PSF of the composite spectra is created by taking the weighted average of the 1.5 keV PSFs from each obsID; the contribution of each PSF is weighted according to the exposure.

### 2.3.3 Response Files

To use the extracted spectra the spectral analysis package XSPEC requires information regarding how the ACIS-I instrument response varies during the observation. This is done using Ancilliary Response Files (ARF) and Response Matrix Files (RMF). The ARFs store the effective area of the ACIS-I instrument as a function of energy (units cm$^2$ counts photon$^{-1}$). To generate the ARFs for each obsID aspect histograms are created for each obsID using the CIAO tool *mkasphist*. By combining information from the aspect solution file, level 2 event file and dead time correction factor a 3D histogram of duration versus pointing offset and roll offset is created for each obsID. The CIAO tool *mkarf* is then used to create ARFs for each obsID. The ARF generated assumes a 100% EEF was used in the source count extraction so it must be scaled to the 95% EEF employed in the spectral extraction pipeline. The ARFs for each obsID are then combined to create a composite ARF using the FTOOL *addarf*, with their contributions weighted according to the exposure of their respective obsIDs.

The RMF is a 2D matrix file that describes the relationship between X-ray photons' energy and their pulse heights. They are combined with the ARF to predict the number of counts within a given channel assuming the fitted spectral model is valid. RMFs are created for each obsID at the source positions on the ACIS-I CCDs using the CIAO tool *mkacisrmf* by applying the appropriate gain file from the CALDB. The FTOOL *addrmf* is then used to create a composite RMF (with the contribution of an obsID weighted by its exposure) to be used with the composite spectra.

## 2.4 Spectral Fitting

### 2.4.1 Choosing the Goodness of Fit measure

The XSPEC package (v12.4.0; Arnaud 1996) has been used throughout this thesis to interpret X-ray spectra (and associated data products detailing instrument response) and carry out X-ray spectral fitting. The optimum parameters for any model fitted to a spectrum are established by iteratively varying the free input parameters until the 'goodness of fit' measure can no longer be improved. The 'goodness of fit' statistic can then be directly compared to those of other models to establish which model best fits the observed data. In this work the Cash statistic (C-statistic; Cash 1979) is used to measure the 'goodness of fit'; the lower the C-statistic the better the fit of the model. The goodness of fit obtained using the C-statistic is a relative measure by which models fitted to the same spectrum can be compared. It is preferred to other techniques such as the minimum Chi-squared because it is better suited to deal with low count spectra, of which there are numerous examples within this work. The C-statistic does not yield an objective measure of how sensible/realistic the best fitting model is, therefore all optimum spectral fits were visually inspected as a precaution. The XSPEC package features a GOODNESS command which can be used to calculate a numerical measure of the confidence for a spectral fit to Poissonian data. It does so by generating numerous fake models using the covariance matrix of the best-fitting model and comparing their goodness of fit values. In theory the GOODNESS value gives an objective measure regarding the suitability of the best-fitting model relative to competing models. In practice the GOODNESS values returned were often uninformative, with confidence values of the best-fitting models rarely differentiating themselves from competing models with poorer C-statistic values. Given the execution of the GOODNESS command was more time consuming than visual inspection, it was not employed in the final spectral analysis.

### 2.4.2 Spectral Models

A variety of X-ray spectral models have been implemented to characterise the spectra of X-ray sources. These spectral models are drawn from a pool of 4 base models which are used in multiple combinations and iterations to simulate the emission of various types of AGN. A brief summary of these models follows:

(i) Simple power-law (Figure 2.12): The most basic model used in the spectral analysis, the POWERLAW model of the standard XSPEC library is designed to replicate a power-law X-ray continuum produced by inverse Compton scattering. This is the only model which is redshift independent and there are only two parameters to be calibrated; Photon index ($\Gamma$) of the power-law and the normalisation. A spectrum that is best fit by power-law emission is most likely an unobscured AGN.

(ii) Spherical obscuration (Figure 2.13): Custom additive XSPEC model designed by Murray Brightman (see Brightman et al. 2011) simulating the emission profile of an inverse Compton scattering power-law being obscured by a spherical distribution of matter. The obscuring matter is assumed to be a 'warm absorber', with photoexcitation of Fe, C, N, and O atoms acting as the dominant obscuration processes, producing absorption edge features. The model also features self-consistent line emission from Fe K$\alpha$ transitions. There are potentially 5 parameters that can be calibrated in the model; the obscuring column density (N$_H$), the elemental and Fe abundances as well as the $\Gamma$ and normalisation. In practice the elemental and Fe abundances are held at solar levels and the $\Gamma$ is fixed at 1.9 (typical AGN synchrotron emission profile; see Nandra et al 1997) throughout all spectral fitting analyses. This model spectrum is thought to be the best analogue for AGN whose emission is dominated by galactic absorption.

(iii) Toroidal obscuration (Figure 2.14): Custom additive XSPEC model designed by Murray Brightman (see Brightman et al 2012) this model is designed to simulate the emission profile of an inverse Compton scattering power-law that is being absorbed by toroidally distributed obscuring material. The obscuring matter is assumed to be a 'warm absorber' where photoexcitation is the dominant process. As with spheroidal obscuration this model also features self consistent Fe K$\alpha$ line emission. This model requires 7 input parameters: $N_H$, the elemental and Fe abundances, $\Gamma$, the normalisation, the opening angle of the dust torus and the viewing angle of the observer. As with the spheroidal obscuration model, elemental and Fe abundances are held at solar levels and $\Gamma$=1.9. The choice of viewing angle can fundamentally alter the nature of the observed emission. If the viewing angle is greater than the opening angle then the spectrum will simply resemble obscured inverse Compton scattering power-law emission. If, however, the viewing angle is less than the opening angle then the central engine is observed directly and the absorption effects are greatly reduced. This will not default to a simple power-law though, as strong reflection components (ie Iron K$\alpha$ line complexes) will still be present within the spectrum. Throughout this work different combinations of torus opening angles and viewing angles are utilised, although they are always fixed prior to fitting to avoid rampant model degeneracy. A secondary POWERLAW model is always used in conjunction with this model to simulate inverse Compton scattering power-law emission from the central source that has been scattered into the line of sight by hot electrons in the ionisation cone. The scattered power-law is fixed to the same $\Gamma$ as the central source (1.9) but the normalisation is left free. This is a reasonable assumption for low S/N data, but is should be noted that scattered emission from the ionisation cone is thought to produce the soft excess observed in local Type 2 AGN (Kinkhabwala et al., 2002; Brinkman et al., 2002). Overlooking this additional complexity could adversely affect spectral fits to more detailed spectra. This scattered component is included regardless of the viewing angle. This model spectrum is representative of an AGN which has a torus of obscuring dust surrounding it. The obscuring dust torus is in close proximity to the central source, just beyond the accretion disc (1-10 parsecs) and is an intrinsic structural component of the AGN (ie Antonucci 1993).

(iv) Reflection dominated (Figure 2.15): Custom additive model developed by Nandra et al. (2007b) that is now part of the XSPEC package extended library simulating the profile of a reflected inverse Compton scattering power-law. The PEXMON model is based on the neutral reflection model of Magdziarz and Zdziarski (1995) which describes reflection off of a slab geometry. Nandra et al. (2007b) then added Fe K$\alpha$

line emission with strengths calibrated according to the Monte Carlo calculations of George and Fabian (1991). Additionally Fe K$\beta$ (7.05 keV) and Ni K$\alpha$ (7.47 keV) emission lines, with fluxes 11.3% and 5% of the Fe K$\alpha$ flux respectively, are included (Nandra et al., 2007b). The model has 7 parameters that must be calibrated; $\Gamma$, the cutoff energy, the scaling factor for reflected component relative to the source, elemental and Fe abundances, the inclination angle and the normalisation. Elemental and Fe abundances are fixed to solar values and $\Gamma$ is fixed as 1.9 and the cutoff energy is fixed at the default of 1000keV. The scaling factor is fixed at -1. This is equivalent to there being no direct component in the observed spectrum (ie PEXMON is the pure reflection component). The inclination angle is fixed at 60 degrees throughout because it has negligible impact on the final C-statistic value when left free. As with the toroidal obscurer a secondary POWERLAW model is appended, in this case to serve as a substitute for a scattered power-law spectrum; once again assumed to originate from scattering off of hot electrons in the ionisation cone. The $\Gamma$ of the direct POWERLAW is tied to that used for the PEXMON model ($\Gamma$ = 1.9) and the normalisation is left free. The normalisation of the PEXMON component (representative of pure reflection from the central source) is representative of the true source intensity. The scattered component is only a fraction of the emission from the central source, with its intensity, and hence the normalisation factor, scaling linearly with that of the central source. Thus the ratio of the normalisations for the reflected and scattered components (henceforth R-value) can be used as an indicator of the severity of the obscuration. For heavily obscured AGN the normalisation of the scattered component will be much lower than that of the PEXMON component, and hence will exhibit a high R-value. There is a great deal of uncertainty when scaling the R-value to obscuration, however, thus it is only used to sort reflection dominated AGN into two broad categories; Compton thick and Compton thin AGN. Compton thick AGN ($N_H \geq 10^{24}$cm$^{-2}$) typically exhibit an R-value$\geq$30, whereas for R-value<30 the AGN is assumed to be Compton thin ($10^{22} < N_H < 10^{24}$cm$^{-2}$). This model specialises in identifying AGN whose spectra are reflection dominated.

### 2.4.3 Accommodating Additional Free Parameters

Many of the models used within this work have a differing number of free parameters (see Section 2.4.2). Models with more free parameters can potentially achieve lower C-statistic values (especially if emission profiles are similar) even if they are a poorer fit for the spectrum in question. This is because the model with more free parameters has fewer degrees of freedom contributing to their final C-statistic value. Therefore when comparing the basic C-statistic values of models with different numbers of free parameters, the models with more free parameters typically appear to provide superior fits. To correct for this effect the typical offset between the C-statistic values model pairings with differing numbers of free parameters (henceforth $\Delta_{cstat}$) must be estimated.

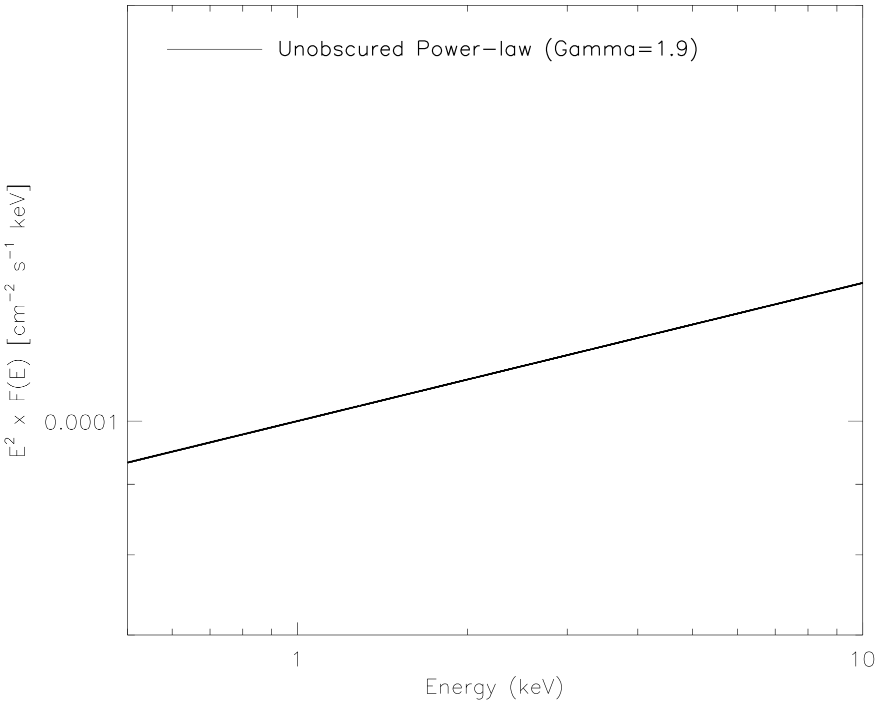

**Figure 2.12:** Model spectrum used to approximate unobscured AGN synchrotron X-ray emission. For the purposes of this plot the photon index has been fixed at $\Gamma = 1.9$ for the purposes of this plot.

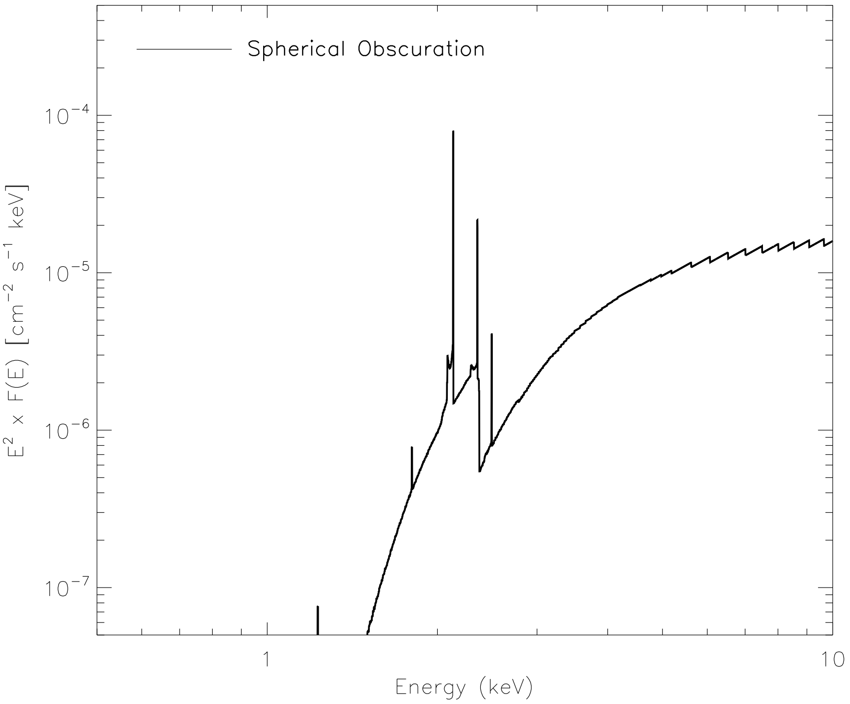

**Figure 2.13:** Model spectrum used to approximate the X-ray emission of an AGN at $z = 2$ obscured by spherically distributed matter. For the purposes of this plot the photon index has been fixed at $\Gamma = 1.9$ and the column density has been set at $N_H = 10^{24}\text{cm}^{-2}$.

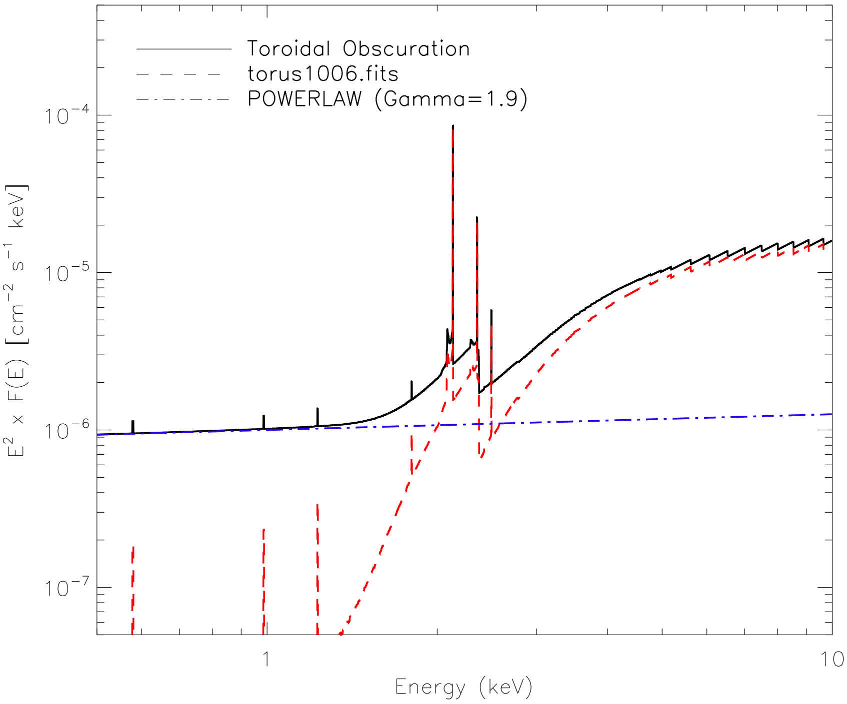

**Figure 2.14:** Model spectrum used to approximate the X-ray emission of an AGN at $z = 2$ obscured by a close proximity dust torus ($\sim$ 10parsecs). For the purposes of this plot the photon index has been fixed at $\Gamma = 1.9$ and the column density has been set at $N_H = 10^{24}cm^{-2}$. The dust torus is assumed to have an opening angle of 30 degrees a viewing angle of 80 degrees. This model spectrum has an additional reflected component which is assumed to be a power-law ($\Gamma = 1.9$) which has been normalised to 1% of the strength of the torus obscured emission.

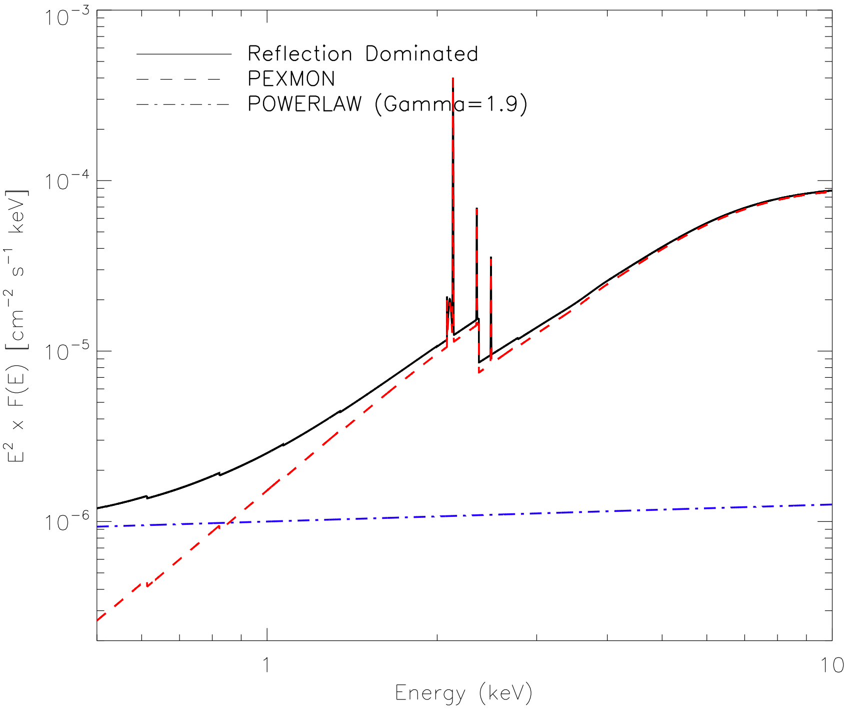

**Figure 2.15:** Model spectrum used to approximate the X-ray emission of an AGN at $z = 2$ which is reflection dominated. For the purposes of this plot the photon index has been fixed at $\Gamma = 1.9$. This model spectrum has an additional direct emission component which is assumed to be a power-law ($\Gamma = 1.9$) which has been normalised to 1% of the strength of the reflected emission.

To estimate the $\Delta_{cstat}$ values for a specific spectral model relative to other models is a non-trivial process. Fist multiple fake spectra are generated based upon one of the models (base model) using the XSPEC FAKEIT command in conjunction with the best fit for the model in question to a real X-ray spectrum. The base model is then fitted to the resulting fake X-ray spectra and the C-statistic values are recorded. The fake spectra are then fitted with model spectra with differing amounts of free parameters to the base model, again recording the resulting C-statistic values. This creates an array of C-statistic values from which the offset of various models relative to the base model can be calculated for each fake spectrum. Collating the offsets for all the fake spectra and ordering them lowest to highest percentile thresholds for the $\Delta_{cstat}$ value for each (necessary) model pairing are then calculated. This process is repeated as necessary until $\Delta_{cstat}$ threshold values for all permutations of model pairings were calculated. In each calculation of the $\Delta_{cstat}$ 1000 fake spectra were generated. This minimised the computational workload while ensuring the $\Delta_{cstat}$ thresholds drawn from offset distributions were statistically robust to outliers. For each model pairing the 90, 95 and 99 percentile thresholds for $\Delta_{cstat}$ were estimated by drawing the 900th, 950th and 990th largest offset values respectively.

### 2.4.4 Selecting the Optimal Grouping Method

To interpret the spectra using the XSPEC package they must be grouped by either spectral counts or energy channels. Grouping the spectrum by counts requires that all bins contain a minimum number of counts (obviously $\geq 1$). The resolution of a count grouped spectrum varies according to the distribution of counts; the size of each bin is determined by the number of energy channels that must be incrementally added to fulfil the minimum count requirement. Grouping the spectrum by counts ensures that all the bins are occupied, but to facilitate this bins may be elongated/smeared in faint objects creating misleading spectral profiles. Grouping by energy channels limits the number of channels contributing to each bin. The resolution of a channel grouped spectrum is fixed but some bins may contain zero counts (unoccupied), especially if the source is faint. The temptation is to maximise the spectral resolution by using the smallest grouping limits possible so as to gain greater insights into complex features in the spectra. However, over-sampling significantly reduces the statistical robustness of the spectral fitting process and unoccupied bins can cause the XSPEC cstat fitting procedure to fail (see https://astrophysics.gsfc.nasa.gov/XSPECwiki/low_count_spectra [17-06-2013]). Therefore minimum grouping sizes were empirically derived for count grouped and channel grouped spectra of 4 counts and 8 channels respectively. These minimum groupings offer the highest spectral resolution while maintaining a reasonable level of statistical robustness for spectral fits.

There are subtle differences in energy resolution between spectra grouped by counts compared to spectra grouped according to energy channels. While in X-ray bright sources the spectral fits obtained should be identical, the differences in energy resolution can

**Table 2.1:** Description models used for spectral fitting analysis comparing count binned and channel binned spectra. Columns (3) to (7) describe the parameters of the various models used. Free parameters are labeled as such, otherwise the parameter has been fixed to the value quoted. Solar abundance values were assumed for elements heavier than He (including Fe).Column (1): name of model (see Section 2.4.2); column (2): model ID; column (3): number of free parameters in the model; column (4): photon index of power-law emission from the central source; column (5): normalisation factor for power-law emission from the central source; column (6): column density of obscuring material; column (7): photon index of central scattered power-law emission; column (8): normalisation factor for scattered power-law emission.

| Model name (1) | Model ID (2) | $N_{free}$ (3) | $\Gamma_{src}$ (4) | $Norm_{src}$ (5) | $N_H$ (6) | $\Gamma_{scat}$ (7) | $Norm_{scat}$ (8) |
|---|---|---|---|---|---|---|---|
| Simple Power-law | A | 2 | Free | Free | ... | ... | ... |
| Simple Power-law | B | 1 | 1.9 | Free | ... | ... | ... |
| Spherical obscuration | C | 2 | 1.9 | Free | Free | ... | ... |
| Toroidal obscuration | D | 3 | 1.9 | Free | Free | 1.9 | Free |
| Reflection dominated | E | 2 | 1.9 | Free | ... | 1.9 | Free |

significantly alter the choice of best fitting model for X-ray faint sources. Given the sizeable proportion of X-ray faint sources in this thesis it was decided that only one of either count or channel grouping should be consistently used for all spectral analyses, unless exceptional circumstances dictated otherwise. The ideal grouping method should provide conservative spectral fits for X-ray sources, avoiding misclassification of random fluctuations as complex spectral features.

The most suitable grouping method was chosen using a sample of 22 X-ray detected quiescent galaxies in the CDFS 4Ms, with well defined redshifts and a range of X-ray fluxes. Quiescent (ie red) galaxies were used to minimise the contamination of the X-ray spectrum by star formation. The spectra were grouped by counts and channels (4 and 8 respectively; the minimum reasonable amounts as defined above) and then subjected to equivalent spectral fitting processes. The X-ray spectral models used in this fitting process are drawn from the same pool as those used for all further spectral analysis in this thesis. Then by comparing the resulting best fitting spectra for each source the most suitable grouping method was chosen based on visual inspection of spectra with differing best fits. It is important that when plotting spectra XSPEC combines the spectral counts, spectral model and instrument response to predict the final spectrum. Therefore the count distribution will be subtly biased towards the model spectrum being used, making it difficult to visually disentangle the optimum model spectrum.

Five models were used for the purpose of this spectral fitting analysis (see Table 2.1).

**Table 2.2:** Threshold values of $\Delta_{cstat}$ used to establish best fitting models for channel grouped (minimum 8 channels) and count grouped (minimum 4 counts) spectra. The $\Delta_{cstat}$ thresholds quoted are added to the C-statistic value of the model with more free parameters involved in the comparison prior to deciding which model is the superior fit. These $\Delta_{cstat}$ values were only used in the spectral analysis carried out to establish whether count grouped or channel grouped spectra provided more accurate spectral fits. Only the 99% confidence levels have been used in this analysis. Column (1): Number of counts in the X-ray spectrum subjected to fitting analysis; column (2): threshold $\Delta_{cstat}$ when comparing count grouped spectrum to one another; column (3): threshold $\Delta_{cstat}$ (99% confidence) when comparing channel grouped spectrum to one another.

| Spectral Counts (1) | Count Grouped $\Delta_{cstat}$ (2) | Channel Grouped $\Delta_{cstat}$ (3) |
|---|---|---|
| $< 100 counts$ | 1.0 | 3.0 |
| $100 \leq$ counts $< 500$ | 2.0 | 4.0 |
| $\geq 500$ counts | 5.0 | 5.0 |

Models A and B are free and fixed photon index variants of the simple power-law model. Models C, D and E are the spherical obscuration model, toroidal obscuration model and the reflection dominated model respectively. Descriptions of these models can be found in Section 2.4.2.

The final C-statistic and hence the $\Delta_{cstat}$ of count binned data varies according to the number of bins. The more bins a spectrum possesses the larger $\Delta_{cstat}$ values are due to the additional degrees of freedom. Therefore samples of spectra binned by counts are split into three cases dependent upon the number of counts as a proxy for bins; $< 100$ counts, $100 \leq$ counts $< 500$ and $> 500$ counts (see Table 2.2). Channel grouped data has the same number of bins regardless of the X-ray spectral counts but obviously sources with more counts will have more robust emission features and thus there will be a greater spread in the resulting C-statistic values. Consequently the $\Delta_{cstat}$ thresholds also evolve according to the number of counts, although not to the same degree as count grouped data. Ideally $\Delta_{cstat}$ values are calculated for all permutations of competing spectral models (see Section 2.4.3). For the purpose of this simplified analysis, however, a uniform $\Delta_{cstat}$ threshold is used for all permutations of model comparisons where one model has more free parameters than the other (see Table 2.2). The $\Delta_{cstat}$ thresholds were chosen based on values used by similar spectral analyses in the literature (e.g. Brightman et al. 2011a). The reliability of these $\Delta_{cstat}$ thresholds were tested by comparing the best fitting models for these galaxies to those obtained by Brightman et al 2011a. Generally the fits obtained showed good agreement although differences in the spectral models used in the two analyses led to some variation.

The results of spectral fitting using count and channel grouped data can be found in Table 2.3. The two grouping methods showed fairly good agreement across the sample with 15/22 spectra assigned identical best fitting models. As expected these were primarily the most X-ray bright sources in the sample. A comparison of the remaining 7 sources follows:

(i) cdfs4Ms_083 - the brightest source in which the best fitting models differ (901 counts). The count binned data is best fit by an unobscured power-law with a hard X-ray spectrum $\Gamma \sim 1.6$ whereas channel binned data is best fit by the spherical obscuration model with $N_H = 1.9 \times 10^{22}\mathrm{cm}^{-2}$. The X-ray power-law fit to the count grouped data is harder than typically observed in unobscured AGN ($\sim 1.9$). A hard X-ray power-law spectrum such as this can be indicative of obscured AGN emission, so it is likely that the count grouped spectrum has been misclassified. Visual inspection reveals the count grouped spectrum to be very noisy with a higher energy resolution than the channel binned data. Very faint increase in counts at ~2keV equated to weak Iron K$\alpha$ line emission in channel grouped data leading to classification as spherically obscured AGN. C-statistic of spherical obscuration model for count grouped data only marginally worse ($\Delta_{cstat} \sim 1$) than the unobscured free power-law and the resultant best fit has a column density which is consistent at the $1\sigma$ level ($N_H = 1.80 \pm 0.5 \times 10^{22}\mathrm{cm}^{-2}$). The unobscured power-law does not characterise the E< 1keV regime as capably as the spherical obscuration model. In light of visual inspection it appears that the count grouped spectrum is being oversampled and the spectrum was misclassified as a result.

(ii) cdfs4Ms_116 - a moderately bright source (counts=405) classified as a torus obscured AGN with $N_H = 91.2 \times 10^{22}\mathrm{cm}^{-2}$ when grouped by counts but as a spherically obscured AGN with $N_H = 70.8 \times 10^{22}\mathrm{cm}^{-2}$ when grouped by channels. Column density estimates for each source are consistent at the $1\sigma$ level. Visual inspection of each best fitting model indicates they are of equivalent energy resolution with the only major difference in the behaviour at E< 1keV where the flux in the torus model is boosted by the reflected component. The most conservative model to adopt in this case is the spherical obscuration model as it has fewer degrees of freedom.

(iii) cdfs4Ms_135 - a faint source (counts=40) classified as a reflection dominated Compton thick AGN when grouped by counts but as a simple unobscured fixed powerlaw ($\Gamma = 1.9$) when grouped by channels. Visual inspection of the count grouped spectrum suggests a faint Iron k$\alpha$ line but the energy resolution is too low for this to be considered definitive. The unobscured power-law is a more pragmatic choice for the best fitting spectral model given the faint nature of the source.

(iv) cdfs4Ms_266 - a bright X-ray source (counts=970) classified as a reflection dominated spectrum when grouped by counts but classified as a dust torus obscured AGN when grouped by channels. Both models classify the source as a Compton thick AGN ($N_H > 10^{24}\mathrm{cm}^{-2}$). Visual inspection of the spectral fits indicates these are the optimum models for each spectral grouping method. In this case, the count grouped data was attributed the more conservative model (fewer free parameters).

(v) cdfs4Ms_317 - A faint source (counts=85) classified as a torus obscured Compton thick AGN when grouped by counts but classified as an unobscured fixed power-law AGN when grouped by channels. Visual inspection of the spectrum in both grouping regimes reveals an emission line feature at observed frame $\sim$ 2.3keV, but Iron K$\alpha$ line emission in the observed frame is expected at $\sim$ 2.45keV for this source. It may be the case the emission line feature is a random fluctuation, so the unobscured fixed power-law model identified using channel binned data appears a more prudent selection given this inconsistency.

(vi) cdfs4Ms_412 and cdfs4Ms_443 - Both sources are faint ($<$ 100 counts) and classified as Compton thick torus obscured AGN when grouped by counts, but are better fit by reflection dominated Compton thick AGN spectra when binned by channels. Both spectra show evidence of iron K$\alpha$ line emission consistent with a strong reflected X-ray emission component. In the Compton thick regime ($N_H > 10^{24}\mathrm{cm}^{-2}$) the torus obscured model is very similar to the reflection dominated model and it is not possible to disentangle the models visually with such faint sources. The reflection dominated model chosen for the channel binned data is the more conservative model of the two as it has fewer free parameters.

For the sources where count and channel grouped data present different best fits the models are often only subtly different, with features such as the column density of the competing models remaining very similar. The channel binned spectrum appears to be the most conservative approach, selecting the most fits with fewer free parameters (except for cdfs4Ms_083 and cdfs4Ms_266) when there are disagreements between the methods. The consistent energy resolution of the channel grouped spectra appears to produce more stable and pragmatic best fits. The basic properties of the spectra should be nominally the same as those produced by count grouping but there is reduced risk of claiming more complex behaviour that is only proved incorrect in hindsight/future observations. Therefore for all further spectral analysis in this thesis only channel grouped spectra are used.

**Table 2.3:** Results of spectral fitting analysis for 22 quiescent galaxies in the CDFS 4Ms whose spectra have been grouped by counts and by channels. Column (1): X-ray source ID taken from the Imperial College London CDFS 4Ms point source catalogue; column (2): X-ray counts in spectrum over the 0.5-8.0 keV energy range; column (3): best redshift estimate for source, spectroscopic redshifts are denoted with †; column (4): best fitting spectral model when using a count grouped spectrum; column (5): obscuring column density according to best fitting model for count grouped spectrum (where applicable), units $10^{22}$cm$^{-2}$; column (6): spectral index of best fitting model for count grouped spectrum; column (7): best fitting spectral model when using a channel grouped spectrum; column (8): obscuring column density according to best fitting model for channel grouped spectrum (where applicable), units $10^{22}$cm$^{-2}$; column (9): spectral index of best fitting model for channel grouped spectrum.

| | | | Count Grouped | | | Channel Grouped | | |
|---|---|---|---|---|---|---|---|---|
| X-ray ID (1) | Counts (2) | $z_{best}$ (3) | model (4) | N$_H$ (5) | $\Gamma$ (6) | model (7) | N$_H$ (8) | $\Gamma$ (9) |
| cdfs4Ms_024 | 69 | 1.78† | B | | 1.9 | B | ... | 1.9 |
| cdfs4Ms_050 | 641 | 1.54† | D | 65.88 | 1.9 | D | 65.21 | 1.9 |
| cdfs4Ms_054 | 98 | 0.58† | C | 0.99 | 1.9 | C | 0.97 | 1.9 |
| cdfs4Ms_059 | 99 | 0.70 | A | ... | 2.5 | A | ... | 2.5 |
| cdfs4Ms_060 | 152 | 1.33† | B | ... | 1.9 | B | ... | 1.9 |
| cdfs4Ms_061 | 184 | 2.52 | C | 13.79 | 1.9 | C | 13.34 | 1.9 |
| cdfs4Ms_066 | 700 | 1.02† | C | 6.77 | 1.9 | C | 6.88 | 1.9 |
| cdfs4Ms_067 | 55 | 0.83† | B | ... | 1.9 | B | ... | 1.9 |
| cdfs4Ms_083 | 911 | 2.53 | A | ... | 1.6488 | C | 1.91 | 1.9 |
| cdfs4Ms_089 | 325 | 1.73† | D | 37.60 | 1.9 | D | 38.45 | 1.9 |
| cdfs4Ms_116 | 405 | 2.59† | D | 91.15 | 1.9 | C | 70.84 | 1.9 |
| cdfs4Ms_127 | 212 | 0.74† | B | ... | 1.9 | B | ... | 1.9 |
| cdfs4Ms_135 | 40 | 1.7453 | E | >100.0 | 1.9 | B | ... | 1.9 |

*Continued on next page*

Table 2.3 – *Continued from previous page*

| | | Count Grouped | | | Channel Grouped | | | |
|---|---|---|---|---|---|---|---|---|
| X-ray ID | Counts | $z_{best}$ | model | N$_H$ | $\Gamma$ | model | N$_H$ | $\Gamma$ |
| (1) | (2) | (3) | (4) | (5) | (6) | (7) | (8) | (9) |
| cdfs4Ms_237 | 124 | 1.00 | D | 3.8971 | 1.9 | C | 4.05 | 1.9 |
| cdfs4Ms_266 | 970 | 2.61† | E | >100.0 | 1.9 | D | 239.01 | 1.9 |
| cdfs4Ms_267 | 750 | 0.98† | C | 10.76 | 1.9 | C | 10.70 | 1.9 |
| cdfs4Ms_317 | 85 | 1.61† | D | 625.58 | 1.9 | B | ... | 1.9 |
| cdfs4Ms_412 | 63 | 2.49† | D | 226.59 | 1.9 | E | >100.0 | 1.9 |
| cdfs4Ms_423 | 74 | 1.05† | C | 27.93 | 1.9 | C | 29.35 | 1.9 |
| cdfs4Ms_437 | 48 | 2.47† | C | 147.14 | 1.9 | C | 145.62 | 1.9 |
| cdfs4Ms_443 | 71 | 0.90† | D | 228.06 | 1.9 | E | >100.0 | 1.9 |
| cdfs4Ms_460 | 190 | 2.14† | C | 145.24 | 1.9 | C | 147.15 | 1.9 |

### 2.4.5 Luminosity Calculations

The precision of estimates for the X-ray luminosity of sources is greatly improved once a model spectrum is fitted. It is also possible to calculate the unabsorbed luminosity for X-ray sources where obscuration has been detected. The X-ray luminosity provides an objective measure of AGN activity (ie accretion rate of AGN). The absorbed and unabsorbed luminosities for all models subjected to spectral fitting analysis are calculated using the LUMIN function of XSPEC. Absorbed luminosity measurements for spherical obscuration, toroidal obscuration and reflection dominated models are made using the best fitting model parameters. Obviously there can be no absorbed luminosity for the unobscured POWERLAW model. The absorption corrected luminosity for the unobscured POWERLAW model is taken directly using the LUMIN function when the best fitting parameters are in place. The absorption corrected luminosity for the spherically obscured model is calculated by setting the column density to $N_H = 10^{20}\text{cm}^{-2}$ (approximately the column density of the Milky Way when observing the CDFS, ie unobscured AGN) while holding all other parameters at the values assigned by the best-fit and measuring the luminosity. The absorption corrected luminosity of the toroidal obscuration model is calculated in similar fashion, with the additional requirement that the reflected component be removed as well prior to measuring the luminosity. The absorption corrected luminosity of the reflection dominated spectrum is calculated by setting the normalisation of the direct component (POWERLAW) equal to that of the reflected component and then removing the reflected component and measuring the luminosity.

## 2.5 X-ray Stacking Analysis

### 2.5.1 What is Stacking Analysis?

In an astronomical context, stacking analyses involve combining the emission of multiple sources that are considered to be similar to obtain a single high signal-to-noise measurement (see Figure 2.16). The stacked signal provides information regarding the aggregate contribution of the sources and can be used to infer the average properties of the individual sources. Stacking analyses are typically used to investigate the properties of sources that have been designated as interesting but lie below the detection limit of observations in the desired waveband. Although stacking analyses are used extensively throughout astronomy there is no consensus view for the optimal stacking method; instead there are numerous competing methods each tailored to suit the populations they are analysing. The low count statistics of the sources typically studied using stacking analyses make them very sensitive to random fluctuations and biases that may be inadvertently introduced by the chosen method (e.g. sky subtraction).

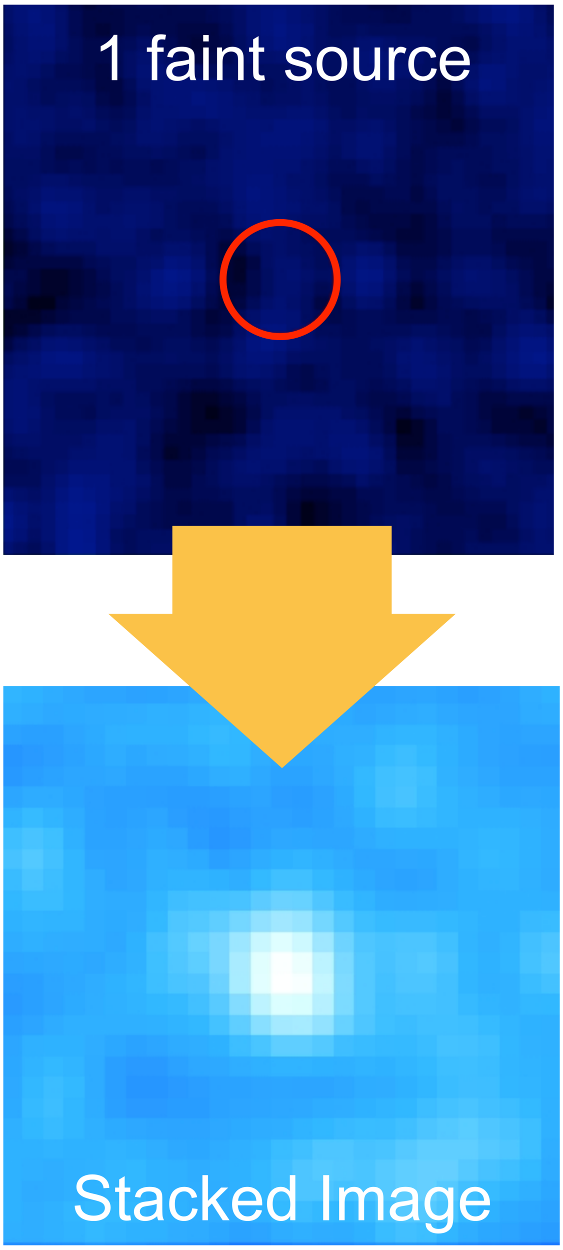

**Figure 2.16:** Images illustrating the improvement in signal-to-noise achieved through stacking X-ray undetected galaxies. The top panel is a postage stamp of one of the X-ray undetected sources while the bottom panel is an image created by stacking 80 X-ray undetected galaxies. The red circle in the X-ray undetected source image depicts the approximate position of the source from which source counts were extracted during stacking analysis (see Section 2.5.3).

### 2.5.2 Stacking X-ray emission

X-ray stacking analyses can be subdivided into two broad genres; spectral stacking and broad band stacking. Spectral stacking is typically used to improve the signal-to-noise of detected sources with low resolution spectra to identify shared complex features such as the iron K-alpha line. For instance Brusa et al. (2005) stacked the emission of X-ray detected sources to examine the evolution of iron K$\alpha$ line emission from $z = 0{-}3$. Using the signal-to-noise ratios, Brusa et al. (2005) were able to deduce the Equivalent Widths (EW) of iron lines remained constant out to $z \sim 3$ which implies the Iron abundance remains constant over this redshift range. Broad band stacking on the other hand typically focuses on boosting the signal-to-noise of broad band emission of X-ray undetected sources. These broad bands are usually determined by the energy ranges of image data from which the source counts for the X-ray undetected sources are extracted. While not as detailed the broad band information can be used to infer basic properties of the spectra (e.g. whether or not the stacked sources are obscured) and calculate rough estimates of the average X-ray fluxes and luminosities. Laird et al. (2005) stacked the broad band emission of X-ray undetected Balmer Break galaxies (BBG) and found their spectra to be dominated by soft X-ray emission ($\Gamma \sim 1.8$) which implied the majority of sources contained unobscured AGN. They also found a strong correlation between the X-ray flux and rest-frame UV fluxes of the BBGs.

Regardless of whether one is stacking spectra or broad band emission, the most precarious element of any stacking analysis is correctly disentangling source emission from the background. The most basic approach is to define separate source and background regions from which to extract the counts and then interpret the net emission as the true source emission. More complex methods “clip” the background to account for random fluctuations due to instrumental effects or flare events. Overzealous implementation of clipping techniques can lead to artificial biases and misleading results. One such example is the work of Treister et al. (2011) who presented X-ray stacking analysis of $z \sim 6{-}8$ galaxies with the aim of investigating AGN accretion activity in the early universe. Clipping the localised backgrounds for each source they recorded significant stacked signal in both hard and soft energy regimes, which they used to place limits on the black hole growth in the $z \sim 6 - 8$ redshift regime and conclude that the most copiously accreting black holes are heavily obscured. Subsequent publications (e.g. Willott 2011) showed the X-ray stacking methodology to be flawed as the clipping procedure was suppressing the actual background, hence artificially boosting the apparent stacked signal. Correct application of the clipping technique revealed no significant emission in the stacked signal at either hard or soft energies (Willott, 2011).

### 2.5.3 Stacking Methodology

In this thesis a broad band stacking technique is implemented to probe the X-ray properties of samples of X-ray undetected galaxies. The primary aim of this analysis is to search for low luminosity (soft emission) and heavily obscured (hard emission) AGN activity lying below the detection threshold of the X-ray observations. To maximise the efficacy and accuracy of the stacking technique only galaxy samples that are thought to possess consistent X-ray spectral profiles are stacked together. As such the galaxy samples are grouped according to specific features e.g. their SEDs in non-X-ray wavelengths or their physical properties (ie mass or size). The X-ray contribution of stacked sources and the background are extracted from the merged broad band images created using the Imperial College X-ray reduction pipeline created by Elise Laird (see Section 2.2.2). The positional information for all stacked galaxies was taken from the observations with the most accurate astrometry (optical wavelengths in most cases).

The stacking methodology is based on the work of Nandra et al. (2002) and Laird et al. (2005). Fixed radius circular apertures are used to sample the emission from sources contributing to the stacked signal. The emission from within these apertures should be a combination of both background and source counts. Variable apertures were considered for source extraction but previous studies have found this to provide either a negligible or detrimental effect on the signal-to-noise ratio of the stacked signal (Laird et al., 2005). Local backgrounds are calculated for each source to mitigate the effects of background anisotropies across the observation field. The background counts are extracted from annuli surrounding each source with fixed dimensions. The underlying ethos for the background sampling method is simplicity, therefore no clipping methods are implemented in the background analysis thus avoiding the pitfalls to which previous stacking analyses fell foul (e.g. Treister et al. 2011). It is assumed with great confidence that the overwhelming majority of instrumental and flare effects have been removed given the exhaustive and conservative nature of the image data reduction pipeline (see Section 2.2.2) rendering background clipping unnecessary. The background annuli all have inner radii of 10 arcseconds and outer radii of 30 arcseconds (see Figure 2.17). The size of these annuli was chosen based on the average PSF of sources; beyond the inner radius the likelihood of source count contamination drops significantly. The background is estimated by randomly shuffling to 10,000 positions within the annulus and sampling the counts from the pixel nearest each position. The total counts extracted within the annulus are then scaled to match the corresponding extraction aperture according to both pixel area and exposure to derive the localised background. The stacked signal is the difference between the sum of counts extracted from the source apertures and the sum of the local backgrounds. The signal-to-noise ratio (SN=$S/\sqrt{N}$; where $S$ = source counts and $N$ = total counts) of the stacked signal is calculated to determine the significance of the stacked emission. Throughout this thesis stacked signals with SN$\geq$3 are considered significant detections, 2.5$\leq$SN<3.0 are considered low significance detections and SN< 2.5 are considered non-detections.

It is imperative that the contributions of bright X-ray sources to the stack remain at an absolute minimum. The low count statistics of the contributing X-ray undetected sources make the stacked signal very sensitive to bright source contamination. For example, an X-

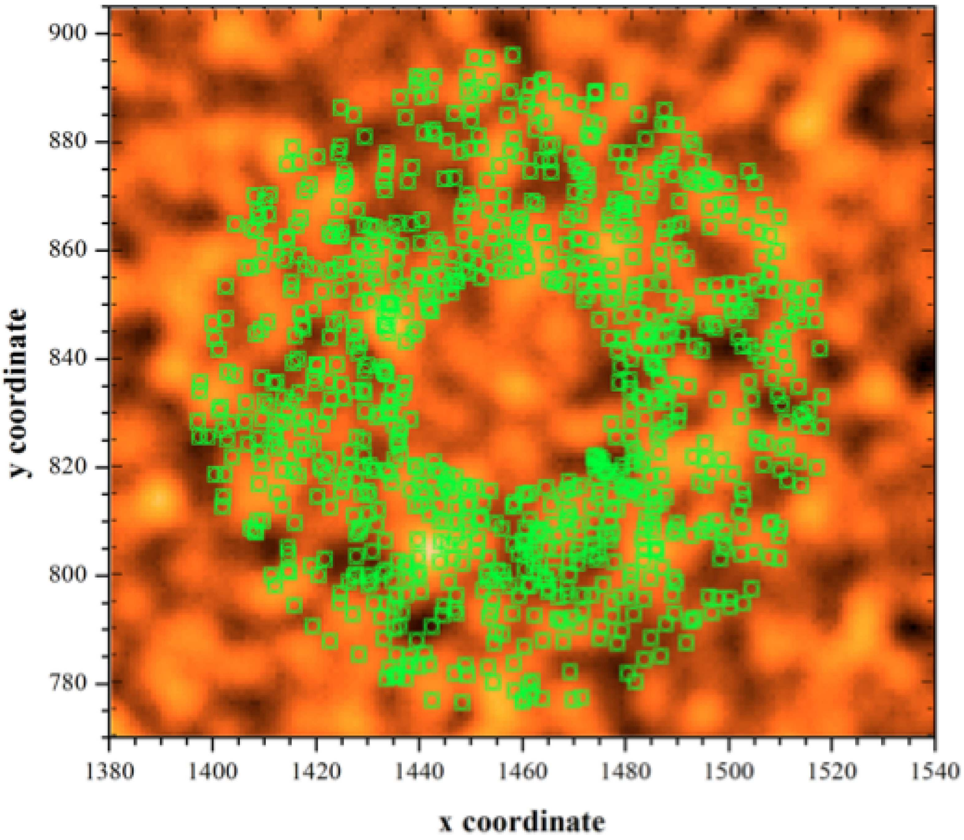

**Figure 2.17:** Postage stamp image illustrating background sampling methodology used in the stacking analysis. Pixels sampled for counts during the random shuffle are highlighted with green squares. For the purpose of this diagram only 1000 pixels have been sampled to improve image fidelity.

ray source of moderate brightness ($F_{0.5-10keV}$ of order $10^{-16}$erg s$^{-1}$cm$^{-2}$) emits $N_{cts} \sim 80$ whereas the average X-ray undetected source emits $N_{cts} \sim 3$. Therefore the stacked signal of order 100 X-ray undetected sources could be skewed into a non-representative X-ray spectral profile by a single X-ray detected source. To circumvent this problem, all X-ray sources from the point source catalogues (generated using the Imperial college X-ray data reduction pipeline; see Section 2.2.4) are masked from the merged images when stacking. The circular masking regions are equivalent to twice the 90% EEF of the source in question, with the EEFs extracted from the point source catalogue (see Section 2.2.4). If the position of a source falls within one of the masked regions it is excluded from the stack. Likewise any pixels from the background annulus of a source that overlap with a masked region are excluded from the background analysis (see Figure 2.18).

Using a fixed circular aperture returns an accurate representation of the signal-to-noise ratio of the stacked signal but it is unlikely to have captured all the source counts. Therefore the measured flux from a fixed circular aperture will be lower than the actual

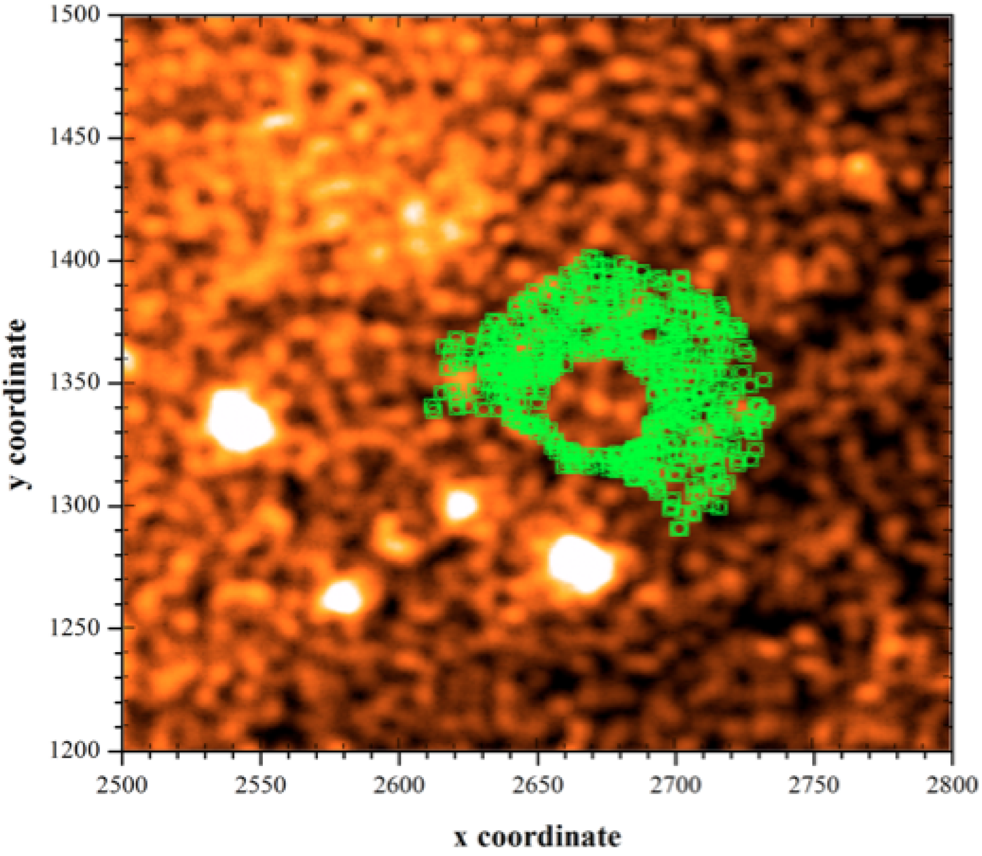

**Figure 2.18:** Postage stamp image illustrating where background region has been partially masked due to the close proximity of bright sources (ie falls within 2 times the 90% PSF). For the purpose of this diagram only 1000 pixels were sampled. These are highlighted by the green squares.

source flux. This problem increases exponentially as the OAA increases due to widening of the PSFs caused by aberrations on the grazing incidence mirrors (see Figure 2.11). The aperture correction is designed to assess and compensate for the incomplete sampling of source counts by the fixed apertures. For this stacking method the aperture correction is a singular multiplicative factor (based on the weighted contributions of the aperture corrections for individual sources) that is applied to the stacked signal.

$$apcorr_{total} = \sum_{i}^{N_{src}} apcorr_i * \frac{counts_i}{counts_{sum}} \tag{2.3}$$

The individual aperture correction ($apcorr_i$) of each source is defined as the inverse of the EEF of the fixed circular aperture used; the EEFs for individual sources were derived using the MARX ray-tracing software. These individual aperture corrections are then weighted by the contribution of the source to the stacked signal ($\frac{counts_i}{counts_{sum}}$) and summed to generate the final aperture correction ($apcorr_{total}$). The aperture correction is only applied to the stacked fluxes, and the raw counts data and hence the signal-to-noise ratios are left uncorrected. This is because some of the X-ray undetected sources may have irregular PSFs that are not adequately modelled by the MARX ray-tracing software. Therefore there may be some random artificial bias within the aperture correction that cannot be characterised. The signal-to-noise ratios determine whether the emission is considered significant and any bias propagated by the aperture correction could have a serious impact on the conclusions drawn from the stacked signal. Leaving the signal-to-noise calculations uncorrected is a more conservative approach which provides greater confidence in any subsequent analysis. On the other hand a slight incorrect bias introduced to the fluxes would have a less drastic impact upon the results.

The last step before stacking X-ray undetected sources is the calibration of the radius of the fixed circular apertures (extraction radius) and the maximum OAA of sources included in the stacking analysis (inclusion radius). The extraction and inclusion radii are empirically calibrated each time the stacking analysis is implemented for a different sample of X-ray undetected galaxies (ie recalibrated for each X-ray undetected galaxy sample). The optimal extraction radius should mimic the PSF of the X-ray undetected sources, hence maximising the signal obtained. Holding the inclusion radius at a fixed value (typically 5.5 arcminutes, the same value used by Laird et al. 2005) the stacking analysis is run repeatedly while the extraction radius was varied between 0.5-3.0 arcseconds at 0.25 arcsecond intervals. The extraction radius which produces the best SN is chosen as the optimum extraction radius for the stacking analysis. The inclusion radius is put in place to exclude high OAA sources with wide, elliptical PSFs that may adversely affect the stacked signal. These high OAA sources are poorly modelled by the fixed radius circular apertures and introduce significantly more background relative to low OAA sources. Holding the extraction radius at the optimum value, the stacking analysis is repeated with inclusion radius incrementally varied between 5.0-11.0 arcminutes at 0.5 arcminute intervals. The inclusion radius that achieves the maximum SN without producing an average aperture correction exceeding 2.0 is chosen as the optimum value. The aperture correction limit was deemed necessary because simply selecting the inclusion radius with the maximum SN did not necessarily exclude the sources with large PSFs poorly characterised by the fixed circular aperture. Once the extraction and inclusion radii are calibrated the galaxy sample and any subsamples derived from it can be subjected to stacking analysis.

# Chapter 3

# X-ray properties of BzK-selected galaxies in the deepest X-ray fields

## Overview

The research presented in this chapter concerns the X-ray properties of a sample of IR luminous BzK colour selected galaxies (BzK; Daddi et al. 2004). A subset of IR luminous star forming BzK galaxies (sBzK) which exhibit excess IR emission have been identified as containing a highly obscured AGN fraction in previous studies (e.g. Daddi et al. 2007b; Alexander et al. 2011). With the benefit of deep 24$\mu$m observations the sample of IR luminous sBzKs presented in this work is larger than equivalent samples found in previous studies. The BzK sample selection process is described along with the calculation of rest-frame properties. Then the cross-matching of BzKs to X-ray point sources is outlined as is the calibration of inclusion and extraction radii to be used when stacking X-ray undetected sBzKs. The results of cross-matching X-ray sources with BzK galaxies suggest that excess IR emission is not indicative of increased obscured AGN activity. By controlling for IR luminosity it becomes evident that IR excess and IR Non-Excess galaxies have similar X-ray detected fractions and that the increased AGN activity in IR excess sBzKs noted by previous studies is a consequence of the bias towards higher IR luminosities in this subsample. There is no clear evidence of widespread Compton thick AGN activity in either X-ray detected IR Excess sBzKs or the stacked signal of X-ray undetected IR Excess sBzKs. The hard X-ray signal observed for the latter by Daddi et al. 2007b is due to contamination of the stacked signal of IR excess sBzKs by a handful of hard X-ray sources that have now been directly detected with the benefit of deeper X-ray data. Passively evolving BzKs (pBzK) have a higher X-ray detected fraction than the sBzKs, so there is no evidence for coeval black hole growth and star formation from X-ray analysis of the BzK population. Because increased AGN activity in the IR excess population is not indicated by the X-ray analysis, it appears that the bulk of the IR Excess sBzK population is formed from luminous star-forming galaxies whose SFRs are either overestimated at

$24\mu$m, underestimated in the UV, or both. This conclusion reinforces recent results from *Herschel* which show similar effects.

The results of this study have been published in Rangel et al. (2013).

## 3.1 Introduction

Extensive deep multi-wavelength observations across the sky have vastly improved our knowledge of star-formation and AGN activity across a range of redshifts. It has become abundantly clear that the Universe at $z \sim 1-3$, was much more active than it is currently, at $z \sim 0$. For example, the star-formation rate density steadily rises from $z = 0$ to $z = 1$, flattens out until at least $z \sim 3$ and then falls off again at the highest redshifts (Lilly et al., 1996; Madau et al., 1996; Hopkins et al., 2005). The evolution of AGN activity over cosmic time correlates well with star formation activity, with luminous AGN activity peaking at $z = 2-3$ (e.g. Osmer et al. 1994; Hasinger 1998) and low luminosity AGN activity peaking at $z \sim 1$ (Ueda et al., 2003; Hasinger et al., 2005), and is consistent with coevolutionary schemes for supermassive black holes and their host galaxies (e.g. Boyle et al. 1993; Silverman et al. 2008; Aird et al. 2010). Therefore observing galaxies and AGN at z$\sim$2 should provide useful insight into AGN evolution and the interplay between AGN and star-formation in their host galaxies during this more active phase. Spectroscopic identifications of galaxies at $z \sim 2$, however, are complicated by the "redshift desert"; a range of redshifts ($1.4 \leq z < 2.5$) in which the observed frame of optical spectroscopic instruments is almost devoid of spectral features. In response to this problem numerous selection techniques have been developed that use broad band photometry instead of spectroscopy to select $z \sim 2$ candidate galaxies. For example, the Lyman-break and Balmer break features have been used to select galaxies with $1 < z < 3$ (Erb et al., 2003; Adelberger et al., 2004).

The BzK selection technique of Daddi et al. (2004) combines optical ($B$ and $z$ band) and near-IR ($K$ band) photometry to target the Balmer and 4000 Å break features of star-forming and passively evolving galaxies at $z \sim 2$ (Reddy et al., 2005; Shapley et al., 2005; Wuyts et al., 2008). The selection technique is expected to be largely independent of reddening (Daddi et al., 2004) and the near-IR photometry allows extremely red passively evolving galaxies to be selected, as well as bluer, star-forming galaxies (Thompson et al., 1999; Franx et al., 2003; McCarthy, 2004). BzK selection shows good agreement with other $z \sim 2$ galaxy selection techniques, although it is liable to miss the bluest/youngest star-forming galaxies ($K_S > 21$ Vega mag; Reddy et al. 2005). Many sBzKs show strong emission in the mid-IR at $24\mu$m, the majority of which is attributable to dusty star formation (Daddi et al., 2007a). By comparing UV and IR derived star-formation rates (SFR's) Daddi et al. (2007b) identified sBzKs with excess IR emission (IR Excess sBzK) as candidates for containing AGN. Daddi et al. (2007b) attempted to isolate sBzKs which might contain AGN using this mid-IR excess. AGN are expected to exhibit strong continuum emission at mid-IR wavelengths due to re-radiated emission from hot dust

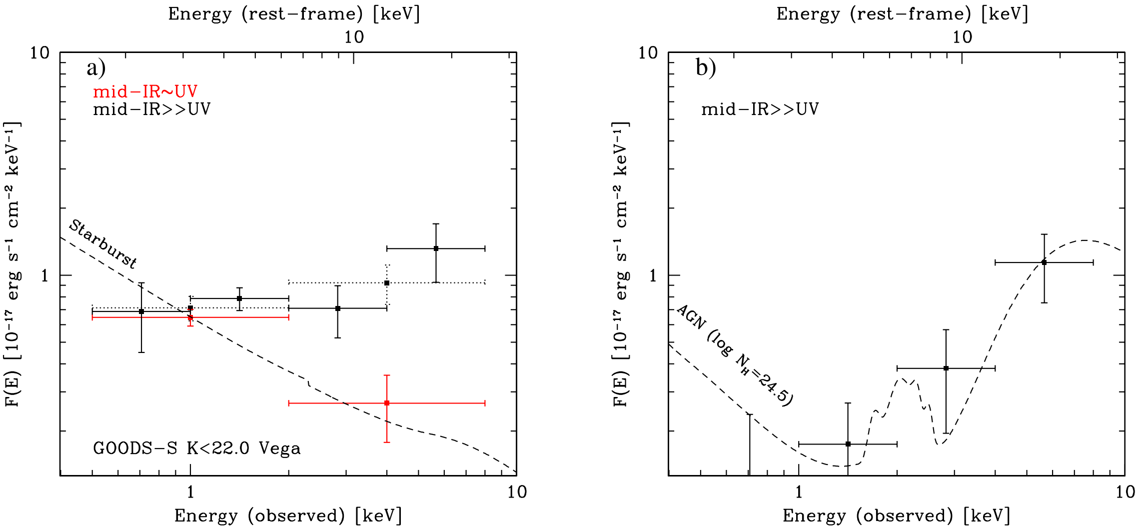

**Figure 3.1:** Average stacked fluxes of X-ray undetected Infrared Excess and Non-Excess sBzKs in the 1Ms CDFS, taken from Daddi et al. (2007b; Figure 9). (a) Stacked fluxes of Infrared Excess and Non-Excess sBzKs in both broad and narrow energy bands. Dashed line represents model starburst spectrum which fits the stacked fluxes of IR Non-Excess galaxies. (b) Stacked fluxes of IR Excess sBzKs with predicted X-ray component from star-formation removed. Stacked narrow band fluxes appear to be well characterised by a Compton thick AGN model spectrum (dashed line).

(e.g. Pier and Krolik 1992; Efstathiou and Rowan-Robinson 1995), a feature that has been exploited previously to identify obscured AGN (Lacy et al., 2004; Stern et al., 2005).

Daddi et al. (2007b) stacked the X-ray emission of IR Excess sBzKs in the GOODS-S field, yielding a hard X-ray signal ($\Gamma \sim 0.8^{+0.4}_{-0.3}$) consistent with a significant population of Compton thick ($N_H > 1.5 \times 10^{24}$ cm$^{-2}$) AGN (see Figure 3.1). The stacked signal of X-ray undetected sBzKs that did not exhibit excessive IR emission (IR Non-Excess sBzKs) was softer ($\Gamma \sim 1.7$) and consistent with pure star-formation. These results have significant implications for co-eval star-formation and black hole growth. The presence of "buried" Compton thick AGN in star-forming galaxies (like sBzKs) has been predicted by numerous models of AGN-galaxy-co-evolution (e.g. Hopkins et al. 2005).

If there is a high concentration of heavily obscured Compton thick AGN within the X-ray undetected IR excess sBzKs, they could play a vital role in resolving the X-ray background. The majority of the X-ray background (Giacconi et al., 1962) has been resolved as emission from discrete X-ray sources (as predicted by Setti and Woltjer 1989). There remains, however, an unexplained deficit in the discrete source emission at hard energies (E > 6 keV) relative to the XRB (Worsley et al., 2005). Some models of the X-ray background predict the hard X-ray background deficit represents a large population of as yet undiscovered Compton thick AGN at $z \sim 1-2$ (Comastri et al., 1995; Gilli et al., 2007). Extrapolating the stacked X-ray emission of the X-ray undetected IR-Excess sBzKs over all the sky at the observed co-moving space density would explain a substantial fraction ($\sim 10\% - 25\%$) of the hard X-ray background deficit (Daddi et al., 2007b).

Alexander et al. (2011) carried out further analysis of the X-ray properties of the sBzK sample from Daddi et al. (2007a,b) using new, deeper 4Ms CDFS X-ray data. They found that stacking the X-ray spectra of 11 heavily obscured ($\Gamma \leq 1$) X-ray detected sBzKs produced a hard, reflection dominated spectrum consistent with Compton thick AGN emission. The resultant stacked spectrum also features a large EW Iron line at rest-frame E $\sim$ 6.4 keV similar to that observed in Compton thick AGN in the local Universe (Matt et al., 1996; Iwasawa and Comastri, 1998) and distant Universe (Georgantopoulos et al., 2009; Comastri et al., 2011; Feruglio et al., 2011; Gilli et al., 2011). Stacking the X-ray undetected sBzKs in deeper 4Ms CDFS data did not yield conclusive evidence of a high fraction of heavily obscured AGN in the more general sBzK population, however, in contrast with the earlier work of Daddi et al. (2007b) using the CDFS 1Ms. These observations imply that the space density of Compton thick AGN at $z \sim 2$ is comparable to that of unobscured AGN at $z \sim 2$.

The IR excess analysis of Daddi et al. (2007b) is reliant upon the accuracy of IR and UV SFR estimates. Mid-IR observations have been found to be reliable proxies for bolometric IR luminosities (Dale et al., 2005), thus it has been common practice to fit rest-frame 8$\mu$m observations (observed-frame 24$\mu$m for galaxies at $z \sim 2$) with empirically derived star-forming galaxy templates (e.g. Chary and Elbaz 2001; Dale and Helou 2002) to estimate the SFR. With the advent of *Herschel* our understanding of the Far-IR spectra of star-forming galaxies has improved markedly, especially at $z > 1$. Using Far-IR *Herschel* data Elbaz et al. (2011) calculated $L_{IR}$ for numerous galaxies with MIPS coverage and compared them to $L_{IR}$ estimates made using 24$\mu$m selected star-forming templates of Chary and Elbaz (2001). Based on this analysis it is concluded that the star-forming templates of Chary and Elbaz (2001) are overestimating the bolometric IR luminosity for galaxies with $L_{IR} > 10^{12}\ L_{\odot}$. Additionally Nordon et al. (2012) find that the IR Excess emission at rest-frame 8$\mu$m can be explained entirely by PAH features, removing the necessity for mid-IR continuum emission from AGN assumed by previous IR selection techniques. The UV estimates of SFR are known to suffer in dusty (ie heavily star-forming) galaxies because reddening corrections become less accurate as the dust opacity increases (Goldader et al., 2002). Thus, selection of AGN via comparison of IR and UV-derived SFRs may not be as robust as previously thought. Indeed, recent work had suggested that some IR excess selection techniques (e.g. Fiore et al. 2008) have been shown to select equal parts heavily obscured AGN, low-luminosity AGN and purely star-forming galaxies (Donley et al., 2008; Georgakakis et al., 2010) when followed up using X-ray data.

Throughout this chapter a standard, flat $\Lambda$CDM cosmology with $\Omega_{\Lambda} = 0.7$ and $\mathrm{H}_0 = 70$ km s$^{-1}$ Mpc$^{-1}$ is assumed.

## 3.2 Data

### 3.2.1 Optical and IR data

The BzK samples in CDFS and CDFN are produced using the GOODS-MUSIC-v2 (Santini et al., 2009) and MOIRCS Deep Survey (MODS; Kajisawa et al. 2011) multi- wavelength datasets respectively. For the purpose of this work *Hubble* ACS F435W, F606W, F775W and F850LP band (henceforth $B, v, i$ and $z$ respectively), ISAAC $K$ band, IRAC 3.6$\mu$m and MIPS 24$\mu$m band data from the GOODS-MUSIC-v2 catalogue are used. All sources in the GOODS-MUSIC v2 catalogue have either a spectroscopic (64%) or a photometric (36%) redshift. The GOODS-MUSIC-v2 catalogue presents identical $B, v, i, z, K$ and 3.6$\mu$m photometry to the GOODS-MUSIC catalogue (Grazian et al. 2006) that was used by Daddi et al. (2007b) but incorporates deeper MIPS 24$\mu$m band data from the FIDEL survey (PI: Mark Dickinson). The 24$\mu$m source fluxes in GOODS-MUSIC-v2 were identified and matched to the multi-wavelength data using the ConvPhot software (de Santis et al., 2007), as opposed to matching the MIPS sources to multi-wavelength data using a more basic fixed matching radius method (as was the case for Daddi et al. 2005 and subsequently Daddi et al 2007a,b). The additional depth and use of the ConvPhot software allows the identification of additional 24$\mu$m sources and therefore increases our sample size compared to Daddi et al. (2007b). The GOODS-MUSIC-v2 catalogue has more spectroscopic redshifts than the GOODS-MUSIC catalogue, improving the accuracy of luminosity calculations for numerous sources relative to those presented by Daddi et al. (2007a,b). From the MODS catalogue *Hubble* ACS $B, V, i$ and $z$ band, MOIRCS $K_S$, IRAC 3.6$\mu$m and MIPS 24$\mu$m band photometry are used to produce a BzK galaxy sample in the CDFN. MODS is the only publicly available catalogue in CDFN to date to have matched K band to 24$\mu$m sources. Much like the GOODS-MUSIC-v2 catalogue, sources have a mixture of spectroscopic (70%) and photometric (30%) redshifts.

To ensure the reliability of the BzK selection and IR excess analysis, any source that is subjected to these analyses must satisfy the following criteria:

(i) possess secure K-band detection ($K_S < 22$ Vega).

(ii) have less than 0.5 arcseconds separation from an IRAC 3.6um selected source to verify that the source is genuine (large PSFs of 24$\mu$m sources leads to source blending).

(iii) have an error on $(B - z)_{AB} < 0.4$ to ensure reddening corrections are reliable.

In total 5,685 galaxies across the GOODS-MUSIC-v2 and MODS catalogues combined satisfy these criteria. These sources are plotted on a BzK diagram; Figure 3.2.

### 3.2.2 BzK sample selection

The BzK selection technique is an optical and near IR two-colour selection method designed by Daddi et al. (2004) with the aim of identifying galaxies at $z > 1.4$ through their

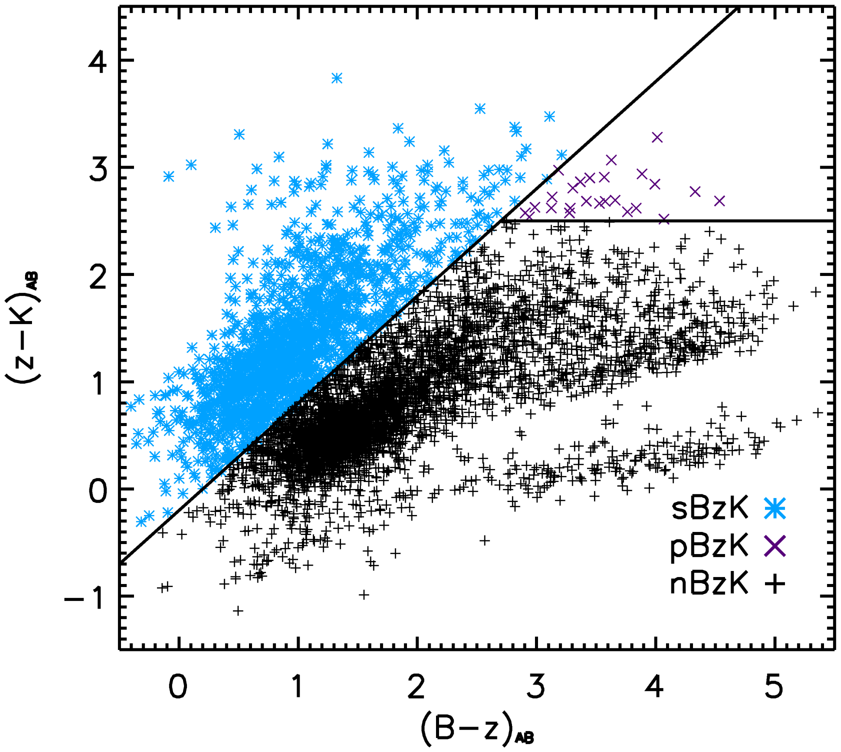

**Figure 3.2:** BzK diagram of galaxies in the GOODS-MUSIC-v2 and MODS catalogues. Solid Black lines represent the boundaries between different BzK galaxy type criteria.

broadband photometry. The BzK selection technique separates galaxies into three distinct groups; star-forming galaxies at $z > 1.4$ (sBzK), passively evolving galaxies at $z > 1.4$ (pBzK) and normal galaxies at $z < 1.4$ (see Figure 3.2). The two colour criteria for these galaxies are as follows:

$$sBzK : (z - K)_{AB} - (B - z)_{AB} \geq -0.2 \tag{3.1}$$

$$pBzK : (z - K)_{AB} - (B - z)_{AB} < -0.2 \cap (z - K)_{AB} > 2.5 \tag{3.2}$$

$$nBzK : (z - K)_{AB} - (B - z)_{AB} < -0.2 \cap (z - K)_{AB} \leq 2.5 \tag{3.3}$$

The $z - K$ colour acts a proxy for stellar mass, probing the optical SED about the Balmer and 4000 Å breaks for galaxies with $z \sim 2$ (Reddy et al., 2005; Shapley et al., 2005; Wuyts et al., 2008), while the $B - z$ colour corrects for reddening effects (see Equation 3.8). Additionally the sBzK selection was empirically calibrated to make it independent of reddening effects (Daddi et al. 2004). This is an important feature because emission from regions of intense star-formation is expected to be heavily reddened.

Only galaxies that satisfy the sBzK criterion are subjected to 24$\mu$m excess analysis. While the sBzK criterion primarily selects $z \sim 2$ galaxies there remains a fraction of low redshift interlopers (see Figure 3.4). Additionally, a large spread in redshift distribution would also adversely affect the X-ray stacking analysis. Therefore the redshift range for sBzKs subjected to IR Excess analysis is narrowed to $1.2 \leq z < 3.0$. The results of BzK selection and the subsequent IR Excess analysis are outlined in Table 1.

### 3.2.3 Calculation of Rest-frame Quantities

To calculate UV and IR luminosities required for the IR Excess analysis, it is necessary to correct the observed fluxes to their rest frame values. For UV data the approach is fairly simplistic, since the observed $B, v, i$ and $z$ bands cover rest-frame UV wavelengths at $z \sim 2$. Assuming the UV emission can be approximated by a power-law, the $B, v, i$ and $z$ bands can be used to derive the UV power-law for a source, which can be used subsequently to estimate UV fluxes at a desired wavelength.

For IR data the star forming galaxy templates of Chary and Elbaz (2001), see Figure 3.3, are used to derive a k-correction to convert observed 24$\mu$m fluxes into rest frame 8$\mu$m fluxes. The Chary and Elbaz (2001) templates are IR SEDs empirically derived from observations of local star-forming galaxies, with each corresponding to a different bolometric IR luminosity between 8 and 1000$\mu$m ($L_{IR}$). Magnelli et al. (2009) found that the Chary and Elbaz (2001) templates exhibit a stronger correlation to the emission of observed galaxies at $z \sim 1$ and thus are preferred to the star-forming galaxy templates of Dale and Helou (2002) and Lagache et al. (2003). The k-correction for each sBzK galaxy is calculated following the method of Hogg et al. (2002). The appropriate Chary and Elbaz (2001) template is selected by making a rough estimate of $L_{IR}$ from the observed 24$\mu$m

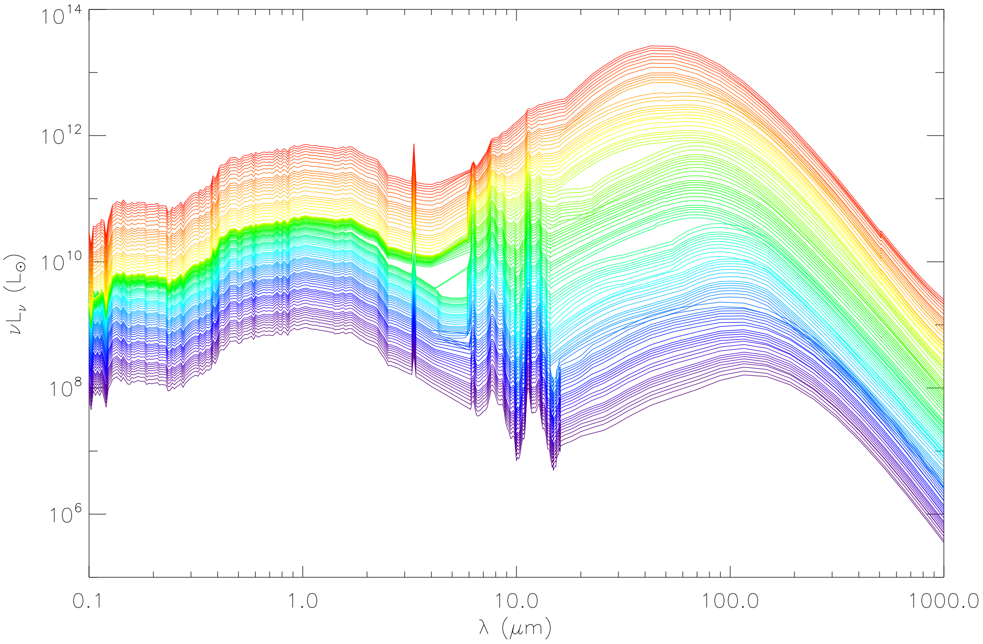

**Figure 3.3:** Empirically derived star forming templates of Chary and Elbaz (2001).

emission and interpolating to the best fitting template. The 24$\mu$m and 8$\mu$m response filters are then convolved over the selected template and the ratio of the fluxes yields the k-correction for observed 24$\mu$m to rest-frame 8$\mu$m flux.

### 3.2.4 IR Excess sBzK selection

IR excess sBzK galaxies are defined as those which exhibit excess IR emission compared to that expected for star formation. The excess IR emission is predicted to originate from AGN accretion due to an AGN dust torus presumably absorbing optical and UV emission from the accretion disk and re-emitting at mid-IR wavelengths. Therefore, if a sBzK is not directly detected at X-ray wavelengths but displays significant dust torus emission, it is likely that the X-ray emission is being suppressed and the IR excess sBzK is a strong obscured AGN candidate.

Star formation can be traced by UV emission, however, galaxies with significant star formation (e.g. sBzKs) contain significant amounts of dust which absorb UV emission and re-emit it at IR wavelengths. Therefore the total star formation rate (SFR) of an sBzK should be equal to the sum of the IR SFR ($\mathrm{SFR}_{IR}$) and UV SFR ($\mathrm{SFR}_{UV}$) estimates. Reddening of UV by dust can be corrected using the empirically derived relation of Calzetti et al. (2000) to reflect the original UV emission, presumably from star formation. Thus the SFR calculated from reddening corrected UV emission ($\mathrm{SFR}_{UVcorr}$) should equal the total star formation. By comparing these two estimates of the total star formation it is possible to identify sBzK galaxies with excess IR emission.

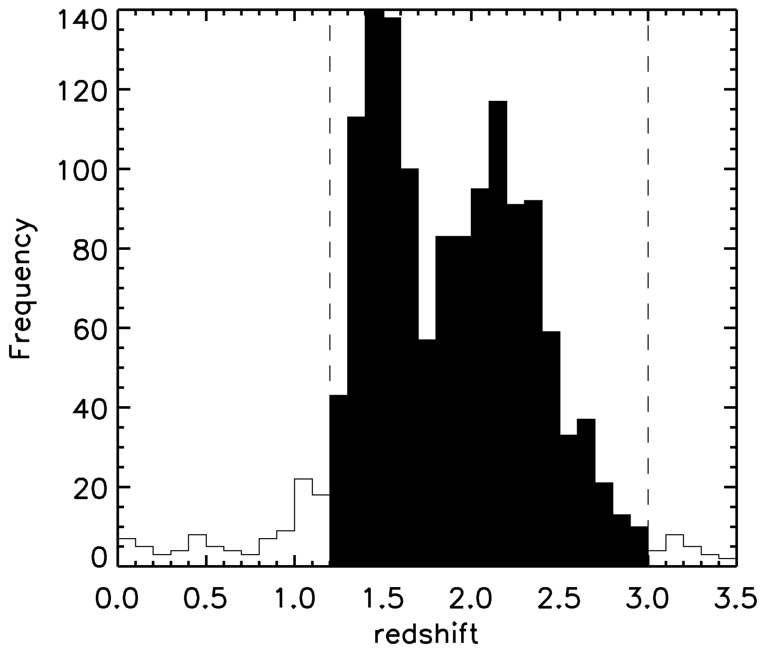

**Figure 3.4:** Redshift distribution of 1485 sBzK galaxies. Filled portion of the histogram represents sBzK galaxies subjected to IR Excess analysis ($1.2 \leq z \leq 3.0$). The remaining galaxies are omitted as they possess either $z < 1.2$ or $z > 3$.

For the purposes of this work the methods for estimating SFR$_{IR}$, SFR$_{UV}$ and SFR$_{UVcorr}$ presented in Daddi et al. (2007b) have been adhered to as closely as possible. With this in mind, SFR$_{IR}$ is calculated using the relationship of Kennicutt (1998):

$$SFR_{IR}(M_{\odot}yr^{-1}) = 1.73 \times 10^{-10} L_{IR}(L_{\odot}) \tag{3.4}$$

where $L_{IR}$ is the bolometric IR luminosity of the galaxy between 8 and 1000 $\mu$m. The observed 24$\mu$m flux is corrected to rest-frame 8$\mu$m flux, using a k-correction derived following the method outlined in Section 3.2.3, which is then used to calculate the monochromatic 8$\mu$m luminosity ($L_{8\mu m}$). The bolometric $L_{IR}$ is inferred from ($L_{8\mu m}$) using the relationships for Chary and Elbaz (2001) templates defined in Daddi et al. (2007b).

$$log(\frac{L_{IR}}{L_{\odot}}) = 1.50log(\frac{L_{8\mu m}}{L_{\odot}}) - 4.31 \tag{3.5}$$

if $log(\frac{L_{8\mu m}}{L_{\odot}}) > 9.75$ and

$$log(\frac{L_{IR}}{L_{\odot}}) = 0.93log(\frac{L_{8\mu m}}{L_{\odot}}) + 1.23 \tag{3.6}$$

if $log(\frac{L_{8\mu m}}{L_{\odot}}) < 9.75$.

The SFR$_{UV}$ is estimated from rest-frame UV emission using Equation 3.7, a relation-

**Table 3.1:** BzK galaxy samples and IR Excess and Non-Excess sBzK subsamples for the CDFS and CDFN. Column (1): Subsample name; column (2): size of subsample in CDFS; column (3): size of subsample in CDFN; column (4): size of subsample when CDFS and CDFN sources are combined.

| Galaxy type<br>(1) | Total CDFS<br>(2) | Total CDFN<br>(3) | Total Combined<br>(4) |
|---|---|---|---|
| pBzK | 21 | 5 | 26 |
| nBzK | 2168 | 2006 | 4174 |
| sBzK | 851 | 594 | 1445 |
| IRX ($1.2 \leq z \leq 3.0$) | 158 | 198 | 356 |
| IRNX ($1.2 \leq z \leq 3.0$) | 543 | 336 | 879 |

ship derived by Daddi et al. (2004):

$$SFR(M_{\odot}yr^{-1}) = \frac{L_{1500}(ergs^{-1}Hz^{-1})}{8.85 \times 10^{27}} \tag{3.7}$$

where $L_{1500}$ is the 1500 Å monochromatic luminosity. The UV emission is corrected for reddening, following the empirically derived reddening correction method of Calzetti et al. (2000; Equations 2, 3 and 4). The dust reddening factor $E(B-V)$ is estimated using an empirically derived relationship from Daddi et al. (2004):

$$E(B-V) = 0.25(B - z + 0.1)_{AB} \tag{3.8}$$

The reddening corrected UV emission was then used to again calculate SFR$_{UVcorr}$.

To be defined as an IR Excess sBzK (hereafter IRX; Compton thick AGN candidate) a galaxy must satisfy Equation 3.9.

$$log_{10}(\frac{SFR_{tot}}{SFR_{UVcorr}}) > 0.5 \tag{3.9}$$

where $SFR_{tot} = SFR_{IR} + SFR_{UV}$. The sBzKs that do not satisfy this criterion are classified as IR Non-Excess sBzKs (hereafter IRNXs).

If an apparent IRX (see Equation 3.9) possesses a 24$\mu$m flux that is less than 3 times the background noise it is not considered a secure-detection and removed from the sample because the measurement of an IR excess is not sufficiently robust. Clearly it is neither necessary nor desirable to apply this cut to IRNXs. Combining the CDFS and CDFN samples yields 356 IRXs and 879 IRNXs. A K-S test demonstrates that the IRXs and IRNXs have significantly different redshift distributions, with null hypothesis p<0.001. The IRXs have higher redshifts on average (median $z$ = 2.06) compared to the IRNXs (median $z$ = 1.78), see Figure 3.5. The high density of spectroscopic observations at $z = 1.6$ is due to a galaxy cluster in the CDFS sample that has been extensively observed (Castellano et al., 2007). There is also a strong positive correlation between $L_{IR}$ and the

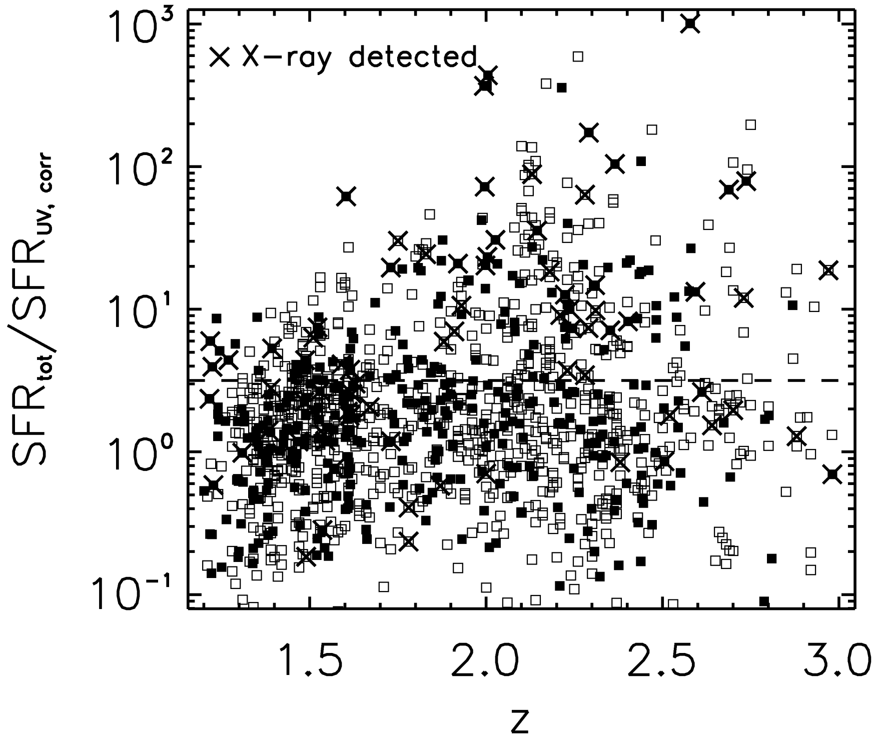

**Figure 3.5:** Plot of $\mathrm{SFR}_{tot}/\mathrm{SFR}_{UVcorr}$ versus redshift for sBzK galaxies subjected to IR excess analysis. Galaxies above the horizontal dashed line satisfy the IR excess galaxy criterion, galaxies below are IR non-excess. Filled squares are galaxies with spectroscopic redshifts while open squares are galaxies with photometric redshift estimates only. Black crosses represent galaxies that have been directly detected in the 4Ms CDFS and 2Ms CDFN data.

ratio of $SFR_{tot}/SFR_{UV,corr}$ (the IR excess parameter) in Figure 3.6. As a consequence, the overwhelming majority of IR luminous sBzKs are classified as IRXs (85.3%; 304/356 with $L_{IR} > 10^{12}L_{\odot}$) as opposed to IRNXs (19.1%; 168/879 with $L_{IR} > 10^{12}L_{\odot}$).

### 3.2.5 X-ray Point Source Catalogues

The 4Ms CDFS *Chandra* data was obtained over the course of 3 separate Chandra observing cycles: 1 Megasecond (Ms) between May 27th 2000 and December 23rd 2000, another 1Ms between September 20th 2007 and November 4th 2007 and the final 2Ms between May 18th 2010 and July 22nd 2010. The 2Ms CDFN data was collected between February 23rd 2000 and February 22nd 2002. All observations were taken using the Advanced CCD Imaging Spectrometer imaging array (ACIS-I; Garmire et al. 2003). X-ray point source catalogues for CDFS 4Ms and CDFN 2Ms were generated from these observations following the methods outlined in Section 2.2.4. Throughout the data reduction and point source detection CIAO data analysis software version 4.2 and CALDB 4.4.10 were used. The CDFS 4Ms and CDFN 2Ms X-ray point source catalogues can be found in the appendix for reference purposes.

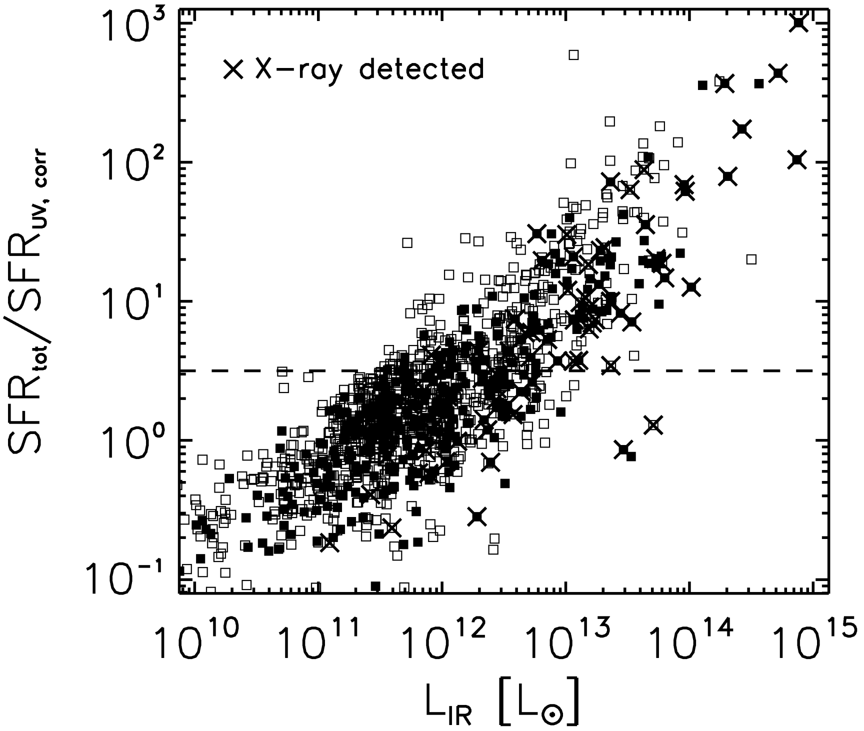

**Figure 3.6:** Plot of $SFR_{tot}/SFR_{UVcorr}$ versus $L_{IR}$ for sBzK galaxies subjected to IR excess analysis. Filled squares are galaxies with spectroscopic redshifts while open squares are galaxies with photometric redshift estimates only. The horizontal dashed line denotes the IR excess criterion; galaxies above the line are IR excess, below the line are IR non-excess. Black crosses represent galaxies that have been directly detected in the 4Ms CDFS and 2Ms CDFN data.

An additional astrometric correction to each obsID is calculated by comparing X-ray source positions to those of a reference source catalogue with superior astrometry. Running the CIAO wavdetect tool on each obsID, bright X-ray sources are selected using a threshold probability $10^{-6}$. These obvious X-ray sources should be common to the majority of individual obsIDs and ideal for marrying up the astrometry. Reference astrometry for CDFS is taken from a catalogue of H-band selected galaxies from the GOODS-MUSYC survey (Gawiser et al. 2006), with a magnitude cut of $18 < H_{AB} < 23$ applied and sources with photometric flags removed. The magnitude cut removes the brightest sources to eliminate extended objects with potentially incorrect positions, and faint sources were omitted to reduce the likelihood of chance associations. The reference astrometry for 2Ms CDFN is from an r-band selected catalogue of Capak et al. (2004). It was decided that a magnitude cut was unnecessary for the r-band catalogue because it made no practical difference to the astrometry correction.

In the CDFS 4Ms field, 569 X-ray point sources have been identified, while the CDFN 2Ms catalogue contains 504 X-ray point sources. The Imperial College CDFS 4Ms point source catalogue has considerably fewer sources than the Xue et al. 2011 CDFS 4Ms catalogue (740 sources). Cross-matching the Imperial College CDFS 4Ms catalogue to the Xue et al. 2011 CDFS 4Ms X-ray point source catalogue using a nearest neighbour cross-matching technique (fixed 1.5 arcsecond radius with a corresponding false identification rate of 1.0%), 500 sources are found to be coincident. Xue et al. 2011 identify more X-ray point sources than the Imperial College point source detection because the acis_extract software used by the former is less conservative than the method implemented by the Imperial College point source detection (see Section 2.2.4). The majority of additional sources identified by Xue et al 2011 are found within the initial seed catalogues we employ which suggests these could be very low significance sources. The useful science possible using these sources is limited due to the large errors relative to their low fluxes. The CDFN 2Ms X-ray point source catalogue, again created using the Imperial College X-ray reduction pipeline, contains 504 sources. Alexander et al. 2003 find 503 X-ray point sources in the CDFN 2Ms of which 417 are coincident with sources from the Imperial College CDFN 2Ms X-ray point source catalogue (again cross-matched using a 1.5 arcsecond radius with a corresponding 1.0% false identification rate). Similar to what was observed when comparing the CDFS 4Ms X-ray catalogues, the majority of sources that are unique to the Alexander et al. 2003 CDFN 2Ms catalogue have been identified in the low significance seed catalogues from which the final Imperial College CDFN 2Ms catalogue was generated.

### 3.2.6 X-ray Stacking Calibration

X-ray stacking analysis is used to calculate the average X-ray emission of the X-ray undetected sBzKs and various subsamples derived from them. The stacking technique is described in detail in Section 2.5.3. The extraction and inclusion radii were calibrated for broad band stacking analysis using the full sBzK galaxy sample following the method outlined in Section 2.5.3 . A fixed aperture of radius 1.5 arcseconds provides the best SN ratio for stacked signals for both 4Ms CDFS and 2Ms CDFN data. An inclusion radius of 5.5 arcminutes meanwhile is found to yield the maximum SN ratio possible for the stacked signal without generating aperture corrections that exceed 2 for both 4Ms CDFS and 2Ms CDFN. Some variation in PSF sizes and CCD sensitivity are expected to occur when stacking the sBzKs in narrower energy bands but the effect on the optimal extraction and inclusion radii is expected to be negligible. Thus the inclusion and extraction radii calibrated for broad band stacking analysis are also employed in narrow band stacking analysis.

## 3.3 Results

### 3.3.1 Direct X-ray Detections

The sBzK galaxies are matched to X-ray point sources in the 4Ms CDFS and 2Ms CDFN catalogues using a nearest neighbour cross correlation method, with a circular 1.25 arcsecond search radius to establish direct detections. The BzK source density is sufficiently low that at 1.25 arcseconds all matches are unique and the corresponding false match probability is 1.1%. Additionally the astrometry corrections detailed in Section 2.2.2 have greatly reduced the overall offsets between the optical and X-ray positions. Using this method 5.8±0.8% (49/851) of sBzKs in the 4Ms CDFS image and 5.4±1.0% (32/594) of sBzKs in the 2Ms CDFN image are found to have an X-ray counterpart (see Tables 3.2 and 3.3). The rest-frame 2-10 keV luminosities ($L_{2-10keV}$; derived from $F_{0.5-2keV}$) of sBzKs range from $1.1 \times 10^{41} - 3.5 \times 10^{44}$ erg s$^{-1}$ with median $L_{2-10keV} = 3.5 \times 10^{42}$ erg s$^{-1}$. Approximately 70% (57/81) of the X-ray detected sBzKs possess $L_{2-10keV} > 10^{42}$ erg s$^{-1}$ and it is reasonable to assume all of these objects host an AGN. The X-ray emission of the remaining 26 sBzKs is probably also mostly from AGN, but a significant contribution from stellar processes is also a possible explanation for these lower luminosity X-ray sources.

The detection rate of X-ray sources is a strong function of $L_{IR}$ (see Figure 3.6). This agrees with previous observations that AGN are more prevalent amongst the most IR luminous galaxies (Sanders and Mirabel 1996; Risaliti et al. 2000). The Hardness Ratio (HR) is defined as HR= $(H - S)/(H + S)$, where $H$ and $S$ are hard- and soft-band count rates respectively. The HR distribution of X-ray detected sBzK galaxies is notionally bimodal (Figure 3.8), covering a wide range of HR (-0.70 to 0.82). Using a simple photoelectric absorption model, an AGN at $z \sim 2$ with power-law emission $\Gamma = 1.9$ obscured by material with N$_H > 10^{23}$ cm$^{-2}$ should possess a HR$> -0.08$. Therefore 44% (36/81) of the X-ray detected sBzKs possess N$_H = 10^{23}$ cm$^{-2}$ or greater according to their HR. This suggests the X-ray detected sBzKs are a mixture of obscured AGN, unobscured AGN and purely star-forming galaxies.

**Table 3.2:** X-ray properties of sBzK and pBzK galaxies detected in the 4Ms CDFS. Column (1): X-ray source name, galaxies suffixed with † have been detected in the 1Ms CDFS also; column (2): BzK subsample; columns (3) and (4): right ascension (RA) and declination (Dec.) of source; column (5): redshift, redshift's are spectroscopic where available (suffixed with $^{s}$), otherwise photometric redshifts are used (suffixed with $^{p}$); column (6): soft band flux, units $10^{-16}$ erg cm$^{-2}$ s$^{-1}$; column (7): hard band flux, units $10^{-16}$ erg cm$^{-2}$ s$^{-1}$; column (8): rest-frame hard band Luminosity derived from the soft band flux, units $10^{42}$ ergs s$^{-1}$; column (9): HR, HR= $(H-S)/(H+S)$, where $H$ and $S$ are hard- and soft-band count rates respectively.

| Name (1) | Type (2) | RA (3) | Dec (4) | Redshift (5) | $F_{0.5-2keV}$ (6) | $F_{2-10keV}$ (7) | $L_{2-10keV}$ (8) | HR (9) |
|---|---|---|---|---|---|---|---|---|
| cdfs4Ms_031† | IRX | 53.15731 | -27.87007 | $1.60^{s}$ | $65.69^{+1.18}_{-1.14}$ | $119.92^{+3.43}_{-3.29}$ | $88.47^{+1.59}_{-1.53}$ | $-0.43^{+0.01}_{-0.01}$ |
| cdfs4Ms_043† | IRX | 53.16146 | -27.85597 | $2.97^{p}$ | $0.84^{+0.15}_{-0.14}$ | $7.31^{+1.09}_{-0.90}$ | $7.78^{+1.41}_{-1.28}$ | $0.30^{+0.10}_{-0.10}$ |
| cdfs4Ms_077† | IRX | 53.14879 | -27.82116 | $2.58^{s}$ | $0.49^{+0.11}_{-0.10}$ | $3.52^{+0.69}_{-0.62}$ | $2.92^{+0.65}_{-0.57}$ | $0.21^{+0.13}_{-0.12}$ |
| cdfs4Ms_078† | IRX | 53.1801 | -27.82061 | $1.92^{s}$ | $28.11^{+0.75}_{-0.72}$ | $58.78^{+2.39}_{-2.21}$ | $66.15^{+1.77}_{-1.69}$ | $-0.37^{+0.02}_{-0.02}$ |
| cdfs4Ms_079 | IRX | 53.05903 | -27.81944 | $2.28^{p}$ | $0.25^{+0.09}_{-0.08}$ | $< 1.10$ | $1.02^{+0.36}_{-0.31}$ | $-0.08^{+0.31}_{-0.22}$ |
| cdfs4Ms_091† | IRX | 53.18579 | -27.80996 | $2.59^{s}$ | $3.76^{+0.29}_{-0.25}$ | $11.12^{+1.19}_{-1.02}$ | $22.68^{+1.77}_{-1.54}$ | $-0.21^{+0.06}_{-0.06}$ |
| cdfs4Ms_120† | IRX | 53.18344 | -27.77658 | $2.69^{s}$ | $5.56^{+0.35}_{-0.31}$ | $8.04^{+1.10}_{-0.93}$ | $37.53^{+2.37}_{-2.11}$ | $-0.51^{+0.05}_{-0.05}$ |
| cdfs4Ms_123† | IRX | 53.04907 | -27.7745 | $2.21^{p}$ | $8.52^{+0.45}_{-0.40}$ | $25.24^{+1.74}_{-1.56}$ | $31.09^{+1.62}_{-1.48}$ | $-0.21^{+0.04}_{-0.04}$ |
| cdfs4Ms_126† | IRX | 53.13114 | -27.77308 | $2.22^{s}$ | $0.60^{+0.12}_{-0.11}$ | $1.92^{+0.60}_{-0.55}$ | $2.22^{+0.44}_{-0.40}$ | $-0.14^{+0.16}_{-0.16}$ |
| cdfs4Ms_131† | IRX | 53.09394 | -27.76773 | $1.73^{s}$ | $3.26^{+0.27}_{-0.23}$ | $35.16^{+1.85}_{-1.68}$ | $5.55^{+0.46}_{-0.39}$ | $0.40^{+0.04}_{-0.04}$ |
| cdfs4Ms_144† | IRX | 53.12491 | -27.75832 | $1.22^{s}$ | $52.01^{+1.03}_{-0.99}$ | $124.08^{+3.44}_{-3.20}$ | $30.26^{+0.60}_{-0.57}$ | $-0.31^{+0.01}_{-0.02}$ |
| cdfs4Ms_161† | IRX | 53.04549 | -27.73748 | $1.62^{s}$ | $54.79^{+1.09}_{-1.05}$ | $114.69^{+3.47}_{-3.29}$ | $75.51^{+1.50}_{-1.44}$ | $-0.37^{+0.01}_{-0.02}$ |
| cdfs4Ms_175† | IRX | 53.10697 | -27.71826 | $2.29^{s}$ | $13.07^{+0.55}_{-0.51}$ | $55.59^{+2.53}_{-2.35}$ | $53.40^{2.26}_{-2.09}$ | $-0.04^{+0.03}_{-0.03}$ |
| cdfs4Ms_183† | IRX | 53.1337 | -27.69866 | $1.39^{s}$ | $6.68^{+0.43}_{-0.039}$ | $16.35^{+1.90}_{-1.72}$ | $5.85^{+0.38}_{-0.34}$ | $-0.30^{+0.05}_{-0.06}$ |
| cdfs4Ms_215† | IRX | 53.15812 | -27.88552 | $2.73^{p}$ | $0.91^{+0.18}_{-0.16}$ | $< 1.34$ | $6.44^{+1.26}_{-1.17}$ | $-0.49^{+0.24}_{-0.24}$ |
| cdfs4Ms_224 | IRX | 53.17406 | -27.85968 | $1.93^{p}$ | $0.38^{+0.13}_{-0.12}$ | $1.08^{+0.62}_{-1.08}$ | $0.91^{+0.31}_{-0.28}$ | $-0.06^{+0.29}_{-0.22}$ |

*Continued on next page*

Table 3.2 – *Continued from previous page*

| Name<br>(1) | Type<br>(2) | RA<br>(3) | Dec<br>(4) | Redshift<br>(5) | $F_{0.5-2keV}$<br>(6) | $F_{2-10keV}$<br>(7) | $L_{2-10keV}$<br>(8) | HR<br>(9) |
|---|---|---|---|---|---|---|---|---|
| cdfs4Ms_264† | IRX | 53.05881 | -27.70842 | $2.03^{s}$ | $1.62^{+0.28}_{-0.24}$ | $7.57^{+1.70}_{-1.53}$ | $4.51^{+0.78}_{-0.66}$ | $0.02^{+0.13}_{-0.12}$ |
| cdfs4Ms_334 | IRX | 53.16222 | -27.71213 | $2.23^{p}$ | $0.50^{+0.20}_{-0.19}$ | $6.56^{+1.55}_{-1.39}$ | $1.89^{+0.76}_{-0.73}$ | $0.42^{+0.15}_{-0.15}$ |
| cdfs4Ms_369 | IRX | 53.06313 | -27.69953 | $2.40^{s}$ | $1.76^{+0.30}_{-0.25}$ | $4.25^{+1.77}_{-1.76}$ | $8.32^{+1.41}_{-1.20}$ | $-0.25^{+0.18}_{-0.15}$ |
| cdfs4Ms_434 | IRX | 53.19878 | -27.84391 | $1.51^{p}$ | $0.28^{+0.13}_{-0.12}$ | $8.64^{+1.24}_{-1.07}$ | $0.31^{+0.14}_{-0.13}$ | $0.69^{+0.09}_{-0.09}$ |
| cdfs4Ms_438 | IRX | 53.16685 | -27.79876 | $2.00^{s}$ | $0.26^{+0.09}_{-0.08}$ | $0.94^{+0.50}_{-0.54}$ | $0.68^{+0.24}_{-0.20}$ | $-0.02^{+0.27}_{-0.21}$ |
| cdfs4Ms_451 | IRX | 53.1312 | -27.84129 | $1.61^{s}$ | $< 0.08$ | $1.06^{+0.50}_{-0.47}$ | $< 0.11$ | $0.48^{+0.28}_{-0.18}$ |
| cdfs4Ms_460 | IRX | 53.09755 | -27.71552 | $2.14^{s}$ | $< 0.14$ | $4.40^{+1.29}_{-1.16}$ | $< 0.46$ | $0.76^{+0.21}_{-0.09}$ |
| cdfs4Ms_515 | IRX | 53.05683 | -27.79852 | $1.83^{p}$ | $0.14^{+0.08}_{-0.07}$ | $< 0.60$ | $0.28^{+0.16}_{-0.15}$ | $-0.19^{+0.42}_{-0.35}$ |
| cdfs4Ms_013† | IRNX | 53.19605 | -27.89266 | $2.74^{p}$ | $5.45^{+0.40}_{-0.35}$ | $22.19^{+2.00}_{-1.92}$ | $39.08^{+2.83}_{-2.53}$ | $-0.06^{+0.06}_{-0.05}$ |
| cdfs4Ms_042† | IRNX | 53.15067 | -27.85735 | $1.61^{s}$ | $2.15^{+0.23}_{-0.19}$ | $6.12^{+0.97}_{-0.80}$ | $2.95^{+0.31}_{-0.26}$ | $-0.22^{+0.08}_{-0.08}$ |
| cdfs4Ms_050† | IRNX | 53.07463 | -27.84865 | $1.54^{s}$ | $1.58^{+0.19}_{-0.18}$ | $47.66^{+2.21}_{-2.03}$ | $1.87^{0.23}_{-0.21}$ | $0.73^{+0.03}_{-0.03}$ |
| cdfs4Ms_083† | IRNX | 53.04569 | -27.81555 | $1.39^{p}$ | $11.49^{+0.48}_{-0.45}$ | $22.20^{+1.54}_{-1.38}$ | $9.99^{+0.42}_{-0.39}$ | $-0.40^{+0.03}_{-0.03}$ |
| cdfs4Ms_088† | IRNX | 53.14987 | -27.81405 | $1.31^{s}$ | $1.22^{+0.16}_{-0.15}$ | $1.98^{+0.56}_{-0.52}$ | $0.88^{+0.12}_{-0.11}$ | $-0.44^{+0.11}_{-0.11}$ |
| cdfs4Ms_089† | IRNX | 53.17929 | -27.81254 | $1.73^{s}$ | $1.22^{+0.17}_{-0.16}$ | $19.82^{+1.48}_{-1.31}$ | $2.07^{+0.29}_{-0.26}$ | $0.55^{+0.06}_{-0.05}$ |
| cdfs4Ms_133† | IRNX | 53.16283 | -27.76716 | $1.22^{s}$ | $16.02^{+0.59}_{-0.55}$ | $52.66^{+2.32}_{-2.14}$ | $9.27^{+0.34}_{-0.32}$ | $-0.23^{+0.03}_{-0.03}$ |
| cdfs4Ms_155† | IRNX | 53.02409 | -27.74643 | $1.61^{s}$ | $3.78^{+0.33}_{-0.29}$ | $8.01^{+1.49}_{-1.32}$ | $5.14^{+0.45}_{-0.39}$ | $-0.35^{+0.09}_{-0.07}$ |
| cdfs4Ms_157† | IRNX | 53.16272 | -27.74424 | $2.52^{p}$ | $5.11^{+0.35}_{-0.31}$ | $20.13^{+1.61}_{-1.43}$ | $28.13^{+1.92}_{-1.70}$ | $-0.07^{+0.05}_{-0.05}$ |
| cdfs4Ms_206† | IRNX | 53.08925 | -27.93046 | $2.61^{s}$ | $5.07^{+0.42}_{-0.38}$ | $14.16^{+2.32}_{-1.77}$ | $31.25^{+2.61}_{-2.33}$ | $-0.18^{+0.07}_{-0.08}$ |
| cdfs4Ms_208† | IRNX | 53.20484 | -27.91799 | $2.02^{p}$ | $7.21^{+0.52}_{-0.47}$ | $13.50^{+2.56}_{-2.13}$ | $19.87^{+1.44}_{-1.30}$ | $-0.41^{+0.07}_{-0.08}$ |
| cdfs4Ms_226† | IRNX | 53.0601 | -27.8529 | $1.54^{s}$ | $0.45^{+0.13}_{-0.12}$ | $6.83^{+1.12}_{-0.94}$ | $0.55^{+0.16}_{-0.14}$ | $0.50^{+0.12}_{-0.09}$ |
| cdfs4Ms_246 | IRNX | 53.18171 | -27.78293 | $1.57^{s}$ | $0.31^{+0.11}_{-0.10}$ | $< 0.71$ | $0.39^{+0.14}_{-0.12}$ | $-0.37^{0.33}_{-0.32}$ |
| cdfs4Ms_258 | IRNX | 53.06154 | -27.73409 | $1.67^{p}$ | $1.08^{+0.19}_{-0.18}$ | $3.31^{+1.16}_{-1.06}$ | $1.65^{+0.29}_{-0.27}$ | $-0.16^{+0.17}_{-0.15}$ |

*Continued on next page*

Table 3.2 – *Continued from previous page*

| Name<br>(1) | Type<br>(2) | RA<br>(3) | Dec<br>(4) | Redshift<br>(5) | $F_{0.5-2keV}$<br>(6) | $F_{2-10keV}$<br>(7) | $L_{2-10keV}$<br>(8) | HR<br>(9) |
|---|---|---|---|---|---|---|---|---|
| cdfs4Ms_271 | IRNX | 53.14107 | -27.70119 | $1.23^s$ | $0.55^{+0.23}_{-0.22}$ | $2.27^{+1.90}_{-1.03}$ | $0.33^{+0.13}_{-0.13}$ | $0.05^{+0.29}_{-0.22}$ |
| cdfs4Ms_283 | IRNX | 53.08729 | -27.92957 | $2.88^p$ | $1.93^{+0.32}_{-0.28}$ | $18.48^{+2.41}_{-2.19}$ | $16.19^{+2.72}_{-2.35}$ | $0.35^{+0.08}_{-0.08}$ |
| cdfs4Ms_321 | IRNX | 53.02796 | -27.74872 | $2.38^p$ | $0.73^{+0.18}_{-0.17}$ | $1.99^{+1.40}_{-0.94}$ | $3.37^{+0.85}_{-0.79}$ | $-0.12^{+0.26}_{-0.19}$ |
| cdfs4Ms_370 | IRNX | 53.05303 | -27.69705 | $1.78^p$ | $1.51^{+0.31}_{-0.26}$ | $4.06^{+1.92}_{-1.85}$ | $2.81^{+0.57}_{-0.49}$ | $-0.19^{+0.23}_{-0.14}$ |
| cdfs4Ms_405 | IRNX | 53.041 | -27.83608 | $1.78^p$ | $0.20^{+0.11}_{-0.10}$ | $1.94^{+0.84}_{-0.82}$ | $0.38^{+0.20}_{-0.19}$ | $0.28^{+0.26}_{-0.18}$ |
| cdfs4Ms_441 | IRNX | 53.09494 | -27.75793 | $1.87^p$ | $< 0.07$ | $1.60^{+0.66}_{-0.62}$ | $< 0.15$ | $0.67^{+0.26}_{-0.13}$ |
| cdfs4Ms_459 | IRNX | 53.12284 | -27.72285 | $1.63^p$ | $< 0.14$ | $3.85^{+1.18}_{-1.04}$ | $< 0.20$ | $0.70^{+0.23}_{-0.12}$ |
| cdfs4Ms_494 | IRNX | 53.1255 | -27.88646 | $2.64^p$ | $0.66^{+0.15}_{-0.14}$ | $< 1.11$ | $4.18^{+0.95}_{-0.87}$ | $-0.46^{+0.26}_{-0.26}$ |
| cdfs4Ms_498 | IRNX | 53.12022 | -27.79886 | $1.38^s$ | $0.28^{+0.10}_{-0.08}$ | $< 0.48$ | $0.24^{+0.08}_{-0.07}$ | $-0.50^{+0.26}_{-0.32}$ |
| cdfs4Ms_503 | IRNX | 53.16382 | -27.7735 | $2.70^p$ | $0.15^{+0.09}_{-0.08}$ | $< 0.66$ | $1.05^{+0.59}_{-0.53}$ | $-0.17^{+0.41}_{-0.33}$ |
| cdfs4Ms_512 | IRNX | 53.11056 | -27.8236 | $1.47^s$ | $0.24^{+0.09}_{-0.07}$ | $< 0.32$ | $0.25^{+0.09}_{-0.07}$ | $-0.70^{+0.08}_{-0.30}$ |
| cdfs4Ms_301 | pBzK | 53.24571 | -27.86106 | $1.10^p$ | $3.02^{+0.36}_{-0.31}$ | $9.08^{+1.97}_{-1.81}$ | $1.22^{+0.14}_{-0.13}$ | $-0.18^{+0.11}_{-0.10}$ |
| cdfs4Ms_318 | pBzK | 53.04476 | -27.77442 | $1.61^s$ | $0.80^{+0.15}_{-0.14}$ | $< 1.29$ | $1.08^{+0.21}_{-0.19}$ | $-0.45^{+0.22}_{-0.20}$ |
| cdfs4Ms_457 | pBzK | 53.02676 | -27.76529 | $1.33^s$ | $< 0.21$ | $2.95^{+1.17}_{-1.09}$ | $< 0.16$ | $0.49^{+0.25}_{-0.19}$ |

**Table 3.3:** X-ray properties of sBzK and pBzK galaxies detected in the 2Ms CDFN. Column (1): X-ray source name, galaxies suffixed with † have been detected in the 1Ms CDFS also; column (2): BzK subsample; columns (3) and (4): right ascension (RA) and declination (Dec.) of source; column (5): redshift, redshift's are spectroscopic where available (suffixed with $^s$), otherwise photometric redshifts are used (suffixed with $^p$); column (6): soft band flux, units $10^{-16}$ erg cm$^{-2}$ s$^{-1}$; column (7): hard band flux, units $10^{-16}$ erg cm$^{-2}$ s$^{-1}$; column (8): rest-frame hard band Luminosity derived from the soft band flux, units $10^{42}$ ergs s$^{-1}$; column (9): HR, HR= $(H - S)/(H + S)$, where $H$ and $S$ are hard- and soft-band count rates respectively.

| Name (1) | Type (2) | RA (3) | Dec (4) | Redshift (5) | $F_{0.5-2keV}$ (6) | $F_{2-10keV}$ (7) | $L_{2-10keV}$ (8) | HR (9) |
|---|---|---|---|---|---|---|---|---|
| hdfn_015 | IRX | 189.13587 | 62.13338 | $1.99^s$ | $1.32^{+0.31}_{-0.28}$ | $13.99^{+2.29}_{-1.94}$ | $3.49^{+0.81}_{-0.74}$ | $0.35^{+0.12}_{-0.11}$ |
| hdfn_050 | IRX | 189.06689 | 62.18556 | $1.91^p$ | $17.52^{+0.85}_{-0.77}$ | $149.24^{+5.29}_{-4.95}$ | $40.57^{+1.96}_{-1.79}$ | $0.28^{+0.02}_{-0.03}$ |
| hdfn_060 | IRX | 189.22245 | 62.19449 | $1.27^s$ | $0.77^{+0.19}_{-0.16}$ | $< 1.25$ | $0.51^{+0.12}_{-0.11}$ | $-0.47^{+0.20}_{-0.20}$ |
| hdfn_067 | IRX | 189.23252 | 62.20028 | $2.74^s$ | $1.30^{+0.23}_{-0.21}$ | $1.53^{+0.80}_{-0.73}$ | $9.32^{+1.64}_{-1.48}$ | $-0.52^{+0.14}_{-0.15}$ |
| hdfn_080 | IRX | 189.14395 | 62.2115 | $1.22^s$ | $0.76^{+0.18}_{-0.16}$ | $2.44^{+0.85}_{-0.74}$ | $0.45^{+0.11}_{0.09}$ | $-0.16^{+0.18}_{-0.17}$ |
| hdfn_082 | IRX | 189.26096 | 62.21223 | $2.31^p$ | $2.49^{+0.31}_{-0.28}$ | $4.26^{+1.94}_{-0.93}$ | $10.46^{+1.28}_{-1.19}$ | $-0.45^{+0.09}_{-0.11}$ |
| hdfn_098 | IRX | 189.35108 | 62.23327 | $1.59^p$ | $5.29^{+0.51}_{-0.43}$ | $55.17^{+3.49}_{-3.12}$ | $6.95^{+0.66}_{-0.56}$ | $0.37^{+0.04}_{-0.05}$ |
| hdfn_107 | IRX | 189.14843 | 62.24015 | $2.01^s$ | $1.78^{+0.26}_{-0.24}$ | $20.20^{+2.02}_{-1.70}$ | $4.81^{+0.70}_{-0.64}$ | $0.39^{+0.07}_{-0.07}$ |
| hdfn_119 | IRX | 189.21598 | 62.25136 | $2.18^p$ | $7.10^{+0.55}_{-0.48}$ | $22.20^{+2.21}_{-1.86}$ | $24.82^{+1.92}_{-1.67}$ | $-0.21^{+0.05}_{-0.06}$ |
| hdfn_120 | IRX | 189.25198 | 62.25248 | $2.29^p$ | $3.31^{+0.38}_{-0.36}$ | $13.61^{+1.78}_{-1.65}$ | $13.51^{+1.56}_{-1.45}$ | $-0.07^{+0.08}_{-0.09}$ |
| hdfn_127 | IRX | 189.34672 | 62.2607 | $2.24^s$ | $4.42^{+0.47}_{-0.40}$ | $15.77^{+2.19}_{-1.82}$ | $16.90^{+1.81}_{-1.51}$ | $-0.14^{+0.09}_{-0.07}$ |
| hdfn_137 | IRX | 189.27041 | 62.26714 | $1.88^p$ | $27.65^{+1.04}_{-0.97}$ | $80.18^{+3.98}_{-3.63}$ | $60.95^{+2.30}_{-2.14}$ | $-0.25^{+0.03}_{-0.03}$ |
| hdfn_144 | IRX | 189.31159 | 62.27141 | $1.52^s$ | $8.93^{+0.62}_{-0.55}$ | $24.56^{+2.46}_{-2.10}$ | $10.24^{+0.72}_{-0.63}$ | $-0.27^{+0.06}_{-0.05}$ |
| hdfn_158 | IRX | 189.17957 | 62.28656 | $2.28^p$ | $11.17^{+0.73}_{-0.65}$ | $30.20^{+2.80}_{-2.39}$ | $44.94^{+2.94}_{-2.60}$ | $-0.28^{+0.05}_{-0.05}$ |
| hdfn_168 | IRX | 189.42735 | 62.30341 | $2.31^s$ | $83.05^{+1.87}_{-1.80}$ | $158.46^{+6.07}_{-5.69}$ | $347.76^{+7.85}_{-7.52}$ | $-0.43^{+0.02}_{-0.02}$ |
| hdfn_173 | IRX | 189.3245 | 62.3155 | $2.24^s$ | $37.72^{+1.23}_{-1.16}$ | $74.93^{+4.14}_{-3.78}$ | $143.06^{+4.68}_{-4.40}$ | $-0.41^{+0.03}_{-0.02}$ |

*Continued on next page*

Table 3.3 – *Continued from previous page*

| Name<br>(1) | Type<br>(2) | RA<br>(3) | Dec<br>(4) | Redshift<br>(5) | $F_{0.5-2keV}$<br>(6) | $F_{2-10keV}$<br>(7) | $L_{2-10keV}$<br>(8) | HR<br>(9) |
|---|---|---|---|---|---|---|---|---|
| hdfn_322 | IRX | 189.36066 | 62.34105 | $2.37^s$ | $2.29^{+0.50}_{-0.47}$ | $16.67^{+3.58}_{3}.14$ | $10.33^{+2.28}_{-2.13}$ | $0.19^{+0.14}_{-0.12}$ |
| hdfn_354 | IRX | 189.04882 | 62.17086 | $1.75^p$ | $< 0.30$ | $17.13^{+2.29}_{-1.95}$ | $< 0.52$ | $0.82^{+0.10}_{-0.07}$ |
| hdfn_364 | IRX | 189.30019 | 62.22381 | $2.00^s$ | $0.22^{+0.13}_{-0.12}$ | $6.83^{+1.35}_{-1.24}$ | $0.57^{+0.35}_{-0.31}$ | $0.63^{+0.14}_{-0.11}$ |
| hdfn_371 | IRX | 189.18504 | 62.24811 | $1.49^s$ | $< 0.11$ | $1.74^{+0.78}_{-0.68}$ | $< 0.11$ | $0.53^{+0.28}_{-0.18}$ |
| hdfn_401 | IRX | 189.20154 | 62.2379 | $2.00^s$ | $0.24^{+0.11}_{-0.09}$ | $< 0.50$ | $0.64^{+0.30}_{-0.24}$ | $-0.50^{+0.22}_{-0.40}$ |
| hdfn_476 | IRX | 189.16426 | 62.16842 | $2.35^s$ | $0.52^{+0.18}_{-0.15}$ | $< 0.72$ | $2.32^{+0.79}_{-0.68}$ | $-0.65^{+0.10}_{-0.35}$ |
| hdfn_490 | IRX | 189.25484 | 62.17116 | $2.13^p$ | $0.38^{+0.16}_{-0.14}$ | $< 0.71$ | $1.23^{+0.53}_{-0.46}$ | $-0.60^{+0.12}_{-0.40}$ |
| hdfn_044 | IRNX | 189.06021 | 62.17937 | $1.62^p$ | $1.90^{+0.31}_{-0.29}$ | $27.89^{+2.62}_{-2.27}$ | $2.64^{+0.43}_{-0.40}$ | $0.49^{+0.07}_{-0.06}$ |
| hdfn_062 | IRNX | 189.02426 | 62.19673 | $1.48^s$ | $5.45^{+0.57}_{-0.48}$ | $10.77^{+2.04}_{-1.90}$ | $5.81^{+0.60}_{-0.51}$ | $-0.40^{+0.08}_{-0.09}$ |
| hdfn_087 | IRNX | 189.09401 | 62.21847 | $2.98^s$ | $0.61^{+0.18}_{-0.16}$ | $1.59^{+0.88}_{-0.85}$ | $5.70^{+1.72}_{-1.47}$ | $-0.19^{0.22}_{-0.23}$ |
| hdfn_103 | IRNX | 189.08754 | 62.23701 | $1.77^p$ | $3.31^{+0.36}_{-0.34}$ | $10.63^{+1.55}_{-1.32}$ | $6.06^{+0.66}_{-0.62}$ | $-0.19^{+0.09}_{-0.08}$ |
| hdfn_232 | IRNX | 189.2976 | 62.22523 | $2.00^p$ | $0.73^{+0.19}_{-0.16}$ | $5.09^{+1.18}_{-1.07}$ | $1.95^{+0.50}_{-0.43}$ | $0.17^{+0.16}_{-0.13}$ |
| hdfn_355 | IRNX | 189.02883 | 62.17255 | $2.51^s$ | $0.45^{+0.24}_{-0.24}$ | $5.73^{+1.87}_{-1.78}$ | $2.45^{+1.28}_{-1.29}$ | $0.35^{+0.22}_{-0.19}$ |
| hdfn_356 | IRNX | 189.24513 | 62.17294 | $1.54^p$ | $0.19^{+0.12}_{-0.12}$ | $12.43^{+1.67}_{-1.56}$ | $0.23^{+0.14}_{-0.14}$ | $0.78^{+0.09}_{-0.07}$ |
| hdfn_424 | IRNX | 189.3924 | 62.27346 | $1.49^p$ | $0.75^{+0.31}_{-0.28}$ | $8.48^{+2.21}_{-2.07}$ | $0.80^{+0.33}_{-0.30}$ | $0.34^{+0.19}_{-0.15}$ |
| hdfn_478 | IRNX | 189.18971 | 62.19094 | $1.53^s$ | $0.27^{+0.13}_{-0.11}$ | $< 0.51$ | $0.32^{+0.16}_{-0.13}$ | $-0.63^{+0.10}_{-0.37}$ |
| hdfn_045 | pBzK | 189.12127 | 62.17952 | $1.01^s$ | $1.82^{+0.28}_{-0.26}$ | $20.09^{+2.11}_{-1.78}$ | $0.61^{+0.09}_{-0.09}$ | $0.38^{+0.06}_{-0.08}$ |

Splitting the sBzK galaxies into IRX and IRNX sub-samples we directly detect 13.2±1.9% (47/356) and 3.9±0.7% (34/879) respectively. It is clear that a greater proportion of IRXs than IRNXs are detected in X-rays. The IRXs are also significantly more X-ray luminous (median $L_{2-10keV} = 6.44 \times 10^{42}$ erg $s^{-1}$) than IRNXs (median $L_{2-10keV} = 2.26 \times 10^{42}$ erg $s^{-1}$). The higher detection fraction of IR Excess sBzKs may be more related to their IR luminosity, rather than the IR excess per se. Figure 3.6 clearly demonstrates a very strong correlation between the excess parameter and $L_{\mathrm{IR}}$, such that almost all of the most IR-luminous BzK galaxies also exhibit an IR excess.

If the sBzKs are binned by IR luminosity, as in Figure 3.7, the detected fractions of IRXs and IRNXs are largely similar. If anything, when controlled for IR luminosity, the IRNXs show a higher detected fraction, although this is not statistically significant. A similar fraction of IRXs and IRNXs possess $L_{2-10keV} > 10^{42}$ erg $s^{-1}$ (74% and 65% respectively), so the conclusion should also hold for the AGN fraction as well (i.e. as opposed to the detected fraction), especially when considering that the strongest star-formation will be in the most IR-luminous (and hence excess) galaxies.

The IRXs and IRNXs have very similar distributions of HR (see Figure 3.8). There are 14 (30%) IRXs and 11 (32%) IRNXs with HR > 0.2. These hard X-ray sources are almost certainly obscured AGN candidates, but there is no evidence that there is a heavier concentration of heavily obscured AGN within the IRX sample compared to the IRNX sample. A K-S test shows that, based on their HR distributions, the IRXs and IRNXs are consistent with each other (null hypothesis probability p=0.829). There are 4 sBzKs in this sample (all from the CDFS) that have previously been confirmed using X-ray spectroscopy as containing Compton thick AGN: cdfs4Ms_077 and cdfs4Ms_283 by Feruglio et al. (2011) and cdfs4Ms_126 and cdfs4Ms_226 by Brightman and Ueda (2012) (note that cdfs4Ms_077 was also identified by Brightman and Ueda 2012 as containing a Compton thick AGN). Only cdfs4Ms_226 is an IRNX, while cdfs4Ms_077, cdfs4Ms_126 and cdfs4Ms_283 are IRXs. The fraction of IRXs confirmed as Compton thick AGN from their X-ray spectra is lower than expected (3/49), but the X-ray detected IRX sample is too small to draw any strong conclusions regarding the nature of IRXs as a whole.

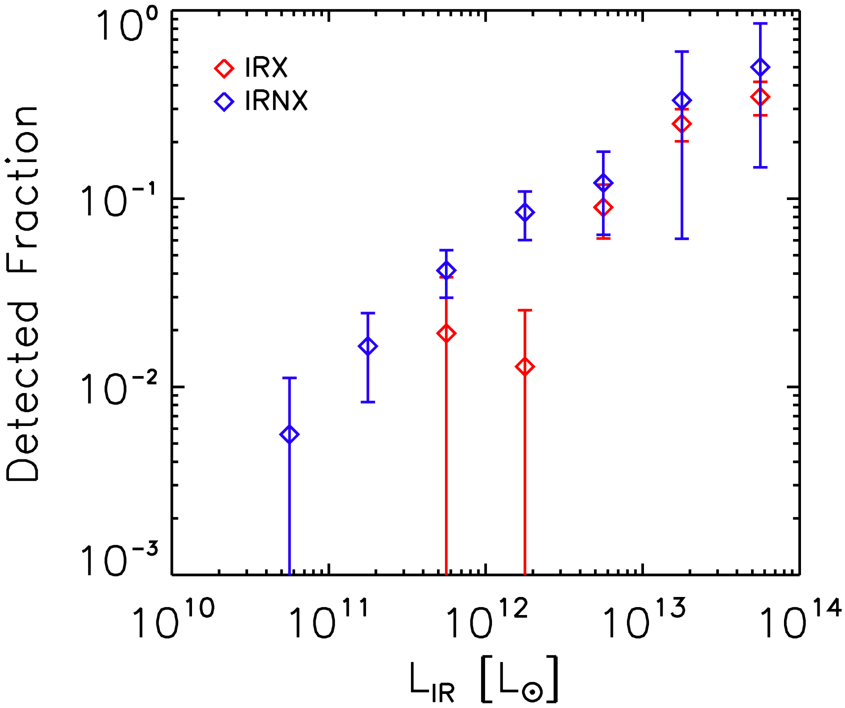

**Figure 3.7:** Plot of detected fraction of sBzKs against $L_{IR}$. The red diamonds are IRXs and the blue diamonds are IRNXs. Multinomial errors for sBzK detected fraction.

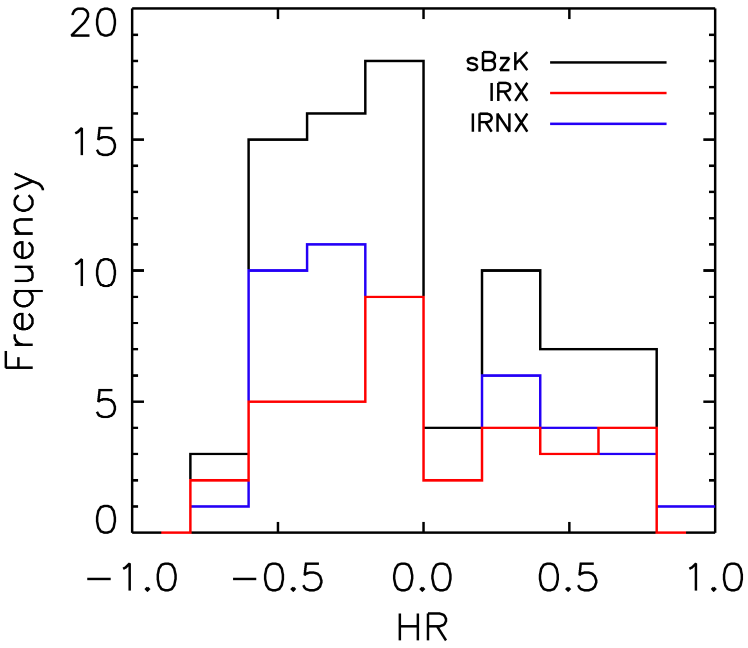

**Figure 3.8:** Histogram of the HRs of directly detected sBzK galaxies. The black line represents all sBzKs, the red line represents IRXs and the blue line represents IRNXs.

**Table 3.4:** Broad band stacking of X-ray undetected sBzK and pBzK galaxies in 4Ms CDFS and 2Ms CDFN. All fluxes calculated using flux conversion assuming $\Gamma = 1.4$. Column(1): Sample of galaxies stacked; column (2): No. of galaxies used stacked; column (3): soft (0.5-2keV) band SN; column (4): hard (2-7keV) band SN; column (5): full (0.5-7keV) band SN; column (6): 0.5-2keV flux, derived from soft band stacked counts, units $10^{-17}$ erg cm$^{-2}$ s$^{-1}$, if we assume $\Gamma = 2.0$ the soft band fluxes would be systematically 10% lower; column (7): 2-10keV flux, derived from hard band stacked counts, units $10^{-17}$ erg cm$^{-2}$ s$^{-1}$; column (8): 0.5-10keV flux, derived from full band stacked counts, units $10^{-17}$ erg cm$^{-2}$ s$^{-1}$; column (9): HR, HR= $(H - S)/(H + S)$, where $H$ and $S$ are hard- and soft-band count rates respectively; column (10): effective $\Gamma$ of stacked emission, derived from HR.

| Sample (1) | No. Src (2) | SN$_{soft}$ (3) | SN$_{hard}$ (4) | SN$_{full}$ (5) | $F_{soft}$ (6) | $F_{hard}$ (7) | $F_{full}$ (8) | HR (9) | $\Gamma_{eff}$ (10) |
|---|---|---|---|---|---|---|---|---|---|
| 4Ms CDFS sBzKs | 370 | 16.00 | 4.24 | 12.97 | $0.51 \pm 0.03$ | $0.90 \pm 0.21$ | $1.71 \pm 0.13$ | $-0.53 \pm 0.08$ | $2.1^{+0.3}_{-0.2}$ |
| 4Ms CDFS IRXs | 72 | 10.64 | 3.42 | 9.33 | $0.82 \pm 0.08$ | $1.66 \pm 0.49$ | $2.90 \pm 0.31$ | $-0.48 \pm 0.11$ | $2.0^{+0.3}_{-0.3}$ |
| 4Ms CDFS IRNXs | 298 | 12.40 | 3.02 | 9.75 | $0.43 \pm 0.03$ | $0.71 \pm 0.24$ | $1.43 \pm 0.15$ | $-0.55 \pm 0.11$ | $2.2^{+0.4}_{-0.3}$ |
| 2Ms CDFN sBzKs | 318 | 12.88 | 4.17 | 11.50 | $0.59 \pm 0.05$ | $1.22 \pm 0.29$ | $2.10 \pm 0.18$ | $-0.47 \pm 0.09$ | $2.0^{+0.2}_{-0.2}$ |
| 2Ms CDFN IRXs | 107 | 10.34 | 3.31 | 9.34 | $0.88 \pm 0.09$ | $1.69 \pm 0.51$ | $3.08 \pm 0.33$ | $-0.50 \pm 0.12$ | $2.0^{+0.4}_{-0.2}$ |
| 2Ms CDFN IRNXs | 211 | 8.20 | 2.74 | 7.34 | $0.44 \pm 0.05$ | $0.98 \pm 0.36$ | $1.61 \pm 0.22$ | $-0.45 \pm 0.15$ | $1.9^{+0.5}_{-0.3}$ |
| Combined sBzKs | 688 | 20.44 | 5.77 | 17.07 | $0.55 \pm 0.02$ | $1.04 \pm 0.18$ | $1.89 \pm 0.11$ | $-0.50 \pm 0.06$ | $2.0^{+0.2}_{-0.1}$ |
| Combined IRXs | 179 | 14.81 | 4.73 | 13.12 | $0.86 \pm 0.06$ | $1.68 \pm 0.36$ | $3.00 \pm 0.23$ | $-0.49 \pm 0.08$ | $2.0^{+0.3}_{-0.2}$ |
| Combined IRNXs | 509 | 14.84 | 3.95 | 12.08 | $0.43 \pm 0.03$ | $0.82 \pm 0.20$ | $1.50 \pm 0.13$ | $-0.51 \pm 0.09$ | $2.1^{+0.4}_{-0.2}$ |
| Combined pBzKs | 13 | 2.99 | 2.09 | 3.47 | $0.49 \pm 0.16$ | ... | $2.23 \pm 0.62$ | ... | ... |

### 3.3.2 Stacking X-ray Undetected sBzKs in Broad Energy Bands

In addition to analysing the direct detections, X-ray undetected sBzKs in 4Ms CDFS and 2Ms CDFN were stacked to probe their average X-ray properties. In the first instance the X-ray photons are stacked in 3 broad bands: $0.5-2$ keV (soft), $2-7$ keV (hard) and $0.5-7$ keV (full). The stacked photon count rates are then converted to fluxes assuming a $\Gamma = 1.4$ power-law: $F_{0.5-2keV}$ (soft), $F_{2-10keV}$ (hard), and $F_{0.5-10keV}$ (full). Starting with the full sample, 370 X-ray undetected sBzKs were stacked in the 4Ms CDFS, producing a highly significant signal in the soft and hard band. The stacked signal possessed a HR $= -0.53 \pm 0.08$. In the 2Ms CDFN, 318 X-ray undetected sBzKs were stacked and again producing significant soft and hard band signals, with a HR $= -0.47 \pm 0.09$. The stacked flux of the X-ray undetected sBzKs in CDFN is higher than for those in CDFS (see Table 3.4) because the 4Ms CDFS is deeper, and the brightest sources stacked in the CDFN 2Ms image would be detected and resolved out in the CDFS 4Ms image. For the total sample, both CDFS and CDFN sBzK galaxies exhibit soft HRs in these broad bands and there is no evidence to suggest a substantial proportion of the sBzKs contain heavily obscured AGN.

Splitting the sBzKs using the IR excess criterion (Equation 3.9), samples of 72 X-ray undetected IRXs and 298 X-ray undetected IRNXs in 4Ms CDFS were stacked. The stacked signal of the X-ray undetected IRXs is significantly detected in both soft and hard band with a HR $= -0.48 \pm 0.11$. The stacked signal of X-ray undetected IRNXs is also significantly detected in the soft and hard band, but is more X-ray faint (see Table 3.4) and has a softer HR ($-0.55 \pm 0.11$). The higher flux of the stacked IRXs is in agreement with the fluxes observed in the directly detected sources (Section 3.3.1). Again, however, this can be attributed to the higher IR luminosity for the excess sources, whose median $L_{\rm IR} = 3.6 \times 10^{12} L_{\odot}$ is over an order of magnitude higher than the IRNX sources (median $L_{\rm IR} = 3.1 \times 10^{11} L_{\odot}$). Additionally the HR and effective $\Gamma$ of X-ray undetected IRXs and IRNXs in CDFS are consistent with each other at the $1\sigma$ level (see Table 3.4) which suggests the composition of the sub-samples is similar.

Turning to the 2Ms CDFN, samples of 107 X-ray undetected IRXs and 211 X-ray undetected IRNXs were stacked. As with the stacking in 4Ms CDFS, the IRXs are significantly detected in both the soft and hard bands. The HR ($-0.50 \pm 0.12$), agrees with the stacked signal of 4Ms CDFS X-ray undetected IRXs at the $1\sigma$ level. The X-ray undetected IRNXs are significantly detected in the soft band (SN $= 8.2$) but the hard band is a low significance detection (SN $= 2.7$). The stacked fluxes are again higher than 4Ms CDFS X-ray undetected IRNXs (see Table 3.4) and the HR $= -0.45 \pm 0.15$. The HRs of X-ray undetected IRXs and IRNXs are consistent at the $1\sigma$ level although the low significance hard band detection of X-ray undetected IRNXs means the HR is probably softer than our current estimate. Ultimately all stacks of X-ray undetected sBzKs and the IRX and IRNX subsamples agree at the $1\sigma$ level (Table 3.4) and there is no evidence from broad band stacking that heavily obscured AGN are more prevalent among X-ray undetected

IRXs than X-ray undetected IRNXs.

As discussed in Section 3.2.4, the IR excess criterion (Equation 3.9) is positively correlated with redshift and $L_{IR}$ (Figures 3.5 and 3.6 respectively) and this is likely to account for the higher X-ray fluxes of the IRXs. To investigate this further, samples binned by redshift and $L_{IR}$ were stacked. The sBzK galaxy samples from CDFS and CDFN have been combined to maximise the SN ratio in each redshift and $L_{IR}$ bin.

The X-ray undetected sBzKs are split into 3 redshift bins with ranges that have been chosen to distribute the sources as evenly as possible: $1.2 \leq z < 1.8$, $1.8 \leq z < 2.4$ and $2.4 \leq z < 3.0$. The stacked emission of X-ray undetected sBzKs with $1.2 \leq z < 1.8$ and $1.8 \leq z < 2.4$ possess HR $= -0.47 \pm 0.10$ and HR$= -0.48 \pm 0.09$ respectively and exhibit similar X-ray fluxes (see Table 3.5). The effective $\Gamma$ values are consistent with those observed for X-ray undetected IRX and IRNX subsamples at the $1\sigma$ level. The $2.4 \leq z < 3.0$ X-ray undetected sBzKs have a similar flux to the lower redshift sources in the soft band, but no detection in the hard band (SN $= 0.6$). The HR is therefore very uncertain, but inferring the hard flux from the full band detection shows X-ray colours which are entirely consistent with the lower redshift bins. As the fluxes of each redshift-binned subsample are all similar, this naturally implies that the higher redshift sources are on average more luminous in the X-ray, but this is likely to be a selection effect due to the fact that the parent sample is magnitude limited, meaning that the higher redshift sources need to be more luminous overall to enter the sample.

The X-ray undetected sBzKs were also split into 4 $L_{IR}$ bins to explore the connection between $L_{IR}$ and the IR excess criterion (Section 4.2): $L_{IR} < 10^{11}L_{\odot}$, $10^{11}L_{\odot} \leq L_{IR} < 10^{12}L_{\odot}$ , $10^{12}L_{\odot} \leq L_{IR} < 10^{13}L_{\odot}$ and $L_{IR} \geq 10^{13}L_{\odot}$. There is a strong correlation between X-ray brightness and $L_{IR}$ of the sBzKs (see Table 3.5). This result is in agreement with our observations of directly detected X-ray sources. All bins are significantly detected in hard and soft bands except for $L_{IR} < 10^{11}L_{\odot}$ which has a low significance detection in the hard band (SN=2.1). The HR values of all the $L_{IR}$ binned sBzK sub-samples are consistent with one another at the $1\sigma$ level and the stacked signal of X-ray undetected IRXs and X-ray undetected IRNXs in CDFN and CDFS. As with the redshift selected galaxies, none of the $L_{IR}$ bins appear to preferentially select heavily obscured AGN, but the X-ray undetected BzK galaxies which are more luminous in the IR have brighter stacked X-ray fluxes.

**Table 3.5:** Broad band stacking of redshift and IR luminosity binned X-ray undetected sBzKs. Galaxies in 4Ms CDFS and 2Ms CDFN have been combined to boost the SN ratio of the stacks. All fluxes calculated using flux conversion assuming $\Gamma \sim 1.4$. Column(1): Sample of galaxies stacked; column (2): No. of galaxies used stacked; column (3): soft (0.5-2keV) band SN; column (4): hard (2-7keV) band SN; column (5): full (0.5-7keV) band SN; column (6): 0.5-2keV flux, derived from soft band stacked counts, units $10^{-17}$ erg cm$^{-2}$ s$^{-1}$, if we assume $\Gamma = 2.0$ the soft band fluxes would be systematically 10% lower; column (7): 2-10keV flux, derived from hard band stacked counts, units $10^{-17}$ erg cm$^{-2}$ s$^{-1}$; column (8): 0.5-10keV flux, derived from full band stacked counts, units $10^{-17}$ erg cm$^{-2}$ s$^{-1}$; column (9): HR, HR= $(H - S)/(H + S)$, where $H$ and $S$ are hard- and soft-band count rates respectively; column (10): effective $\Gamma$ of stack, derived from HR.

| Sample<br>(1) | No. Src<br>(2) | SN$_{soft}$<br>(3) | SN$_{hard}$<br>(4) | SN$_{full}$<br>(5) | $F_{soft}$<br>(6) | $F_{hard}$<br>(7) | $F_{full}$<br>(8) | HR<br>(9) | $\Gamma_{eff}$<br>(10) |
|---|---|---|---|---|---|---|---|---|---|
| $1.2 \leq z < 1.8$ | 340 | 12.62 | 4.06 | 10.91 | $0.38 \pm 0.03$ | $0.71 \pm 0.18$ | $1.29 \pm 0.12$ | $-0.47 \pm 0.10$ | $2.0^{+0.3}_{-0.3}$ |
| $1.8 \leq z < 2.4$ | 304 | 14.28 | 4.12 | 11.97 | $0.47 \pm 0.03$ | $0.84 \pm 0.19$ | $1.54 \pm 0.13$ | $-0.48 \pm 0.09$ | $2.0^{+0.3}_{-0.2}$ |
| $2.4 \leq z < 3.0$ | 97 | 6.46 | 0.62 | 4.31 | $0.36 \pm 0.05$ | ... | $1.01 \pm 0.21$ | ... | ... |
| $L_{IR} < 10^{11}$ | 108 | 5.96 | 2.12 | 5.31 | $0.33 \pm 0.06$ | $0.71 \pm 0.33$ | $1.16 \pm 0.21$ | $-0.42 \pm 0.20$ | $1.8^{+0.7}_{-0.4}$ |
| $10^{11} \leq L_{IR} < 10^{12}$ | 393 | 11.16 | 3.60 | 9.46 | $0.29 \pm 0.03$ | $0.64 \pm 0.16$ | $1.01 \pm 0.11$ | $-0.40 \pm 0.11$ | $1.8^{+0.3}_{-0.2}$ |
| $10^{12} \leq L_{IR} < 10^{13}$ | 203 | 13.42 | 3.73 | 11.31 | $0.56 \pm 0.04$ | $0.86 \pm 0.23$ | $1.78 \pm 0.16$ | $-0.54 \pm 0.10$ | $2.1^{+0.4}_{-0.2}$ |
| $L_{IR} \geq 10^{13}$ | 59 | 13.44 | 7.03 | 14.14 | $1.21 \pm 0.09$ | $2.89 \pm 0.47$ | $4.40 \pm 0.33$ | $-0.37 \pm 0.08$ | $1.7^{+0.2}_{-0.1}$ |

**Table 3.6:** Narrow band stacking of X-ray undetected sBzK galaxies in 4Ms CDFS and 2Ms CDFN. Column (1): energy range of narrow band; column (2): number of sBzKs stacked; column (3): SN of stacked sBzKs; column (4): narrow band flux of stacked sBzKs, units $10^{-18}$ erg cm$^{-2}$ s$^{-1}$; column (5): number of IRXs stacked; column (6): SN of stacked IRXs; column (7): narrow band flux of stacked IRXs, units $10^{-18}$ erg cm$^{-2}$ s$^{-1}$; column (8): number of IRNXs stacked; column (9): SN of stacked IRNXs; column (10): narrow band flux of stacked IRNXs, units $10^{-18}$ erg cm$^{-2}$ s$^{-1}$.

| | sBzKs | | | IRXs | | | IRNXs | | |
|---|---|---|---|---|---|---|---|---|---|
| Band (keV) (1) | No. Src (2) | SN (3) | Flux (4) | No. Src (5) | SN (6) | Flux (7) | No. Src (8) | SN (9) | Flux (10) |
| 0.5-1.0 | 688 | 10.15 | $40.63 \pm 3.94$ | 179 | 6.51 | $51.35 \pm 8.08$ | 509 | 7.93 | $36.87 \pm 4.50$ |
| 1.0-1.5 | 688 | 15.21 | $8.07 \pm 0.55$ | 179 | 11.71 | $14.83 \pm 1.30$ | 509 | 10.47 | $5.70 \pm 0.59$ |
| 1.5-2.0 | 688 | 9.27 | $1.18 \pm 0.13$ | 179 | 6.22 | $1.65 \pm 0.28$ | 509 | 7.09 | $1.01 \pm 0.15$ |
| 2.0-2.5 | 688 | 3.92 | $1.12 \pm 0.29$ | 179 | 3.12 | $1.84 \pm 0.60$ | 509 | 2.72 | $0.86 \pm 0.32$ |
| 2.5-3.5 | 688 | 3.44 | $5.34 \pm 1.62$ | 179 | 1.32 | $2.86 \pm 3.16$ | 509 | 3.19 | $6.21 \pm 1.89$ |
| 3.5-5.0 | 688 | 2.40 | $5.01 \pm 2.09$ | 179 | 2.03 | $9.92 \pm 4.36$ | 509 | 1.61 | $3.29 \pm 2.38$ |
| 5.0-7.0 | 688 | 1.57 | $6.92 \pm 4.23$ | 179 | 2.25 | $17.29 \pm 8.76$ | 509 | 0.51 | $3.28 \pm 4.82$ |

### 3.3.3 Stacking X-ray Undetected sBzKs in Narrow Energy Bands

When stacked in broad bands (Section 3.3.2) the X-ray undetected IRXs and X-ray undetected IRNXs both appear to have relatively soft X-ray spectra, with effective $\Gamma \sim 2$. Based on this analysis there is no evidence for obscured AGN in either subsample. The broad bands, however, may mask more complex spectral features and give a misleading picture of the actual spectral shape and hence the level of obscuration (see e.g. Brightman and Nandra 2012). Therefore the sBzKs are stacked in narrower energy bands to obtain a more accurate representation of their spectra (Table 3.6 and Figure 3.9). The bands in Table 4 have been designed to provide the optimum balance of resolution and signal strength. Narrower bands have fewer counts so the CDFS and CDFN sBzKs have been combined to maximise the SN ratio in these bands. This analysis shows clearly that the naive interpretation of the broad band colours gives a misleading impression of the true spectral shape, which does not resemble a single power law. The total spectrum is clearly "composite" in nature with a soft component dominating the soft energies, and a flat, hard component coming through at high energies. The latter is a clear signature of obscured AGN in the sBzK galaxies. The soft component is more ambiguous and could originate from a range of sources. There could be contributions from unobscured AGN, scattered light in heavily obscured AGN and/or X-rays from pure star forming processes. The stacked spectrum indicates that there is a mixture of these effects within the sample.

Splitting the sample into IRXs and IRNXs, what is instantly obvious are their remarkably similar spectral shape with the only noticeable difference being that IRNXs are consistently less X-ray bright (see Figure 3.9), just as was observed for broad band stacking (see Section 3.3.2). Thus, while the narrow band analysis confirms the presence of residual AGN activity in the population of sBzK galaxies as a whole, there is no evidence that obscured AGN or AGN generally are preferentially hosted by those with excess emission at 24 $\mu$m.

### 3.3.4 X-ray Properties of Passively Evolving BzK Galaxies

There are 21 passively evolving BzKs (pBzK) in CDFS and 5 pBzKs in CDFN. From these samples, X-ray counterparts are attributed to 3 pBzKs in the CDFS 4Ms and 1 pBzK in the CDFN 2Ms, see Tables 3.2 and 3.3. While these samples are small, and hence the uncertainties large, the pBzK detection fraction (15±8.0%; 4/26) is actually greater than for sBzKs (7±0.7%; 81/1235). The sources cdfs4Ms_301, cdfs4Ms_457 and hdfn_045 have hard signals which suggest the presence of obscured AGN. The source cdfs4Ms_318 lacks a hard band detection but $L_{0.5-2.0keV} = 1.1 \times 10^{42}$ erg s$^{-1}$ (derived from $F_{0.5-2kev}$). The X-ray emission probably originates from either unobscured AGN activity or from a hot gas halo within the galaxy (Forman et al., 1985; Sarazin, 1997). Intense star-formation is unlikely to be the source of the observed X-ray emission, recalling that these objects have been selected as passively evolving galaxies. Stacking the X-ray emission of the 13 undetected pBzKs in CDFS and CDFN yields a marginal signal in the soft band, with

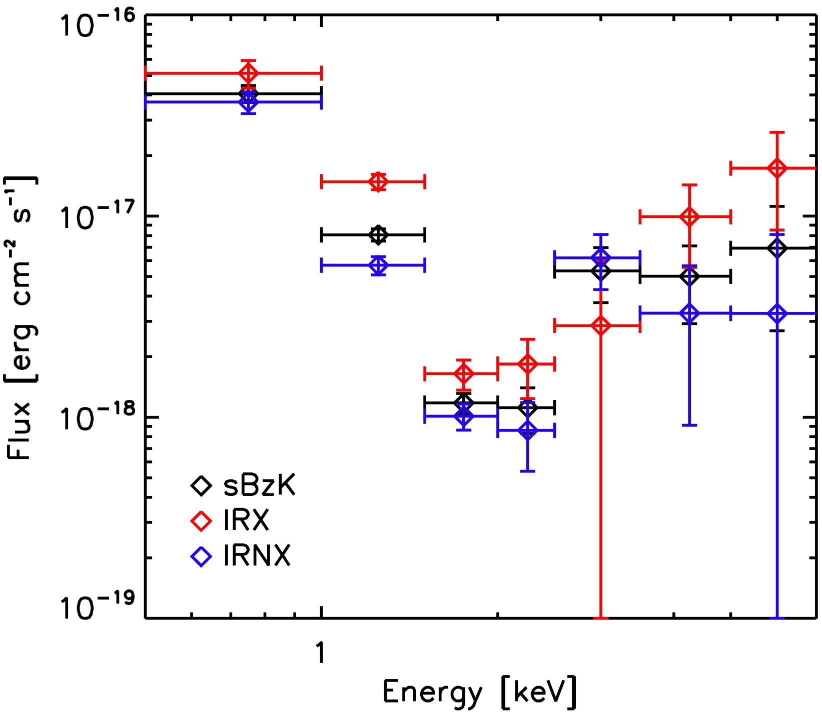

**Figure 3.9:** Flux estimates for narrow band stacking of IRXs (red diamonds) and IRNXs (blue diamonds) galaxies in the 4Ms CDFS and 2Ms CDFN. The horizontal error bars represent the width of the energy band that is being stacked. The IRXs stacked in the two highest energy bands are not significantly detected.

average $F_{0.5-2keV} = 2.23 \pm 0.62 \times 10^{-17}$ erg cm$^{-2}$ s$^{-1}$. Stacking the hard band flux does not result in a significant detection.

## 3.4 Comparison to Previous Results

Daddi et al. (2007b) stacked the X-ray emission of 59 IRXs and 175 IRNXs that were not directly detected in X-rays using a 1Ms CDFS image and source list. Their sample of X-ray undetected IRXs had a much harder stacked signal (effective $\Gamma = 0.8^{+0.4}_{-0.3}$) than the X-ray undetected IRXs that have been stacked in this work using 4Ms CDFS and 2Ms CDFN data (see Table 3.4). There are a number of possible reasons for this discrepancy, including differences in the parent BzK sample and deeper X-ray data in our case. To help understand this discrepancy we stacked our samples of X-ray undetected IRXs and X-ray undetected IRNXs using only the 1Ms CDFS images and source list to provide a direct comparison (Table 3.7). Due to the shallower data fewer sBzKs are directly detected in the 1Ms CDFS and therefore more X-ray undetected IRXs (80) and IRNXs (311) are stacked. The samples of X-ray undetected IRXs and IRNXs presented here are different to (and larger than) those of Daddi et al. (2007b). This is because of the updated photometry in GOODS-MUSIC v2 which includes deeper 24$\mu$m data that is used in this work (de Santis et al., 2007).

The X-ray undetected IRXs were significantly detected in both the soft (SN = 5.6) and hard (SN = 3.6) bands with HR = $-0.16 \pm 0.16$ and corresponding effective $\Gamma = 1.3^{+0.4}_{-0.3}$. This effective $\Gamma$ is harder than what was obtained by stacking X-ray undetected IRXs using the CDFS 4Ms data, and while formally softer than that derived by Daddi et al. (2007b), it is consistent with their results at the 1$\sigma$ level. The X-ray undetected IRNXs are significantly detected in the soft band (SN = 7.6), but the hard band is a low significance detection (SN = 2.2), again consistent with the findings of Daddi et al. (2007b). The HR = $-0.52 \pm 0.17$ and corresponding effective $\Gamma = 2.1^{+0.6}_{-0.4}$ are poorly constrained but are also consistent with the effective $\Gamma \sim 1.7$ of Daddi et al. (2007b) at the 1$\sigma$ level.

**Table 3.7:** Broad band stacking of X-ray undetected sBzK galaxies in 1Ms CDFS and sBzKs that were subsequently detected in the 4Ms CDFS. All fluxes calculated using flux conversion assuming $\Gamma = 1.4$. The 4Ms detected galaxies $F_{full}$ is lower than $F_{hard}$ because the power-law ($\Gamma$=1.4) used to approximate the spectra is too soft. Column(1): Sample of galaxies stacked; column (2): No. of galaxies used stacked; column (3): soft (0.5-2keV) band SN; column (4): hard (2-7keV) band SN; column (5): full (0.5-7keV) band SN; column (6): 0.5-2keV flux, derived from soft band stacked counts, units $10^{-17}$ erg cm$^{-2}$ s$^{-1}$; column (7): 2-10keV flux, derived from hard band stacked counts, units $10^{-17}$ erg cm$^{-2}$ s$^{-1}$; column (8): 0.5-10keV flux, derived from full band stacked counts, units $10^{-17}$ erg cm$^{-2}$ s$^{-1}$; column (9): HR, HR= $(H-S)/(H+S)$, where $H$ and $S$ are hard- and soft-band count rates respectively; column (10): effective $\Gamma$ of stack, derived from HR.

| Sample (1) | No. Src (2) | SN$_{soft}$ (3) | SN$_{hard}$ (4) | SN$_{full}$ (5) | $F_{soft}$ (6) | $F_{hard}$ (7) | $F_{full}$ (8) | HR (9) | $\Gamma_{eff}$ (10) |
|---|---|---|---|---|---|---|---|---|---|
| 1Ms CDFS sBzKs | 391 | 9.32 | 3.64 | 8.84 | $0.51 \pm 0.06$ | $1.29 \pm 0.36$ | $1.94 \pm 0.22$ | $-0.39 \pm 0.12$ | $1.8^{+0.3}_{-0.3}$ |
| 1Ms CDFS IRXs | 80 | 5.56 | 3.60 | 6.32 | $0.70 \pm 0.13$ | $2.96 \pm 0.82$ | $3.20 \pm 0.51$ | $-0.15 \pm 0.16$ | $1.3^{+0.4}_{-0.3}$ |
| 1Ms CDFS IRNXs | 311 | 7.58 | 2.17 | 6.62 | $0.46 \pm 0.06$ | $0.86 \pm 0.40$ | $1.62 \pm 0.24$ | $-0.51 \pm 0.17$ | $2.1^{+0.6}_{-0.4}$ |
| 4Ms CDFS detected sBzKs | 12 | 9.69 | 9.96 | 13.74 | $2.41 \pm 0.25$ | $16.02 \pm 1.60$ | $13.89 \pm 1.01$ | $0.07 \pm 0.07$ | $0.8^{+0.2}_{-0.1}$ |
| 4Ms CDFS detected IRXs | 6 | 7.52 | 8.57 | 11.29 | $2.72 \pm 0.36$ | $20.61 \pm 2.40$ | $16.98 \pm 1.50$ | $0.14 \pm 0.09$ | $0.7^{+0.2}_{-0.1}$ |
| 4Ms CDFS detected IRNXs | 6 | 6.13 | 5.27 | 7.37 | $2.11 \pm 0.35$ | $11.15 \pm 2.12$ | $10.80 \pm 1.36$ | $-0.04 \pm 0.12$ | $1.0^{+0.3}_{-0.2}$ |

This analysis, and that of Daddi et al. (2007b), shows that the spectrum is more complex than a simple power-law, so a naive comparison of the two spectral indices does not give the full picture. Nonetheless it is clear that the overall spectrum of X-ray undetected IRXs is softer. The above analysis shows that this can be partially, but not completely explained by the difference in the parent BzK sample. A further possibility is that the 1Ms stack is contaminated by hard sources undetected in the 1Ms image, but detected and resolved out in the 4Ms data. There are 22 sBzKs (9 IRXs; 13 IRNXs) which are detected in the 4Ms CDFS image but are undetected (i.e. fall below the detection limit) in the 1Ms CDFS image (see Table 3.7). Of these 22 sBzKs, 6 IRXs and 6 IRNXs were stacked in the 1Ms CDFS image. The 3 IRXs and 6 IRNXs that were directly detected in the 4Ms CDFS images were omitted from the stacking as they fell outside the 5.5 arcminute inclusion radius (see Section 3.2.6). Focusing on the X-ray detected IRXs (because their signal softened more dramatically) the average HR $= 0.14 \pm 0.09$, with effective $\Gamma = 0.7^{+0.2}_{-0.1}$, is much harder than the stacked signal of IRXs undetected in the 4Ms image (HR $= -0.48 \pm 0.11$). This strongly suggests that the 1Ms CDFS stacked signal is indeed contaminated by hard sources which are subsequently detected in the deeper 4Ms CDFS data. Narrow band stacking of IRXs that are detected in the 4Ms CDFS but not the 1Ms CDFS (Figure 3.10) better illustrates the full effect of the 4Ms detected population. The stacked spectral shapes of X-ray undetected IRXs and 4Ms detected IRXs are similar up to 1.5 keV (approximately 4.5 keV rest-frame). At higher energies the stacked signals diverge and the 4Ms detected IRXs dominate the X-ray undetected IRXs. Including the 4Ms detected sBzKs in the stacking analysis (as in the 1Ms CDFS) causes the X-ray undetected IRXs to appear to have a much harder signal. We conclude that this is the main reason why the stacked signal of X-ray undetected IRXs in Daddi et al. (2007b) is harder than the stacked signal we find for the 4Ms CDFS X-ray undetected IRXs.

Alexander et al. (2011) took a more in depth look at the X-ray properties of X-ray detected sBzKs by limiting their sample of sBzKs, an updated version of the Daddi et al. (2007b) sample, to those with $< 5.5$ arcminute OAA and cross-correlating them with the 4Ms CDFS catalogue of Xue et al. (2011) using a 1.5 arcsecond matching radius. They directly detect 47 sBzKs, where 60% are IRXs and the remaining 40% are IRNXs. Additionally 23% (11/47) of the sBzKs are classified as heavily obscured AGN because they exhibit a hard X-ray spectral shape ($\Gamma \leq 1$). If a similar cut in OAA is applied to the sBzK sample presented in this work (see Table 3.2), there are 35 X-ray detected sBzKs, with 51% classified as IRXs and 49% classified as IRNXs. Based on the HR of these sBzKs, 46% of these sBzKs are defined as heavily obscured (HR $> -0.08$; see Section 3.3.1).

By cross correlating the X-ray detected sBzKs of Alexander et al. (2011) and the 35 X-ray detected sBzKs (within OAA $< 5.5$) presented in this work (using a nearest neighbour method with 1.25 arcsecond matching radius), 23 sBzKs are found to be common to both samples. There are 19 IRXs and 14 IRNXs within this “shared” sample. According to Alexander et al. (2011), 8 of these sources are heavily obscured, whereas in this work 9

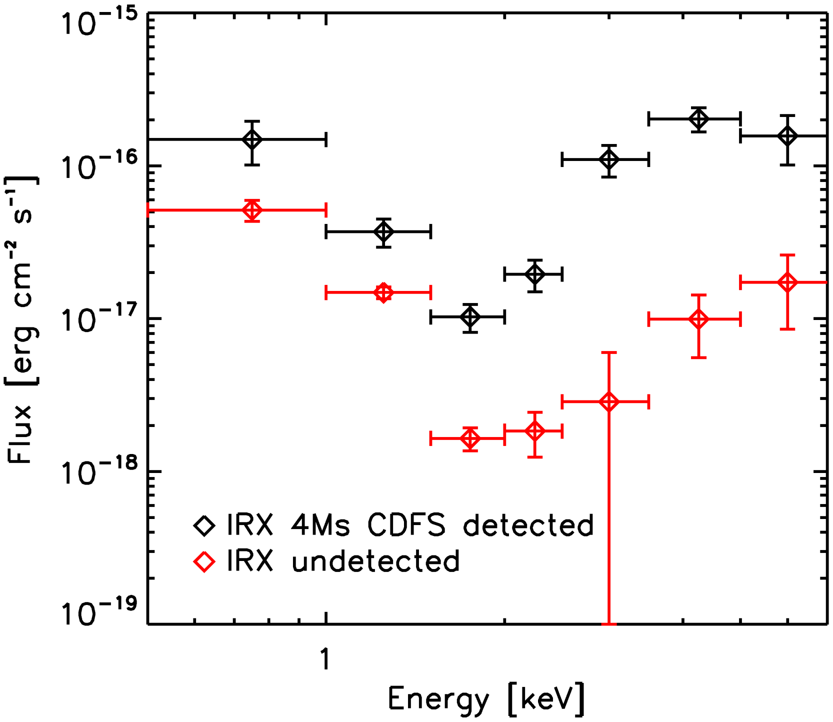

**Figure 3.10:** Flux estimates for narrow band stacking of 72 X-ray undetected IRXs (red diamonds) and 6 IRXs that were only detected in the 4Ms CDFS data (black diamonds) using 4Ms CDFS images. The horizontal error bars represent the width of the energy band that is being stacked.

sources are defined as heavily obscured according to their HR (see Section 3.3.1). These two samples of heavily obscured sources show good agreement, 7 of the sBzKs are defined as heavily obscured by Alexander et al. (2011) and by their HRs. X-ray fluxes from the Xue et al. (2011) 4Ms CDFS catalogue, used by Alexander et al. (2011), were measured for 0.5-2 keV (soft), 2-8 keV (hard) and 0.5-8 keV (full) ranges. The fluxes were calculated assuming a power-law type spectrum, where the photon indices of each source were derived from the hard-to-soft band count ratio ($H/S$). Therefore to provide a more direct comparison of the X-ray fluxes of the 23 "shared" sources the X-ray fluxes presented in this work were recalculated using the same energy ranges as the Xue et al. (2011) 4Ms CDFS catalogue and $\Gamma = 1.4$. There are inevitably some discrepancies between the fluxes presented in this work and those presented by Xue et al. (2011) because of the difference between the $\Gamma$ values used to calculate flux. Irrespective of this the majority of fluxes show good agreement (lie within $1\sigma$ error bars).

The Alexander et al. (2011) sample has 24 X-ray detected sBzKs which were not present in the sample presented here. Of these 24 galaxies, 8 sources were present in the sBzK sample but were not detected in the Imperial College 4Ms CDFS catalogue, while the remaining 16 were not in the sBzK sample presented here. The Xue et al. (2011) 4Ms CDFS catalogue has 740 sources while the more conservative Imperial College 4Ms catalogue has 569 sources (see Section 3.2.5), so it is to be expected that the former would detect a larger number of sBzKs. The 8 galaxies that were identified as sBzKs in this work but are not detected in the Imperial College 4Ms catalogue are all low significance detections (have low binomial detection probabilities) in the Xue et al. (2011) 4Ms CDFS catalogue, hence probably lie just below the detection threshold of our catalogue. The remaining 16 X-ray detected sBzKs in the Alexander et al. (2011) sample were omitted from our sBzK sample because they did not satisfy one or more of the criteria given in Section 3.2.1. The sample presented here has been selected in a manner that should replicate the sample of Daddi et al. (2007b) as closely as possible. There are, however, two key differences between the sBzK sample selection methods, necessitated by updates to multiwavelength photometry in CDFS since the publication of Daddi et al. (2007b). First a different IRAC 3.6$\mu$m selected catalogue was used in this work to ensure the 24$\mu$m sources are deblended. Secondly, 24$\mu$m source photometry in the sample presented here was extracted using the ConvPhot software (de Santis et al., 2007), whereas the Daddi et al. (2007b) sample uses a more basic fixed matching radius method. These modifications are the most likely source of discrepancies between the Daddi et al. (2007b) sample and the sBzK sample used in this work. There are also 12 X-ray detected sBzKs in this sample which are not present in the Alexander et al. (2011) sample. Again this is due to the aforementioned discrepancies between the respective X-ray point source catalogues and optical sample selection criteria.

Alexander et al. (2011) stack the remaining X-ray undetected sBzKs in a similar fashion to Daddi et al. (2007b) using the 4Ms CDFS images. They stack 47 X-ray undetected IRXs and 116 X-ray undetected IRNXs and find effective $\Gamma = 1.4 \pm 0.3$ and $\Gamma = 2.0 \pm 0.4$ respectively. The effective $\Gamma$ values of the stacked emission of X-ray undetected IRXs and IRNXs are consistent with those presented in this work for 4Ms CDFS data at the 1 $\sigma$ level (see Table 3.4). The effective $\Gamma$ of the X-ray undetected IRXs is also significantly softer than the value calculated in Daddi et al. (2007b). Similar to this work, Alexander et al. (2011) conclude that the majority of hard sources have been resolved in the 4Ms CDFS data and that there is no longer strong evidence that heavily obscured AGN are the dominant population amongst the remaining X-ray undetected sBzKs.

## 3.5 Discussion

Using the deepest data available, the X-ray properties of a large sample of star-forming BzK-selected galaxies in the redshift range $z = 1.2 - 3.0$ have been investigated in the CDFN and CDFS regions. The X-ray emission is particularly important for assessing the AGN content of these galaxies. Specifically, a direct detection of the X-ray emission makes the presence of an actively growing supermassive black hole very likely, as the implied luminosity ($L_X > 10^{42}$ erg s$^{-1}$) can only be exceeded by the most extreme star-forming galaxies. The sBzK galaxies are found to have a relatively high (6 % approximately), direct X-ray detection fraction overall, indicating a very substantial AGN content. Also, consistent with previous analysis, a very large fraction of the X-ray detected sBzKs are found to be heavily obscured, based on their hardness ratios. The implied column densities are substantial (usually $N_H > 10^{23}$ cm$^{-2}$). Four of the X-ray detected sBzKs have been identified as Compton thick AGN based on their X-ray spectra in previous work: cdfs4Ms_077 and cdfs4Ms_283 by Feruglio et al. (2011) and cdfs4Ms_126 and cdfs4Ms_226 by Brightman and Ueda (2012). Of these four Compton thick AGN, 3 are IRXs and 1 is an IRNX.

Stacking the emission from the sBzKs which are not detected directly by X-rays produces a strong signal in both the soft and hard X-ray bands. By stacking in relatively narrow energy bands a crude stacked spectrum was constructed for these X-ray undetected objects. The stacked spectrum is composite in nature, with a soft component dominating at low energies and harder emission at high energy. The hard spectrum above $\sim 2$ keV is a clear signature of obscured AGN activity in part of the sBzK population at a level below the X-ray detection threshold in each field. Part of the soft emission could be scattered light from these obscured AGN. On the other hand it is likely that low luminosity unobscured AGN emission and soft X-rays from star-forming processes also contribute to the stacked emission at low energies. Therefore the simplest and most cohesive explanation is that the stacked emission embodies a mixture of obscured AGN, unobscured AGN and star-forming galaxies. Disentangling these signals from one another is rather difficult and would require greater spectral resolution than the narrow energy bands offer. On the whole, however, these results support the idea that sBzK galaxies contain a rather active population of obscured AGN, confirming previous work (Daddi et al., 2007b; Alexander et al., 2011).

Where these observations diverge somewhat from previous analysis (e.g. that of Daddi et al 2007b) is when considering subsamples of the sBzK population. Specifically when considering the direct detections and stacked X-rays of subsamples defined by their "IR Excess", the ratio of the total star formation rate to that of the dust-corrected UV SFR. IRXs do exhibit a significantly higher X-ray detection fraction (by a factor $3-4$) than IRNXs. However, the majority of this can be relatively simply explained given the extremely strong correlation between the IR excess parameter and the total infrared luminosity. When controlling for IR luminosity, there is no statistically-significant difference in the X-ray detected fraction comparing IRXs and IRNXs (see Figure 3.7).

Stacking results for the X-ray undetected sources confirms the similarity of IRXs and IRNXs X-ray properties. The stacked IRXs give a slightly higher flux, but the hardness ratios of the IRXs and IRNXs are very similar. Stacking in narrow bands further demonstrates that these two populations have very similar spectra to each other. In particular, both stacks display a hard component indicating the presence of obscured AGN in some of the objects, too faint to be detected individually. Overall, it seems clear that the IR excess parameter is not decisive in selecting obscured AGN or AGN more generally from the sBzK population. The fact that the IR-luminous sBzKs show a high X-ray detection fraction could be attributable to a number of factors. First the BzK selection will tend to yield samples of galaxies with high stellar mass and red colours, which are known to preferentially host luminous AGN (e.g. Nandra et al. 2007b; Bundy et al. 2008). Galaxies with high IR luminosities will also tend to be the most luminous and massive sources themselves. The high IR luminosities and star formation rates also suggest copious amounts of gas and dust, which could account for the high levels of obscuration in these sources. On the other hand, it is puzzling why the presence of an AGN as inferred by the presence of (hard) X-ray emission apparently bears so little relation to excess $24\mu$m emission. Apparently there are many galaxies without a strong hot dust component which nonetheless must host an AGN based on their X-ray emission and, similarly, many which have very strong $24\mu$m but without a powerful AGN.

Daddi et al. (2007b) have suggested that the obscuration levels in the IRXs may in fact be so high that they are "Compton thick" AGN, where even the X-ray emission is suppressed and observed only in scattered light. If so a considerable amount of additional black hole growth may be hiding in these objects. This issue has been investigated further by Alexander et al. 2011 who examined the X-ray spectral properties of directly detected sBzKs using the 4Ms CDFS data. Their analysis resulted in a sharp downward revision in the estimated Compton thick AGN fraction in BzKs compared to Daddi et al. (2007b), who used X-ray stacking analysis to show that the hard X-ray emission of the IRXs resembled the typical spectrum of Compton thick AGN, with a very hard spectrum at high energies.

The narrow band stacking results presented here confirm the presence of a hard high energy spectrum in the sBzK population. Overall the spectrum of the stacked sources is of a "composite" nature, with soft emission either from star formation or unobscured AGN, and a hard signal from obscured AGN. Determining the level of AGN obscuration, ie is it Compton thin or Compton thick, is extremely difficult as the X-ray continuum from moderately obscured Compton thin AGN ($N_{\rm H} \sim 10^{23}$ cm$^{-2}$) and the reflection dominated spectrum of Compton thick AGN are quite similar. The telltale signature is the intense iron K$\alpha$ line (E = 6.4keV rest-frame) predicted in the Compton thick case. This signature has been found in at least one sBzK galaxy (Feruglio et al., 2011) and is inferred by Alexander et al. (2011) to be present in a handful of additional X-ray detected sBzKs, based on the co-addition of the X-ray spectra of several directly detected sBzKs with hard X-ray colours in the 4Ms CDFS data. As discussed above. the conclusion of widespread Compton thick AGN in BzKs by Daddi et al. (2007b) was based on the shape of the stacked spectrum. With a much larger sample of sBzK galaxies, and far deeper X-ray data, it may have been hoped that this stacking analysis would reveal the iron K$\alpha$ line predicted in the Compton thick AGN case. In reality, however, the results of narrow band stacking neither confirm nor deny the presence of intense iron K$\alpha$ emission in the galaxies. The primary issue is that the deeper X-ray data are able to resolve out the brighter X-ray sources from the stack which carry the majority of the signal-to-noise ratio, especially at higher energies. As noted by Alexander et al. (2011), and confirmed by the analysis in Section 3.4, a great number of the objects directly detected in the 4Ms CDFS Chandra data, but not in the 1Ms data used by Daddi et al. (2007b), have very hard spectra. These sources are undoubtedly obscured, and a fraction of them may be Compton thick, but once removed from the stack evidence for a Compton thick AGN in the residual sBzK population is weakened, rather than strengthened. The obvious conclusion is that it is particularly difficult to base estimates of the contribution of Compton thick AGN on a stacking analysis, as stacking will result in a mixture of X-rays from obscured AGN, unobscured AGN and stellar processes, and can be strongly affected or even dominated by a relatively small number of sub-threshold sources. Definitive conclusions regarding the presence of the tell-tale iron K$\alpha$ emission in faint Compton thick AGN awaits future experiments with much larger collecting area than *Chandra*, such as the *Athena* concept (Barcons et al., 2012).

In addition to impacting upon the current knowledge of the AGN content of sBzK galaxies, these X-ray results also have interesting implications about the nature of the IR-excess sBzK population. The basis of the X-ray analysis of the IRXs is that the additional emission at 24$\mu$m could be due to hot dust emission powered by a buried AGN. This analysis has clearly shown, however, that the AGN content (and obscuration properties) of IRXs and IRNXs are very similar. This raises the question of the origin of the large discrepancy between the 24$\mu$m-derived star formation rates and the dust-corrected UV measurements. As these are apparently not due to AGN activity it indicates that the derivation of one or other of the SFRs using the methodology adopted in this analysis is at fault. The discrepancy is largest at high IR luminosity, where the 24$\mu$m SFR greatly exceeds the UV estimates, in extreme cases by 2 orders of magnitude. This implies either that the 24$\mu$m SFR is overestimated, the UV underestimated, or both. Recent results from *Herschel* suggest that both effects could be in play. Firstly, 24$\mu$m fluxes appear systematically to over-estimate the SFRs, especially of high redshift galaxies (Elbaz et al., 2011; Nordon et al., 2012). Secondly, at the highest IR luminosities and thus SFRs, the lines of sight to the star forming regions may become completely opaque to UV emission, being obscured by optically thick dust (Goldader et al., 2002). This makes the rest-frame UV emission, even if corrected for dust extinction, an extremely unreliable estimate of the star formation rate and specifically it will lead one to underestimate the SFR.

A final interesting point from the current work stems from the X-ray analysis of the passive BzK galaxies. While this sample of pBzK is not large (26 objects) it is sufficient to be able to make the first estimate of the AGN content of these galaxies. From the 18 pBzKs in the redshift range $z = 1.2 - 3.0$, two are found to possess X-ray counterparts. Expanding out the full redshift range spanned by the sample subjected to BzK analysis, the detections rise to 4/26 objects. While the number statistics are still small, the X-ray detection rate and AGN content of the pBzKs is at least consistent with and perhaps even slightly higher than the detection rate in sBzKs. The high AGN fraction in sBzKs has been interpreted by Daddi et al. (2007b) as evidence for rapid coeval star formation and black hole growth in this galaxy class. It appears, however, that this is not robust, as BzK galaxies without rapid star formation also show an unusually high fraction of AGN. So while a large amount of black hole growth in galaxies at $z \sim 2$ does indeed occur in galaxies that are also actively growing their stellar component, this is arguably more likely to be due to the fact that most massive galaxies at $z \sim 2$ are star forming galaxies. It does not necessarily present a causal and or astrophysical link between black hole growth and star formation.

## 3.6 Summary

Using 4Ms CDFS and 2Ms CDFN *Chandra*/ACIS imaging the X-ray properties of BzK-selected galaxies at $z \sim 2$ have been investigated. The AGN content and obscuration properties have been studied using a combination of direct detection, broad band stacking and narrow band stacking analyses. The main results are listed below:

(i) By cross-correlating the sBzK sample with X-ray point source catalogues, X-ray counterparts are identified for $5.6 \pm 0.6\%$ (81/1445) of star-forming BzKs, finding 49 X-ray bright sBzKs in the 4Ms CDFS and 32 X-ray bright sBzKs in the 2Ms CDFN *Chandra* ACIS-I images. The direct detection limits are such that almost all of these will host AGN. A greater proportion of IR Excess sBzKs are directly detected in X-ray observations relative to IR Non-Excess sBzKs. However, this can be attributed entirely to the fact that the IR excess criterion also selects the most IR luminous sBzKs. The X-ray detected fractions of IR Excess sBzKs and IR Non-Excess sBzKs are very similar when binned by $L_{IR}$.

(ii) A high proportion (44%) of X-ray detected sBzKs are heavily obscured AGN (HR $> -0.08$), while the remaining sBzKs are relatively unobscured AGN, with a few perhaps purely star-forming. The IR Excess sBzK and IR Non-Excess sBzK subsamples exhibit very similar proportions of heavily obscured AGN. Four of the X-ray detected sBzKs have been identified as Compton thick AGN from their X-ray spectra in the work of Feruglio et al. (2011) and Brightman and Ueda (2012).

(iii) Broad band stacking of 688 X-ray undetected sBzKs, as well as IR Excess sBzK and IR Non-Excess sBzK subsamples, in the 4Ms CDFS and 2Ms CDFN yields soft stacked signals with effective $\Gamma \sim 2$. Stacking of sBzKs binned by redshift and $L_{IR}$ produces similar results.

(iv) Narrow band stacking of sBzKs reveals a "composite" spectrum with soft emission at low energies and hard emission at high energies. It is not possible to disentangle the emission from heavily obscured AGN, unobscured AGN and star-formation within the stacked signal. The resolution of the narrow band stacking is not sufficient to confirm or reject the presence of Iron K$\alpha$ line emission, so it cannot be established definitively whether or not a significant population of Compton thick AGN reside in the sBzKs. The IR Excess sBzKs and IR Non-Excess sBzKs have almost identical spectral shapes and, as with broad band stacking, there is no evidence that Compton thick AGN are more prevalent within IR Excess sBzKs than IR Non-Excess sBzKs.

(v) The stacked emission of IR Excess sBzKs in the 1Ms CDFS is dominated by 6 IR Excess sBzKs lying just below the detection threshold at this depth, and these were subsequently detected in the deeper 4Ms CDFS. These sources are on average much harder (effective $\Gamma = 0.7^{+0.2}_{-0.1}$) than the X-ray undetected sBzKs and are responsible for the hard stacked signal observed by Daddi et al. (2007b).

(vi) These results demonstrate that on the whole the discrepancy between 24$\mu$m and UV-derived star formation in the BzK population is not due to AGN activity enhancing the 24$\mu$m flux. At high $L_{IR}$ (hence SFR) the 24$\mu$m overestimates the SFR, and the UV underestimates SFR for these BzK galaxies. The apparent lack of correspondence between X-ray emission from an AGN and 24$\mu$m excess is a puzzle which needs to be investigated in detail on an object-by-object basis.

(vii) Passively evolving BzKs have an even higher X-ray detection rate ($\sim$ 15%) than sBzKs ($\sim$ 7%) and hence a high fraction of AGN. This is contradictory to the idea that black hole growth at $z \sim 2$ is co-eval with star-formation. The connection between the two appears to be purely circumstantial, rather than causal.

# Chapter 4

# Evidence for two modes of black hole accretion in massive galaxies at $z \sim 2$

## Overview

In this chapter the relationship between AGN activity and host galaxy properties, in particular galaxy compactness, is investigated using a sample of massive galaxies at $z \sim 2$ in the Chandra Deep Field South (CDFS) region. A sample of 268 galaxies with $\mathrm{M}_* > 10^{10.5}\mathrm{M}_\odot$ at $1.4 < z < 3$ are selected from HST WFC3 H-band observations in CDFS taken as part of the CANDELS survey. A large fraction of these massive galaxies ($22.0 \pm 2.5\%$) is detected in the 4Ms Chandra/ACIS observations in the field, implying a high AGN content in them. To investigate further the relationship between these AGN and their hosts, four subsamples were created based on their star-formation rates (star-forming vs. quiescent) and galaxy size (compact versus extended), following Barro et al. (2013). X-ray spectral fitting was used to determine the intrinsic luminosity and absorption column density in the line-of-sight, as well as to assess the number of “Compton thick” AGN in each subsample. The most striking result comes from a comparison of the luminosities and obscuration properties of compact versus extended galaxies. There is a clear effect whereby the compact galaxies - be they star-forming or quiescent - show significantly higher AGN luminosities and levels of obscuration than the extended galaxies. These results provide clear evidence for two modes of black hole growth in massive galaxies at high redshift. The dominant growth mode is a luminous, obscured phase which occurs overwhelmingly in compact galaxies. The second is a lower luminosity, unobscured phase predominantly seen in extended, quiescent galaxies. The former mode may be associated with transformative feedback which quenches star formation and, plausibly causes the observed size evolution of the galaxies. The latter is likely to be a gentler “maintenance mode” of feedback which prevents further star formation in massive quiescent galaxies.

The results presented in this chapter are set to be published in Rangel et al. 2013 (submitted to MNRAS).

## 4.1 Introduction

The massive galaxy population in the local universe is dominated by large, quiescent early-type galaxies (ETGs) with extended light profiles. At $z \sim 2$, however, this population consists of significantly smaller galaxies, with half-light radii up to $\sim 5$ times smaller than the ETGs (e.g. Daddi et al. 2005; Trujillo et al. 2006; Longhetti et al. 2007; Toft et al. 2007; Zirm et al. 2007; Cassata et al. 2011). It has been postulated that the reduction in galaxy size is an observational effect, with simulations predicting that the low surface brightness of galaxies at $z \sim 2$ could cause the full extent of their haloes to be underestimated (Hopkins et al., 2009; Mancini et al., 2010). Observations of compact quiescent galaxies at $z \sim 2$, however, show no evidence of the faint outer envelopes predicted by simulations (Szomoru et al., 2010). Thus the dichotomy in the size of massive galaxies at low and high redshifts appears to be genuine. Observations of the central bulges of ETGs in the local universe reveal old stellar cores of comparable size (approximately 1 kpc) to the compact galaxies at $z \sim 2$ (Heavens et al., 2004; Feulner et al., 2005; Thomas et al., 2005). Therefore it is thought that the compact galaxies at $z \sim 2$ could act as progenitors for local ETGs (Hopkins et al., 2009; Cassata et al., 2011).

Multiple studies suggest the strongest size evolution in the massive galaxy population occurs at $1 < z < 2$ (e.g. Fontana et al. 2004; Glazebrook et al. 2004; Abraham et al. 2007; Arnouts et al. 2007; Cassata et al. 2013). Measurements of the number densities of ETGs reveal the population is in place by $z \sim 0.7$ (Fontana et al., 2004; Yamada et al., 2005; Cimatti et al., 2006; Brown et al., 2007; Scarlata et al., 2007). With this greater understanding of the rate of size/morphology evolution of massive galaxies across cosmic time (e.g. Trujillo et al. 2007; Buitrago et al. 2008) the next step is to gain an understanding of the processes driving this evolution. The simplest explanation would be for the compact massive galaxies at $z \sim 2$ to evolve passively into extended galaxies similar to the ETGs at $z \sim 0$. However, the passive evolution scenario would produce redder galaxies than have been observed in the nearby universe (Kriek et al., 2008). Additionally, the increase in average galaxy mass since $z \sim 2$ would remain unexplained. Hence their size evolution must have been an active process, one for which a cornucopia of possible mechanisms have been postulated.

What remains unclear is the precise nature of the processes driving massive galaxy evolution from small compact intensely star forming galaxies to extended elliptical quiescent galaxies. Hierarchical growth of the galaxies (Toomre, 1977; White and Frenk, 1991) through mergers is thought to play a significant role in the evolution of massive galaxies over cosmic time. There are two varieties of merger to consider: gas rich (wet) and gas poor (dry). Wet mergers are common in the early universe ($z > 2$) where cold gas is more abundant (Khochfar & Silk 2006a,b; Croton 2009). The large amounts of gas make this process highly dissipative and remnants of wet mergers produced by simulations tend to have smaller, more disk-like structures than dry mergers remnants (e.g. Springel and Hernquist 2005; Khochfar and Silk 2006b; Cox et al. 2006). These remnants bear a striking resemblance to the compact galaxies observed at $z \sim 2$ and it could well be that they originate from wet mergers (Khochfar and Silk, 2006a; Trujillo et al., 2007; Naab and Ostriker, 2009), although this remains a point of contention (e.g. Kocevski et al. 2012; Schawinski et al. 2012; Kaviraj et al. 2013a,b). Additionally wet mergers alone do not explain the formation of the extended galaxies that are thought to act as the progenitors for massive ETGs in the local universe. Dry mergers on the other hand are non-dissipative, promoting both galaxy mass and size growth. Dry minor mergers are the dominant form of galaxy interaction at $z < 1$ and the observed merger rate is sufficient to replicate the observed galaxy evolution at these redshifts (Shen et al., 2003; van Dokkum, 2005; Bell et al., 2006; Trujillo et al., 2007; Kaviraj et al., 2011; Trujillo et al., 2011). At $1 < z < 3$, however, the minor merger rate drops and cannot fully explain size evolution in this redshift regime (Conselice, 2006; Newman et al., 2012). Dry major mergers are also too infrequent; a galaxy is expected to undergo only one dry merger since $z = 3$ (Bluck et al., 2009; Man et al., 2012), far too few to reproduce the required size evolution (Ciotti and van Albada, 2001; Nipoti et al., 2003; Naab et al., 2009).

AGN feedback mechanisms potentially play a key role in the evolution of massive galaxies. Previous studies have demonstrated intense AGN activity at $z \sim 1-3$ (e.g. Boyle and Terlevich 1998; Silverman et al. 2008; Aird et al. 2010), coinciding with the period of strongest evolution in the massive galaxy population. AGN are capable of producing powerful feedback effects that can affect both the star formation and host properties profoundly (e.g. Silk and Rees 1998; King 2003) and possibly size evolution of their host galaxies (Fan et al., 2008; Damjanov et al., 2009; Ishibashi et al., 2013). For example, Hopkins et al. (2006) postulate a violent, event-driven “quasar-mode” of feedback able to rapidly transform galaxies from star-forming to quiescent via powerful outflows. If an AGN is sufficiently luminous it is possible to generate winds that rapidly expel gas from the central regions of the galaxy, swiftly quenching star formation. These quasar-driven winds can also cause the galaxy to expand in size (Fan et al., 2008). For massive galaxies ($M_* > 2 \times 10^{10} M_\odot$) the predicted expansion is consistent with the observed size increase at $1 < z < 3$ (Fan et al., 2010).

Alternatively, or additionally, heating from low luminosity AGN can prevent star formation in already-formed quiescent galaxies, via a gentler mode of feedback sometimes termed the “radio-mode” (Croton et al., 2006). In this scenario hot gas gradually falls onto the host galaxy, with some trickling through and accreting onto the low luminosity unobscured AGN. Conventionally the gas falling onto the host galaxy should cool and condense triggering star formation. The accretion of hot gas onto the low luminosity AGN stimulates gentle feedback which suppresses further cooling and thus quenching star formation. This phenomenon maintains a red, old stellar population within the host galaxy, similar to what is observed in massive ETGs in the local universe.

While either or both of these feedback processes can plausibly reproduce the observed properties of galaxies, and arguably are necessary to do so, direct observational evidence for AGN feedback impacting massive galaxy evolution has remained scarce.

A further incidence of AGN implicated in galaxy evolution was given by Barro et al. (2013), who presented a study of the evolution of the number density of massive galaxies ($M_* > 10^{10} M_\odot$) in the Chandra Deep Field South (CDFS) at $1.2 < z < 3$. Using the galaxy compactness and specific star formation rates (sSFRs) Barro et al. (2013) divided the massive galaxies into 4 subsamples; compact quiescent galaxies (QGs), compact star forming galaxies (SFGs), extended QGs and extended SFGs. The extended QGs are analogous to the ETGs in the local universe and represent the endpoint for massive galaxies in this evolutionary model. Barro et al. (2013) propose two tracks via which the extended QGs may form; an "early" path where the extended QGs form through the morphological evolution of compact galaxies and a "late" path where extended QGs are formed by the quenching of extended SFGs.

The number density of the compact SFGs peaks at $2 < z < 3$ as they are formed by wet mergers (e.g. Springel and Hernquist 2005; Khochfar and Silk 2006b; Cox et al. 2006) in the gas rich early universe. These compact SFGs are the starting point for the "early" track. The number density of compact SFGs declines at $z < 2$ and the population is almost non-existent by $z = 1.4$ while the compact QG number density climbs during this period. Barro et al. (2013) propose that this is due to star formation in compact SFGs quenching to form the compact QGs. A high fraction of X-ray luminous AGN in the compact SFGs is reported and suggests that AGN feedback drives the rapid formation of compact QGs through quenching of compact SFGs at $z \sim 2$. At $z < 1.4$ the compact QG number density drops and the extended QG number density increases. Barro et al. (2013) suggest the morphology of the compact QGs is being disrupted by processes such as minor mergers and cold gas accretion, increasing their size until they are extended QGs. The buildup of the extended QG population cannot be entirely explained by compact galaxies, however, so it would appear some are formed via the quenching of SFGs.

Throughout this chapter a standard, flat ΛCDM cosmology with $\Omega_\Lambda = 0.7$ and $H_0 = 70$ km s$^{-1}$ Mpc$^{-1}$ is assumed.

## 4.2 Data

### 4.2.1 Optical data

Here follows a brief description of the optical data used to define the massive galaxy sample and subsamples therein. The massive galaxies in this sample are all HST/WFC3 F160W ($H$-band) selected sources from the GOODS-S region in the CANDELS survey (Grogin et al., 2011; Koekemoer et al., 2011) which is wholly contained within the X-ray coverage of the CDFS. The H-band observations taken using the WFC3 instrument have limiting AB magnitude $H_{5\sigma} = 27$ mag. Multi-wavelength photometry ($U$-band to 8 $\mu$m) has been extracted by Guo et al. (2013) for each of these sources using TFIT (Laidler et al., 2007), following the method of Guo et al. (2011). TFIT uses the spatial distribution of light of a galaxy from high resolution imaging (in this case WFC3 $H$-band) to constrain the photometric measurements of lower-resolution imaging by using high resolution imaging to generate templates for the light profile. The best fit light profile is chosen using $\chi^2$ minimisation and is used to compute the photometric flux in the lower resolution image. The $H$-band sources have been attributed photometric redshifts calculated using the EAZY software (Brammer et al., 2008), with $\Delta z/(1+z) = 3\%$ error for $z > 1.5$ (where $\Delta z = z_{phot} - z_{spec}$). The final sample of massive galaxies at $z \sim 2$ is limited to $z > 1.4$ and $\mathrm{M} > 10^{10.5}\mathrm{M}_{\odot}$. The redshift cut is the same as that employed by Barro et al. (2013). The mass cut is slightly higher: a more conservative approach is adopted here to ensure that the masses of the various subsamples are similar, and in particular to ensure that the sample is not dominated by the large number of extended SFGs in the $10^{10} < \mathrm{M}_{*} < 10^{10.5}\mathrm{M}_{\odot}$ mass range.

### 4.2.2 X-ray data reduction

The X-ray data used in this work originates from the CDFS 4Ms survey taken with the Advanced CCD Image Spectrometer Imaging array (ACIS-I; Garmire et al. 2003) aboard the *Chandra* X-ray observatory. A detailed description of the X-ray image reduction is presented in Sections 2.2 and 3.2.5.

Subsequent to X-ray point source detection, 480 (of 569) X-ray sources have been attributed spectroscopic (Hathi et al., in preparation) or photometric redshifts by Hsu et al (in preparation) based on either CANDELS (Guo et al. 2013) or MUSYC (Cardamone et al. 2010) photometry. The photometric redshifts were calculated using the LePhare SED fitting codes (Ilbert et al., 2006, 2009) and have excellent accuracy with a low catastrophic failure rate (see Hsu et al. in prep for details). Spectroscopic redshifts take priority over photometric redshifts unless they are flagged as being of poor quality. Otherwise we adopted the photometric redshifts of Hsu et al. (in prep). These were used in preference to the photometric redshifts measured for optical sources using the EAZY software (Brammer et al., 2008) because they include AGN templates known to give more accurate results for X-ray sources, with associated $\Delta z/(1+z) = 1.4\%$ (Salvato et al., 2009, 2011).

X-ray spectra were extracted for the 567 point sources using the ACIS EXTRACT IDL package (Broos et al., 2010) following the method presented in Section 2.3. Each of the 52 obsIDs used to create the 4Ms image have slightly different roll angles and central pointing Right Ascensions (RA) and Declinations (Dec). As a consequence a source will have a slightly different source profile/PSF/EEF in each obsID depending on the off-axis angle (OAA) and roll angle. The ACIS EXTRACT software overcomes this problem by extracting source and background spectral counts from each obsID individually, using extraction regions tailored to each obsID, and then combining this data to create a final X-ray spectrum for each source. Only observations taken at the same temperature were merged because it is essential to maintain a consistent detector response when producing the response matrix functions (RMF) and auxiliary response function (ARF) of a spectrum. As a consequence, obsIDs 581 and 1431 were omitted because they were taken before the $29^{th}$ January 2000 when the focal plane temperature was altered from 163 K to 153K. This in turn meant it was not possible to extract spectra for two point sources identified in the CDFS 4Ms catalogue (cdfs4Ms_278 and cdfs4Ms_389). Neither of these sources was covered by CANDELS observations. All remaining obsIDs were taken at 153K.

## 4.3 Method

### 4.3.1 Likelihood Ratio matching

The astrometric errors for a typical *Chandra* point source range from 0.5 arc-seconds on-axis to 5 arc-seconds at 12 arc-minutes off-axis (Weisskopf et al., 2002). In deep optical surveys such as the CANDELS GOODS-S region, the source density is sufficiently high that numerous optical sources may lie within the astrometric errors of the X-ray sources. The X-ray data used in this work has been subjected to astrometric corrections (see Rangel et al. 2013), derived by matching bright X-ray sources to $H$-band selected sources from the MUSYC survey (Gawiser et al., 2006). This improves the reliability of nearest neighbour matching but there is still a high false matching rate for X-ray faint and large OAA X-ray sources. Therefore a likelihood ratio (LR) matching technique (Sutherland and Saunders, 1992; Ciliegi et al., 2003; Brusa et al., 2005, 2007) is used in this work to establish X-ray to optical associations.

The LR matching used in this work was carried out by Marcella Brusa between the X-ray point source catalogue and CANDELS GOODS-S epoch-4 $H$-band selected sources. What follows is a brief description of the LR matching technique used in this work. A more detailed description of the method is presented in Brusa et al. (2007). In this work the LR is a ratio of the likelihood that an optical source is the true counterpart to an X-ray source and the likelihood that it is a background object.

$$LR = \frac{q(m) * f(r)}{n(m)} \tag{4.1}$$

where $q(m)$ is the expected probability distribution of true counterparts as a function of the optical magnitude, $m$, $f(r)$ is the distribution function of the X-ray positional errors as a function of the positional offset, $r$, and $n(m)$ is the surface density of background objects. The probability distribution of positional errors $f(r)$ is assumed to be a two-dimensional gaussian (Civano et al., 2012).

$$f(r) = \frac{1}{2 * \pi * \sigma^2} * e^{-\frac{r^2}{2*\sigma^2}} \tag{4.2}$$

where $r$ is the positional offset of the optical source and the X-ray source position and $\sigma$ is a function of the positional uncertainties. The probability distribution $f(r)$ is normalised to unity.

To discriminate between real and spurious associations a threshold likelihood ($L_{th}$) was chosen by following the method of Civano et al. (2012). The $L_{th}$ must be small enough to ensure high sample completeness but not so low as to adversely affect the reliability of associations. In this case a $L_{th}$=0.65 was the most suitable, offering the optimal balance of completeness C=0.88 and reliability R=0.88. LR matching to the massive galaxy sample following the mass and redshift cuts outlined in Section 4.2.1 ($z > 1.4$ and M$> 10^{10.5}$M$_{\odot}$) reveals 59 massive galaxies possess X-ray counterparts, with a false matching rate of 1.5% (see Table 4.1).

The X-ray point source detection pipeline is more conservative than the method employed by Xue et al. (2011) and consequently identifies fewer X-ray point sources (569 and 740 respectively; see Rangel et al. 2013/Section 3.2.5 for a detailed analysis). Using a simple nearest neighbour analysis with a 1 arcsecond matching radius, the massive galaxy sample was cross correlated to Xue et al. (2011) X-ray point sources. All bar one of the X-ray sources in the massive galaxy sample have counterparts in the 4MS CDFS catalogue of Xue et al. (2011) that are classified as AGN ($L_X > 10^{42}$erg s$^{-1}$ or HR$> -0.1$) by their analysis. One extended SFG, cdfs4Ms_532, does not have a counterpart in the Xue et al. (2011) 4Ms CDFS catalogue, but its $L_{2-10keV} > 10^{42}$erg s$^{-1}$. Therefore the X-ray emission from cdfs4Ms_532 is assumed to be dominated by an AGN. This method also identifies 18 X-ray point sources from the Xue et al. (2011) catalogue that were of too low significance to be included in the final X-ray point source catalogue produced by the Imperial college source detection pipeline. All of these sources are X-ray faint, possessing very few spectral counts, and it is reasonable to assume the results of a spectral fitting analysis would be uninformative. Therefore it is deemed unnecessary to include these 18 additional faint X-ray sources from the catalogue of Xue et al. (2011).

### 4.3.2 Massive galaxy sample selection

Following Barro et al. (2013), the massive galaxies were split into subsamples based on their specific SFR (sSFR) and compactness. The SFR calculation method is dependent on whether the galaxy has been detected in MIPS 24$\mu$m data; a combination of IR and rest-frame UV SFR estimates is used if the galaxy is detected, a purely UV based SFR estimate is adopted if not. By using IR emission to estimate the SFR it is possible to detect star formation activity that has been reddened by obscuring dust and would otherwise have been missed (Bauer et al., 2011; Banerji et al., 2012). The IR luminosities of the MIPS 24$\mu$m detected galaxies were calculated by fitting the 24$\mu$m flux derived by TFIT to Chary and Elbaz (2001) star-forming galaxy templates and applying *Herschel* based corrections (Elbaz et al., 2011). The IR and rest-frame UV (uncorrected for dust emission) luminosities are converted into SFRs following the methods of Kennicutt (1998)

**Table 4.1:** Sample sizes and X-ray detected fractions of massive galaxies. Columns (2) to (4) describe the sample prior to the mass and redshift cuts while columns (5) to (7) describe the sample post the mass and redshift cuts. The X-ray detected fractions have multinomial errors. Column (1): type of galaxy; column (2): number of galaxies in the sample; column (3): number of galaxies with X-ray associations according to LR matching; column (4): percentage of galaxies that are X-ray detected; column (5): number of galaxies in the sample; column (6): number of galaxies with X-ray associations according to LR matching; column (7): percentage of galaxies that are X-ray detected.

| | All | | | $M_* > 10^{10.5}M_\odot$ and $1.4 < z < 3$ | | |
|---|---|---|---|---|---|---|
| Type<br>(1) | $N_{tot}$<br>(2) | $N_X$<br>(3) | $Frac_X$<br>(4) | $N_{tot}$<br>(5) | $N_X$<br>(6) | $Frac_X$<br>(7) |
| All | 1321 | 172 | 13.0±0.9 | 268 | 59 | 22.0±2.5 |
| cQG | 127 | 19 | 14.9±3.2 | 52 | 10 | 19.2±5.5 |
| cSFG | 69 | 22 | 31.9±5.6 | 55 | 19 | 34.5±6.4 |
| eQG | 273 | 53 | 19.4±2.4 | 21 | 10 | 47.6±10.9 |
| eSFG | 852 | 78 | 9.2±1.0 | 140 | 20 | 14.3±3.0 |

and Bell et al. (2005) respectively. If the galaxy is an X-ray source or undetected in MIPS $24\mu$m then the SFR is estimated using the extinction corrected, rest-frame UV luminosity as derived by Wuyts et al. (2011). Stellar masses for each source were calculated using the FAST software (Kriek et al., 2009), and were combined with the SFR estimates to calculate the sSFR. Using the sSFR the massive galaxies are split into quiescent (QG) and star-forming (SFG) subsamples; QGs possess sSFR $< 10^{-0.5}$Gyr$^{-1}$ and SFGs possess sSFR $\geq 10^{-0.5}$Gyr$^{-1}$. The compactness of each galaxy is determined based on the ratio of galaxy mass, M, and the effective radius according to H-band imaging, $r_e$, where $r_e$ is determined using GALFIT (Peng et al., 2002), following the methodology of van der Wel et al. (2012). The threshold value for compactness (ie the boundary between compact and extended galaxies) is based on the mass-size relation for QGs at $z > 1.5$ (Newman et al., 2012). Galaxies with $M/r_e^\alpha$ (henceforth $\Sigma_{1.5}$)$> 10.3M_\odot$kpc$^{-\alpha}$, where the growth efficiency $\alpha = 1.5$, are defined as compact while the remainder are defined as extended.

It is clear from Figure 4.1 that the extended SFGs make up the overwhelming majority of the sample below M$= 10^{10.5}M_\odot$. Including these galaxies could produce a mass bias in the host galaxies of extended SFGs relative to the other samples, rendering them unsuitable for comparison (see McLure et al. 2006 and references therein). Additionally the extended QGs and compact SFGs and QGs samples below $10^{10.5}M_\odot$ are not large enough to provide statistically significant comparisons to the extended SFGs. For these reasons galaxies with M$< 10^{10.5}M_\odot$ have been omitted.

Using the calculated sSFR and compactness values, 52 compact QGs, 55 compact SFGs, 21 extended QGs and 140 extended SFGs (Table 4.1) with $z > 1.4$ and M$> 10^{10.5}M_\odot$ were identified. From these subsamples, LR matching (Section 4.3.1) associates 10 compact QGs, 19 compact SFGs, 10 extended QGs and 20 extended SFGs with X-ray point sources. Composite multiwavelength (UV, optical and IR) SED template fitting reveals that less

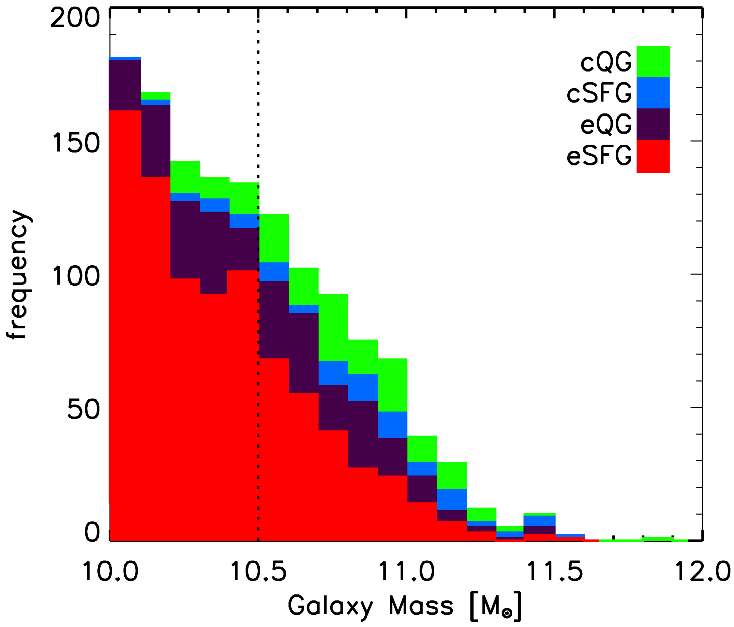

**Figure 4.1:** Histogram of galaxy mass for massive galaxies with $z_{best} > 1.4$ and M> $10^{10.0}M_{\odot}$. The vertical dashed line indicates the mass cutoff of M= $10^{10.5}M_{\odot}$ used to define the final sample.

than 1/3 of galaxies with X-ray counterparts suffer from significant AGN contamination in their UV-IR SEDs. The impact on the computed mass and SFR for these sources predicted by Santini et al. (2012) and Mainieri et al. (2011) is not sufficiently large to change their sSFR or compactness classifications.

AGN contamination can also alter the light profile of the host galaxy which may lead to GALFIT assigning an incorrect size as only a sersic profile was used. In turn, this could slightly alter the measured compactness. However, this would only affect classification of galaxies close to the compactness boundary ($\Sigma_{1.5}$=10.3) and the net change in subsample sizes is estimated to be negligible. AGN contamination has the potential to scatter low mass galaxies beyond the M> $10^{10.5}M_{\odot}$ limit that has been imposed on the sample and vice versa. This will only affect galaxies with stellar masses close to M= $10^{10.5}M_{\odot}$ and it is anticipated that this affects all subsamples equally.

### 4.3.3 X-ray spectral fitting

To better understand the nature of the X-ray detected massive galaxies a variety of models were fitted to the X-ray spectra. The *Chandra* ACIS-I instrument can detect photons over a range of 0.2-10 keV but the detector response drops off markedly at the highest and lowest energies, especially for sources at a large OAA, so the energy range was limited to 0.5-8 keV. The goodness of fit was determined using a maximum likelihood statistic (C-statistic; Cash 1979) because it is well suited to analysing sources with a low number of

**Table 4.2:** Description of how parameters for spectral fitting of massive galaxies. Columns (4) to (7) describe the potentially free parameters of the various models used. Free parameters are labeled as such, otherwise the parameter has been fixed to the value quoted. Solar abundance values were assumed for elements heavier than He (including Fe). Column (1): model ID; column (2): number of free parameters in the model; column (3): photon index of power-law emission from the central source; column (4): normalisation factor for power-law emission from the central source; column (5): column density of obscuring material; column (6): photon index of central scattered power-law emission; column (7): normalisation factor for scattered power-law emission.

| Model ID (1) | $N_{free}$ (2) | $\Gamma_{src}$ (3) | $\mathrm{Norm}_{src}$ (4) | $N_H$ (5) | $\Gamma_{scat}$ (6) | $\mathrm{Norm}_{scat}$ (7) |
|---|---|---|---|---|---|---|
| A | 1 | 1.9 | Free | ... | ... | ... |
| B | 2 | 1.9 | Free | Free | ... | ... |
| C | 3 | 1.9 | Free | Free | 1.9 | Free |
| D | 2 | 1.9 | Free | ... | 1.9 | Free |

counts (see Section 2.4.4). The spectra were grouped according to energy channel, with 8 raw channels per bin producing 63 bins for each spectrum over the 0.5-8 keV range. This preserves the spectral resolution even with very low numbers of counts (compared, e.g. to binning by counts).

The parameters for each model used in this analysis are presented in Table 4.2. The photon index has been fixed at $\Gamma = 1.9$ for all of the models. This is because leaving the photon index free does not reduce the C-statistic sufficiently to warrant the inclusion of an additional free parameter.The following models have been chosen for use in the spectral fitting:

A) Simple unobscured power-law emission, POWERLAW, from the XSPEC (Arnaud, 1996) model library. A fixed local galactic absorption of $N_H = 9 \times 10^{19}\mathrm{cm}^{-2}$ (Dickey and Lockman, 1990) was also applied. This is the simplest of the models used in this analysis with only 1 free parameter; the power-law normalisation.

B) Brightman and Nandra (2011a) model of power-law emission obscured by material configured in a spherical geometry. This model is preferred to the neutral absorption model, ZWABS, of XSPEC because it includes line emission and Compton scattering, which can be important for the most heavily obscured objects. This model has 2 free parameters; the power-law normalisation and the $N_H$ of the spherical obscurer.

C) Brightman and Nandra (2011a) model of power-law emission obscured by material configured in a toroidal geometry with an additional scattered power-law component. This model features self-consistent iron K$\alpha$ line emission along with a Compton hump generated by reflection off the obscuring torus. The opening angle of the torus has been fixed at 30 degrees because the spectra are rather insensitive to the opening angle. The torus is always assumed to be observed with an almost edge-on orientation (fixed at 80 degrees) assuming the power-law emission is undergoing maximum obscuration. This model has 3 free parameters; the power-law normalisation, the torus $N_H$ and the scattered power-law normalisation.

D) Model of neutral reflection from a Compton thick obscurer, PEXMON, devised by Nandra et al. (2007b) with an illuminating power-law component. Derived from the PEXRAV model (Magdziarz and Zdziarski, 1995) it features self-consistent iron K$\alpha$ line emission with a Compton hump and iron K$\beta$ line emission (George and Fabian, 1991). This model has 2 free parameters; the power-law normalisation and the illuminating power-law normalisation.

For models with the same number of free parameters, the model with lowest C-statistic is adopted as the best-fitting model. If, however, the models have differing amounts of free parameters then selecting the best fit is non-trivial. In this case a critical threshold is defined, $\Delta cstat_{AB}$, for a more complex model (B) to be preferred over a model with fewer free parameters (A), ie $cstat_A - cstat_B > \Delta cstat_{AB}$ must be satisfied to prefer model B to model A. Threshold $\Delta cstat$ values for comparing models with differing numbers of free parameters were calculated following the method described in Section 2.4.3. The spectral fitting analysis presented in this chapter (and in similar analyses presented in this thesis) uses a 99% $\Delta cstat$ threshold is used because it will provide the most conservative estimate. As stated previously, the $\Delta cstat$ threshold is dependent on the number of counts in a spectrum as brighter spectra have more well defined emission features. Thus critical $\Delta cstat$ values were calculated for 3 different ranges of counts; $< 100$ counts (low), $100 \leq$counts$< 500$ (medium) and $> 500$ counts (high). The results of this $\Delta cstat$ analysis are given in Table 4.3.

The best fitting model was determined by following the logic tree/flow chart shown in Figure 4.2. The process is designed to compare iteratively models of increasing numbers of free parameters to one another until either additional free parameters cannot be justified by their C-statistic values or the model with the maximum number of free parameters is chosen (model C). Initially the C-statistic value of the simplest model (model A) is compared to all the more complex models. By measuring $\Delta cstat_{AB}$, $\Delta cstat_{AC}$ and $\Delta cstat_{AD}$ it is determined whether or not model A is the best fit. If not, then the $\Delta cstat_{BC}$ and $\Delta cstat_{DC}$ are calculated to determine whether model C is the best fit. If model C is not suitable then whichever model has the lowest C-statistic between B and D is chosen as the best fit. The absorbed and unabsorbed 2-10 keV luminosities were calculated following the methods described in Section 2.4.5.

**Table 4.3:** The 90%, 95% and 99% threshold values of $\Delta cstat$ required to justify the inclusion of additional free parameters when selecting the best-fitting models using C-statistic in CDFS 4Ms data. Column (1): the pairing of models to which the threshold values correspond i.e. $\Delta cstat_{XY}$ is value required to prefer model Y to model X; column (2): 90% certainty threshold for low count source; column (3): 95% certainty threshold for low count source; column (4): 99% certainty threshold for low count source; column (5): 90% certainty threshold for medium count source; column (6): 95% certainty threshold for medium count source; column (7): 99% certainty threshold for medium count source; column (8): 90% certainty threshold for high count source; column (9): 95% certainty threshold for high count source; column (10): 99% certainty threshold for high count source.

| | $< 100$ counts | | | $100 \leq$counts$< 500$ | | | $\geq 500$ counts | | |
|---|---|---|---|---|---|---|---|---|---|
| Threshold | 90% | 95% | 99% | 90% | 95% | 99% | 90% | 95% | 99% |
| (1) | (2) | (3) | (4) | (5) | (6) | (7) | (8) | (9) | (10) |
| $\Delta cstat_{AB}$ | 1.94 | 3.16 | 7.00 | 1.79 | 2.80 | 5.24 | 1.56 | 2.93 | 5.66 |
| $\Delta cstat_{AC}$ | 2.25 | 3.80 | 6.90 | 2.23 | 3.59 | 6.65 | 1.96 | 3.35 | 5.76 |
| $\Delta cstat_{AD}$ | 1.86 | 2.86 | 7.19 | 1.75 | 3.07 | 5.88 | 1.67 | 2.72 | 5.30 |
| $\Delta cstat_{BC}$ | 1.62 | 2.72 | 5.89 | 1.38 | 2.68 | 5.50 | 1.39 | 2.68 | 5.82 |
| $\Delta cstat_{DC}$ | 3.01 | 3.72 | 6.45 | 2.51 | 3.09 | 4.67 | 1.72 | 4.53 | 7.52 |

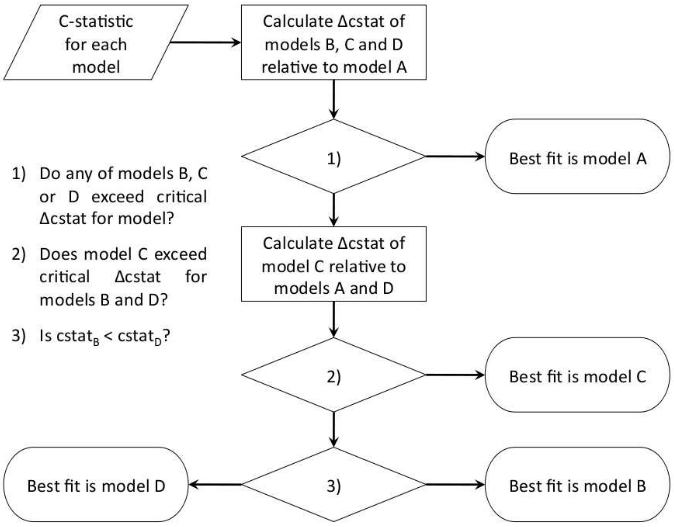

**Figure 4.2:** Logic tree outlining the process used to select the best-fitting X-ray emission model using the C-statistic values from spectral fitting.

## 4.4 Results

### 4.4.1 X-ray detected massive galaxies

H-band selected massive galaxies (M$>10^{10.5}$M$_\odot$ and $1.4 < z < 3$) were matched to X-ray point sources from the CDFS 4Ms survey using LR matching (the results of which are detailed in Table 4.1), yielding a $22.0 \pm 2.5\%$ (59/268) detection rate. This X-ray detected fraction is significantly higher than would be obtained using the entire H-band selected galaxy sample (i.e. without mass and redshift cuts; see Table 4.1), a result that is significant at the $3\sigma$ level. The high X-ray detected fraction is probably a result of limiting the sample to massive galaxies (M$>10^{10.5}$M$_\odot$) with high X-ray detected fractions previously observed in similar galaxies (e.g. Brusa et al. 2009; Aird et al. 2012; Pimbblet and Jensen 2012). The extended QGs have the highest detection rate (10/21, $\sim 50\%$) which is roughly consistent with the observations of Olsen et al. (2013) and suggests AGN activity might play a role in the evolution of extended QGs, although the large errors (due to small sample size) limit the significance of this result. The compact SFGs also exhibit strong AGN activity ($> 30\%$ X-ray detected). The extended SFGs have a much lower detection rate than compact SFGs ($\sim 14\%$), a result that is significant at the $> 3\sigma$ level. The compact QGs formally also have a low X-ray detection rate of around 19 % which is similar, within errors, to that of the extended SFGs.

The HR distribution of the X-ray detected massive galaxies as a whole is bimodal (see Figure 4.3), but the peak at large HR is almost entirely due to compact galaxies, which dominate the sample at the hardest HRs (72.2% of galaxies with HR$>$ 0.2). A K-S test indicates that it is unlikely the compact and extended galaxy HR distributions could be drawn from the same parent distribution (null hypothesis probability $p = 0.09$). The predominantly large HRs of compact galaxies suggests that they are typically more heavily obscured.

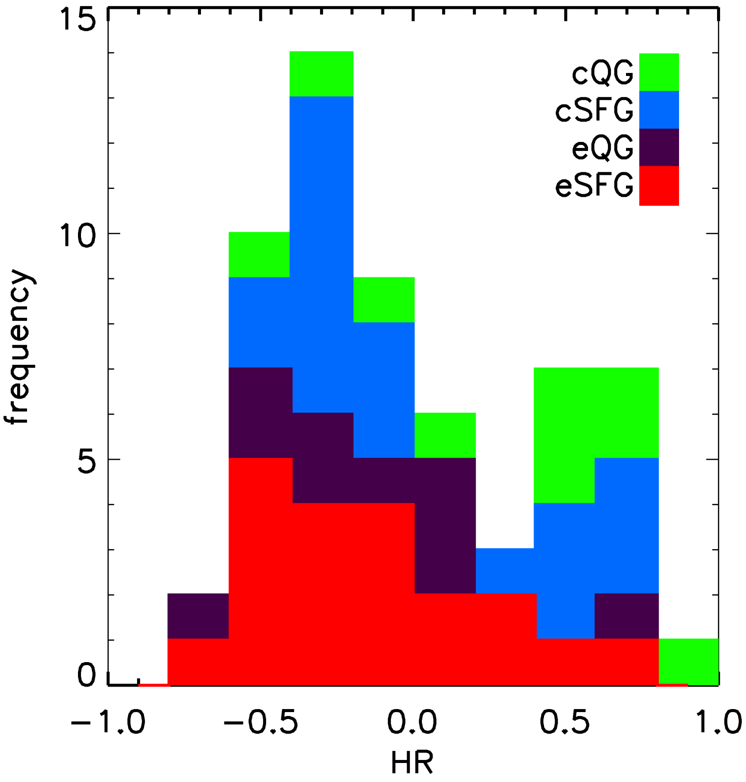

**Figure 4.3:** Histogram of HR for massive galaxies with $z_{best} > 1.4$ and M> $10^{10.5}$M$_{\odot}$. HR=(H-S)/(H+S) where H is the 2.0-7.0 keV count rate and S is the 0.5-2.0 keV count rate.

**Table 4.4:** X-ray spectral fitting results for LR matched compact galaxies with $1.4 < z < 3.0$ and M$> 10^{10.5}$M$_\odot$. Analysis for the R-values (reflected component/illuminated component) for sources best fit by model D show them all to be extremely reflection dominated, thus they are all classified as Compton thick AGN with N$_H > 10^{24}$ cm$^{-2}$. Column (1): optical source ID from the CANDELS GOODS-S epoch-10; column (2): compact galaxy classification; columns (3) and (4): Right Ascension and Declination of the optical source; column (5): ID of X-ray counterpart source identified using LR matching; column (6): redshift of X-ray source, spectroscopic redshifts are denoted with †; column (7): hardness ratio (HR) of the X-ray source, HR=(H-S)/(H+S) where H and S are the hard- (2.0-7.0 keV) and soft-band (0.5-2.0 keV) count rates respectively; column (8): spectral counts over 0.5-8.0 keV range; column (9): best fitting model for X-ray emission, for definitions see Section 4.3.3; column (10): column density of obscuring material in units 10$^{22}$cm$^{-2}$; column (11): observed 2.0-10.0 keV luminosity in units 10$^{42}$ ergs s$^{-1}$; column (12): absorption corrected 2.0-10.0 keV luminosity, corrected for X-ray absorption, in units 10$^{42}$ ergs s$^{-1}$.

| ID$_{opt}$ (1) | Class (2) | RA$_{opt}$ (3) | Dec$_{opt}$ (4) | XID (5) | $z$ (6) | HR (7) | cts (8) | Model (9) | N$_H$ (10) | L$_{abs}$ (11) | L$_{abscorr}$ (12) |
|---|---|---|---|---|---|---|---|---|---|---|---|
| 6752 | cQG | 53.0764 | -27.8487 | cdfs4Ms_050 | 1.536† | $0.73^{+0.03}_{-0.03}$ | 646 | C | $65 \pm 5.4$ | $21.75^{+0.93}_{-0.98}$ | $170.22^{+7.25}_{-7.69}$ |
| 10405 | cQG | 53.0457 | -27.8156 | cdfs4Ms_083 | 2.53 | $-0.40^{+0.03}_{-0.03}$ | 901 | B | $1.9 \pm 0.46$ | $76.25^{+2.84}_{-2.69}$ | $91.63^{+3.42}_{-3.23}$ |
| 10767 | cQG | 53.1793 | -27.8125 | cdfs4Ms_089 | 1.73† | $0.55^{+0.06}_{-0.05}$ | 328 | C | $34 \pm 2.6$ | $13.68^{+0.75}_{-0.81}$ | $60.68^{+3.34}_{-3.58}$ |
| 15377 | cQG | 53.0223 | -27.7789 | cdfs4Ms_116 | 2.5883 | $0.42^{+0.06}_{-0.05}$ | 409 | B | $71 \pm 2.1$ | $17.70^{+0.95}_{-0.81}$ | $169.68^{+9.09}_{-7.78}$ |
| 17147 | cQG | 53.1192 | -27.7658 | cdfs4Ms_135 | 1.7453 | $0.07^{+0.30}_{-0.22}$ | 44 | A | ... | $0.80^{+0.09}_{-0.10}$ | $0.80^{+0.09}_{-0.10}$ |
| 26766 | cQG | 53.0624 | -27.7069 | cdfs4Ms_266 | 2.6087† | $-0.18^{+0.04}_{-0.05}$ | 970 | C | $240 \pm 74$ | $67.12^{+3.57}_{-2.35}$ | $257.65^{+13.70}_{-9.03}$ |
| 16065 | cQG | 53.0522 | -27.7748 | cdfs4Ms_317 | 1.605† | $-0.33^{+0.30}_{-0.33}$ | 85 | A | ... | $0.99^{+0.08}_{-0.07}$ | $0.99^{+0.08}_{-0.07}$ |
| 11823 | cQG | 53.1787 | -27.8026 | cdfs4Ms_412 | 2.4925 | $0.59^{+0.18}_{-0.14}$ | 67 | D | $> 10^2$ | $1.97^{+0.26}_{-0.10}$ | $32.34^{+4.20}_{-1.62}$ |
| 11079 | cQG | 53.1632 | -27.8090 | cdfs4Ms_437 | 2.47† | $0.89^{+0.11}_{-0.03}$ | 54 | B | $150 \pm 12$ | $0.89^{+0.13}_{-0.18}$ | $38.73^{+5.79}_{-8.00}$ |
| 23845 | cQG | 53.0976 | -27.7153 | cdfs4Ms_460 | 2.1447† | $0.76^{+0.21}_{-0.09}$ | 192 | B | $150 \pm 6.1$ | $1.11^{+0.13}_{-0.13}$ | $49.79^{+5.86}_{-5.69}$ |
| 4526 | cSFG | 53.1573 | -27.8701 | cdfs4Ms_031 | 1.603† | $-0.43^{+0.01}_{-0.01}$ | 4561 | B | $1.1 \pm 0.11$ | $165.43^{+1.97}_{-2.73}$ | $184.36^{+2.20}_{-3.04}$ |
| 9834 | cSFG | 53.1488 | -27.8211 | cdfs4Ms_077 | 2.578† | $0.21^{+0.13}_{-0.12}$ | 94 | D | $> 10^2$ | $4.41^{+0.76}_{-0.28}$ | $72.67^{+12.60}_{-4.64}$ |
| 10973 | cSFG | 53.1858 | -27.8100 | cdfs4Ms_091 | 2.593† | $-0.21^{+0.06}_{-0.06}$ | 367 | B | $9.6 \pm 1.3$ | $28.30^{+1.35}_{-1.76}$ | $53.83^{+2.57}_{-3.35}$ |
| 14781 | cSFG | 53.0333 | -27.7826 | cdfs4Ms_111 | 2.6123† | $-0.24^{+0.03}_{-0.03}$ | 1120 | C | $17 \pm 3.6$ | $105.50^{+5.30}_{-3.10}$ | $153.08^{+7.69}_{-4.50}$ |

*Continued on next page*

Table 4.4 – *Continued from previous page*

| ID$_{opt}$ (1) | Class (2) | RA$_{opt}$ (3) | Dec$_{opt}$ (4) | XID (5) | $z$ (6) | HR (7) | cts (8) | Model (9) | N$_H$ (10) | L$_{abs}$ (11) | L$_{abscorr}$ (12) |
|---|---|---|---|---|---|---|---|---|---|---|---|
| 15955 | cSFG | 53.0490 | -27.7745 | cdfs4Ms_123 | 1.6335 | $-0.21^{+0.04}_{-0.04}$ | 722 | B | $4.0 \pm 0.44$ | $27.64^{+1.29}_{-0.92}$ | $38.90^{+1.82}_{-1.29}$ |
| 16274 | cSFG | 53.1311 | -27.7731 | cdfs4Ms_126 | 2.223† | $-0.14^{+0.16}_{-0.16}$ | 78 | D | $> 10^2$ | $3.62^{+0.40}_{-0.52}$ | $19.19^{+2.12}_{-2.76}$ |
| 16085 | cSFG | 53.0939 | -27.7677 | cdfs4Ms_131 | 1.73† | $0.40^{+0.04}_{-0.04}$ | 596 | C | $31 \pm 3.5$ | $25.84^{+0.88}_{-0.99}$ | $83.88^{+2.87}_{-3.20}$ |
| 19298 | cSFG | 53.0127 | -27.7472 | cdfs4Ms_154 | 2.573† | $-0.28^{+0.05}_{-0.06}$ | 754 | B | $4.3 \pm 0.28$ | $49.61^{+1.20}_{-1.69}$ | $71.10^{+1.72}_{-2.43}$ |
| 21937 | cSFG | 53.0066 | -27.7242 | cdfs4Ms_171 | 2.7212† | $-0.29^{+0.02}_{-0.02}$ | 2431 | B | $4.3 \pm 0.44$ | $216.91^{+4.99}_{-4.71}$ | $311.87^{+7.17}_{-6.77}$ |
| 22603 | cSFG | 53.1070 | -27.7182 | cdfs4Ms_175 | 2.291† | $-0.04^{+0.03}_{-0.03}$ | 1349 | B | $14 \pm 0.90$ | $92.25^{+2.70}_{-3.11}$ | $211.44^{+6.19}_{-7.13}$ |
| 26637 | cSFG | 53.1049 | -27.7052 | cdfs4Ms_182 | 1.617† | $-0.49^{+0.03}_{-0.02}$ | 1747 | A | ... | $54.16^{+1.23}_{-0.98}$ | $54.16^{+1.23}_{-0.98}$ |
| 6278 | cSFG | 53.0601 | -27.8530 | cdfs4Ms_226 | 1.544† | $0.50^{+0.12}_{-0.09}$ | 138 | C | $150 \pm 16$ | $2.34^{+0.25}_{-0.18}$ | $57.14^{+6.22}_{-4.36}$ |
| 23896 | cSFG | 53.1008 | -27.7160 | cdfs4Ms_262 | 2.3027† | $-0.35^{+0.09}_{-0.09}$ | 331 | A | ... | $15.50^{+0.59}_{-0.61}$ | $15.50^{+0.59}_{-0.61}$ |
| 19143 | cSFG | 53.0279 | -27.7487 | cdfs4Ms_321 | 2.3273 | $-0.12^{+0.26}_{-0.19}$ | 238 | A | ... | $4.90^{+0.22}_{-0.16}$ | $4.90^{+0.22}_{-0.16}$ |
| 23382 | cSFG | 53.1623 | -27.7121 | cdfs4Ms_334 | 2.2209 | $0.42^{+0.15}_{-0.15}$ | 303 | D | $> 10^2$ | $5.11^{+0.20}_{-0.04}$ | $83.33^{+3.31}_{-0.66}$ |
| 26056 | cSFG | 53.0633 | -27.6996 | cdfs4Ms_369 | 2.402† | $-0.25^{+0.18}_{-0.15}$ | 454 | A | ... | $11.85^{+0.40}_{-0.42}$ | $11.85^{+0.40}_{-0.42}$ |
| 11701 | cSFG | 53.0940 | -27.8041 | cdfs4Ms_410 | 2.2139 | $0.76^{+0.10}_{-0.08}$ | 74 | B | $78 \pm 9.5$ | $3.07^{+0.41}_{-0.52}$ | $34.91^{+4.62}_{-5.93}$ |
| 22123 | cSFG | 53.1228 | -27.723 | cdfs4Ms_459 | 1.609† | $0.70^{+0.23}_{-0.12}$ | 140 | B | $86 \pm 5.9$ | $1.43^{+0.07}_{-0.08}$ | $19.11^{+0.90}_{-1.09}$ |
| 26211 | cSFG | 53.0660 | -27.7019 | cdfs4Ms_474 | 2.7875 | $0.67^{+0.19}_{-0.15}$ | 333 | B | $220 \pm 8.6$ | $0.85^{+0.12}_{-0.12}$ | $125.27^{+17.61}_{-17.75}$ |

**Table 4.5:** X-ray spectral fitting results for LR matched extended galaxies with $1.4 < z < 3.0$ and M> $10^{10.5}$M$_{\odot}$. As with the compact galaxies, R-values (reflected component/illuminated component) for sources best fit by model D show them all to be extremely reflection dominated, thus they are all classified as Compton thick AGN with N$_H > 10^{24}$ cm$^{-2}$. Column (1): Optical source ID from the CANDELS GOODS-S epoch-10; column (2): extended galaxy classification; columns (3) and (4): Right Ascension and Declination of the optical source; column (5): ID of X-ray counterpart source identified using LR matching; column (6): redshift of X-ray source, spectroscopic redshifts are denoted with †; column (7): hardness ratio (HR) of the X-ray source, HR=(H-S)/(H+S) where H and S are the hard- (2.0-7.0 keV) and soft-band (0.5-2.0 keV) count rates respectively; column (8): spectral counts over 0.5-8.0 keV range; column (9): best fitting model for X-ray emission, for definitions see Section 4.3.3; column (10): column density of obscuring material in units $10^{22}$cm$^{-2}$; column (11): observed 2.0-10.0 keV luminosity in units $10^{42}$ ergs s$^{-1}$; column (12): absorption corrected 2.0-10.0 keV luminosity, corrected for X-ray absorption, in units $10^{42}$ ergs s$^{-1}$.

| ID$_{opt}$ (1) | Class (2) | RA$_{opt}$ (3) | Dec$_{opt}$ (4) | XID (5) | $z$ (6) | HR (7) | cts (8) | Model (9) | N$_H$ (10) | L$_{obs}$ (11) | L$_{abscorr}$ (12) |
|---|---|---|---|---|---|---|---|---|---|---|---|
| 4094 | eQG | 53.1193 | -27.8737 | cdfs4Ms_024 | 1.7809 | $-0.32^{+0.32}_{-0.34}$ | 72 | A | ... | $1.03^{+0.13}_{-0.11}$ | $1.03^{+0.13}_{-0.11}$ |
| 5867 | eQG | 53.1076 | -27.8557 | cdfs4Ms_044 | 2.5443 | $-0.69^{+0.14}_{-0.15}$ | 100 | A | ... | $7.29^{+0.75}_{-0.90}$ | $7.29^{+0.75}_{-0.90}$ |
| 6422 | eQG | 53.0619 | -27.8510 | cdfs4Ms_048 | 1.5569 | $0.07^{+0.05}_{-0.06}$ | 408 | B | $8.3 \pm 0.76$ | $14.87^{+0.74}_{-0.76}$ | $26.59^{+1.32}_{-1.37}$ |
| 8396 | cQG | 53.0579 | -27.8335 | cdfs4Ms_061 | 2.5235 | $-0.14^{+0.09}_{-0.10}$ | 186 | B | $13 \pm 1.6$ | $12.34^{+0.82}_{-0.86}$ | $27.26^{+1.82}_{-1.90}$ |
| 11979 | eQG | 53.0938 | -27.8013 | cdfs4Ms_099 | 2.1974 | $-0.33^{+0.12}_{-0.14}$ | 87 | A | ... | $5.28^{+0.58}_{-0.34}$ | $5.28^{+0.58}_{-0.34}$ |
| 16375 | eQG | 53.0449 | -27.7744 | cdfs4Ms_318 | 1.607† | $-0.45^{+0.22}_{-0.20}$ | 111 | A | ... | $1.80^{+0.12}_{-0.13}$ | $1.80^{+0.12}_{-0.13}$ |
| 26558 | eQG | 53.0026 | -27.7044 | cdfs4Ms_367 | 2.0918 | $-0.53^{+0.22}_{-0.27}$ | 509 | A | ... | $9.27^{+0.26}_{-0.24}$ | $9.27^{+0.26}_{-0.24}$ |
| 7230 | eQG | 53.1507 | -27.8436 | cdfs4Ms_404 | 1.608† | $0.69^{+0.10}_{-0.08}$ | 108 | C | $99 \pm 18$ | $2.70^{+0.31}_{-0.37}$ | $37.92^{+4.36}_{-5.17}$ |
| 10348 | eQG | 53.0668 | -27.8166 | cdfs4Ms_453 | 1.413† | $0.17^{+0.35}_{-0.25}$ | 40 | D | $> 10^2$ | $0.58^{+0.08}_{-0.08}$ | $5.76^{+0.75}_{-0.79}$ |
| 16689 | eQG | 53.0715 | -27.7698 | cdfs4Ms_456 | 1.7611 | $0.16^{+0.21}_{-0.17}$ | 70 | D | $> 10^2$ | $1.88^{+0.29}_{-0.19}$ | $19.12^{+2.91}_{-1.89}$ |
| 5761 | eSFG | 53.1507 | -27.8574 | cdfs4Ms_042 | 1.615† | $-0.22^{+0.08}_{-0.08}$ | 224 | B | $2.3 \pm 0.59$ | $6.91^{+0.42}_{-0.42}$ | $8.56^{+0.52}_{-0.52}$ |
| 10014 | eSFG | 53.0589 | -27.8195 | cdfs4Ms_079 | 1.974 | $-0.08^{+0.31}_{-0.22}$ | 61 | A | ... | $1.57^{+0.13}_{-0.14}$ | $1.57^{+0.13}_{-0.14}$ |
| 10294 | eSFG | 53.1416 | -27.8166 | cdfs4Ms_080 | 2.33 | $0.38^{+0.11}_{-0.10}$ | 99 | B | $31 \pm 5.0$ | $6.12^{+0.85}_{-0.60}$ | $22.93^{+3.17}_{-2.25}$ |
| 10493 | eSFG | 53.1313 | -27.8149 | cdfs4Ms_084 | 1.8716 | $-0.21^{+0.14}_{-0.15}$ | 78 | B | $3.8 \pm 1.6$ | $3.59^{+0.45}_{-0.45}$ | $4.97^{+0.63}_{-0.62}$ |

*Continued on next page*

Table 4.5 – *Continued from previous page*

| ID$_{opt}$ (1) | Class (2) | RA$_{opt}$ (3) | Dec$_{opt}$ (4) | XID (5) | $z$ (6) | HR (7) | cts (8) | Model (9) | N$_H$ (10) | L$_{obs}$ (11) | L$_{abscorr}$ (12) |
|---|---|---|---|---|---|---|---|---|---|---|---|
| 16934 | eSFG | 53.1656 | -27.7698 | cdfs4Ms_129 | 1.552† | $-0.18^{+0.04}_{-0.04}$ | 799 | B | $3.1 \pm 0.32$ | $28.15^{+1.04}_{-0.96}$ | $37.21^{+1.37}_{-1.27}$ |
| 25873 | eSFG | 53.1337 | -27.6987 | cdfs4Ms_183 | 1.982† | $-0.30^{+0.05}_{-0.06}$ | 745 | B | $1.5 \pm 0.44$ | $27.64^{+1.28}_{-0.77}$ | $32.01^{+1.49}_{-0.89}$ |
| 4634 | eSFG | 53.0537 | -27.8692 | cdfs4Ms_220 | 2.0433 | $-0.67^{+0.10}_{-0.33}$ | 131 | A | ... | $3.05^{+0.25}_{-0.19}$ | $3.05^{+0.25}_{-0.19}$ |
| 10000 | eSFG | 53.0720 | -27.8189 | cdfs4Ms_238 | 1.7519 | $0.09^{+0.38}_{-0.26}$ | 40 | A | ... | $0.62^{+0.08}_{-0.09}$ | $0.62^{+0.08}_{-0.09}$ |
| 10252 | eSFG | 53.1810 | -27.8172 | cdfs4Ms_239 | 1.603† | $-0.54^{+0.20}_{-0.38}$ | 57 | A | ... | $0.72^{+0.05}_{-0.06}$ | $0.72^{+0.05}_{-0.06}$ |
| 26554 | eSFG | 53.1411 | -27.7011 | cdfs4Ms_271 | 1.604† | $0.05^{+0.29}_{-0.22}$ | 301 | C | 314.07 | $2.16^{+0.07}_{-0.07}$ | $88.35^{+2.75}_{-3.06}$ |
| 25511 | eSFG | 53.0713 | -27.6936 | cdfs4Ms_337 | 1.892 | $0.37^{+0.10}_{-0.08}$ | 601 | B | $24 \pm 0.83$ | $13.95^{+0.33}_{-0.31}$ | $43.58^{+1.03}_{-0.97}$ |
| 7246 | eSFG | 53.1989 | -27.8439 | cdfs4Ms_434 | 1.615† | $0.69^{+0.09}_{-0.09}$ | 199 | B | $43 \pm 4.4$ | $5.09^{+0.58}_{-0.41}$ | $25.71^{+2.93}_{-2.06}$ |
| 12624 | eSFG | 53.1669 | -27.7987 | cdfs4Ms_438 | 1.998† | $-0.02^{+0.27}_{-0.21}$ | 55 | A | ... | $1.72^{+0.22}_{-0.26}$ | $1.72^{+0.22}_{-0.26}$ |
| 7551 | eSFG | 53.1314 | -27.8413 | cdfs4Ms_451 | 1.613† | $0.48^{+0.28}_{-0.18}$ | 38 | D | $> 10^2$ | $0.61^{+0.06}_{-0.05}$ | $8.64^{+0.82}_{-0.68}$ |
| 12526 | eSFG | 53.1083 | -27.7976 | cdfs4Ms_500 | 1.9096 | $-0.53^{+0.19}_{-0.41}$ | 26 | A | ... | $1.01^{+0.19}_{-0.16}$ | $1.01^{+0.19}_{-0.16}$ |
| 16972 | eSFG | 53.0820 | -27.7672 | cdfs4Ms_504 | 1.6403 | $-0.53^{+0.24}_{-0.32}$ | 46 | A | ... | $0.71^{+0.13}_{-0.08}$ | $0.71^{+0.13}_{-0.08}$ |
| 12537 | eSFG | 53.0568 | -27.7983 | cdfs4Ms_515 | 1.74† | $-0.19^{+0.42}_{-0.35}$ | 41 | A | ... | $0.50^{+0.07}_{-0.08}$ | $0.50^{+0.07}_{-0.08}$ |
| 3943 | eSFG | 53.1052 | -27.8751 | cdfs4Ms_524 | 1.9345 | $-0.41^{+0.30}_{-0.32}$ | 75 | A | ... | $1.42^{+0.20}_{-0.15}$ | $1.42^{+0.20}_{-0.15}$ |
| 9951 | eSFG | 53.1848 | -27.8198 | cdfs4Ms_530 | 2.1055 | $-0.39^{+0.33}_{-0.38}$ | 51 | A | ... | $1.19^{+0.18}_{-0.16}$ | $1.19^{+0.18}_{-0.16}$ |
| 15261 | eSFG | 53.0203 | -27.7798 | cdfs4Ms_532 | 1.8979 | $-0.54^{+0.18}_{-0.41}$ | 98 | A | ... | $1.94^{+0.14}_{-0.12}$ | $1.94^{+0.14}_{-0.12}$ |

### 4.4.2 X-ray spectral analysis of massive galaxies

The X-ray spectra of the massive galaxy sample (M$> 10^{10.5}$M$_\odot$, $1.4 < z < 3.0$) are fitted to 4 X-ray spectral emission models (described in Section 4.3.3) in order to study the nature of the X-ray emission in more detail. Model A is a fixed power-law ($\Gamma = 1.9$) of the type expected to be produced by unobscured (Nandra and Pounds, 1994) AGN while models B, C and D are three different obscured AGN models. The results of this analysis are presented in Tables 4.4 (compact galaxies) and 4.5 (extended galaxies). The majority of massive galaxies are best-fit by models A and B ($\sim$ 75% of all massive galaxies). The preference of Model B in the obscured AGN population could be because it has one less free parameter than Model C, while the reflection dominated spectra best-fit by Model D is applicable only to the most heavily obscured AGN.

Example spectral fits for each of the models used in this spectral analysis to sources from this sample are presented in Figure 4.4. The errors on the flux of the unfolded spectrum increase dramatically at E> 6keV in all the spectra as a result of the reduced effective area of the ACIS-I instrument at these energies (Weisskopf et al., 2002). The unobscured AGN spectrum (cdfs4Ms_532; model A) has a low number of spectral counts (98), large errors on the unfolded spectrum and none of the emission features associated with obscuration (e.g. soft absorption or iron K$\alpha$ line emission). The obscured AGN spectrum with spherically distributed obscuring matter (cdfs4Ms_175; model B) has heavily suppressed soft X-ray emission (E $<$ 1.0keV) and Iron K$\alpha$ line emission at rest-frame 6.4keV although the relatively low column density means this feature is not very pronounced. Suppression of softer energy photons is partially mitigated in the obscured AGN with a toroidally distributed obscuring matter (cdfs4Ms_050; model C) because of the scattered emission component produced by the ionistation cones. There is also a prominent iron K$\alpha$ emission line with a self-consistent Compton hump at rest-frame $\sim$ 6.4keV. The reflection dominated spectrum (cdfs4Ms_334; model D) exhibits suppression of soft X-ray emission with iron K$\alpha$ line emission and a self consistent Compton hump. The obscuration is so severe that the contribution from the illuminating component contribution is almost negligible, thus beyond the range of this plot.

A breakdown of the obscured and Compton thick AGN fractions for each subsample is presented in Table 4.6. Note that the R-values (ratio of reflected emission component relative to the illuminating component) of all sources best-fit by Model D indicate that they are reflection dominated in the extreme (R>7). Such high R-values are consistent with those observed in Compton thick AGN spectra. Therefore a column density of N$_H$ $> 10^{24}$cm$^{-2}$ has been assumed for all these sources. A more accurate estimate of the obscuring column density is not possible because the obscuration is too severe. The observed frame 0.5-8.0 keV energy range of spectra used in this analysis is insensitive to sources with N$_H$ $< 10^{22}$cm$^{-2}$ because the photoelectric turnover used to characterise sources with lower N$_H$ values has been redshifted below the energy range of these *Chandra* measurements. As a result no obscured sources possess N$_H$ $< 10^{22}$cm$^{-2}$.

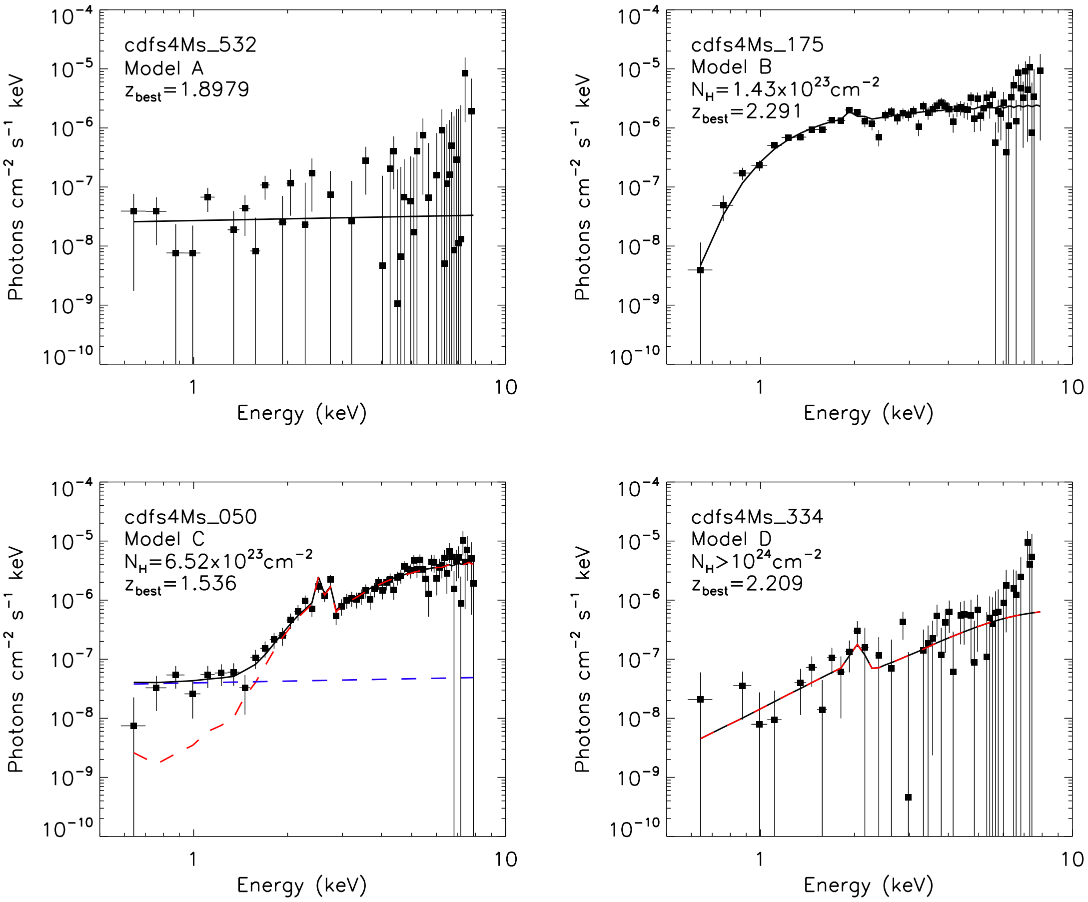

**Figure 4.4:** Typical spectra from the massive galaxy sample, with one example spectrum provided for each model. The black line represents the model spectrum and the black squares correspond to the unfolded spectrum with errors. In the bottom-left panel (Model C) the red dashed line represents the torus emission component while the blue dashed is the scattered component. In the bottom-right panel (Model D) the red dashed line is the PEXMON model component but the illuminating component is almost negligible (lying beyond the range of the plot) so has been omitted.

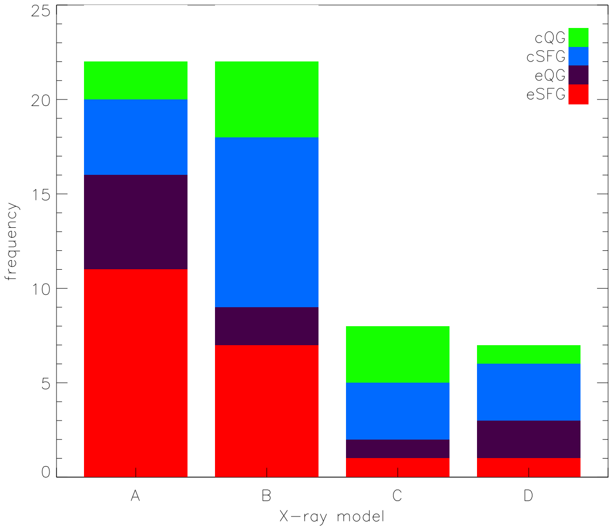

**Figure 4.5:** Bar chart illustrating the distribution of best-fitting X-ray models across the sample. The letter for each column corresponds to the lettering used in Section 4.3.3 when describing the X-ray emission models used in the spectral fitting.

**Table 4.6:** Obscured and Compton thick fractions for compact and extended massive galaxy subsamples. Column (1): type of galaxy; column (2): number of X-ray sources LR matched to optical counterparts; column (3): number of galaxies with signatures of obscured emission; column (4): percentage of galaxies with obscured emission (ie best fit by models B, C or D), with $1\sigma$ binomial error from Gehrels (1986); column (5): number of galaxies exhibiting Compton thick emission; column (6): percentage of galaxies exhibiting Compton thick emission.

| Type (1) | $N_{src}$ (2) | $N_{obs}$ (3) | $F_{obs}$ (4) | $N_{CT}$ (5) | $F_{CT}$ (6) |
|---|---|---|---|---|---|
| cQG | 10 | 8 | $80.0^{+12.8}_{-20.5}$ | 4 | $40.0^{+20.5}_{-18.0}$ |
| cSFG | 19 | 15 | $78.9^{+9.4}_{-22.4}$ | 5 | $26.3^{+17.2}_{-14.6}$ |
| eQG | 10 | 5 | $50.0^{+19.5}_{-19.5}$ | 2 | $20.0^{+20.5}_{-12.8}$ |
| eSFG | 20 | 9 | $45.0^{+16.2}_{-11.1}$ | 2 | $10.0^{+19.4}_{-8.3}$ |

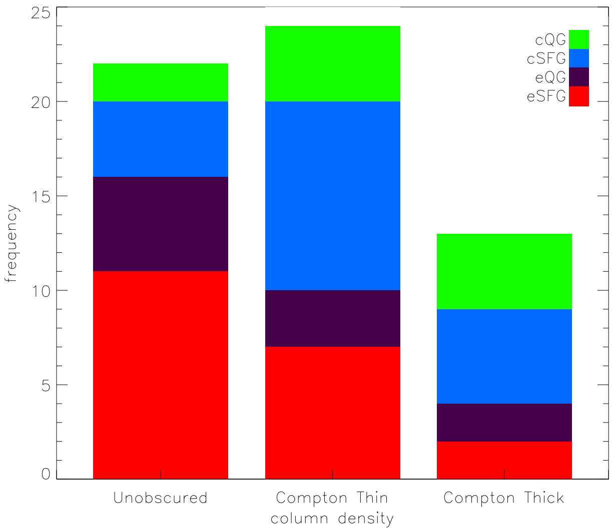

**Figure 4.6:** Bar chart demonstrating the severity of AGN obscuration in each subsample. The unobscured bin consists of galaxies whose X-ray spectra are best fit by Model A. The Compton thin bin contains obscured AGN with $N_H < 10^{24}$xm$^{-2}$ while the Compton thick bin contains galaxies with $N_H \geq 10^{24}$xm$^{-2}$. Obscuration is far more prevalent in the compact galaxies, particularly true when considering the Compton thick sources.

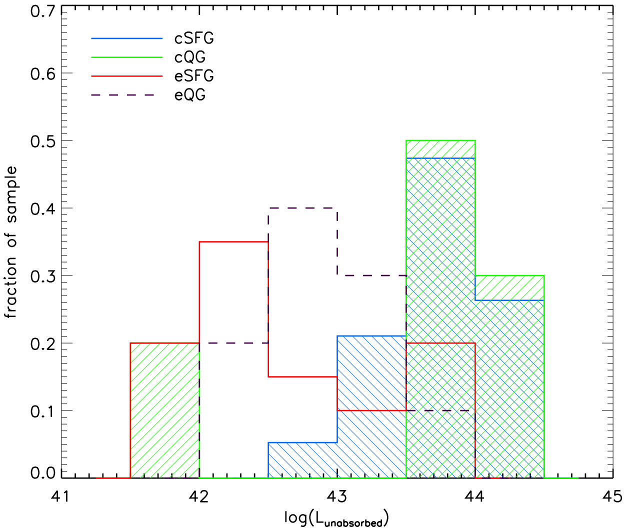

**Figure 4.7:** Plot of the fraction of each subsample in bins of log($L_{abscorr}$) for X-ray sources LR matched to optical counterparts with $z_{best} > 1.4$ and M> $10^{10.5}M_{\odot}$. Using fraction of sample as opposed to number frequency because of the differing sizes of each subsample.

The massive galaxies have also been binned according to their column densities in Figure 4.6. It is immediately evident that the compact galaxies contain a significantly higher fraction of obscured AGN (80 %; ie best fit by models B, C or D) than the extended galaxies ( 45 %), a result that has 99% significance according to the Fishers exact test. Considering the most obscured objects, $\sim$ 30 % of the X-ray detected AGN in the compact galaxy sample are found to be Compton thick, compared to just 13 % of the X-ray detected AGN hosted by extended galaxies. The compact QGs are the most heavily obscured of all the subsamples with 70% possessing $\mathrm{N}_H > 10^{23.5}\mathrm{cm}^{-2}$ (see Table 4.4).

Having determined the obscuration properties of the AGN, it is then possible to make a reasonably accurate measurement of their intrinsic (absorption-corrected) luminosities in the 2-10 keV band. There are a wide range of luminosities across the sample, starting at $4 \times 10^{41}$ erg $\mathrm{s}^{-1}$ (cdfs4Ms_453; an extended SFG) and climbing to $3 \times 10^{44}$ erg $\mathrm{s}^{-1}$ (cdfs4Ms_171; a compact SFG). The compact galaxies are found to be much more luminous than the extended galaxies, particularly once their emission has been corrected for obscuration (see Figure 4.7). The compact galaxies possess a median luminosity of $5.7 \pm 3.8 \times 10^{43}$ erg $\mathrm{s}^{-1}$ while the median luminosity of extended galaxies is ten times lower, at $5.8 \pm 4.5 \times 10^{42}$ erg $\mathrm{s}^{-1}$.

### 4.4.3 Stacking undetected massive galaxies

Most of the massive galaxy sample is not detected directly in X-rays, so X-ray stacking has been used to investigate the average properties of the undetected massive galaxies, following the method presented in 2.5.3. The massive galaxies are stacked in three broadbands: 0.5-7.0 keV (full), 0.5-2.0 keV (soft) and 2.0-7.0 keV (hard). The stacked photon count rates are converted to fluxes assuming a single power-law $\Gamma = 1.4$ (equivalent to the X-ray background): $F_{0.5-10keV}$ (full), $F_{0.5-2keV}$ (soft) and $F_{2-10keV}$ (hard). The inclusion and extraction radii used when stacking were calibrated using the full massive galaxy sample, following the prescription described in Section 2.5.3. The best inclusion and extraction radii were found to be 8.0 arcminutes and 1.50 arcseconds respectively. These inclusion and extraction radii are used when stacking all of the massive galaxy subsamples. Although this may not produce the optimum SN possible for these sources, it removes potential sampling bias in the low count statistics between the stacking analysis of each subsample.

**Table 4.7:** Results of stacking massive galaxies and the subsamples of compact and extended massive galaxies that do not have an X-ray counterpart. All stacked fluxes are calculated assuming the emission has an unobscured power-law profile with $\Gamma = 1.4$. Column (1): subsample name; column (2): number of X-ray undetected galaxies that have been stacked; column (3): SN of the full band (0.5-7.0 keV) stacked emission; column (4): SN of the soft band (0.5-2.0 keV) stacked emission; column (5): SN of the hard band (2.0-7.0 keV) stacked emission; column (6): average 0.5-10 keV flux per galaxy derived from the full band stacked emission, units $10^{-17}$ erg s$^{-1}$ cm$^{-2}$; column (7): average 0.5-2 keV flux per galaxy derived from the soft band stacked emission, units $10^{-17}$ erg s$^{-1}$ cm$^{-2}$; column (8): average 2-10 keV flux per galaxy derived from the hard band stacked emission, units $10^{-17}$ erg s$^{-1}$ cm$^{-2}$; column (9): hardness ratio of stacked emission, HR=(H-S)/(H+S) where H and S are the hard- and soft-band stacked emission count rates respectively; column (10): median 0.5-2.0 keV luminosity for stacked sources derived from the observed soft band flux, units $10^{41}$ erg s$^{-1}$; column (11): median 2.0-10.0 keV luminosity for stacked sources derived from the observed hard band flux, units $10^{41}$ erg s$^{-1}$.

| | | Signal-to-Noise Ratio | | | Stacked Flux | | | | | |
|---|---|---|---|---|---|---|---|---|---|---|
| Class (1) | $N_{stack}$ (2) | $SN_{full}$ (3) | $SN_{soft}$ (4) | $SN_{hard}$ (5) | $F_{full}$ (6) | $F_{soft}$ (7) | $F_{hard}$ (8) | HR (9) | $L_{0.5-2keV}$ (10) | $L_{2-10keV}$ (11) |
| All | 174 | 14.09 | 14.86 | 6.40 | 3.42±0.24 | 0.90±0.06 | 2.65±0.41 | -0.35±0.07 | 2.56 | 7.61 |
| cQG | 33 | 2.93 | 3.88 | 0.75 | 1.51±0.52 | 0.45±0.12 | ... | ... | 0.98 | ... |
| cSFG | 29 | 6.96 | 6.69 | 3.67 | 5.03±0.41 | 1.14±0.17 | 4.40±1.20 | -0.24±0.14 | 6.12 | 23.61 |
| eQG | 9 | 2.16 | 2.21 | 0.99 | 2.30±1.07 | 0.49±0.22 | ... | ... | 1.37 | ... |
| eSFG | 103 | 12.35 | 12.82 | 5.53 | 4.13±0.33 | 1.04±0.08 | 2.99±0.54 | -0.36±0.08 | 3.03 | 8.70 |

For the purpose of this analysis a stacked signal with SN$\geq 3$ is deemed "statistically significant", while a stacked signal of SN$< 3$ is classed as a non-detection. The average HR and corresponding $\Gamma$ values for an X-ray undetected subsample are only calculated if the stacked signals of the Full, Soft and Hard bands are statistically significant. The results of stacking the X-ray undetected massive galaxies and the various subsamples are presented in Table 4.7. When using the massive galaxy sample 197 X-ray undetected galaxies were stacked. This yielded significant detections ($> 3\sigma$) in the full, soft and hard bands and HR=-0.35±0.07. The observed HR would be replicated by a power-law $\Gamma = 1.70^{+0.2}_{-0.1}$. This power-law is consistent, within errors, with a typical unobscured AGN spectrum ($\Gamma \sim 1.9$; Nandra and Pounds 1994) and X-ray emission from star formation ($\Gamma \sim 1.7$; Persic and Rephaeli 2002. The average $L_{2-10keV}$ of these sources greatly exceeds the X-ray luminosity expected from pure star formation estimated using the relation of Ranalli et al. (2003).

$$SFR = 2.2 \times 10^{-40} L_{0.5-2keV} M_{\odot}/yr \tag{4.3}$$

$$SFR = 2.0 \times 10^{-40} L_{2-10keV} M_{\odot}/yr \tag{4.4}$$

Next each of the X-ray undetected massive galaxies were separated into compact and extended QG and SFG subsamples and then subjected to the same stacking analysis (see Table 4.7). Both X-ray undetected SFG subsamples (ie compact and extended) exhibit statistically significant stacked signals in the full, hard and soft broad bands. The X-ray undetected compact SFGs possess an average HR=-0.24±0.14 with corresponding $\Gamma = 1.4^{+0.2}_{-0.2}$ which, unlike the parent massive galaxy sample, is no longer consistent with that of typical unobscured AGN emission. The X-ray undetected compact SFGs are the most X-ray luminous of all the subsamples and their $L_{2-10keV}$ is too large to have originated from star formation alone. The stacked signal of X-ray undetected extended SFGs has a similar soft band flux but a lower hard band flux than the X-ray undetected compact SFGs resulting in a softer HR (see Table 4.7). As with the X-ray undetected compact SFGs, however, the $L_{2-10keV}$ of X-ray undetected extended galaxies still exceeds that predicted by star formation. The $L_{0.5-2keV}$ of both X-ray undetected compact SFGs and X-ray undetected extended SFGs are consistent with pure star formation.

The X-ray undetected QGs exhibit much weaker stacked signals than the X-ray undetected SFGs. The X-ray undetected compact QGs only possess a statistically significant stacked signal in the soft band while the X-ray undetected extended QGs do not possess a statistically significant signal in any of the broad bands. The lack of a statistically significant signal for X-ray undetected QGs is likely a result of the small size of the sample (9 contributing galaxies). Despite the low stacked signal, $L_{0.5-2keV}$ of both X-ray undetected compact QGs and X-ray undetected eQGs exceeds that predicted by their average star formation. Thus there appears to be an additional faint soft X-ray component within these galaxies, possibly originating from low luminosity unobscured AGN. The lack of hard X-ray emission in the stacked signal of X-ray undetected QGs means there is little or no evidence supporting the presence of heavily obscured or Compton thick AGN within these galaxies.

### 4.4.4 Comparison to previous work

Barro et al. (2013) found that, at $z > 2.2$ and $\mathrm{M}_* > 10^{10}\mathrm{M}_\odot$, compact SFGs are 30 times more likely to exhibit luminous AGN activity ($L_X > 10^{43}$erg s$^{-1}$) than extended SFGs. The assertion is that this is proof luminous AGN feedback is quenching star formation in the compact galaxies to form compact QGs. Applying the same mass redshift and X-ray luminosity cuts we find a compact SFG X-ray detected fraction of 27.2% (12/44) and an extended SFG X-ray detected fraction of 2.0% (4/196). These agree with the results of Barro et al. (2013) at the $1\sigma$ level. If the subsamples are split into merely compact and extended galaxies a very similar result is observed; 28.6% (18/63) compact galaxies X-ray detected compared to 2.4% (5/206) extended galaxies X-ray detected. This implies that the more X-ray luminous AGN are predominantly found in compact galaxies at $z > 2.2$.

## 4.5 Discussion

### 4.5.1 Summary of Results for X-ray Detected Sources

Using 4Ms observations in the CDFS, the X-ray properties and AGN content of H-band selected massive ($\mathrm{M}_* > 10^{10.5}$ $\mathrm{M}_\odot$) galaxies at $z \sim 2$ has been investigated. The massive galaxy sample used in this work was originally presented in Barro et al. (2013). It was derived from a catalogue of H-band selected galaxies with $1.4 \leq z \leq 3.0$ and M> $10^{10.0}$ $\mathrm{M}_\odot$ created from observations taken as part of the CANDELS GOODS-S region survey. The massive galaxies were subdivided according to their sSFR and compactness; compact QGs and SFGs, and extended QGs and SFGs. The mass constraint on the sample was raised to $\mathrm{M}_* > 10^{10.5}$ $\mathrm{M}_\odot$ as this ensures the compact and extended subsamples share similar stellar mass distributions. This is because the extended SFGs dominate the sample at $10^{10.0}$ $\mathrm{M}_\odot < M < 10^{10.5}$ $\mathrm{M}_\odot$. Likelihood ratio matching of X-ray sources to the massive galaxies reveals a high detected fraction ($22.0 \pm 2.5$%; see Table 4.1). Previous studies have shown elevated AGN activity in galaxies with high stellar masses (e.g. Brusa et al. 2009; Pimbblet and Jensen 2012) and $z \sim 2$ (e.g. Boyle and Terlevich 1998; Silverman et al. 2008; Aird et al. 2010). Therefore by applying mass and redshift selection criteria (M> $10^{10.5}\mathrm{M}_\odot$ and $1.4 < z < 3$) the sample has been restricted to a parameter space with high AGN activity. Therefore a large X-ray detected fraction is to be expected.

When split into subsamples it is found that the X-ray detected AGN are not distributed evenly. The highest X-ray detected fraction is seen in extended QGs (> 45%) and is consistent with the observations of Olsen et al. (2013) for QGs at similar redshifts. The extended SFGs have a much lower X-ray detected fraction. Thus it would appear that in extended galaxies the processes that fuel star formation do not also promote AGN accretion. The converse is true, however, of the compact galaxies. Star forming compact galaxies are detected at more than twice the rate of compact QGs. This reversal of the relationship between star-formation and AGN activity when splitting the galaxies by compactness indicates that the extended and compact galaxies have different triggering and/or fuelling mechanisms: in other words this effect represents evidence for two different accretion modes in massive galaxies at high redshift.

X-ray spectral analysis of the massive galaxies reveals more detail about the obscuration phenomenon. A much larger fraction of obscured AGN is found amongst the compact QGs and SFGs compared to the extended QGs and SFGs (99% significance from Fishers exact test; see Table 4.6 and Figure 4.5), verifying the HR analysis. There is also a higher incidence of Compton thick AGN amongst the compact galaxies. Compact galaxies also have much higher absorption corrected luminosities than the extended galaxies (see Figure 4.7), by a factor of at least 10 on average. The correlations between galaxy properties and AGN obscuration and X-ray luminosity found here represent clear evidence of a relationship between obscured AGN activity and host galaxy type.

Relatively few robust correlations between AGN and galaxy properties have been found in well-selected samples, especially when controlled for stellar mass (e.g. Xue et al. 2010; Bongiorno et al. 2012; Kocevski et al. 2012; Rosario et al. 2013a). What effects there are are relatively subtle, small, and are only revealed through analysis of large samples (e.g. Juneau et al. 2013; Rosario et al. 2013b; Trump et al. 2013). In this work, clear relationships have been found between a galaxy property (compactness, or alternatively surface mass density) and two AGN properties: luminosity and obscuration. The AGN in compact galaxies are very X-ray luminous; they are over an order of magnitude more luminous than those found in extended galaxies, and are around twice as likely to be obscured or Compton thick. These results clearly imply that there must be an evolutionary and/or causal connection between the black hole and its host galaxy. This is particularly interesting when considering the fact that the compact galaxy population is generally considered to be the progenitor of the extended galaxies. The connection with AGN obscuration may have especially important implications, considering that the obscuration is likely to be at galactic scale. Otherwise, it is difficult to see why this obscuration would be related to a large scale galaxy property (i.e. compactness).

### 4.5.2 Two modes of black hole accretion in massive galaxies

Splitting the sample according to compactness, there is strong evidence for two distinct modes of accretion within massive galaxies at $z \sim 2$. X-ray detected compact galaxies contain high luminosity, heavily obscured AGN with median $L_X \sim 6 \times 10^{43}$erg s$^{-1}$ and median N$_H = 3 \times 10^{23}$cm$^{-2}$. The X-ray detected extended galaxies on the other hand contain low luminosity, low column density AGN with median $L_X = 6 \times 10^{42}$erg s$^{-1}$. Sorting the extended galaxies by column density, the median object is classified as an unobscured AGN. All galaxies with $L_X > 10^{44}$erg s$^{-1}$ are classified as compact, $\sim 28\%$ of

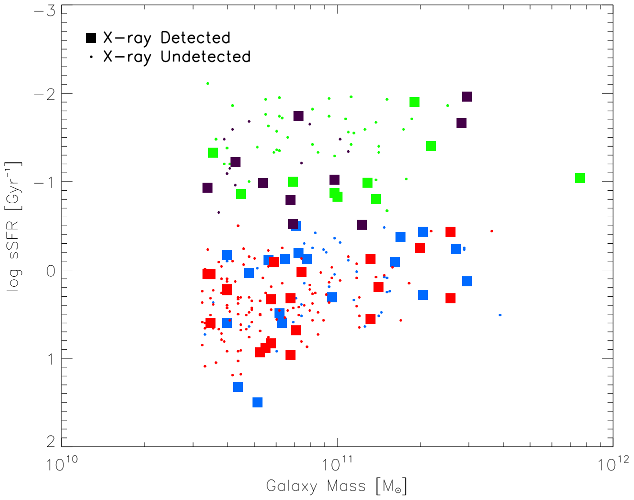

**Figure 4.8:** Plot of galaxy mass versus the sSFR, with X-ray detected sources highlighted.

all X-ray detected compact galaxies. Typically small area surveys such as the CDFS are not well suited to finding high luminosity AGN, thus such a strong concentration among the compact galaxies is striking. The luminosity at which AGN in this sample transition between the two modes of accretion (a few times $10^{43}$erg $s^{-1}$) is lower than what has been predicted by previous studies (e.g. Hopkins et al. 2006), fortuitously placing it within a range of luminosities that is well covered by this small area survey. The majority of the obscured AGN within both compact and extended galaxies are best fit by a spherical obscuration model (model B) as opposed to a toroidal obscuration model (model C). It could be that spherical obscuration is preferred as the obscuring material is distributed on a galaxy wide scale as opposed to being concentrated locally. This is quite plausible given the strong connection observed between black hole obscuration and the host galaxy properties. There is not sufficient information regarding the ratio of scattered emission to direct emission expected from the toroidal geometry, however, to draw a statistically robust conclusion on this hypothesis.

One possible explanation for the differing properties of AGN inhabiting compact and extended galaxies is that they are related to the host galaxy gas density. Compact galaxies are selected based on their high mass to size ratios (see Section 4.3.2), and it is plausible therefore that the nuclear regions of compact galaxies contain substantial amounts of gas. The effects of such a high concentration of gas surrounding the AGN could result in rapid fuelling, driving up the accretion rate and hence the X-ray luminosity. This may also lead to more severe obscuration. Extended galaxies are by definition less dense than compact galaxies and therefore the central regions of the host galaxy could be more diffuse. This provides a simple explanation for the observed difference between the X-ray properties of AGN in compact and extended galaxies.

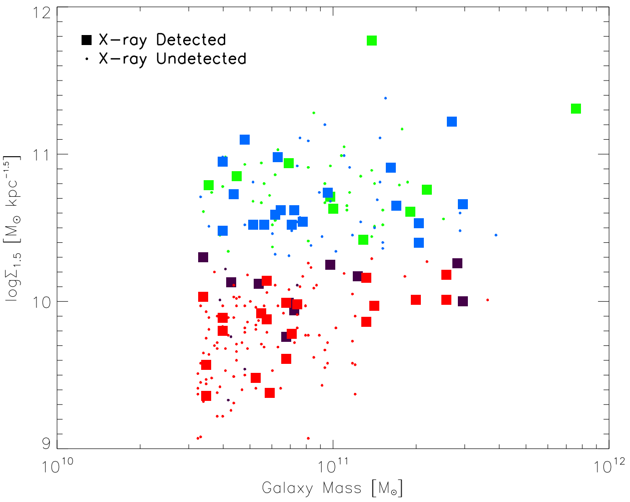

**Figure 4.9:** Plot of galaxy mass versus the compactness ($\Sigma_{1.5}$), with X-ray detected sources highlighted.

The two criteria used to select the various subsamples, sSFR and $\Sigma_{1.5}$, are both dependent on galaxy mass. Thus there is a risk that the trends in AGN properties observed across these subsamples are simply the product of a mass bias. Figures 4.8 and 4.9 demonstrate this is not the case, with X-ray detected and X-ray undetected galaxies across the various subsamples possessing similar mass distributions to one another.

The observation of two accretion modes - one luminous and heavily obscured - the other weak and unobscured, can also be linked immediately to theoretical ideas about the role of AGN feedback in the evolution of galaxies. The luminous obscured phase may be associated with the "quasar-mode" of e.g. Hopkins et al. (2006). This is a "transformative mode" of feedback, which shuts off star formation turning star-forming galaxies into quiescent ones. These observations are fully consistent with such an idea. There are powerful obscured AGN in both star-forming compact galaxies, and quiescent ones, showing that the AGN continues after quenching has occurred. On the other hand the incidence of AGN in quiescent galaxies is less consistent with the AGN shutting themselves down at some point during the feedback process. The shorter duty cycle of compact QGs suggests that they are a transitional population where an AGN in transformative mode has just quenched star formation within the host galaxy (see Figure 4.10). If this were not the case then higher star formation rates should be observable given that these galaxies are gas-rich, something that can be clearly inferred from the galaxy-scale X-ray absorption. Hopkins et al. (2006) also postulate that the quasar mode is triggered by a major merger, but there is no evidence to substantiate such a claim from the spectral fitting analysis of transformative mode AGN. This is consistent with the AGN host galaxy morphology study at $z \sim 2$ of Kocevski et al. (2012) which finds $\sim$ 80% of accretion is triggered through secular processes as opposed to major mergers. Schawinski et al. (2012) find a similar result for heavily obscured quasars at $z \sim 2$.

The less luminous and unobscured AGN seen in massive extended galaxies can be identified with the “radio mode” predicted by e.g. Croton et al. (2006) and Bower et al. (2006). This is a “maintenance mode”, preventing further star formation in galaxies which have already quenched, and grown most of their black holes presumably via the transformative mode discussed above. If these massive galaxies reside in hot gas haloes (e.g. in groups or clusters), gas should gradually cool and fall onto them, condensing to form stars (Kereš et al., 2005). If a small percentage of that gas trickles down and is accreted onto the black hole, the resulting low luminosity AGN can reheat the gas preventing further gas infall, star formation and, ultimately, accretion. The extended galaxies in the maintenance mode could thereby oscillate back and forth across the star forming and quiescent border (see Figure 4.10). The extended QGs seem to have a longer duty cycle (X-ray detected fraction of $> 45\%$) compared to their star-forming equivalents (15 %), and hence the suppression of star formation within these galaxies continues for an extended period.

As intimated above, the dominant fraction of black hole growth in massive galaxies appears to occur while the AGN are in the transformative mode and in the compact phase, rather than in the maintenance mode. While the two populations show similar X-ray detected fractions overall ($\sim 20$ %), black holes in compact galaxies are growing more than 10 times faster than their extended counterparts. More of this growth is concentrated in the star-forming compact galaxies rather than the quiescent ones. This is consistent with recent results examining the star-formation rates in X-ray selected AGN derived from *Herschel*, which show that they are more likely to occur in star-forming galaxies overall (Rosario et al., 2013b). The results presented in this work extend this, showing that this effect is present only for compact galaxies, whereas the opposite is true for extended ones at $z \sim 2$.

### 4.5.3 The impact of AGN feedback on massive galaxies at $z \sim 2$

The clear identification of two modes of black hole growth in massive galaxies at $z \sim 2$, and their consistency with the two major AGN feedback models, comes with the strong implication that the AGN are not only related to, but are influencing the galaxy properties and evolution.

There is strong evidence that the properties of the AGN are related to the host galaxy compactness, which is known to evolve substantially from high redshifts to the present day. Compact massive galaxies are not common in the local universe, and therefore the compact galaxies seen at high redshift are thought to be progenitors of their extended counterparts. Studying the variation of massive galaxy number densities over time, it appears that compact massive galaxies start evolving into extended massive galaxies at $z \sim 2$ (Barro et al., 2013), with minor mergers often being evoked as the mechanism (e.g. van Dokkum 2005; Bell et al. 2006; Trujillo et al. 2007). This result implies that, while

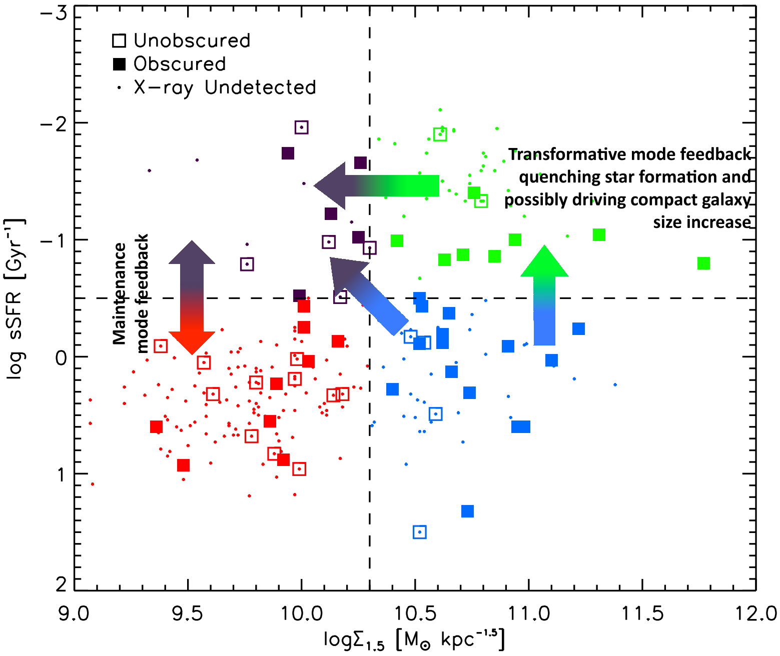

**Figure 4.10:** Plot of the galaxy compactness ($\Sigma_{1.5}$) versus the sSFR illustrating potential evolutionary tracks leading to the formation of extended quiescent galaxies. Extended QGs are purple, extended SFGs are red, compact QGs are green and compact SFGs are blue. Extended quiescent galaxies at $z \sim 2$ are thought to be the progenitors of massive early type galaxies in the local universe.

undergoing this size evolution, the compact galaxies must also be subject to processes which reduce both the accretion luminosity and the obscuration of the AGN.

Some of the size evolution may therefore be related to AGN feedback, especially at earlier times when the merger rate appears to be insufficient (Conselice, 2006; Newman et al., 2012). The AGN feedback model proposed by Fan et al. (2008) predicts that following the expulsion of matter from the central regions of the galaxy, the size will increase in order to restore virial equilibrium within the system. Once AGN feedback has swept out gas from the central regions of the galaxy, the remnant AGN is expected to become less obscured and less luminous. This is very similar to the transition in AGN properties observed when comparing compact galaxies to extended galaxies. Additionally the resultant galaxy should be quiescent, as the transformative mode first and foremost quenches star formation. Therefore compact galaxies with AGN in the transformative mode could directly form extended QGs following this form of AGN feedback (see Figure 4.10). Alternatively size evolution in compact galaxies may be driven by a form of positive feedback similar to that proposed by Ishibashi et al. (2013). In this case the AGN drives a shell of gas and dust from the central regions of the galaxy outwards which compresses pockets of gas within the host galaxy as it propagates outwards and triggers star formation. The stars that are formed will carry momentum from the passing shell of gas and dust and thus migrate towards the outer reaches of the host galaxy. This causes a buildup of new stars in the outskirts of the host galaxy, increasing its size. This size increase would be quite moderate. Therefore several episodes of Ishibashi et al. (2013) feedback would be necessary to turn a compact galaxy into an extended galaxy and the resultant extended galaxy would also be star forming.

The results of this study strongly imply that the AGN must quench star-formation before causing size evolution, as otherwise we would see luminous obscured AGN in extended star-forming galaxies, rather than compact quiescent ones. If it is assumed that the Ishibashi et al. (2013) feedback mechanism is occurring in transformative mode AGN then a much higher fraction of AGN activity among the extended SFG population would be expected. The highest fraction of AGN activity is observed among the extended QGs, while the extended SFGs possess the lowest X-ray detected fraction. Therefore it is concluded that the Fan et al. (2008) feedback model is the likeliest candidate for AGN driving size evolution in this massive galaxy sample. Speculating further, there are two paths a compact galaxy could follow to form an extended QG (see Figure 4.10). The simplest is that the transformative mode AGN rapidly quenches star formation and increases galaxy size to directly form an extended QG. Alternatively the galaxy may enter a transitional compact QG phase and increase in size more slowly before forming an extended QG.

### 4.5.4 Possible evidence for AGN accretion in X-ray undetected massive galaxies

By stacking the X-ray emission of X-ray undetected massive galaxies it is possible to gain insight into their behaviour outside of the "transformative" and "maintenance" accretion modes. Using this information one can speculate as to how these X-ray undetected galaxies are related to the X-ray detected population. Strong stacked signals are observed in the X-ray undetected SFGs but the X-ray undetected QGs produce weak stacked signals (see Table 4.7), a result that is consistent with previous observations of massive galaxies at $z \sim 2$ by Olsen et al. (2013).

The hard HR and high (for X-ray undetected sources) $L_{2-10keV}$ of X-ray undetected compact SFGs suggests the presence of AGN within this population, a significant fraction of which are heavily obscured. These obscured AGN are likely the progenitors of the heavily obscured, highly luminous AGN observed in X-ray detected compact SFGs preparing to enter the transformative mode. Like the X-ray undetected compact SFGs, the $L_{2-10keV}$ of X-ray undetected extended SFGs also suggests additional contributions from AGN. The HR of X-ray undetected extended SFGs, however, is lower than the HR of the X-ray undetected compact SFGs. This implies that the stacked emission from X-ray undetected extended SFGs is generated primarily by low luminosity unobscured AGN activity as opposed to heavily obscured AGN. These low luminosity unobscured AGN might be preparing to enter maintenance mode, with the gas that is fuelling star formation within the galaxy having just begun to trickle down and accrete onto the central AGN. The strong stacked signal of X-ray undetected SFGs obviously raises questions regarding the true AGN content of the extended SFG sample. This in turn might have implications regarding the proposed maintenance mode feedback that appears to be occurring in extended galaxies.

Neither of the X-ray undetected QG subsamples produces a statistically significant signal in the hard band when stacked. As such there is nothing to suggest the presence of obscured AGN activity in either of these populations. The $L_{0.5-2keV}$ of both populations do suggest a contribution from unobscured low luminosity AGN in addition to (very limited) star formation. In the case of X-ray undetected compact QGs these are likely the remnants of AGN that have left the transformative mode having exhausted their fuel supply and removed obscuring matter from the central regions of the host galaxy. For X-ray undetected extended QGs the emission could be from AGN that have just left either the transformative or maintenance modes, again having exhausted their supply of fuel.

It is difficult to robustly determine the precise nature of the stacked X-ray emission of massive galaxies, but it is possible to interpret them in the context of the two distinct accretion modes (transformative and maintenance) observed in the massive galaxy sample. The stacked emission of X-ray undetected compact SFGs and X-ray undetected extended SFGs is indicative of a high concentration low accretion rate AGN that have yet to enter the transformative and maintenance accretion modes respectively. Conversely the stacked emission of X-ray undetected compact QGs and X-ray undetected extended QGs is consistent with a much lower concentration of low accretion rate AGN that may be leaving the transformative and maintenance modes respectively. In fewer words, there is evidence to support AGN in the X-ray undetected SFGs that are switching on and AGN in the X-ray undetected QGs that are switching off.

## 4.6 Summary

In this chapter, the X-ray properties of massive ($M > 10^{10.5}$ $M_{\odot}$) compact and extended galaxies at $z \sim 2$ have been investigated using 4Ms CDFS observations, finding evidence for two modes of black hole accretion within these massive galaxies. Direct X-ray detections were established using a likelihood ratio matching technique and then subjected to spectral fitting analysis to obtain detailed information regarding their obscuration and X-ray luminosities. The main results are listed below:

(i) It is found that $22.0 \pm 2.5\%$ (59/268) of the massive galaxies possess X-ray counterparts. The luminosity limit of the observations for galaxies at these redshifts is such that almost all of the X-ray detections are due to AGN activity. When the sample is subdivided according to galaxy compactness and sSFR the extended QGs have the highest detection rate ($47.6 \pm 10.9\%$) of any of the subsamples. The high X-ray detection rate of extended QGs implies they have a long duty cycle and that AGN play a role in their evolution. The AGN in compact SFGs also appear to have a long duty cycle with significant amounts of cold gas available to fuel AGN, possibly the same cold gas as is fuelling the star formation. Conversely the extended SFGs have a much lower X-ray detected fraction ($14.3 \pm 3.0\%$) and thus although there is cold gas readily available for star formation the AGN are being starved of fuel. The compact QGs also have a low X-ray detection rate ($19.2 \pm 5.5\%$) which indicates they have a short duty cycle.

(ii) Through X-ray spectral analysis of X-ray detected massive galaxies evidence is found supporting two distinct modes of AGN accretion; a “transformative mode” where AGN are heavily obscured and luminous, and a “maintenance mode” in which the AGN are unobscured and less luminous. It appears that the dominant fraction of black hole growth occurs in AGN in the transformative mode as opposed to the maintenance mode.

(iii) The two AGN accretion modes are directly related to the compactness of the host galaxy, with dense compact galaxies hosting AGN in the transformative mode and more diffuse extended galaxies hosting AGN in the maintenance mode. The high density environment provided by compact galaxies means more gas is readily available to fuel AGN accretion within these galaxies. Conversely the central regions of extended galaxies would appear to be more diffuse, thus gas accretion occurs at a lower rate. The majority of obscured AGN are best fit by a spherical obscuration model (model B) which implies the AGN being primarily obscured by the host galaxy as opposed to a local dust torus (see Figure 4.5). This is consistent with the idea that the observed column density of an AGN is dependent upon the density of the host galaxy.

(iv) The transformative mode is similar to the "quasar mode" postulated by Hopkins et al. (2006), where a highly luminous, heavily obscured AGN quenches star-formation within the host galaxy through AGN feedback. The short duty cycle of X-ray detected compact QGs suggests they are a transitional population where the transformative mode AGN has just quenched star formation within the host galaxy. There is no evidence, however, supporting major mergers acting as trigger for transformative mode accretion.

(v) The maintenance mode is similar to "radio mode" feedback predicted by Croton et al. (2006) and Bower et al. (2006), where lower luminosity, unobscured AGN suppress star formation within their host galaxies by heating infalling gas. Extended galaxies containing AGN in the maintenance mode are thought to oscillate across the quiescent star forming boundary as infalling gas triggers star formation and AGN accretion. Accretion onto the AGN subsequently produces a gentle feedback which heats the gas and suppresses further star formation. The long duty cycle of extended QGs relative to the star forming SFGs suggests the suppression of star formation continues for extended periods.

(vi) The transformative mode could play a role in the size evolution of compact galaxies at $z \sim 2$, when the galaxy merger rate is insufficient (Conselice, 2006; Newman et al., 2012). Two possible methods from the literature have been considered to explain how an AGN in the transformative mode may produce feedback which drives the size evolution of the host galaxy. The first is the feedback model of Fan et al. (2008) in which the AGN drives gas from the central regions of the galaxy, rapidly quenching star formation. The expulsion of gas from the central regions forces the host galaxy to undergo size increase in order to restore virial equilibrium, creating an extended QG. The second is a feedback model proposed by Ishibashi et al. (2013) in which the AGN produces a positive feedback, promoting star formation in the outskirts of the host galaxy. The size of the galaxy increases as a result and after several such episodes an extended SFG would be formed. The remnant AGN of either feedback process are expected to posses a lower luminosity and obscuration than its predecessor. This transformation is consistent with the change in X-ray luminosity and obscuration properties of AGN in compact galaxies compared to those in extended galaxies. Assuming AGN do play a role in the size evolution of massive galaxies, the low fraction of AGN among extended SFG greatly disfavours the Ishibashi et al. (2013) feedback mechanism. Therefore the Fan et al. (2008)

feedback mechanism appears to be the most likely to be driving size evolution in this massive galaxy sample.

# Chapter 5

# The efficacy of optical emission line diagnostics for AGN at $0.3 \leq z \leq 0.8$

## Overview

The research presented in this chapter concerns an investigation into the accuracy with which the colour-excitation (CEx) and mass-excitation (MEx) optical emission line galaxy diagnostic techniques identify obscured AGN populations. Candidate AGN are selected using these techniques from a sample of 1367 galaxies with DEEP2 spectroscopy and $0.3 \leq z \leq 0.8$ in the 800ks EGS footprint. The accuracy with which these techniques select type 2 AGN relative to one another is measured using a combination of X-ray spectral fitting and X-ray stacking analyses. Both techniques select a high fraction of X-ray detected sources and the absorption corrected X-ray luminosities suggest that all these sources are AGN. The CEx selection technique identifies a high fraction of obscured AGN which is consistent with the obscured fraction of type 2 AGN observed in the local universe. The X-ray detected CEx SFGs on the other hand are primarily unobscured AGN with lower absorption corrected X-ray luminosities. The X-ray detected CEx SFGs appear to be AGN-SF composite galaxies. The MEx AGN selection identifies nearly all X-ray detected AGN but has a lower X-ray detected fraction and lower obscured AGN fraction than the CEx AGN subsample. Therefore it appears that the MEx AGN selection identifies numerous unobscured low luminosity AGN and possibly some SFGs in addition to obscured AGN. Stacking the X-ray undetected AGN reveals a hard signal with average stacked X-ray luminosities in excess of those expected from star formation. This is indicative of a large population of heavily obscured actively accreting AGN. The stacked signal of MEx AGN is softer which suggests that the fraction of obscured AGN in this sample is is less than in the CEx AGN. The CEx AGN selection appears to be superior to the MEx AGN selection when trying to specifically identify type 2 AGN. This is probably because unobscured AGN make galaxies appear bluer, biasing the CEx AGN selection against them. The galaxy mass is measured independently of the optical colour thus the same effect is not observed in the MEx AGN selection. Recalibrating the MEx AGN selection region should improve the accuracy with which it identifies type 2 AGN candidates. The [OIII] luminosity of X-ray undetected CEx and MEx AGN suggests that they are obscured as opposed to intrinsically less luminous than the X-ray detected CEx and MEx AGN. The T-ratio may also be used to identify heavily obscured AGN candidates but this technique is prone to contamination from SFGs.

## 5.1 Introduction

Tight relations have been observed between host galaxy bulge mass/velocity dispersion and SMBH mass (Magorrian et al., 1998; Ferrarese and Merritt, 2000; Gebhardt et al., 2000; McLure et al., 2006) which suggest there is a physical link between AGN and their host galaxies. To truly comprehend the extent of possible SMBH-galaxy co-evolution requires a complete census of AGN and their host galaxies throughout the universe. AGN are identified using their unique intrinsic properties; X-ray surveys have long proved fruitful in this endeavour because few phenomena can replicate the hard X-ray emission of AGN (Boyle et al., 1993; Brandt et al., 2001). Additionally X-rays suffer less attenuation due to obscuring gas than longer wavelength radiation allowing AGN to be detected through all but the highest column density obscurers ($N_H > 10^{24}\text{cm}^{-2}$). Deep X-ray observations can resolve the majority of AGN activity (Worsley et al., 2005), but heavily obscured and Compton thick AGN can be missed, as evidenced by the Hard X-ray background deficit (Comastri et al., 2005; Gilli et al., 2007). Thus efforts have been made to provide a more complete census of AGN using alternative techniques. Studying the ratio of high- and low-excitation emission lines is one such method.

Emission line ratio diagnostics were first presented by Baldwin et al. (1981). The aim of this research was to separate galaxies based on their different excitation mechanisms. This type of analysis is now referred to as “BPT” analysis in deference to the authors of the original paper. The work by Veilleux and Osterbrock (1987) further established this emission line diagnostic technique’s usefulness in identifying type 2 AGN. A type 2 AGN, according the *unified model* of AGN (Antonucci, 1993), is obscured by a local dust torus with an edge-on configuration, attenuating the broad line emission that is typically used to identify AGN at optical wavelengths. The presence of the dust torus in the line of sight to the AGN also means it is liable to attenuate X-ray emission if the column density is sufficiently high, lowering the X-ray detected fraction of type 2 AGN. Due to the configuration of the torus, however, the AGN is still capable of exciting gas clouds at larger scales triggering high-excitation narrow line emission such as [OIII] (Baldwin et al., 1981; Busko and Steiner, 1988). The BPT technique isolates these type 2 AGN by essentially comparing the strength of high-excitation line emission (e.g. [OIII]) to the strength of lower-excitation emission lines (e.g. H$\beta$). Sources which exhibit excess high-excitation emission line activity are likely to contain type 2 AGN. Adding a secondary emission line pairing as a proxy for metallicity (e.g. [NII] and H$\alpha$) improves the accuracy of this technique by separating galaxies that produce significant [OIII] line emission through star formation (low metallicity) from those which do not (high metallicity).

The BPT technique in principle allows obscured AGN populations that are often missed by other techniques to be identified. The redshift range of BPT selection is limited to $z < 0.4$ because longer wavelength emission lines (e.g. [NII] and H$\alpha$) leave the optical window. It is possible to detect these emission lines at higher redshifts using NIR spectroscopy, as was done by Trump et al. (2011, 2013), but this is expensive and NIR spectra are still of lower quality than optical spectra. An alternative route was taken by Weiner et al. (2007), replacing the redshift limiting [NII]/H$\alpha$ line pairing with H-band absolute magnitude measurements as these values are typically positively correlated. This "pseudo-BPT" analysis extends the effective redshift range to $z \leq 0.8$, isolating AGN in a similar manner to the original BPT technique. The H-band magnitude is only a crude proxy of the [NII]/H$\alpha$ ratio and produces a fairly coarse cut between SFG and AGN, with many AGN misclassified as SFG because their [OIII]/H$\beta$ ratios are scattered below the AGN boundary. The promise exhibited by this technique, however, inspired the development of more refined methods.

The colour-excitation (CEx) technique, pioneered by Yan et al. (2011), replaces the [NII]/H$\alpha$ ratio with the rest-frame $U - B$ colour. Yan et al. (2011) find the rest-frame $U - B$ colour correlates positively with both bulge mass and metallicity and thus is a suitable replacement for the [NII]/H$\alpha$ ratio. The CEx selection is empirically calibrated using BPT classified sources at low redshifts ($z \sim 0.01$) to split galaxies into AGN and star forming galaxies (SFG). The selection is then applied to galaxies at $0.3 \leq z \leq 0.8$ in the EGS field and matched to X-ray detected sources from the EGS 200ks survey (Laird et al., 2009). At higher redshifts, the CEx AGN exhibit a high X-ray detection rate and the majority of the X-ray detected sources are unambiguous AGN ($L_X > 10^{42}$erg s$^{-1}$). Comparison of the expected and detected fraction of X-ray sources suggests that the column densities of the CEx AGN are similar to those of type 2 AGN observed in the local universe. Consequently there are probably numerous heavily obscured and Compton thick AGN within the CEx AGN subsample that are producing some X-rays but lie below the detection threshold of the EGS 200ks survey. This technique is liable however to miss AGN in blue galaxies, as evidenced by the presence of X-ray detected AGN-SF composites in the CEx SFG sample.

The mass-excitation (MEx) technique, developed by Juneau et al. (2011) adopts a different tactic, replacing the [NII]/H$\alpha$ ratio with galaxy stellar mass. This approach hinges on the assumption that the stellar mass of a galaxy is correlated with the [NII]/H$\alpha$ ratio by the empirically derived mass-metallicity relation (e.g. Tremonti et al. 2004; Savaglio et al. 2005; Kewley and Ellison 2008). Similar to the CEx technique, the MEx technique is calibrated using low redshift optical sources ($z \sim 0.01$) in order to optimise the agreement with BPT AGN and SFG galaxy classifications and minimise contamination. The MEx technique also introduces a classification designed to target the BPT-transition galaxies. The MEx technique is then applied to data taken in the GOODS-N and EGS fields and matched to 2Ms and 200ks X-ray observations respectively. The MEx AGN and MEx transition galaxy regions identify the majority of unambiguous X-ray AGN ($L_X > 10^{42}$erg s$^{-}$1 or HR$> -0.1$) in the sample. The MEx transition galaxy region, in particular, appears to preferentially select AGN-SF composite galaxies that were simply classified as SFGs by the CEx technique. The stacked X-ray emission of X-ray undetected MEx AGN and transition galaxies possesses a hard, flat signal consistent with some of these galaxies possessing an actively accreting SMBH. Furthermore T-ratio analysis (Bassani et al., 1999) identifies 33 absorbed AGN candidates, of which 13 are not detected individually in the X-ray observations. Stacking the 13 X-ray undetected absorbed AGN candidates produces a hard signal, again consistent with accretion onto an SMBH.

The work presented in this chapter aims to investigate the efficiency with which the CEx and MEx AGN selection techniques identify obscured AGN within a sample of galaxies at $0.3 \leq z \leq 0.8$ that lie in the EGS 800ks footprint (Nandra et al. in prep). The obscured AGN activity within the MEx and CEx AGN subsamples is assessed using X-ray spectral fitting for X-ray detected galaxies and X-ray stacking for X-ray undetected galaxies. These are compared to the obscured AGN activity within SFGs, QGs and a control sample of X-ray detected galaxies from the EGS 800ks footprint that have not been covered by optical spectroscopic surveys. A comprehensive analysis of the similarities and differences of the CEx and MEx selection techniques is then undertaken. Finally the role of [OIII] luminosity as an intrinsic measure of the AGN X-ray luminosity is investigated. Throughout this chapter a standard, flat $\Lambda$CDM cosmology with $\Omega_\Lambda = 0.7$ and $H_0 = 70$ km s$^{-1}$ Mpc$^{-1}$ is assumed.

## 5.2 Data

### 5.2.1 Optical data

The optical data used in this chapter was originally presented in Yan et al. (2011). The majority of the optical spectroscopy was taken as part of the DEEP2 galaxy redshift survey using the DEIMOS spectrograph on the Keck-II telescope (Davis et al., 2003). The spectral range of these observations is approximately 6500-9200 Angstroms with a resolution of $R \sim 5000$. Follow-up observations were made for 498 X-ray sources from the EGS 200ks point source catalogue that had optical counterparts because they were missed in the original DEEP2 survey. These observations yielded 288 reliable redshifts for the X-ray sources; 265 galaxies. The rest-frame $U - B$ colours of the galaxies were derived from the spectra using the $K$-correction code of Willmer et al. (2006). The stellar mass estimates were taken from Bundy et al. (2006) where available. These were derived by

**Table 5.1:** Rest-frame band pass and sideband wavelengths used for emission line measurements, taken from Table 3 of Yan et al. (2006). Column (1): name of spectral line; column (2): limits of bandpass, units Angstroms; column (3): limits of sideband red-ward of bandpass, units Angstroms; column (4): limits of sidebands blue-wards of bandpass, units Angstroms.

| Spectral line (1) | Bandpass (2) | Blue Sideband (3) | Red Sideband (4) |
|---|---|---|---|
| H$\beta$ | $4857.45 - 4867.05$ | $4798.875 - 4838.875$ | $4885.625 - 4925.625$ |
| OIII | $4998.2 - 5018.2$ | $4978.2 - 4998.2$ | $5018.2 - 5038.2$ |
| H$\alpha$ | $6554.6 - 6574.6$ | $6483.0 - 6513.0$ | $6623.0 - 6653.0$ |
| NII | $6575.3 - 6595.3$ | $6483.0 - 6513.0$ | $6623.0 - 6653.0$ |

fitting the model SEDs to CFH12K BRI photometry and Palomar/WIRC $J$- and $K_S$-band photometry. For the remaining sources stellar mass estimates were calculated from their absolute $M_B$ magnitudes and rest-frame $B - V$ colour following the method of Bell et al. (2003). These estimates were calibrated to the Bundy et al. (2006) stellar mass scale using colour- and redshift- dependent corrections (Lin et al., 2007; Weiner et al., 2009).

Emission line measurements were made using the DEEP2 and MMT/Hectospec spectra by Yan et al. (2011) following the prescription of Yan et al. (2006), which is paraphrased here. First the wavelengths corresponding to the emission lines of interest are blocked and a model stellar continuum is subtracted from the spectrum. The model stellar continuum is a composite model, a linear combination of an old (7 Gyr) stellar population and a young (0.3 Gyr) stellar population. The spectra for both were generated using the stellar synthesis code of Bruzual and Charlot (2003) assuming solar metallicity and a Salpeter initial mass function (IMF). The equivalent width (EW) of an emission line is calculated by summing the emission line flux and dividing it by the median continuum level. In this work, the line flux is sampled from a predefined band pass while the median continuum is estimated from side-bands either side of the emission line. The band passes and side-bands used in this work (see Table 5.1) are taken from Yan et al. (2006).

Emission line luminosities are calculated for [OIII] and H$\beta$ emission where possible. The emission line fluxes are calibrated using photometry taken from the side-bands. Photometry for the side-bands around [OIII] and H$\beta$ are calculated from their rest-frame magnitudes. These rest-frame magnitudes were derived from the CFH12K photometry catalogue of Coil et al. (2004) using the *k-correct* code v4_1_4 of Blanton and Roweis (2007). This method circumvents the need for a spectrophotometric flux calibration (Weiner et al., 2007) and is more accurate than extracting the raw flux from the emission line band, which would require flux calibration and a correction for slit losses. The emission line luminosities are then computed from the calibrated fluxes. The uncertainty on the EW measurements were calculated following the methods of Balogh et al. (1999) and Yan et al. (2009). The EW uncertainties were propagated through to the luminosity calculations and combined with errors from the photometry and $K$-corrections. Throughout this chapter an emission line is classed as being detected if its EW is at least twice as large as the uncertainty on the measurement (ie SN $> 2\sigma$), unless explicitly stated otherwise. For sources that are classed as non-detections, the luminosity upper limits are taken to be twice the uncertainty on the measurement. The SFR of each galaxy was also estimated from the H$\beta$ line strength using the empirically derived relation of Moustakas et al. (2006).

### 5.2.2 X-ray data reduction

This work uses 800ks observations taken in the EGS with the *Chandra* ACIS-I instrument. The 800ks EGS images data was reduced by Elise Laird using the Imperial College X-ray reduction pipeline, a full description of which can be found in Section 2.2.1. A full description of the reduction of the EGS 800ks image data will be presented in Nandra et al. (in prep). The EGS 800ks survey has a smaller footprint than the EGS 200ks survey (Laird et al., 2009), thus only provides partial coverage for the original optical galaxy sample of Yan et al. (2011). The point source detection software identified 937 X-ray sources in the 800ks EGS images.

X-ray spectra were extracted from all 937 800ks EGS point sources by Murray Brightman, following the method outlined in Section 2.3.1. Additionally photometric and spectroscopic (where available) redshifts were assigned to 923 of the X-ray point sources in the 800ks EGS X-ray point source catalogue through likelihood ratio matching to optical sources by Mara Salvato. The photometric redshifts were calculated using the LePhare SED fitting codes (Ilbert et al., 2006, 2009) and incorporate AGN templates, in addition to standard galaxy templates, which are known to improve the accuracy of photometric redshifts for X-ray sources (Salvato et al., 2009, 2011).

## 5.3 Method

### 5.3.1 Optical sample selection

There are several criteria that an optical galaxy must satisfy to be included in the CEx and MEx analyses in this work. First and foremost, this analysis is restricted to galaxies within the 800ks EGS survey footprint. Also all galaxies must possess an absolute magnitude of $I < 22$. This ensures that the spectral continuum signal to noise ratio is adequate to accurately measure emission line strengths and that only sources with spectroscopic redshift success rate of $> 90\%$ are included in the analysis. All sources must have sufficient spectroscopic coverage around the [OIII] and $H\beta$ wavelengths to distinguish between detections and non-detections. Finally the CEx and MEx analyses used for the bulk of the paper (except Section 5.4) are restricted to galaxies with $0.3 \leq z \leq 0.8$. There are 1367 sources from the sample of Yan et al. (2011) that satisfy all these criteria.

**Table 5.2:** Sample sizes and X-ray detected fractions for galaxies subjected to CEx and MEx diagnostics. The QG sample is the same for both emission line diagnostics. The X-ray detected fractions have multinomial errors. Column (1): type of galaxy according to optical emission line diagnostic; column (2): number of galaxies in the sample; column (3): number of galaxies with X-ray associations according to LR matching; column (4): percentage of galaxies that are X-ray detected.

| Type<br>(1) | $N_{tot}$<br>(2) | $N_X$<br>(3) | $Frac_X$<br>(4) |
|---|---|---|---|
| All | 1367 | 71 | 5.2±0.6 |
| CEx AGN | 147 | 31 | 21.1±3.4 |
| CEx SFG | 808 | 21 | 2.6±0.6 |
| MEx AGN | 348 | 48 | 13.8±1.9 |
| MEx transition | 211 | 3 | 1.4±0.8 |
| MEx SFG | 307 | 1 | 0.33±0.33 |
| QG | 412 | 19 | 4.6±1.0 |

### 5.3.2 Identifying X-ray counterparts

A likelihood ratio (LR) matching technique was used to assign X-ray counterparts from the 800ks EGS to some of the optical sources identified in Section 5.3.1. The LR matching process was carried out by James Aird, with X-ray point sources matched to optical sources from the DEEP3 spectroscopic survey (Cooper et al., 2012). The LR matching yields 652 matches with LR$>0.5$, the LR which offers the greatest completeness while maintaining a reasonable false matching rate. The DEEP3 survey is an extension of the DEEP2 survey (Davis et al., 2003), therefore sources are matched to the Yan et al. (2011) using a nearest neighbour method with negligible false match probability. The DEEP2 redshifts from the Yan et al. (2011) optical galaxy sample are used in preference to the photometric redshifts assigned to X-ray sources in Section 5.2.2. The results of the LR matching are presented in Table 5.2.

### 5.3.3 X-ray spectral fitting

The spectral fitting method used in this work is described fully in Section 2.4. There are 4 spectral models used in this analysis; an unobscured power-law (model A), a spherical obscuration (model B), toroidal obscuration (model C) and reflection dominated spectrum (model D). A full description of these models can be found in Section 2.4.2. A description of the free and fixed parameters for these models is presented in Table 4.2. The optimum values of the $\Delta cstat$ threshold were calibrated for 800ks EGS data following the prescription in Section 2.4.3. The calibration of $\Delta cstat$ used three sources to characterise low, medium and high count spectra; aegis_524 (low counts, $<150$ counts), aegis_235 (medium counts, $150 \leq$ counts $<500$ counts) and aegis_575 (high counts, $\geq 500$ counts). The 99% confidence limits were used throughout this analysis (see Table 5.3). The results of the spectral fitting analysis presented have shown good agreement with spectral fitting carried

**Table 5.3:** The 99% threshold values of $\Delta cstat$ required to justify the inclusion of additional free parameters when selecting the best-fitting models using C-statistic in EGS 800ks data. Column (1): the pairing of models to which the threshold values correspond i.e. $\Delta cstat_{XY}$ is the value required to prefer model Y to model X; column (2): 99% certainty threshold for low count source; column (3): 99% certainty threshold for medium count source; column (4): 99% certainty threshold for high count source.

| Threshold (1) | $< 150$ counts (2) | $150 \leq$ counts $< 500$ (3) | $\geq 500$ counts (4) |
|---|---|---|---|
| $\Delta cstat_{AB}$ | 1.70 | 3.05 | 5.87 |
| $\Delta cstat_{AC}$ | 2.04 | 3.25 | 6.24 |
| $\Delta cstat_{AD}$ | 1.65 | 2.54 | 5.28 |
| $\Delta cstat_{BC}$ | 2.23 | 3.76 | 8.47 |
| $\Delta cstat_{DC}$ | 2.10 | 2.52 | 3.98 |

out by Murray Brightman.

## 5.4 Optical AGN emission line diagnostics

Before implementing the CEx and MEx diagnostics at $0.3 \leq z \leq 0.8$ they must be tested at lower redshifts to ensure that they are in agreement with the BPT diagnostic. To this end, a sample of 414 optical emission line galaxies with $0.2 \leq z \leq 0.4$ that lie within the EGS 800ks footprint are classified using the BPT technique. These sources are then plotted on CEx and MEx diagrams to check the completeness and accuracy of each classification, particularly the AGN selections. There are also 8 sources in the sample that have X-ray counterparts assigned by LR matching.

### 5.4.1 BPT selection

The BPT diagnostic derives its name from the seminal paper by Baldwin et al. (1981); the first time a self-consistent classification scheme was attempted using emission-line diagnostics. The aim of the work was to devise a method by which sources were classified based on their different excitation mechanisms. Emission line pairings were used to segregate a variety of sources from one another based on the relative strength of different excitation mechanisms occurring within them. Through this technique, Baldwin et al. (1981) were able to define boundary conditions for the line ratios that could distinguish between HII regions, power-law photoionisation and shock heating.

Veilleux and Osterbrock (1987) refined the earlier work of Baldwin et al. (1981) with the specific aim of segregating HII region emission from narrow line active galaxies (ie type 2 AGN). Several potential emission line pairings were earmarked for use in this technique due to their insensitivity to reddening. Throughout the emission line analyses presented in this chapter, the [OIII]/H$\beta$ and [NII]/H$\alpha$ line ratios have been used as they are the most commonly observed, thus yielding the largest possible samples. The [OIII]/H$\beta$ line

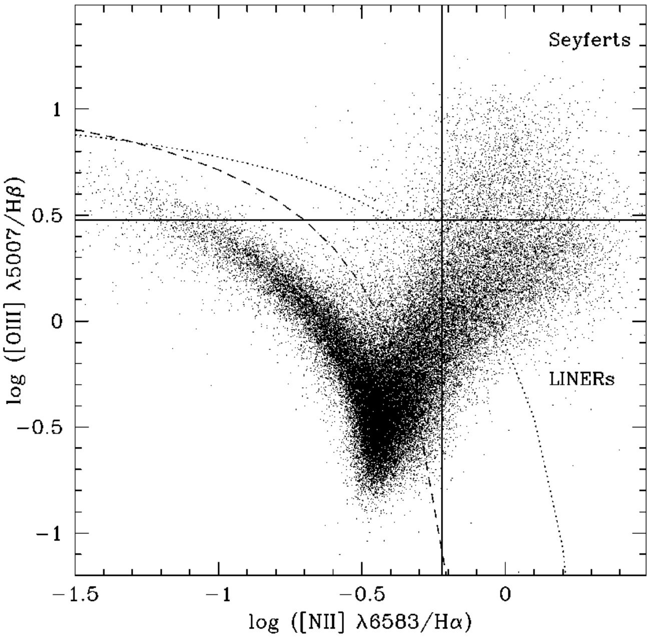

**Figure 5.1:** BPT diagram of SDSS galaxies with Kewley et al. (2001) (dotted line) and Kauffmann et al. (2003) (dashed line) AGN selection boundaries taken from Kauffmann et al. (2003; Figure 1). The solid horizontal and vertical lines, which denote regions designed to select Seyferts and LINERs, were empirically derived by Veilleux and Osterbrock (1987).

ratio is used to separate sources based on the intensity of ionisation processes. High values of [OIII]/H$\beta$ indicate a predominance of high-excitation ionisation processes typically attributed to either AGN or young, low metallicity stars. The [NII]/H$\alpha$ line ratio is an indicator of the gas-phase metallicity of the source (Kewley and Ellison, 2008). The higher the value of [NII]/H$\alpha$ the older and more metal-rich the galaxy is and the more likely it is that the galaxy will contain an AGN. Therefore AGN are expected to have high [OIII]/H$\beta$ and [NII]/H$\alpha$ line ratios, placing them in the upper right corner of the BPT diagram (see Figure 5.1).

The BPT selection method used in this work is identical to that used by Yan et al. (2011). The BPT diagram (Figure 5.2) is split into three regions using the empirically derived boundaries of Kewley et al. (2001) and Kauffmann et al. (2003); emission-line AGN in the upper-right, SFGs in the bottom-left and transition galaxies (composite AGN-SF galaxies) sandwiched between the two. The majority of BPT type diagrams split galaxies which do not exhibit strong SF indicators/high gas-phase metallicity into two populations; high-excitation ionisation Seyferts and LINERs. While the Seyferts were clearly AGN the composition of LINERs was debatable. Kewley et al. (2006) demonstrated that most (if not all) LINERs did in fact contain AGN, and that they formed a continuous sequence with the Seyfert galaxies. Therefore no distinction is made in this analysis between Seyfert galaxies and LINERS, they are both considered AGN in this scheme. Emission line AGN

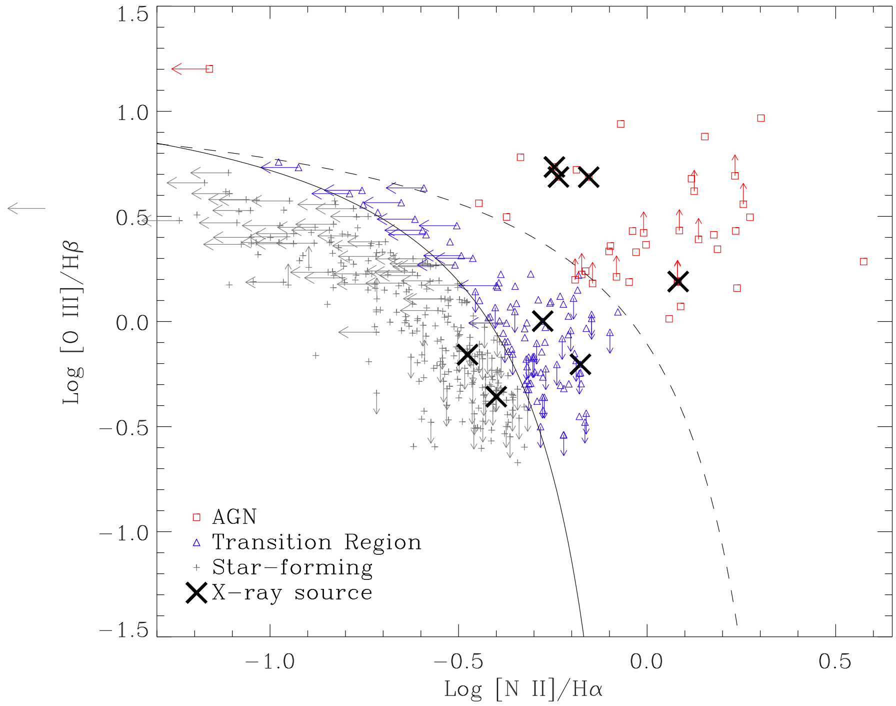

**Figure 5.2:** BPT diagram of optical sources in the EGS 800 ks footprint with $0.2 \leq z \leq 0.4$. All sources have statistically significant (S/N>2) H$\alpha$ line emission. A left facing arrow indicates sources where the [NII] line emission has been approximated with an upper limit (twice the error). An upwards arrow indicates sources where the [OIII] line emission has been approximated with an upper limit. A downward arrow indicates sources where the H$\beta$ line emission has been approximated with an upper limit. X-ray detected galaxies are indicated with a black cross. The solid black line denotes AGN classification boundary of Kauffmann et al. (2003) and the dashed black line denotes the extreme starburst boundary of Kewley et al. (2001).

are defined as galaxies that are above the Kewley et al. (2001) demarcation (dashed line in Figure 5.2; Equation 5.1) because it is considered the more conservative of the two selection boundaries. The Kauffmann et al. (2003) boundary (dotted line in Figure 5.2; Equation 5.2) offers greater completeness in AGN selection at the cost of greater contamination by transition and SF galaxies. Following this logic, galaxies lying below the Kauffmann et al. (2003) boundary are designated SFGs because there is minimal contamination from AGN in this region. The region between the Kewley et al. (2001) and Kauffmann et al. (2003) boundaries is referred to as the transition region, the galaxies within this region exhibit characteristics of both AGN and SF and are thought to be composite in nature.

$$log([OIII]/H\beta) > 0.61/[log[NII]/H\alpha) - 0.47] + 1.19 \tag{5.1}$$

$$log([OIII]/H\beta) > 0.61/[log[NII]/H\alpha) - 0.05] + 1.3 \tag{5.2}$$

All galaxies included in the BPT analysis are required to possess a H$\alpha$ line detection and must have been detected in a minimum of 3 of the emission lines. Sources that lack a detection in one of the emission lines are set to the upper limit for the emission line (twice the error on the measurement) and are denoted with an arrow on Figure 5.2. The BPT analysis yields 37 emission-line AGN, 102 transition galaxies and 275 SFG with 4, 2 and 2 X-ray detected sources in each subsample respectively.

### 5.4.2 Colour Excitation selection

The CEx diagnostic of Yan et al. (2011) replaces the longer wavelength emission line pairing of [NII]/H$\alpha$ with the (U-B) colour, pushing the limiting redshift of the analysis to $z \sim 0.8$. The (U-B) colour is deemed a suitable substitute for the [NII]/H$\alpha$ line ratio as it correlates positively with galaxy bulge mass and metallicity and is negatively correlated to the SFR. Emission-line AGN from the BPT diagram are most often found in either red galaxies or galaxies with colours between red and blue (ie green galaxies). These galaxies are often more massive and thus tend to host larger more luminous AGN (Magorrian et al., 1998; McLure et al., 2006), the latter assuming a constant Eddington ratio distribution across all masses (Aird et al., 2012). Thus using the (U-B) colour in concert with the [OIII]H$\beta$ line ratio it is possible to once again isolate emission-line AGN; expected to be in red galaxies with significant high-excitation ionisation. This selection technique is liable to miss blue galaxies containing AGN, but such sources are rare and usually produce sufficient high-excitation to push them beyond the CEx AGN boundary.

Yan et al. (2011) empirically derived the CEx AGN boundary using a large sample of low redshift optical emission-line galaxies from the SDSS that had been classified using BPT analysis.

$$log([OIII]/H\beta) > max\{1.4 - 1.2(U - B), -0.1\} \tag{5.3}$$

Unlike BPT analysis there is no transition galaxy region because it is not possible to define a distinct parameter space for the transition galaxies in (U-B) and [OIII]/H$\beta$ without catastrophic contamination from the BPT classified SFG and AGN populations (see Figure 2 of Yan et al. 2011). Thus galaxies are simply defined as either AGN or SFGs under the CEx classification scheme, with the majority of BPT transition galaxies lying within the SFG demarcation. Galaxies tend to possess bluer rest-frame colours at higher redshifts (Blanton, 2006) but the predicted shift in magnitude ($\sim$ 0.14 mag; Cooper et al. 2008; Yan et al. 2009) has a minimal impact on the CEx selection over the desired redshift range ($0.3 \leq z \leq 0.8$). Therefore no shift in magnitude has been applied to the CEx AGN demarcation in this analysis.

The sample of optical emission line galaxies classified in Section 5.4.1 have been plotted on a CEx diagnostic diagram (see Figure 5.3); 39 galaxies are defined as CEx AGN and the remaining 375 are CEx SFGs. The AGN has a high completeness (32/37 BPT classified AGN classified as CEx AGN; 86.4±5.6%) and a fairly low contamination rate (6/39 CEx AGN originally BPT transition galaxies; 15.4±5.8%). All the BPT classified

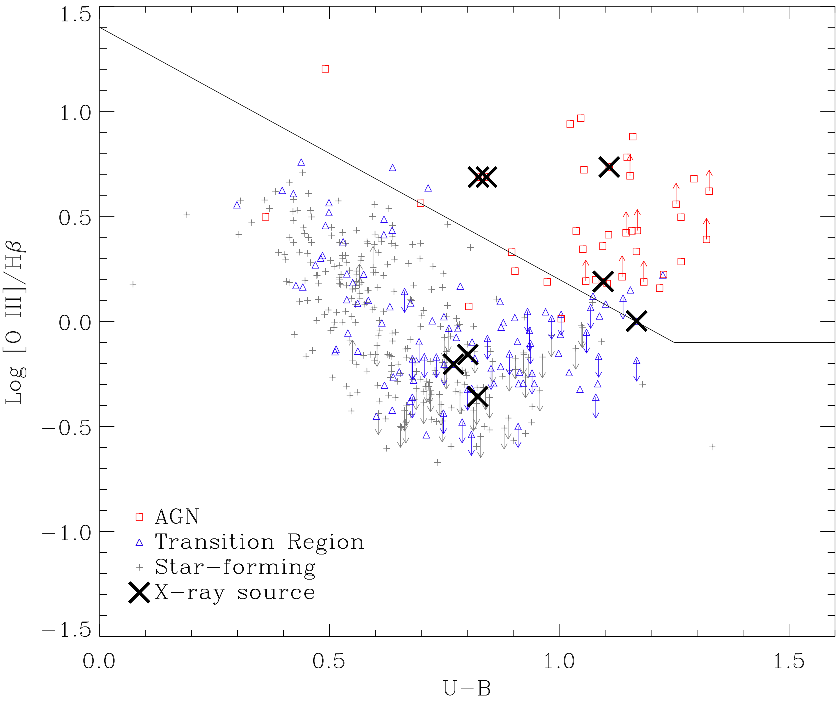

**Figure 5.3:** CEx selection (Yan et al., 2011) plot of optical emission line galaxies with $0.2 \leq z \leq 0.4$ in the EGS 800 ks footprint with BPT source classifications overlaid. All sources have statistically significant (S/N>2) H$\alpha$ line emission. An upwards arrow indicates sources where the [OIII] line emission has been approximated with an upper limit. A downward arrow indicates sources where the H$\beta$ line emission has been approximated with an upper limit. X-ray detected galaxies are indicated with a black cross. The solid black line denotes the empirically calibrated boundary of the CEx technique separating AGN (above) and star forming galaxies (below).

SFGs are also CEx SFGs, as are the majority of BPT transition galaxies. The severe contamination of the CEx SFG region by BPT classified transition galaxies is a concern, but optical classification of AGN is the main focus of this work. Of the 8 BPT classified galaxies with X-ray counterparts identified, 5 are classed as CEx AGN while the remaining 3 are classified as CEx SFGs.

### 5.4.3 Mass Excitation selection

The MEx selection technique of Juneau et al. (2011) substitutes stellar mass for the [NII]/H$\alpha$ line ratio, to push the maximum redshift of sources that can be analysed to $z \sim 0.8$. The empirically derived mass-metallicity relation (e.g. Tremonti et al. 2004; Savaglio et al. 2005; Kewley and Ellison 2008) implies there is a physical connection between the [NII]/H$\alpha$ line ratio and the stellar mass of a galaxy. Additionally, high mass galaxies almost invariably contain AGN (Kauffmann et al., 2003), although there is growing evidence that AGN may be just as prevalent in lower mass systems (Aird et al., 2012). Thus MEx AGN by definition have high masses and high [OIII]H$\beta$ line ratios.

The boundaries used to distinguish between AGN, transition galaxies and SFGs on the MEx diagram were empirically derived using a large sample of $z \sim 0.1$ galaxies from the SDSS, much like the CEx boundaries. Juneau et al. (2011) calibrate the boundaries such that the agreement with BPT classifications are optimised. The MEx analysis splits optical emission-line galaxies into 3 groups in an effort to mimic the classic BPT classification at higher redshifts; MEx AGN, MEx transition galaxies and MEx SFGs. These regions are defined using 2 curves. The region above the upper curve is designed to target optical AGN. The MEx AGN region is denoted by

$$y = 0.37/(x - 10.5) + 1. \tag{5.4}$$

if $x \leq 9.9$, and

$$y = 594.753 - 167.074x + 15.6748x^2 - 0.491215x^3 \tag{5.5}$$

otherwise, where $x$ is the stellar mass and $y$ is the [OIII]/H$\beta$ line ratio. A lower curve is used to distinguish between transition galaxy and SFG regions

$$y = 800.492 - 217.328x + 19.6431x^2 - 0.591349x^3 \tag{5.6}$$

for $9.9 < x < 11.2$, with transition galaxies lying above this curve but below the MEx AGN boundary. The SFGs having to lie below the MEx AGN and MEx transition galaxy boundaries.

The sample of optical emission-line galaxies that have $0.2 \leq z \leq 0.4$ have been plotted in Figure 5.4; there are 76 galaxies which have been classified as MEx AGN. The MEx AGN region has an even higher BPT classified AGN completeness than the CEx AGN region (35/37 AGN; 94.6±3.7%). There are, however, many more transition

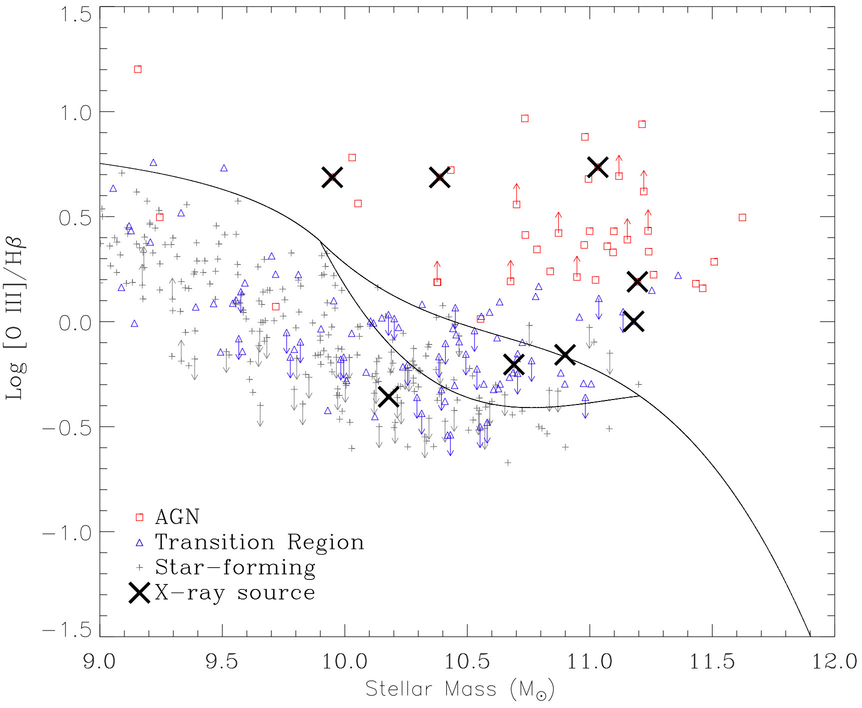

**Figure 5.4:** MEx selection (Juneau et al., 2011) plot of optical emission line galaxies with $0.2 \leq z \leq 0.4$ in the EGS 800 ks footprint with BPT source classifications overlaid. All sources have statistically significant (S/N>2) H$\alpha$ line emission. An upwards arrow indicates sources where the [OIII] line emission has been approximated with an upper limit. A downward arrow indicates sources where the H$\beta$ line emission has been approximated with an upper limit. X-ray detected galaxies are indicated with a black cross. The solid black lines separate MEx classified AGN (upper region), transition galaxies (central region) and SFGs (lower region).

(14) and SF (7) galaxy contaminants within the MEx AGN region (21/76; contaminant fraction 27.6±5.1%) than there are in the CEx AGN region. The majority of these non-AGN contaminants are just above the MEx transition galaxy region. There are 6 MEx AGN with X-ray counterparts compared to 1 MEx transition galaxy and 1 MEx SFG. The transition and SF galaxy regions have lower completeness and higher contamination (primarily by one another) than the MEx AGN region. Exploring the intricacies behind this cross-contamination is beyond the scope of this work.

## 5.5 Results

### 5.5.1 Direct X-ray detections

Optical sources subjected to the CEx and MEx diagnostics were assigned X-ray counterparts from the EGS 800ks survey X-ray point source catalogue (Nandra et al. in prep) using a likelihood ratio matching technique (see Section 5.3.2). The X-ray detected fractions of CEx and MEx AGN subsamples (21.2±3.4% and 13.8±1.9% respectively) are both higher than that of their parent sample (5.2±0.6%), a result that is significant at the $3\sigma$ level (see Table 5.2). The CEx SFG and MEx transition galaxy and MEx SFG X-ray subsamples have considerably lower X-ray detected fractions than the CEx AGN and MEx AGN, a result that is significant at the $> 5\sigma$ level. The QGs, which exhibit no [OIII] or H$\beta$ line emission, have a similar X-ray detected fraction (4.6±1.0%) to the parent sample within errors. Similar to Nandra et al. (2007a), the majority of the X-ray detected AGN possess $(\text{U-B})_0 > 0.6$. Additionally X-ray sources tend to reside in more massive galaxies (66/71 possess $\text{M}> 10^{10.5}\text{M}_\odot$), again consistent with observations from the literature (e.g. Brusa et al. 2009; Pimbblet and Jensen 2012).

The CEx AGN have a higher X-ray detected fraction than MEx AGN ($> 2\sigma$ significance). The CEx SFGs and MEx SFGs and transition galaxies have similar X-ray detected fractions, within errors. The 52 X-ray detected sources exhibiting [OIII] and/or H$\beta$ line emission are distributed more evenly between CEx AGNs and SFGs than MEx AGNs, transition galaxies and SFGs (see Figures 5.9 and 5.10 respectively). The CEx diagnostic identifies 59.6±6.8% (31/52) of X-ray detected sources as emission line AGN while 40.4±6.8% (21/52) are SFGs. The MEx diagnostic, on the other hand, identify nearly all the X-ray detected sources as emission line AGN (92.3±3.7%; 48/52). Only 4 X-ray detected sources are not classified as emission line AGN by the MEx diagnostic; 3 transition galaxies and 1 SFG.

**Table 5.4:** Results of X-ray spectral fitting of optical emission line galaxies with $0.3 \leq z \leq 0.8$ subjected to the CEx and MEx analyses. Column (1): Optical source ID from the DEEP2 catalogue; column (2): spectroscopic redshift from the DEEP2 catalogue; columns (3): CEx analysis classification; (4): MEx analysis classification; column (5): [OIII] luminosity, in units $10^{41}$ ergs s$^{-1}$; column (6): ID of X-ray counterpart source identified using LR matching; column (7): hardness ratio (HR) of the X-ray source, HR=(H-S)/(H+S) where H and S are the hard- (2.0-7.0 keV) and soft-band (0.5-2.0 keV) count rates respectively; column (8): spectral counts over 0.5-8.0 keV range; column (9): best fitting model for X-ray emission, for definitions see Section 5.3.3; column (10): column density of obscuring material in units $10^{22}$cm$^{-2}$; column (11): observed 2.0-10.0 keV luminosity in units $10^{41}$ ergs s$^{-1}$; column (12): absorption corrected 2.0-10.0 keV luminosity, corrected for X-ray absorption, in units $10^{41}$ ergs s$^{-1}$.

| Opt. ID (1) | $z$ (2) | CEx (3) | MEx (4) | $L_{[OIII]}$ (5) | XID (6) | HR (7) | cts (8) | Model (9) | N$_H$ (10) | $L_{abs}$ (11) | $L_{abscorr}$ (12) |
|---|---|---|---|---|---|---|---|---|---|---|---|
| 12012474 | 0.46 | AGN | AGN | 19.83 | aegis_055 | $-0.2^{+0.06}_{-0.06}$ | 329 | D | 1000.0 | $37.08^{+1.85}_{-2.06}$ | $226.33^{+11.27}_{-12.60}$ |
| 12016790 | 0.46 | SFG | TRANS | 11.22 | aegis_105 | $-0.39^{+0.33}_{-0.27}$ | 67 | A | - | $1.75^{+0.22}_{-0.26}$ | $1.75^{+0.22}_{-0.26}$ |
| 12016316 | 0.72 | AGN | AGN | 10.25 | aegis_107 | $0.80^{+0.04}_{-0.04}$ | 244 | B | $18.56 \pm 0.96$ | $111.22^{+6.98}_{-6.62}$ | $293.31^{+18.41}_{-17.46}$ |
| 12016544 | 0.68 | SFG | TRANS | 2.1 | aegis_169 | $0.14^{+0.24}_{-0.20}$ | 36 | A | - | $4.01^{+0.54}_{-0.51}$ | $4.01^{+0.54}_{-0.51}$ |
| 12016752 | 0.72 | QG | QG | 47.04 | aegis_173 | $0.73^{+0.08}_{-0.08}$ | 165 | B | $14.41 \pm 2.00$ | $78.3^{+8.27}_{-6.73}$ | $179.86^{+18.99}_{-15.45}$ |
| 12016714 | 0.42 | SFG | AGN | 0.45 | aegis_183 | $-0.18^{+0.07}_{-0.07}$ | 245 | B | $0.25 \pm 0.11$ | $18.21^{+1.37}_{-1.91}$ | $18.70^{+1.40}_{-1.96}$ |
| 12019630 | 0.55 | AGN | AGN | 2.87 | aegis_184 | $0.20^{+0.16}_{-0.15}$ | 85 | B | $4.06 \pm 0.93$ | $17.12^{+2.38}_{-2.44}$ | $24.19^{+3.36}_{-3.45}$ |
| 12021407 | 0.59 | AGN | AGN | 9.16 | aegis_208 | $-0.14^{+0.15}_{-0.14}$ | 100 | A | - | $17.45^{+1.27}_{-1.37}$ | $17.45^{+1.27}_{-1.37}$ |
| 12021115 | 0.72 | AGN | AGN | 20.2 | aegis_211 | $-0.27^{+0.03}_{-0.03}$ | 859 | B | $0.53 \pm 0.09$ | $241.14^{+9.26}_{-12.04}$ | $254.84^{+9.79}_{-12.72}$ |
| 12019616 | 0.58 | AGN | AGN | 6.14 | aegis_215 | $0.76^{+0.19}_{-0.09}$ | 221 | B | $72.03 \pm 4.18$ | $23.0^{+0.95}_{-1.38}$ | $226.54^{+9.36}_{-13.59}$ |
| 12020035 | 0.55 | SFG | AGN | 4.31 | aegis_227 | $0.63^{+0.17}_{-0.13}$ | 36 | C | $19.92 \pm 4.91$ | $10.77^{+2.10}_{-2.43}$ | $27.35^{+5.33}_{-6.16}$ |
| 12019189 | 0.55 | AGN | AGN | 9.89 | aegis_236 | $0.63^{+0.06}_{-0.06}$ | 415 | B | $8.63 \pm 0.40$ | $110.94^{+4.76}_{-6.34}$ | $201.72^{+8.66}_{-11.53}$ |
| 12019648 | 0.68 | QG | QG | 15.0 | aegis_253 | $-0.30^{+0.27}_{-0.20}$ | 220 | B | $1.38 \pm 0.15$ | $13.63^{+0.71}_{-0.65}$ | $15.64^{+0.81}_{-0.75}$ |
| 12019829 | 0.57 | QG | QG | 0.66 | aegis_255 | $0.53^{+0.26}_{-0.18}$ | 25 | D | 1000.0 | $5.32^{+1.78}_{-1.38}$ | $75.28^{+25.15}_{-19.52}$ |
| 12019136 | 0.73 | AGN | AGN | 45.76 | aegis_261 | $-0.33^{+0.03}_{-0.04}$ | 955 | D | 10.0 | $238.04^{+6.06}_{-7.14}$ | $769.89^{+19.6}_{-23.09}$ |

*Continued on next page*

Table 5.4 – *Continued from previous page*

| Opt. ID<br>(1) | $z$<br>(2) | CEx<br>(3) | MEx<br>(4) | $L_{[OIII]}$<br>(5) | XID<br>(6) | HR<br>(7) | cts<br>(8) | Model<br>(9) | N$_H$<br>(10) | $L_{abs}$<br>(11) | $L_{abscorr}$<br>(12) |
|---|---|---|---|---|---|---|---|---|---|---|---|
| 12020704 | 0.54 | SFG | AGN | 12.12 | aegis_264 | $-0.60^{+0.14}_{-0.36}$ | 15 | A | - | $1.3^{+0.37}_{-0.36}$ | $1.3^{+0.37}_{-0.36}$ |
| 12025302 | 0.46 | AGN | AGN | 11.64 | aegis_294 | $0.49^{+0.01}_{-0.01}$ | 3995 | B | $4.83 \pm 0.09$ | $827.49^{+16.61}_{-15.09}$ | $1228.4^{+24.66}_{-22.40}$ |
| 12024913 | 0.76 | SFG | TRANS | 5.12 | aegis_302 | $-0.35^{+0.13}_{-0.15}$ | 85 | A | - | $19.18^{+2.47}_{-1.98}$ | $19.18^{+2.47}_{-1.98}$ |
| 12024309 | 0.64 | SFG | AGN | 4.33 | aegis_310 | $-0.52^{+0.09}_{-0.08}$ | 297 | A | - | $30.02^{+1.82}_{-0.98}$ | $30.02^{+1.82}_{-0.98}$ |
| 12025262 | 0.74 | AGN | AGN | 45.01 | aegis_346 | $0.64^{+0.04}_{-0.04}$ | 503 | B | $11.20 \pm 0.71$ | $275.09^{+13.31}_{-11.79}$ | $559.07^{+27.05}_{-23.96}$ |
| 12027983 | 0.45 | SFG | SFG | 13.33 | aegis_407 | $-0.56^{+0.20}_{-0.25}$ | 24 | A | - | $1.87^{+0.33}_{-0.50}$ | $1.87^{+0.33}_{-0.50}$ |
| 13004761 | 0.55 | SFG | AGN | 4.81 | aegis_427 | $-0.17^{+0.32}_{-0.26}$ | 37 | D | 1000.0 | $5.11^{+1.02}_{-0.93}$ | $45.36^{+9.09}_{-8.29}$ |
| 13003433 | 0.48 | SFG | AGN | 2.02 | aegis_430 | $-0.59^{+0.13}_{-0.40}$ | 24 | A | - | $1.44^{+0.27}_{-0.24}$ | $1.44^{+0.27}_{-0.24}$ |
| 13003867 | 0.44 | QG | QG | 0.39 | aegis_432 | $0.62^{+0.18}_{-0.12}$ | 29 | D | 1000.0 | $6.54^{+1.2}_{-1.1}$ | $97.19^{+17.82}_{-16.32}$ |
| 13004312 | 0.35 | AGN | AGN | 0.97 | aegis_444 | $-0.48^{+0.20}_{-0.23}$ | 23 | A | - | $0.8^{+0.12}_{-0.18}$ | $0.8^{+0.12}_{-0.18}$ |
| 13011817 | 0.66 | AGN | AGN | 63.74 | aegis_492 | $0.29^{+0.04}_{-0.05}$ | 472 | C | $4.26 \pm 0.44$ | $185.1^{+11.00}_{-7.70}$ | $258.34^{+15.35}_{-10.75}$ |
| 13011701 | 0.74 | SFG | AGN | 5.58 | aegis_496 | $-0.43^{+0.05}_{-0.05}$ | 347 | A | - | $100.14^{+5.56}_{-5.05}$ | $100.14^{+5.56}_{-5.05}$ |
| 13011693 | 0.76 | SFG | AGN | 89.55 | aegis_507 | $-0.39^{+0.29}_{-0.34}$ | 16 | A | - | $3.63^{+1.00}_{-1.17}$ | $3.63^{+1.00}_{-1.17}$ |
| 13012387 | 0.35 | AGN | AGN | 1.3 | aegis_524 | $0.53^{+0.11}_{-0.08}$ | 145 | C | $6.93 \pm 1.04$ | $13.08^{+0.94}_{-1.34}$ | $20.77^{+1.50}_{-2.12}$ |
| 13012268 | 0.68 | AGN | AGN | 31.23 | aegis_526 | $-0.24^{+0.07}_{-0.06}$ | 265 | B | $0.80 \pm 0.17$ | $67.96^{+4.65}_{-3.90}$ | $73.78^{+5.04}_{-4.24}$ |
| 13011062 | 0.37 | QG | QG | 0.5 | aegis_535 | $-0.59^{+0.14}_{-0.39}$ | 18 | A | - | $0.5^{+0.14}_{-0.21}$ | $0.5^{+0.14}_{-0.21}$ |
| 13009690 | 0.54 | AGN | AGN | 6.63 | aegis_539 | $0.86^{+0.05}_{-0.05}$ | 340 | C | $39.62 \pm 1.66$ | $80.49^{+4.38}_{-3.48}$ | $379.52^{+20.64}_{-16.42}$ |
| 13011778 | 0.45 | AGN | AGN | 14.32 | aegis_540 | $0.41^{+0.23}_{-0.18}$ | 29 | C | $225.12 \pm 147.40$ | $5.4^{+1.67}_{-1.38}$ | $344.11^{+106.34}_{-88.09}$ |
| 13010503 | 0.46 | AGN | AGN | 0.45 | aegis_556 | $-0.37^{+0.17}_{-0.15}$ | 133 | A | - | $6.03^{+0.32}_{-0.28}$ | $6.03^{+0.32}_{-0.28}$ |
| 13019868 | 0.54 | AGN | AGN | 34.86 | aegis_567 | $0.28^{+0.19}_{-0.16}$ | 52 | D | 1000.0 | $9.85^{+1.5}_{-2.19}$ | $122.8^{+18.67}_{-27.24}$ |
| 13019982 | 0.78 | SFG | AGN | 10.72 | aegis_568 | $-0.34^{+0.35}_{-0.37}$ | 34 | A | - | $4.7^{+0.88}_{-0.68}$ | $4.7^{+0.88}_{-0.68}$ |
| 13018292 | 0.37 | SFG | AGN | 2.63 | aegis_570 | $0.05^{+0.34}_{-0.21}$ | 65 | A | - | $0.84^{+0.08}_{-0.06}$ | $0.84^{+0.08}_{-0.06}$ |

*Continued on next page*

Table 5.4 – *Continued from previous page*

| Opt. ID<br>(1) | $z$<br>(2) | CEx<br>(3) | MEx<br>(4) | $L_{[OIII]}$<br>(5) | XID<br>(6) | HR<br>(7) | cts<br>(8) | Model<br>(9) | N$_H$<br>(10) | $L_{abs}$<br>(11) | $L_{abscorr}$<br>(12) |
|---|---|---|---|---|---|---|---|---|---|---|---|
| 13018061 | 0.58 | AGN | AGN | 18.87 | aegis_575 | $-0.34^{+0.03}_{-0.04}$ | 992 | B | $0.29 \pm 0.07$ | $146.31^{+4.89}_{-3.21}$ | $150.73^{+5.04}_{-3.31}$ |
| 13101998 | 0.75 | AGN | AGN | 36.52 | aegis_599 | $-0.27^{+0.04}_{-0.04}$ | 821 | D | 10.0 | $148.64^{+6.76}_{-5.14}$ | $601.61^{+27.36}_{-20.80}$ |
| 13019950 | 0.77 | AGN | AGN | 88.4 | aegis_602 | $0.33^{+0.32}_{-0.21}$ | 89 | D | 1000.0 | $17.12^{+1.06}_{-0.83}$ | $250.86^{+15.58}_{-12.12}$ |
| 13019240 | 0.75 | AGN | AGN | 2.72 | aegis_618 | $0.49^{+0.06}_{-0.07}$ | 221 | B | $8.30 \pm 0.72$ | $110.21^{+8.29}_{-8.81}$ | $197.35^{+14.84}_{-15.78}$ |
| 13018239 | 0.75 | QG | QG | 1.81 | aegis_624 | $0.10^{+0.29}_{-0.19}$ | 52 | A | - | $6.24^{+0.53}_{-0.60}$ | $6.24^{+0.53}_{-0.60}$ |
| 13017287 | 0.64 | AGN | AGN | 6.67 | aegis_627 | $0.94^{+0.06}_{-0.01}$ | 111 | B | $36.73 \pm 4.99$ | $61.02^{+5.09}_{-6.16}$ | $266.55^{+22.23}_{-26.91}$ |
| 13018003 | 0.37 | SFG | AGN | 0.06 | aegis_633 | $0.04^{+0.28}_{-0.23}$ | 34 | A | - | $0.74^{+0.11}_{-0.14}$ | $0.74^{+0.11}_{-0.14}$ |
| 13017587 | 0.77 | SFG | AGN | 1.1 | aegis_634 | $0.11^{+0.25}_{-0.20}$ | 48 | B | $2.38 \pm 0.98$ | $9.72^{+1.08}_{-1.37}$ | $12.15^{+1.34}_{-1.71}$ |
| 13026227 | 0.46 | SFG | AGN | 0.26 | aegis_641 | $-0.18^{+0.27}_{-0.22}$ | 38 | A | - | $2.39^{+0.44}_{-0.38}$ | $2.39^{+0.44}_{-0.38}$ |
| 13027442 | 0.77 | QG | QG | 3.17 | aegis_651 | $-0.34^{+0.10}_{-0.11}$ | 202 | A | - | $26.45^{+1.46}_{-1.24}$ | $26.45^{+1.46}_{-1.24}$ |
| 13025417 | 0.75 | AGN | AGN | 5.48 | aegis_652 | $-0.39^{+0.09}_{-0.10}$ | 130 | A | - | $33.25^{+3.55}_{-2.34}$ | $33.25^{+3.55}_{-2.34}$ |
| 13026216 | 0.74 | QG | QG | 3.54 | aegis_655 | $-0.63^{+0.13}_{-0.34}$ | 15 | A | - | $2.74^{+0.77}_{-0.81}$ | $2.74^{+0.77}_{-0.81}$ |
| 13025514 | 0.57 | QG | QG | 0.99 | aegis_667 | $-0.45^{+0.21}_{-0.22}$ | 32 | A | - | $3.69^{+0.69}_{-0.66}$ | $3.69^{+0.69}_{-0.66}$ |
| 13025494 | 0.74 | AGN | AGN | 4.86 | aegis_688 | $0.03^{+0.15}_{-0.12}$ | 78 | B | $2.99 \pm 0.76$ | $29.53^{+3.48}_{-3.40}$ | $38.71^{+4.56}_{-4.46}$ |
| 13026185 | 0.63 | QG | QG | 0.45 | aegis_689 | $-0.33^{+0.10}_{-0.11}$ | 86 | A | - | $16.49^{+1.46}_{-2.07}$ | $16.49^{+1.46}_{-2.07}$ |
| 13025485 | 0.74 | SFG | AGN | 1.53 | aegis_698 | $-0.15^{+0.25}_{-0.23}$ | 53 | A | - | $8.82^{+1.21}_{-1.33}$ | $8.82^{+1.21}_{-1.33}$ |
| 13028098 | 0.45 | QG | QG | 2.08 | aegis_700 | $-0.24^{+0.04}_{-0.05}$ | 669 | D | 10.0 | $46.76^{+2.39}_{-1.86}$ | $181.11^{+9.24}_{-7.19}$ |
| 13025437 | 0.71 | AGN | AGN | 39.29 | aegis_704 | $0.54^{+0.22}_{-0.15}$ | 21 | D | 1000.0 | $9.07^{+2.5}_{-2.34}$ | $129.63^{+35.78}_{-33.46}$ |
| 13102012 | 0.75 | QG | QG | 4.84 | aegis_735 | $0.55^{+0.16}_{-0.13}$ | 49 | B | $7.17 \pm 1.91$ | $20.09^{+3.27}_{-3.67}$ | $34.01^{+5.53}_{-6.22}$ |
| 13032511 | 0.74 | SFG | AGN | 6.33 | aegis_740 | $-0.41^{+0.27}_{-0.23}$ | 158 | A | - | $15.67^{+0.99}_{-1.15}$ | $15.67^{+0.99}_{-1.15}$ |
| 13035250 | 0.74 | AGN | AGN | 14.64 | aegis_745 | $-0.22^{+0.10}_{-0.10}$ | 112 | B | $1.33 \pm 0.41$ | $37.85^{+4.74}_{-4.10}$ | $43.18^{+5.40}_{-4.68}$ |
| 13035323 | 0.75 | AGN | AGN | 6.02 | aegis_757 | $0.39^{+0.21}_{-0.17}$ | 37 | B | $6.85 \pm 2.26$ | $14.72^{+3.19}_{-2.91}$ | $24.5^{+5.30}_{-4.85}$ |

*Continued on next page*

Table 5.4 – *Continued from previous page*

| Opt. ID (1) | $z$ (2) | CEx (3) | MEx (4) | $L_{[OIII]}$ (5) | XID (6) | HR (7) | cts (8) | Model (9) | N$_H$ (10) | $L_{abs}$ (11) | $L_{abscorr}$ (12) |
|---|---|---|---|---|---|---|---|---|---|---|---|
| 13034447 | 0.75 | QG | QG | 1.34 | aegis_768 | $-0.10^{+0.17}_{-0.17}$ | 33 | A | - | $8.64^{+1.33}_{-1.80}$ | $8.64^{+1.33}_{-1.80}$ |
| 13035995 | 0.51 | AGN | AGN | 1.52 | aegis_782 | $-0.37^{+0.19}_{-0.15}$ | 132 | A | - | $7.53^{+0.57}_{-0.29}$ | $7.53^{+0.57}_{-0.29}$ |
| 13034616 | 0.69 | QG | QG | 1.75 | aegis_789 | $-0.52^{+0.22}_{-0.33}$ | 13 | A | - | $3.13^{+0.80}_{-1.24}$ | $3.13^{+0.80}_{-1.24}$ |
| 13033215 | 0.74 | QG | QG | 7.35 | aegis_796 | $0.00^{+0.13}_{-0.11}$ | 155 | B | $2.60 \pm 0.42$ | $42.93^{+3.25}_{-2.84}$ | $54.54^{+4.13}_{-3.61}$ |
| 13033928 | 0.48 | SFG | AGN | 0.97 | aegis_800 | $-0.3^{+0.27}_{-0.24}$ | 38 | A | - | $2.19^{+0.27}_{-0.39}$ | $2.19^{+0.27}_{-0.39}$ |
| 13033804 | 0.74 | QG | QG | 1.52 | aegis_802 | $-0.2^{+0.32}_{-0.27}$ | 30 | A | - | $3.9^{+0.64}_{-1.00}$ | $3.9^{+0.64}_{-1.00}$ |
| 13033925 | 0.42 | SFG | AGN | 13.53 | aegis_808 | $-0.46^{+0.21}_{-0.18}$ | 41 | A | - | $2.33^{+0.29}_{-0.45}$ | $2.33^{+0.29}_{-0.45}$ |
| 13035954 | 0.61 | AGN | AGN | 4.62 | aegis_830 | $-0.37^{+0.06}_{-0.06}$ | 357 | D | 10.0 | $63.27^{+2.66}_{-3.21}$ | $193.89^{+8.15}_{-9.83}$ |
| 13033890 | 0.72 | QG | QG | 0.95 | aegis_844 | $0.00^{+0.22}_{-0.19}$ | 45 | A | - | $8.13^{+1.24}_{-1.11}$ | $8.13^{+1.24}_{-1.11}$ |
| 13042341 | 0.43 | QG | QG | 0.18 | aegis_880 | $-0.13^{+0.33}_{-0.22}$ | 54 | A | - | $2.07^{+0.24}_{-0.28}$ | $2.07^{+0.24}_{-0.28}$ |
| 13043031 | 0.76 | QG | QG | 1.94 | aegis_885 | $-0.42^{+0.24}_{-0.21}$ | 69 | A | - | $12.32^{+1.22}_{-1.06}$ | $12.32^{+1.22}_{-1.06}$ |
| 13050479 | 0.69 | AGN | AGN | 35.68 | aegis_916 | $0.56^{+0.09}_{-0.08}$ | 202 | C | $10.42 \pm 1.82$ | $123.27^{+10.23}_{-11.97}$ | $233.83^{+19.41}_{-22.71}$ |

**Table 5.5:** Obscured and Compton thick fractions for each subsample. Column (1): emission line diagnostic classification; column (2): number of X-ray sources LR matched to optical counterparts; column (3): number of galaxies with signatures of obscured emission; column (4): percentage of galaxies with obscured emission (ie best fit by models C, D or E), with binomial error; column (5): number of galaxies exhibiting Compton thick emission; column (6): percentage of galaxies exhibiting Compton thick emission.

| Type<br>(1) | $N_{src}$<br>(2) | $N_{obs}$<br>(3) | $F_{obs}$<br>(4) | $N_{CT}$<br>(5) | $F_{CT}$<br>(6) |
|---|---|---|---|---|---|
| All | 71 | 37 | 52.1±5.9 | 7 | 9.9±3.5 |
| CEx AGN | 31 | 26 | 83.9±6.6 | 4 | 12.9±6.0 |
| CEx SFG | 21 | 4 | 19.0±8.6 | 1 | 4.8±4.7 |
| MEx AGN | 48 | 30 | 62.5±7.0 | 5 | 10.4±4.4 |
| MEx transition | 3 | 0 | 0.0±0.0 | 0 | 0.0±0.0 |
| MEx SFG | 1 | 0 | 0.0±0.0 | 0 | 0.0±0.0 |
| QG | 19 | 7 | 36.8±11.1 | 2 | 10.5±7.0 |
| Control | 133 | 71 | 53.4±4.3 | 11 | 8.3±2.4 |

### 5.5.2 X-ray spectral fitting analysis

X-ray spectral fitting analysis was carried out on the 71 X-ray detected sources that possess optical spectroscopy (see Section 5.3.3) to study the sources of X-ray emission in greater detail. In particular, spectral fitting provides estimates for the obscuring column densities, configuration of obscuring material and the X-ray luminosity (absorbed and absorption corrected) of each source. To briefly summarise, model A corresponds to an unobscured power-law emission (fixed $\Gamma = 1.9$), while models B, C and D mimic obscured power-law emission with different configurations of obscuring matter (examples can be found in Section 2.4.2). All but 4 of the X-ray detected sources best fit by model D have R-values high enough to conclude that they are Compton thick AGN (ie R-value > 14, reflected component ~7 times stronger than transmitted; assigned $N_H \sim 10^{25}\mathrm{cm}^{-2}$). The 4 sources (aegis_261, aegis_599, aegis_700 and aegis_830) which do not satisfy this criterion, while not Compton thick, are still reflection dominated and likely moderately obscured. Hence these sources are thought to possess $N_H \sim 10^{23}\mathrm{cm}^{-2}$. All the redshifts of these sources have been taken from the work of Yan et al. (2011) and have been measured using optical spectroscopy. The 71 X-ray detected sources all possess X-ray luminosities that exceed their predicted SFRs (computed from H$\beta$ line strength using the empirical relations of (Moustakas et al., 2006)) according to the relation of Ranalli et al. (2003) (see Figure 5.5). Therefore, all of these X-ray sources are thought to contain AGN.

The obscured and Compton thick AGN fractions of the parent sample and subsamples are given in Table 5.5. Approximately 50% (37/71) of the X-ray detected sources in the parent sample are classified as obscured AGN, while ~ 10% (7/71) are thought to be Compton thick AGN. The best fitting model and column density distributions of CEx diagnostic galaxies and QGs is visually represented by Figures 5.6 and 5.7 respectively.

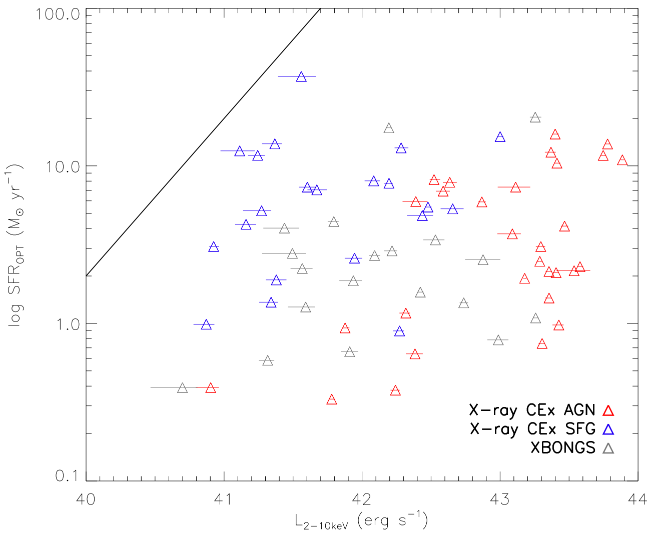

**Figure 5.5:** Plot of absorption corrected X-ray luminosity of X-ray detected galaxies ($0.3 \leq z \leq 0.8$) which have been classified using the CEx diagnostics versus the SFR predicted from the H$\beta$ luminosity. Red triangles represent emission line AGN, blue triangles are SFGs and grey triangles are QGs. The solid black line indicates the $L_{2-10keV}$ predicted from the SFRs using the empirically derived relationship of Ranalli et al. (2003).

Similar plots have not been made for the MEx diagnostic because there are too few MEx transition galaxies (aegis_105, aegis_169 and aegis_302) and SFGs (aegis_407) to provide useful information regarding their column density distributions. Focusing on just the galaxies with obscured X-ray spectra, the spherically distributed obscurer (model B) is clearly the most favoured (20/37; $54.1 \pm 8.2\%$) while a toroidally distributed obscurer (model C) is the least (6/37; $16.2 \pm 6.1$). It is difficult to comment on the distribution of obscuring matter in model D due to the severity of the obscuration (relative to the source strength).

The overwhelming majority of obscured AGN within this sample are identified as CEx AGN ($70.3 \pm 7.5\%$). In fact the CEx AGN subsample has the highest obscured AGN fraction of any subsample, a result that is significant at the $> 3\sigma$ level (see Table 5.5). The CEx SFGs have a much lower obscured AGN fraction than the CEx AGN and the QGs. There are very few Compton thick AGN among the X-ray detected sample, therefore the statistics associated with these sources are less robust. As a result, although 4/7 Compton thick AGN are classified as CEx AGN, the Compton thick fractions of the CEx subsamples and QGs are consistent within errors.

As stated previously, when the MEx diagnostic is used almost all of the X-ray detected sources not classified as QGs are designated MEx AGN. Consequently the obscured AGN fraction of this subsample is lower than that of the CEx AGN ($\sim 3\sigma$ significance). The Compton thick AGN fractions of CEx and MEx AGN, however, are consistent within errors. There are no obscured or Compton thick AGN among the MEx SFGs and MEx

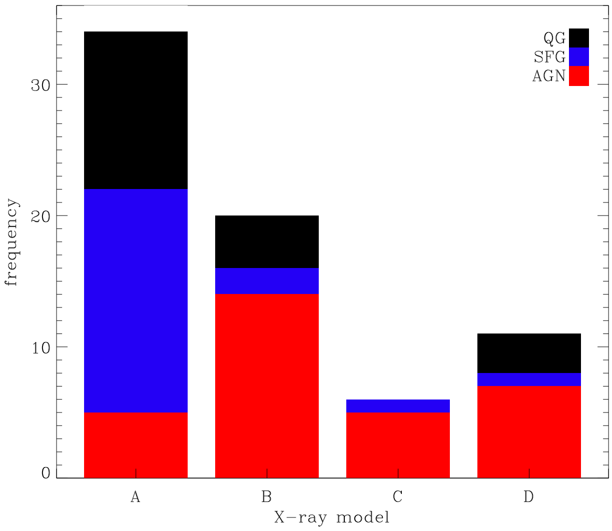

**Figure 5.6:** Bar chart illustrating the distribution of best-fitting X-ray models across the $0.3 \leq z \leq 0.8$ emission line galaxy sample. The CEx galaxy subsamples and QGs have been highlighted.

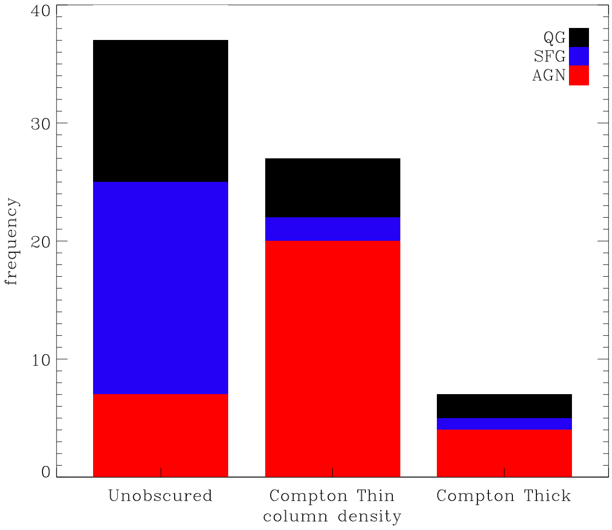

**Figure 5.7:** Bar chart illustrating the distribution of best-fitting X-ray models across the $0.3 \leq z \leq 0.8$ emission line galaxy sample. The CEx galaxy subsamples and QGs have been highlighted. The unobscured bin consists of galaxies whose X-ray spectra are best fit by Model A. The Compton thin bin contains obscured AGN with $N_H < 10^{24}cm^{-2}$ while the Compton thick bin contains galaxies with $N_H \geq 10^{24}cm^{-2}$.

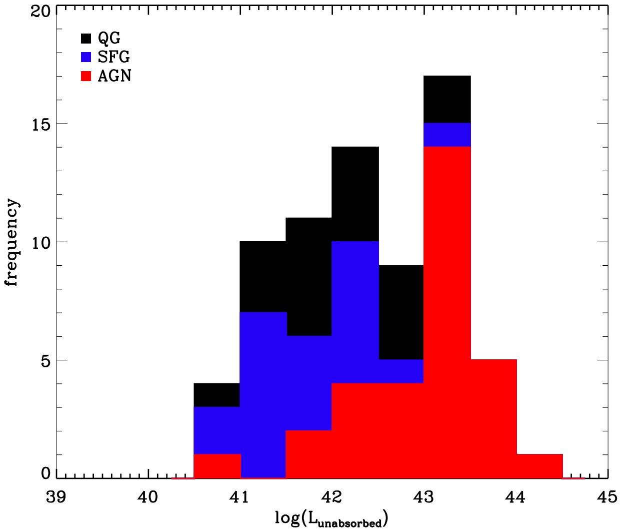

**Figure 5.8:** Histogram of absorption corrected X-ray luminosities for the $0.3 \leq z \leq 0.8$ emission line galaxy sample. The CEx galaxy subsamples and QGs have been highlighted.

transition galaxies, although the X-ray detected population among these subsamples is too small to consider this a statistically significant result.

Using the column densities obtained by spectral fitting analysis it is possible to calculate the absorption corrected 2-10 keV luminosities for X-ray detected sources by following the method outlined in Section 2.4.5. The absorption corrected luminosity distribution of CEx diagnostic galaxies and QGs is presented in Figure 5.8. Again a similar plot has not been made for MEx diagnostic galaxies as there are so few X-ray detected MEx transition galaxies and MEx SFGs. The median absorption corrected X-ray luminosity of the 71 X-ray detected galaxies is $2.45 \times 10^{42}$erg s$^{-1}$. The CEx AGN have higher average absorption corrected X-ray luminosities (median $L_X = 1.97 \times 10^{43}$erg s$^{-1}$) than the CEx SFGs (median $L_X = 4.01 \times 10^{41}$erg s$^{-1}$). A K-S test of the absorption corrected X-ray luminosities indicates it is highly unlikely that the CEx AGN and SFGs could have been derived from the same parent distribution (null hypothesis $6.7 \times 10^{-6}$). The QGs have a similar absorption-corrected X-ray luminosity distribution to the CEx SFGs and possess a median $L_X = 1.23 \times 10^{42}$erg s$^{-1}$. The X-ray detected MEx AGN have a much wider spread in absorption corrected X-ray luminosities because the majority of the X-ray detected galaxies that are not classified as QGs (48/52) have been identified. The median absorption-corrected luminosity of MEx AGN is $L_X = 4.32 \times 10^{42}$ erg s$^{-1}$, similar to that of the full sample (as expected). The 3 X-ray detected MEx transition galaxies possess $L_X = 1.75 \times 10^{41}$, $4.01 \times 10^{41}$ and $1.92 \times 10^{42}$ erg s$^{-1}$. The solitary X-ray detected MEx SFG possesses $L_X = 1.87 \times 10^{41}$ erg s$^{-1}$.

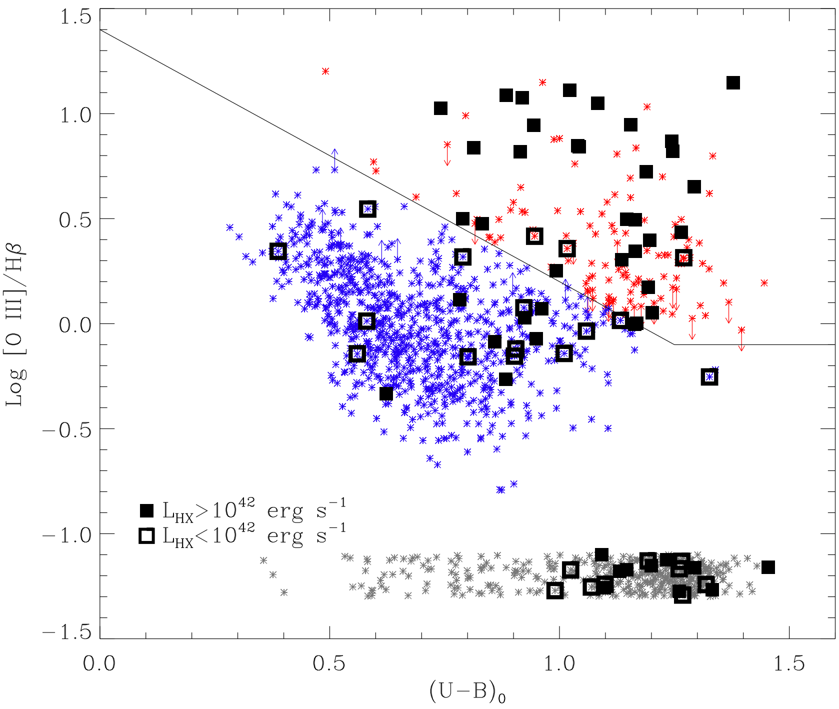

**Figure 5.9:** Colour Excitation diagnostic plot (Yan et al., 2011) of $(U\text{-}B)_0$ versus $\log_{10}$ [OIII]/H$\beta$ for galaxies within the EGS 800 ks footprint. Red crosses represent emission line AGN, blue crosses are SFGs and the grey crosses are QGs with no optical emission lines. An upwards arrow highlights sources for which $\log_{10}$ [OIII]/H$\beta$ is a lower limit (ie no [OIII] detected) whereas a downwards arrow is used when $\log_{10}$ [OIII]/H$\beta$ is an upper limit (ie no H$\beta$ detection). X-ray detections sorted according to X-ray luminosity have been overlaid. The solid black line denotes the boundary between emission line AGN and SFGs.

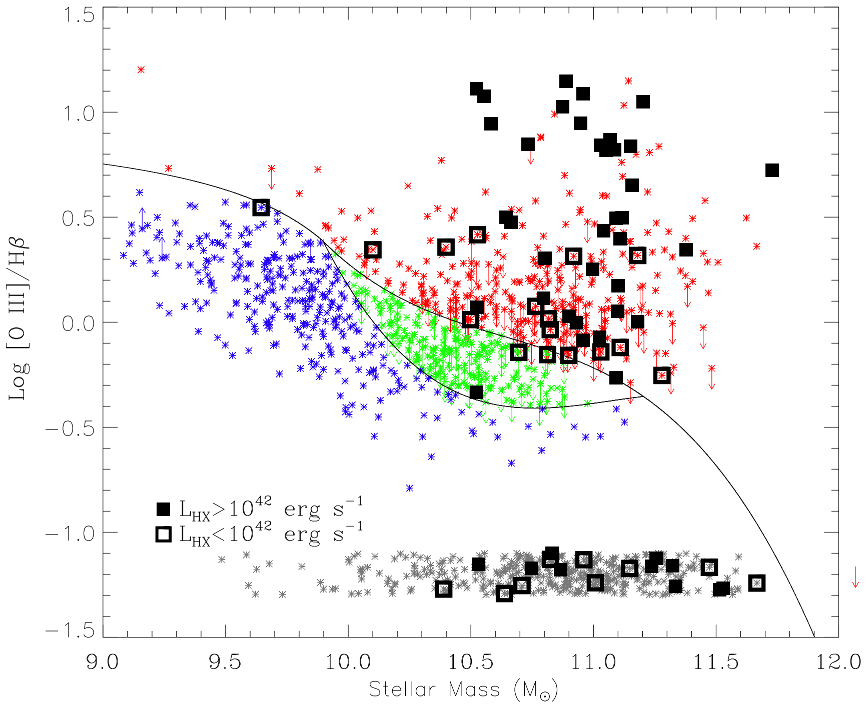

**Figure 5.10:** MEx diagnostic plot (Juneau et al., 2011) for galaxies within the EGS 800ks footprint. Red crosses represent emission line AGN, green crosses are AGN-SF transition galaxies, blue crosses are SFGs and the grey crosses are QGs with no optical emission lines. An upwards arrow highlights sources for which $\log_{10}$ [OIII]/H$\beta$ is a lower limit (ie no [OIII] detected) whereas a downwards arrow is used when $\log_{10}$ [OIII]/H$\beta$ is an upper limit (ie no H$\beta$ detection). X-ray detections sorted according to X-ray luminosity have been overlaid. The upper solid black line denotes the boundary between emission line AGN and other galaxies while the lower solid black line separates AGN-SF transition galaxies and SFGs.

**Table 5.6:** Results of X-ray spectral fitting of the control sample of X-ray detected galaxies with $0.3 \leq z \leq 0.8$. Column (1): ID of X-ray source; column (2): redshift of X-ray source according to LR matching of Mara Savato; column (3): hardness ratio (HR) of the X-ray source, HR=(H-S)/(H+S) where H and S are the hard- (2.0-7.0 keV) and soft-band (0.5-2.0 keV) count rates respectively; column (4): spectral counts over 0.5-8.0 keV range; column (5): best fitting model for X-ray emission, for definitions see Section 5.3.3; column (6): column density of obscuring material in units $10^{22}\mathrm{cm}^{-2}$; column (7): observed 2.0-10.0 keV luminosity in units $10^{41}$ ergs $\mathrm{s}^{-1}$; column (8): absorption corrected 2.0-10.0 keV luminosity, corrected for X-ray absorption, in units $10^{41}$ ergs $\mathrm{s}^{-1}$.

| XID<br>(1) | $z$<br>(2) | HR<br>(3) | cts<br>(4) | Model<br>(5) | $N_H$<br>(6) | $L_{abs}$<br>(7) | $L_{abscorr}$<br>(8) |
|---|---|---|---|---|---|---|---|
| aegis_009 | 0.76 | 0.45 | 146 | B | $8.05 \pm 0.55$ | $70.37^{+3.92}_{-3.88}$ | $124.52^{+6.94}_{-6.87}$ |
| aegis_014 | 0.37 | 0.08 | 128 | A | - | $13.64^{+1.35}_{-1.21}$ | $13.64^{+1.35}_{-1.21}$ |
| aegis_016 | 0.5 | -0.76 | 195 | A | - | $10.21^{+0.43}_{-0.56}$ | $10.21^{+0.43}_{-0.56}$ |
| aegis_026 | 0.48 | -0.5 | 322 | A | - | $42.7^{+1.74}_{-2.25}$ | $42.7^{+1.74}_{-2.25}$ |
| aegis_036 | 0.48 | -0.29 | 655 | B | $0.42 \pm 0.07$ | $230.91^{+11.69}_{-14.31}$ | $241.11^{+12.21}_{-14.94}$ |
| aegis_049 | 0.66 | -0.16 | 175 | B | $0.81 \pm 0.25$ | $25.29^{+2.03}_{-1.99}$ | $27.48^{+2.20}_{-2.16}$ |
| aegis_052 | 0.59 | -0.15 | 409 | B | $0.95 \pm 0.15$ | $60.81^{+4.19}_{-3.72}$ | $66.97^{+4.61}_{-4.10}$ |
| aegis_058 | 0.48 | -0.5 | 752 | A | - | $79.93^{+2.88}_{-3.66}$ | $79.93^{+2.88}_{-3.66}$ |
| aegis_059 | 0.68 | 0.69 | 233 | C | $13.14 \pm 1.41$ | $109.24^{+7.76}_{-6.94}$ | $236.73^{+16.82}_{-15.04}$ |
| aegis_062 | 0.76 | -0.46 | 333 | A | - | $148.04^{+7.26}_{-8.14}$ | $148.04^{+7.26}_{-8.14}$ |
| aegis_064 | 0.58 | -0.85 | 66 | A | - | $5.1^{+0.52}_{-0.58}$ | $5.1^{+0.52}_{-0.58}$ |
| aegis_071 | 0.58 | -0.77 | 155 | A | - | $15.31^{+1.29}_{-1.42}$ | $15.31^{+1.29}_{-1.42}$ |
| aegis_081 | 0.44 | -0.28 | 49 | A | - | $1.41^{+0.17}_{-0.18}$ | $1.41^{+0.17}_{-0.18}$ |
| aegis_086 | 0.55 | 0.04 | 479 | B | $1.80 \pm 0.18$ | $69.34^{+2.77}_{-3.73}$ | $82.43^{+3.29}_{-4.43}$ |
| aegis_092 | 0.48 | -0.46 | 144 | A | - | $9.97^{+0.77}_{-0.87}$ | $9.97^{+0.77}_{-0.87}$ |
| aegis_102 | 0.56 | 0.3 | 101 | B | $6.50 \pm 0.38$ | $12.93^{+0.94}_{-0.73}$ | $21.13^{+1.54}_{-1.19}$ |
| aegis_110 | 0.46 | 0.72 | 95 | D | 1000.0 | $17.73^{+2.29}_{-2.41}$ | $264.22^{+34.19}_{-35.86}$ |
| aegis_115 | 0.42 | 0.16 | 38 | B | $3.34 \pm 1.09$ | $3.24^{+0.48}_{-0.43}$ | $4.35^{+0.64}_{-0.58}$ |
| aegis_122 | 0.68 | -0.12 | 35 | A | - | $3.13^{+0.51}_{-0.42}$ | $3.13^{+0.51}_{-0.42}$ |
| aegis_130 | 0.66 | -0.34 | 316 | D | 10.0 | $5.04^{+0.35}_{-0.28}$ | $19.36^{+1.34}_{-1.07}$ |
| aegis_139 | 0.71 | 0.75 | 77 | B | $18.13 \pm 1.49$ | $23.87^{+1.91}_{-2.37}$ | $62.09^{+4.97}_{-6.16}$ |
| aegis_145 | 0.58 | -0.28 | 368 | B | $0.26 \pm 0.10$ | $42.83^{+3.24}_{-2.53}$ | $44.02^{+3.33}_{-2.60}$ |
| aegis_149 | 0.57 | -0.35 | 52 | A | - | $2.33^{+0.26}_{-0.22}$ | $2.33^{+0.26}_{-0.22}$ |
| aegis_151 | 0.45 | -0.28 | 225 | B | $0.44 \pm 0.13$ | $14.79^{+1.23}_{-1.29}$ | $15.48^{+1.28}_{-1.35}$ |
| aegis_156 | 0.61 | -0.05 | 212 | A | - | $10.71^{+0.74}_{-0.44}$ | $10.71^{+0.74}_{-0.44}$ |
| aegis_159 | 0.64 | -0.5 | 82 | A | - | $195.98^{+28.92}_{-26.98}$ | $195.98^{+28.92}_{-26.98}$ |
| aegis_164 | 0.55 | 0.18 | 173 | B | $2.10 \pm 0.25$ | $26.37^{+1.96}_{-1.28}$ | $32.21^{+2.39}_{-1.57}$ |
| aegis_170 | 0.61 | 0.57 | 35 | C | $142.72 \pm 54.23$ | $10.62^{+1.81}_{-2.56}$ | $301.72^{+51.56}_{-72.82}$ |

*Continued on next page*

Table 5.6 – *Continued from previous page*

| XID<br>(1) | $z$<br>(2) | HR<br>(3) | cts<br>(4) | Model<br>(5) | N$_H$<br>(6) | L$_{abs}$<br>(7) | L$_{abscorr}$<br>(8) |
|---|---|---|---|---|---|---|---|
| aegis_176 | 0.72 | -0.25 | 89 | A | - | $5.9^{+0.47}_{-0.59}$ | $5.9^{+0.47}_{-0.59}$ |
| aegis_190 | 0.55 | -0.06 | 551 | B | $1.65 \pm 0.14$ | $79.13^{+3.31}_{-2.75}$ | $92.94^{+2.89}_{-3.23}$ |
| aegis_196 | 0.71 | -0.7 | 57 | A | - | $7.04^{+0.72}_{-0.67}$ | $7.04^{+0.72}_{-0.67}$ |
| aegis_201 | 0.72 | 0.55 | 65 | B | $52.00 \pm 5.84$ | $20.08^{+2.64}_{-3.03}$ | $126.61^{+16.70}_{-19.11}$ |
| aegis_204 | 0.61 | 0.75 | 13 | C | $158.13 \pm 169.09$ | $3.13^{+0.87}_{-0.79}$ | $110.4^{+30.70}_{-27.74}$ |
| aegis_207 | 0.74 | -0.29 | 59 | A | - | $10.22^{+0.99}_{-1.07}$ | $10.22^{+0.99}_{-1.07}$ |
| aegis_220 | 0.71 | -0.3 | 445 | A | - | $39.62^{+1.32}_{-1.38}$ | $39.62^{+1.32}_{-1.38}$ |
| aegis_240 | 0.57 | -0.65 | 47 | A | - | $6.40^{+1.03}_{-0.74}$ | $6.40^{+1.03}_{-0.74}$ |
| aegis_241 | 0.79 | -0.71 | 14 | A | - | $2.58^{+1.19}_{-0.88}$ | $2.58^{+1.19}_{-0.88}$ |
| aegis_248 | 0.49 | -0.27 | 398 | B | $0.35 \pm 0.04$ | $26.44^{+1.10}_{-0.97}$ | $27.44^{+1.14}_{-1.01}$ |
| aegis_250 | 0.59 | -0.69 | 233 | A | - | $33.26^{+2.19}_{-2.52}$ | $33.26^{+2.19}_{-2.52}$ |
| aegis_257 | 0.73 | 0.31 | 163 | B | $2.51 \pm 0.26$ | $10.85^{+0.62}_{-0.50}$ | $13.69^{+0.78}_{-0.63}$ |
| aegis_259 | 0.41 | -0.37 | 73 | C | $198.97 \pm 122.325$ | $6.87^{+1.17}_{-0.73}$ | $213.31^{+36.25}_{-22.66}$ |
| aegis_269 | 0.76 | 0.66 | 18 | B | $112.79 \pm 79.23$ | $8.38^{+1.42}_{-8.38}$ | $199.61^{+33.75}_{-199.61}$ |
| aegis_278 | 0.73 | -0.24 | 135 | A | - | $12.17^{+0.58}_{-0.87}$ | $12.17^{+0.58}_{-0.87}$ |
| aegis_280 | 0.57 | -0.09 | 95 | B | $1.26 \pm 0.39$ | $17.93^{+2.12}_{-1.86}$ | $20.32^{+2.40}_{-2.11}$ |
| aegis_283 | 0.77 | 0.7 | 28 | B | $9.90 \pm 2.33$ | $14.55^{+3.02}_{-2.79}$ | $28.00^{+5.82}_{-5.37}$ |
| aegis_286 | 0.74 | -0.03 | 53 | B | $2.34 \pm 0.83$ | $14.20^{+1.96}_{-2.16}$ | $17.68^{+2.44}_{-2.69}$ |
| aegis_288 | 0.46 | -0.26 | 139 | A | - | $6.09^{+0.51}_{-0.35}$ | $6.09^{+0.51}_{-0.35}$ |
| aegis_292 | 0.35 | -0.35 | 273 | A | - | $11.73^{+0.67}_{-0.69}$ | $11.73^{+0.67}_{-0.69}$ |
| aegis_299 | 0.55 | -0.39 | 315 | D | 10.0 | $5.67^{+0.31}_{-0.39}$ | $23.64^{+1.29}_{-1.63}$ |
| aegis_318 | 0.58 | -0.46 | 128 | A | - | $3.49^{+0.20}_{-0.21}$ | $3.49^{+0.20}_{-0.21}$ |
| aegis_328 | 0.66 | -0.2 | 89 | A | - | $8.80^{+0.58}_{-0.71}$ | $8.8^{+0.58}_{-0.71}$ |
| aegis_330 | 0.56 | 0.57 | 150 | B | $6.01 \pm 0.66$ | $34.60^{+2.65}_{-2.69}$ | $55.07^{+4.21}_{-4.27}$ |
| aegis_334 | 0.65 | 0.27 | 62 | B | $4.57 \pm 1.06$ | $9.75^{+0.84}_{-0.86}$ | $14.25^{+1.22}_{-1.26}$ |
| aegis_335 | 0.76 | -0.7 | 135 | A | - | $11.62^{+0.68}_{-0.77}$ | $11.62^{+0.68}_{-0.77}$ |
| aegis_343 | 0.71 | -0.53 | 43 | A | - | $3.45^{+0.43}_{-0.44}$ | $3.45^{+0.43}_{-0.44}$ |
| aegis_344 | 0.77 | 0.24 | 413 | C | $8.94 \pm 1.73$ | $80.75^{+4.02}_{-3.64}$ | $120.73^{+6.02}_{-5.44}$ |
| aegis_356 | 0.73 | -0.34 | 36 | A | - | $7.36^{+1.04}_{-1.32}$ | $7.36^{+1.04}_{-1.32}$ |
| aegis_373 | 0.74 | -0.23 | 826 | B | $0.59 \pm 0.12$ | $130.62^{+4.68}_{-4.22}$ | $138.82^{+4.97}_{-4.48}$ |
| aegis_379 | 0.46 | 0.31 | 18 | B | $2.87 \pm 1.32$ | 2.25 | 2.92 |
| aegis_382 | 0.35 | 0.07 | 24 | A | - | $0.75^{+0.15}_{-0.19}$ | $0.75^{+0.15}_{-0.19}$ |
| aegis_398 | 0.36 | -0.16 | 102 | A | - | $3.71^{+0.32}_{-0.30}$ | $3.71^{+0.32}_{-0.30}$ |
| aegis_399 | 0.78 | -0.33 | 1570 | B | $0.52 \pm 0.07$ | $597.38^{+22.82}_{-11.88}$ | $630.82^{+24.10}_{-12.55}$ |
| aegis_403 | 0.67 | -0.22 | 74 | A | - | $16.94^{+1.59}_{-2.09}$ | $16.94^{+1.59}_{-2.09}$ |
| aegis_405 | 0.43 | -0.4 | 1479 | B | $0.11 \pm 0.04$ | $110.05^{+3.85}_{-3.45}$ | $111.22^{+3.89}_{-3.49}$ |

*Continued on next page*

Table 5.6 – *Continued from previous page*

| XID<br>(1) | $z$<br>(2) | HR<br>(3) | cts<br>(4) | Model<br>(5) | N$_H$<br>(6) | L$_{abs}$<br>(7) | L$_{abscorr}$<br>(8) |
|---|---|---|---|---|---|---|---|
| aegis_412 | 0.31 | -0.07 | 325 | A | - | $2.16^{+0.07}_{-0.08}$ | $2.16^{+0.07}_{-0.08}$ |
| aegis_423 | 0.74 | 0.91 | 105 | C | $55.46 \pm 6.67$ | $65.18^{+6.31}_{-7.30}$ | $448.05^{+43.34}_{-50.15}$ |
| aegis_435 | 0.71 | -0.35 | 167 | B | $0.72 \pm 0.23$ | $47.50^{+4.11}_{-3.64}$ | $51.16^{+4.42}_{-3.92}$ |
| aegis_442 | 0.51 | 0.91 | 58 | B | $22.76 \pm 3.51$ | $15.85^{+2.07}_{-2.09}$ | $47.5^{+6.19}_{-6.27}$ |
| aegis_453 | 0.63 | -0.26 | 73 | A | - | $12.22^{+1.40}_{-1.71}$ | $12.22^{+1.40}_{-1.71}$ |
| aegis_457 | 0.75 | 0.25 | 11 | A | - | $1.99^{+0.57}_{-0.68}$ | $1.99^{+0.57}_{-0.68}$ |
| aegis_468 | 0.66 | -0.54 | 212 | A | - | $12.78^{+0.57}_{-0.68}$ | $12.78^{+0.57}_{-0.68}$ |
| aegis_481 | 0.56 | 0.23 | 88 | B | $2.57 \pm 0.56$ | $19.21^{+2.53}_{-1.98}$ | $24.34^{+3.21}_{-2.51}$ |
| aegis_487 | 0.45 | 0.29 | 29 | B | $3.27 \pm 0.82$ | $4.22^{+0.82}_{-0.81}$ | $5.64^{+1.09}_{-1.08}$ |
| aegis_493 | 0.73 | 0.37 | 28 | D | 1000.0 | $8.45^{+1.45}_{-1.93}$ | $94.24^{+16.23}_{-21.57}$ |
| aegis_498 | 0.46 | 0.6 | 35 | B | $7.68 \pm 1.21$ | $6.36^{+1.09}_{-1.09}$ | $11.05^{+1.89}_{-1.89}$ |
| aegis_504 | 0.74 | 0.78 | 14 | C | $28.36 \pm 28.82$ | $6.40^{+1.92}_{-1.50}$ | $22.58^{+6.76}_{-5.29}$ |
| aegis_518 | 0.33 | -0.24 | 417 | B | $0.33 \pm 0.08$ | $10.31^{+0.53}_{-0.55}$ | $10.68^{+0.54}_{-0.57}$ |
| aegis_522 | 0.62 | 0.35 | 294 | B | $4.85 \pm 0.34$ | $127.26^{+8.24}_{-7.16}$ | $189.08^{+12.24}_{-10.64}$ |
| aegis_545 | 0.6 | -0.03 | 234 | B | $2.12 \pm 0.28$ | $56.62^{+4.16}_{-4.26}$ | $69.27^{+5.09}_{-5.21}$ |
| aegis_547 | 0.49 | -0.32 | 646 | B | $0.24 \pm 0.07$ | $65.60^{+2.53}_{-2.65}$ | $67.21^{+2.60}_{-2.71}$ |
| aegis_564 | 0.45 | -0.25 | 771 | B | $0.52 \pm 0.08$ | $81.10^{+2.09}_{-3.52}$ | $85.64^{+2.21}_{-3.72}$ |
| aegis_573 | 0.63 | 0.77 | 64 | B | $21.05 \pm 3.39$ | $10.86^{+0.82}_{-1.00}$ | $30.92^{+2.34}_{-2.84}$ |
| aegis_574 | 0.56 | 0.24 | 76 | B | $2.31 \pm 0.28$ | $42.57^{+5.58}_{-5.31}$ | $52.89^{+6.93}_{-6.60}$ |
| aegis_579 | 0.66 | 0.19 | 82 | B | $3.14 \pm 0.54$ | $23.55^{+2.97}_{-2.80}$ | $31.19^{+3.93}_{-3.71}$ |
| aegis_583 | 0.6 | -0.1 | 157 | B | $1.57 \pm 0.24$ | $120.00^{+9.70}_{-9.90}$ | $140.05^{+11.32}_{-11.55}$ |
| aegis_589 | 0.53 | -0.4 | 252 | A | - | $21.05^{+1.50}_{-1.23}$ | $21.05^{+1.50}_{-1.23}$ |
| aegis_600 | 0.71 | 0.46 | 52 | B | $8.96 \pm 0.79$ | $11.81^{+1.51}_{-1.35}$ | $21.79^{+2.78}_{-2.48}$ |
| aegis_616 | 0.76 | -0.13 | 49 | A | - | $5.60^{+0.81}_{-0.70}$ | $5.60^{+0.81}_{-0.70}$ |
| aegis_620 | 0.66 | -0.19 | 677 | B | $1.4 \pm 0.16$ | $125.99^{+4.41}_{-5.99}$ | $144.70^{+5.06}_{-6.88}$ |
| aegis_622 | 0.68 | -0.53 | 10391 | A | - | $2291.00^{+19.00}_{-22.00}$ | $2291.00^{+19.00}_{-22.00}$ |
| aegis_636 | 0.35 | -0.14 | 156 | A | - | $1.69^{+0.10}_{-0.12}$ | $1.69^{+0.10}_{-0.12}$ |
| aegis_639 | 0.37 | 0.54 | 41 | B | $10.17 \pm 2.17$ | $3.67^{+0.48}_{--.78}$ | $7.15^{+0.93}_{-1.53}$ |
| aegis_656 | 0.75 | 0.2 | 24 | B | $6.39 \pm 2.52$ | $10.41^{+3.05}_{-2.21}$ | $16.92^{+4.95}_{-3.59}$ |
| aegis_657 | 0.68 | -0.52 | 23 | A | - | $4.15^{+0.87}_{-0.96}$ | $4.15^{+0.87}_{-0.96}$ |
| aegis_659 | 0.74 | 0.76 | 48 | D | 1000.0 | $27.96^{+6.79}_{-2.71}$ | $406.83^{+98.78}_{-39.44}$ |
| aegis_666 | 0.67 | -0.65 | 18 | A | - | $3.43^{+0.87}_{-0.82}$ | $3.43^{+0.87}_{-0.82}$ |
| aegis_684 | 0.75 | 0.17 | 118 | C | $39.80 \pm 6.07$ | $32.72^{+2.24}_{-1.79}$ | $115.50^{+7.91}_{-6.31}$ |
| aegis_694 | 0.45 | 0.06 | 92 | B | $1.61 \pm 0.30$ | $11.90^{+1.30}_{-1.66}$ | $13.92^{+1.52}_{-1.94}$ |
| aegis_701 | 0.63 | -0.58 | 233 | A | - | $29.33^{+1.54}_{-1.75}$ | $29.33^{+1.54}_{-1.75}$ |
| aegis_703 | 0.35 | 0.22 | 48 | B | $1.45 \pm 0.50$ | $3.59^{+0.59}_{-0.86}$ | $4.14^{+0.68}_{-0.98}$ |

*Continued on next page*

Table 5.6 – *Continued from previous page*

| XID | $z$ | HR | cts | Model | $N_H$ | $L_{abs}$ | $L_{abscorr}$ |
|---|---|---|---|---|---|---|---|
| (1) | (2) | (3) | (4) | (5) | (6) | (7) | (8) |
| aegis_731 | 0.78 | 0.68 | 33 | C | $213.99 \pm 56.92$ | $18.79^{+4.52}_{-5.23}$ | $1188.10^{+285.56}_{-333.00}$ |
| aegis_736 | 0.56 | -0.56 | 627 | A | - | $107.40^{+4.20}_{-3.10}$ | $107.40^{+4.20}_{-3.10}$ |
| aegis_743 | 0.56 | -0.34 | 57 | A | - | $2.48^{+0.30}_{-0.32}$ | $2.48^{+0.30}_{-0.32}$ |
| aegis_746 | 0.42 | -0.34 | 42 | A | - | $1.19^{+0.15}_{-0.10}$ | $1.19^{+0.15}_{-0.10}$ |
| aegis_747 | 0.76 | -0.13 | 33 | A | - | $6.71^{+1.51}_{-1.08}$ | $6.71^{+1.51}_{-1.08}$ |
| aegis_758 | 0.78 | -0.03 | 96 | B | $2.31 \pm 0.47$ | $41.29^{+4.49}_{-5.14}$ | $51.30^{+5.58}_{-6.39}$ |
| aegis_759 | 0.68 | -0.06 | 145 | A | - | $8.21^{+0.39}_{-0.56}$ | $8.21^{+0.39}_{-0.56}$ |
| aegis_761 | 0.62 | 0.7 | 116 | B | $51.67 \pm 3.63$ | $21.32^{+1.09}_{-1.32}$ | $133.35^{+6.82}_{-8.25}$ |
| aegis_762 | 0.75 | 0.22 | 70 | C | $43.62 \pm 20.65$ | $25.61^{+5.20}_{-4.67}$ | $99.43^{+20.20}_{-18.13}$ |
| aegis_772 | 0.62 | 0.15 | 524 | B | $3.14 \pm 0.21$ | $139.11^{+7.59}_{-6.91}$ | $184.24^{+10.05}_{-9.15}$ |
| aegis_780 | 0.73 | -0.42 | 141 | A | - | $23.48^{+1.49}_{-1.37}$ | $23.48^{+1.49}_{-1.37}$ |
| aegis_790 | 0.74 | -0.33 | 236 | B | $0.69 \pm 0.22$ | $60.24^{+4.28}_{-3.74}$ | $64.67^{+4.59}_{-4.01}$ |
| aegis_791 | 0.61 | -0.3 | 33 | A | - | $3.77^{+0.58}_{-0.53}$ | $3.77^{+0.58}_{-0.53}$ |
| aegis_793 | 0.62 | 0.53 | 144 | B | $9.34 \pm 0.46$ | $32.69^{+2.18}_{-1.79}$ | $61.38^{+2.18}_{-1.79}$ |
| aegis_803 | 0.34 | -0.25 | 248 | B | $0.64 \pm 0.09$ | $10.97^{+0.64}_{-1.03}$ | $11.71^{+0.68}_{-1.10}$ |
| aegis_806 | 0.42 | 0.25 | 25 | A | - | $0.73^{+0.10}_{-0.13}$ | $0.73^{+0.10}_{-0.13}$ |
| aegis_814 | 0.7 | -0.79 | 27 | A | - | $4.68^{+0.84}_{-0.85}$ | $4.68^{+0.84}_{-0.85}$ |
| aegis_815 | 0.74 | -0.42 | 400 | A | - | $453.98^{+29.92}_{-26.18}$ | $453.98^{+29.92}_{-26.18}$ |
| aegis_818 | 0.55 | -0.78 | 14 | A | - | $1.58^{+0.44}_{-0.46}$ | $1.58^{+0.44}_{-0.46}$ |
| aegis_827 | 0.74 | -0.3 | 479 | D | 10.0 | $185.96^{+6.74}_{-12.36}$ | $721.24^{+26.14}_{-47.94}$ |
| aegis_833 | 0.38 | -0.05 | 52 | A | - | $2.02^{+0.25}_{-0.24}$ | $2.02^{+0.25}_{-0.24}$ |
| aegis_838 | 0.74 | -0.31 | 140 | A | - | $47.74^{+2.93}_{-3.23}$ | $47.74^{+2.93}_{-3.23}$ |
| aegis_839 | 0.53 | 0.16 | 123 | B | $2.64 \pm 0.52$ | $27.86^{+3.02}_{-3.69}$ | $35.52^{+3.84}_{-4.71}$ |
| aegis_841 | 0.66 | -0.65 | 24 | A | - | $3.43^{+0.70}_{-0.82}$ | $3.43^{+0.70}_{-0.82}$ |
| aegis_842 | 0.35 | -0.44 | 14 | A | - | $0.44^{+0.15}_{-0.18}$ | $0.44^{+0.15}_{-0.18}$ |
| aegis_850 | 0.56 | 0.61 | 51 | B | $6.98 \pm 1.36$ | $14.56^{+2.22}_{-2.20}$ | $24.42^{+3.72}_{-3.69}$ |
| aegis_859 | 0.56 | -0.49 | 63 | A | - | $7.35^{+0.90}_{-0.72}$ | $7.35^{+0.90}_{-0.72}$ |
| aegis_883 | 0.46 | 0.61 | 89 | D | 1000.0 | $11.54^{+0.79}_{-1.09}$ | $169.39^{+11.55}_{-16.04}$ |
| aegis_886 | 0.45 | -0.36 | 234 | A | - | $17.74^{+1.29}_{-1.47}$ | $17.74^{+1.29}_{-1.47}$ |
| aegis_889 | 0.78 | -0.77 | 92 | A | - | $20.67^{+2.71}_{-3.08}$ | $20.67^{+2.71}_{-3.08}$ |
| aegis_912 | 0.46 | -0.36 | 97 | A | - | $2.90^{+0.17}_{-0.29}$ | $2.90^{+0.17}_{-0.29}$ |
| aegis_917 | 0.72 | -0.38 | 192 | A | - | $38.41^{+2.65}_{-1.75}$ | $38.41^{+2.65}_{-1.75}$ |
| aegis_922 | 0.55 | 0.9 | 42 | B | $31.93 \pm 6.56$ | $17.57^{+2.37}_{-1.95}$ | $67.80^{+9.16}_{-7.51}$ |

A sample of 133 X-ray detected sources from the EGS 800 ks survey with $0.3 \leq z \leq 0.8$ that were not covered by DEEP2 spectroscopy have been subjected to the same spectral

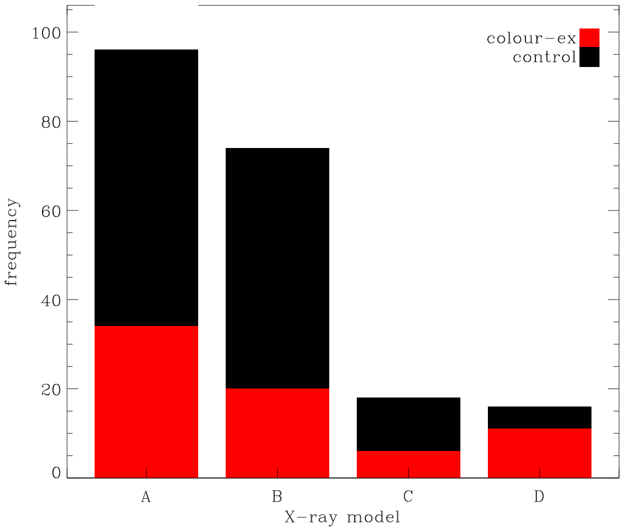

**Figure 5.11:** Bar chart illustrating the distribution how the best-fitting X-ray models of the $0.3 \leq z \leq 0.8$ emission line galaxy sample compare to that of the X-ray detected galaxy control sample.

fitting to provide a control sample. The redshifts for these sources are a mixture of spectroscopic and photometric, the latter derived through SED fitting, that have been LR matched to the X-ray detected sources (see Section 5.2.2). The majority of the sources best fit by model D have R-values that are high enough to conclude that they are Compton thick (ie R> 14). Those sources which do not (e.g. aegis_827) are classified as Compton thin sources with $\mathrm{N}_H > 10^{23}\mathrm{cm}^{-2}$.

The best fitting model, column density and absorption-corrected luminosity distributions for the control sample are compared to the 71 galaxies with optical spectroscopy in Figures 5.11, 5.12 and 5.13 respectively. The majority of the control sample galaxies are best fit by the unobscured power-law model and possess a median $L_X = 2.26 \times 10^{42}$erg s$^{-1}$. The best fitting model, column density and absorption corrected luminosity distributions of the control sample galaxies are very similar to those of the galaxies with optical spectroscopy (see Figures 5.11, 5.12 and 5.13 respectively). These distributions are incredibly similar when comparing the control sample to the emission line diagnostic analysis sample. When the galaxies with optical spectroscopy are split into subsamples, the distributions of the aforementioned properties begin to deviate from that of the control sample. In particular the CEx AGN are much more likely to be obscured and possess higher absorption-corrected luminosities on average. Conversely, the CEx SFGs have a lower obscured fraction and possess lower absorption corrected luminosities. The MEx AGN have a very similar obscured fraction and absorption corrected luminosity distribution to the control sample.

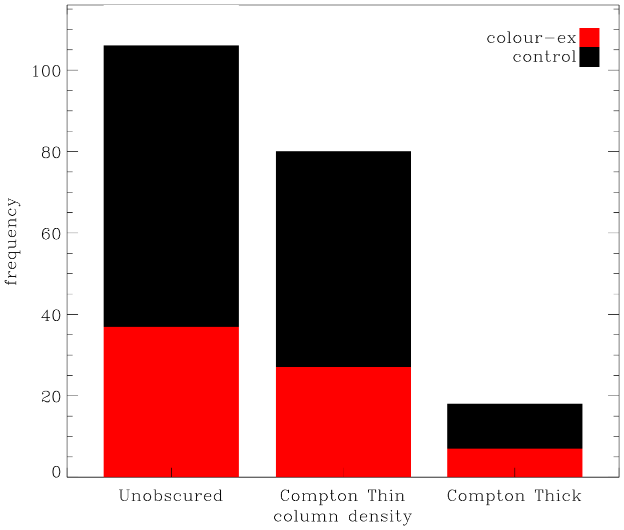

**Figure 5.12:** Bar chart illustrating how the distribution of column densities within the $0.3 \leq z \leq 0.8$ emission line galaxy sample compare to that of the X-ray detected galaxy control sample.

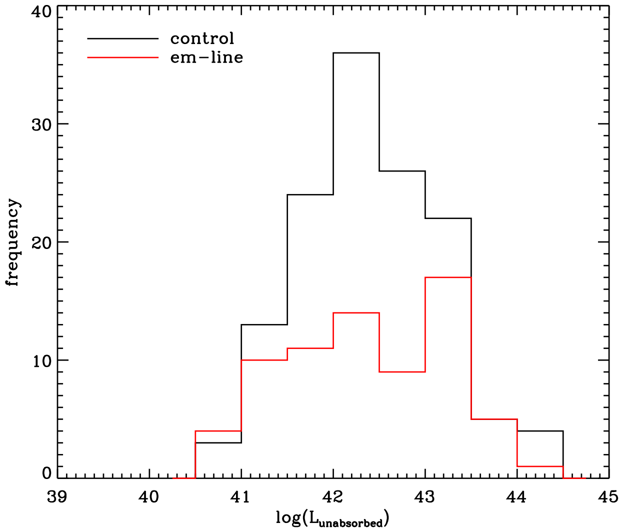

**Figure 5.13:** Histogram comparing the distribution of the absorption corrected X-ray luminosities of the $0.3 \leq z \leq 0.8$ emission line galaxy sample to that of the X-ray detected galaxy control sample.

### 5.5.3 Broad band stacking analysis

Most of the optical galaxies presented in this work do not have an X-ray point source counterpart. These galaxies are subjected to X-ray stacking analysis in order to gain a basic understanding of their average X-ray properties. A detailed description of the stacking analysis methodology is presented in Section 2.5.3, what follows is a brief description specific to the work presented in this chapter. The stacking analysis makes use of 3 broad bands; 0.5-2.0 keV (soft), 2.0-7.0 keV (full) and 0.5-7.0 keV (hard). The broad bands span an energy range over which the sensitivity of the ACIS-I CCDs is acceptable (see Section 2.2.1). The extraction and inclusion radii are calibrated using the full optical sample (1367 sources) following the method presented in Section 2.5.3. The optimum extraction and inclusion radii are found to be 7.5 arcminutes and 1.5 arcseconds respectively. The same extraction and inclusion are used for stacking all subsamples derived from the full optical sample.

For the purpose of this stacking analysis, only stacked signals with SN>3 are deemed statistically significant. The HR of a set of stacked sources is only calculated if statistically significant signals are present in the soft, hard and full bands, otherwise the uncertainty on this value renders it useless. The stacked photon count rates are converted to X-ray fluxes assuming a power-law emission with $\Gamma = 1.4$; $F_{0.5-2keV}$ (soft), $F_{2-10keV}$ (hard) and $F_{0.5-10keV}$ (full). Power-law emission with $\Gamma = 1.4$ is equivalent to the spectrum of the X-ray background over this energy range (Marshall et al., 1980). The 0.5-2 keV and 2-10 keV luminosities are estimated from the soft and hard flux bands respectively assuming a $\Gamma = 1.4$ power-law. The average absorption corrected luminosity of a sample is compared to the average optical SFR using the relationships of Ranalli et al. (2003) to search for evidence of AGN activity within the X-ray undetected subsamples.

**Table 5.7:** Results of stacking optically selected galaxies subjected to CEx and MEx analyses that do not have an X-ray counterpart. All stacked fluxes are calculated assuming the emission has an unobscured power-law profile with $\Gamma = 1.4$. Column (1): subsample name; column (2): number of X-ray undetected galaxies that have been stacked; column (3): SN of the soft band (0.5-2.0 keV) stacked emission; column (4): SN of the hard band (2.0-7.0 keV) stacked emission; column (5): SN of the full band (0.5-7.0 keV) stacked emission; column (6): average flux per galaxy for the 0.5-2.0 keV derived from soft band stacked emission, units $10^{-17}$ erg s$^{-1}$ cm$^{-2}$; column (7): average flux per galaxy for the 2.0-10.0 keV derived from hard band stacked emission, units $10^{-17}$ erg s$^{-1}$ cm$^{-2}$; column (8): average flux per galaxy for the 0.5-10.0 keV derived from the full band stacked emission, units $10^{-17}$ erg s$^{-1}$ cm$^{-2}$; column (9): hardness ratio of stacked emission, HR=(H-S)/(H+S) where H and S are the hard- (2.0-7.0 keV) and soft-band (0.5-2.0 keV) stacked emission count rates respectively; column (10): median 0.5-2.0 keV luminosity for stacked sources, units $10^{39}$ erg s$^{-1}$; column (11): median 2.0-10.0 keV luminosity for stacked sources, units $10^{39}$ erg s$^{-1}$.

| | | Signal-to-Noise Ratio | | | | Stacked Flux | | | | |
|---|---|---|---|---|---|---|---|---|---|---|
| Class (1) | N$_{stack}$ (2) | SN$_{soft}$ (3) | SN$_{hard}$ (4) | SN$_{full}$ (5) | F$_{soft}$ (6) | F$_{hard}$ (7) | F$_{full}$ (8) | HR (9) | $L_{0.5-2keV}$ (10) | $L_{2-10keV}$ (11) |
| All | 512 | 21.76 | 9.59 | 21.44 | 2.09±0.10 | 5.12±0.53 | 7.77±0.36 | -0.41±0.05 | 8.81±0.36 | 23.09±2.40 |
| CEx AGN | 41 | 6.83 | 5.62 | 8.72 | 1.45±0.36 | 12.23±2.18 | 12.40±1.42 | -0.08±0.11 | 10.33±2.55 | 88.44±15.75 |
| CEx SFG | 325 | 19.53 | 7.54 | 18.65 | 2.48±0.13 | 5.05±0.67 | 8.65±0.46 | -0.48±0.06 | 8.42±0.43 | 14.42±1.9 |
| MEx AGN | 112 | 19.44 | 10.24 | 21.15 | 5.60±0.29 | 13.55±1.32 | 20.68±0.95 | -0.42±0.05 | 26.91±1.37 | 76.88±7.51 |
| MEx trans | 82 | 6.08 | 1.35 | 4.95 | 1.31±0.22 | 1.67±1.25 | 4.11±0.83 | ... | 14.44±2.37 | ... |
| MEx SFG | 132 | 7.06 | 2.67 | 6.46 | 1.14±0.16 | 2.61±0.99 | 4.15±0.65 | ... | 5.08±0.72 | ... |
| QG | 146 | 7.43 | 3.42 | 7.28 | 1.16±0.16 | 3.27±0.96 | 4.56±0.63 | -0.35±0.14 | 6.31±0.84 | 32.92±9.65 |

There are 512 sources with optical spectroscopy which fall within the 7.50 arcminute inclusion radius and are sufficiently far from X-ray point sources to rule out potential signal contamination (see Table 5.7). Stacking the 512 galaxies produces statistically significant signals in the soft, hard and full bands with $F_{0.5-2keV} = 2.09 \pm 0.10 \times 10^{-17}$, $F_{2-10keV} = 5.12 \pm 0.53 \times 10^{-17}$ and $F_{0.5-10keV} = 7.77 \pm 0.36 \times 10^{-17}$ erg s$^{-1}$ cm$^{-2}$. The stacked signal has HR=-0.41±0.05 which could be replicated by a power-law with photon-index $\Gamma = 1.8^{+0.1}_{-0.1}$. The predicted power-law spectrum is consistent, within errors, with both typical unobscured AGN emission ($\Gamma \sim 1.9$; Nandra and Pounds 1994) and X-ray emission from star-formation ($\Gamma \sim 1.7$; Persic and Rephaeli 2002). The average stacked X-ray luminosities of the X-ray undetected sources is also consistent with the X-ray luminosities predicted from average SFR of the sample (using the relationship of Ranalli et al. 2003).

Separating the X-ray undetected galaxies into CEx and MEx subsamples, it is possible to search for evidence of obscured and low luminosity AGN activity that lies below the detection limit of the 800ks EGS observations. The CEx AGN subsample possesses the hardest stacked signal of any subsample (HR=-0.08±0.11) and has an equivalent effective photon index of $\Gamma = 1.1^{+0.3}_{-0.2}$. This is consistent with emission from obscured AGN. The average $L_{0.5-2keV}$ of the X-ray undetected CEx AGN is consistent with the average $L_{0.5-2keV}$ predicted from the SFR of these galaxies. The average $L_{2-10keV}$ of the X-ray undetected AGN, however, greatly exceeds the average $L_{2-10keV}$ predicted from the SFRs. Therefore the stacked emission of CEx AGN is consistent with significant X-ray undetected obscured and/or Compton thick AGN activity. The stacked signal of CEx SFG subsample is softer than that of the CEx AGN and they possess lower average $L_{0.5-2keV}$ and $L_{2-10keV}$. The soft HR suggests there is little or no contribution from obscured AGN and the average $L_{0.5-2keV}$ and $L_{2-10keV}$ are less than those predicted from their average SFRs. Therefore the stacked emission of CEx SFGs is consistent with pure star formation.

The MEx AGN sample is much larger than the CEx AGN subsample. The resulting stacked signal is also much softer (HR=-0.42±0.05; $\Gamma = 1.8^{+0.1}_{-0.1}$) than that of the CEx AGN (and almost identical to that of the full X-ray undetected galaxy sample). Similar to the CEx AGN, the average $L_{0.5-2keV}$ of the MEx AGN is consistent with the average $L_{0.5-2keV}$ predicted from their SFRs. The average $L_{2-10keV}$, however, exceeds the average $L_{2-10keV}$ predicted from their SFRs, again like the CEx AGN. The high $L_{2-10keV}$ of the MEx AGN strongly suggests a significant contribution from AGN to the stacked signal but the soft HR indicates the fraction of obscured AGN is lower than that of the CEx AGN subsample. The MEx transition galaxies and MEx SFGs lack statistically significant stacked signals in the hard band, thus the HR has not been estimated. The average $L_{0.5-2keV}$ of both the MEx transition galaxies and MEx SFGs are both less than the average $L_{0.5-2keV}$ predicted from their SFRs. This information coupled with the lack of significant hard X-ray emission in these subsamples implies there is little or no AGN activity (obscured or otherwise) contributing to the stacked emission of X-ray undetected MEx SFGs and MEx

**Table 5.8:** X-ray detected fractions of MEx classified galaxies when limited to galaxies which possess optical emission lines with SN> 3. This sample is more suited for direct comparison to those presented in Juneau et al. (2011).

| Type<br>(1) | $N_{src}$<br>(2) | $N_X$<br>(3) | $F_X$<br>(4) |
|---|---|---|---|
| All | 414 | 31 | 7.5±1.3 |
| MEx AGN | 116 | 29 | 25.0±4.0 |
| MEx transition | 81 | 1 | 1.2±1.2 |
| MEx SFG | 217 | 1 | 0.5±0.5 |

transition galaxies.

Stacking the X-ray undetected QG subsample produces statistically significant signals all 3 broad X-ray bands. The HR of the stacked signal of the QGs is consistent with the stacked signal of the full sample. The QGs by definition lack a secure H$\beta$ detection and as a result only an upper limit can be determined for the H$\beta$ luminosities and the associated SFRs have been calculated (average $SFR_{H\beta} < 1.76\mathrm{M}_{\odot}\mathrm{yr}^{-1}$). The average $L_{0.5-2keV}$ is consistent, within errors, with the average $L_{0.5-2keV}$ predicted from their SFRs. Their average $L_{2-10keV}$, however, exceeds the average $L_{2-10keV}$ predicted from their SFR. Therefore there appears to be some AGN activity contributing to the stacked emission of X-ray undetected QGs as well, although there is no evidence of significant obscured AGN activity.

## 5.6 Comparison to previous results

### 5.6.1 CEx galaxies

Yan et al. (2011) examined the X-ray properties of galaxies classified using the CEx diagnostic using 200ks observations of the EGS region (Laird et al., 2009). X-ray counterparts are assigned to some of the optical emission line galaxies using an LR matching technique. The EGS 200ks covers a larger area than the EGS 800ks survey but has a lower sensitivity, limiting the minimum X-ray luminosities that can be explored. The wider survey area means all samples presented in Yan et al. (2011) are larger than those used in this work. The CEx AGN of Yan et al. (2011) have a similar X-ray detected fraction (23/97; 23.7±0.7%) consistent with that of the CEx AGN in this work (see Table 5.2). The CEx SFGs and QGs presented in Yan et al. (2011), however, have lower X-ray detected fractions than those presented in this work. This is because the CEx SFGs tend to have lower luminosity X-ray counterpart sources (ie $L_X < 10^{42}\mathrm{erg\ s}^{-1}$) whereas the CEx AGN contain more X-ray luminous sources (ie $L_X > 10^{42}\mathrm{erg\ s}^{-1}$), as demonstrated in Figure 5.9. The higher sensitivity of the EGS 800ks means the X-ray sample presented in this work has higher completeness of $L_X < 10^{42}\mathrm{erg\ s}^{-1}$ galaxies than Yan et al. (2011). Therefore the X-ray detected fractions of CEx SFGs in this work are higher.

Yan et al. (2011) compare the X-ray luminosity of X-ray detected CEx SFGs to the estimates of the X-ray luminosity made from their SFRs using the relationship of Ranalli et al. (2003). The measured X-ray luminosities are found to be in excess of the X-ray luminosities predicted from the SFRs of the CEx SFGs. This indicates that the X-ray detected CEx SFGs have some AGN contribution. The X-ray luminosities obtained from X-ray spectral fitting of CEx SFGs in this work are consistent with the results of Yan et al. (2011), see Figure 5.5. The majority of X-ray bright, optically normal galaxies (XBONGs; X-ray detected QGs in this analysis) identified by Yan et al. (2011) are thought to be dominated by AGN. The X-ray luminosities of all XBONGs in this work exceed those predicted from their SFRs (see Figure 5.5) and therefore all probably contain AGN. Additionally, Yan et al. (2011) find little or no evidence to suggest the XBONGs represent a different population to standard X-ray detected galaxies. The distribution of column density and absorption corrected X-ray luminosity of XBONGs in this work (see Figures 5.7 and 5.8 respectively) are consistent with those of a control sample of X-ray detected galaxies with $0.3 \leq z \leq 0.8$ and thus corroborate the findings of Yan et al. (2011). Finally, Yan et al. (2011) predict a significant obscured population within the X-ray undetected CEx AGN based on the expected source counts. The hard stacked emission produced by undetected CEx AGN in this analysis is consistent with this prediction (see Section 5.5.3).

### 5.6.2 MEx galaxies

Before attempting to compare the results of this work to those of Juneau et al. (2011) there are two differences in the source data that must be considered. Firstly, Juneau et al. (2011) use data from across multiple X-ray fields, including the CDFN 2Ms data. Therefore some of the X-ray data used in Juneau et al. (2011) is deeper than the 800ks EGS observations used in this work and therefore has a lower X-ray sensitivity threshold. Secondly, the galaxy sample presented in Juneau et al. (2011) implements a more conservative constraint on the statistical significance required to class an emission line as detected (SN> 3) than has been used in this work (SN> 2). Therefore in order to make a meaningful comparison between this work and Juneau et al. (2011) the same emission line detection threshold constraints are applied to the former. Doing so reduces the size of the MEx samples to 116 MEx AGN, 81 MEx transition galaxies and 217 MEx SFGs (see Table 5.8). The significant reduction in the size of the MEx sample suggests that using poor SN might significantly contaminate the AGN, transition galaxy and SFG subsamples identified with the MEx technique. The X-ray detected fractions of the conservative MEx AGN sample is a factor of 2 higher than that presented in Table 5.2.

Juneau et al. (2011) investigate the distribution of unambiguous X-ray AGN selection ($L_X > 10^{42}$erg s$^{-1}$ or HR>-0.1) across the MEx subsamples. Of the 40 unambiguous X-ray AGN presented in Juneau et al. (2011), 85.0±5.6% (34/40) are classified as either MEx AGN (26) or MEx transition galaxies (8). In this work, there are 31 galaxies in the conservative optical sample that possess X-ray counterparts, of which 23 satisfy the unambiguous X-ray AGN criteria ($L_X > 10^{42}$erg s$^{-1}$ or HR>-0.1). All 23 of the unambiguous X-ray AGN in this work are classified as MEx AGN, a significantly higher completeness than the MEx AGN of Juneau et al. (2011) (26/40). Unlike Juneau et al. (2011), none of the MEx transition galaxies or MEx SFGs are classified as unambiguous X-ray AGN. This is probably because the X-ray detected sample used in this work is significantly smaller than that used by Juneau et al. (2011). The expectation is that given a sample of comparable size, more X-ray detected sources (and hence more unambiguous X-ray AGN) would be present in the MEx transition and MEx SFG subsamples.

Juneau et al. (2011) also stacked X-ray undetected MEx classified galaxies in the GOODS-N 2Ms, creating a subsample based upon the likelihood of a galaxy containing an AGN (as opposed to simply following the specific MEx criteria). A sample of 34 galaxies with P(AGN)>30% (effectively the MEx AGN and MEx transition galaxies combined) yielded a hard signal which corresponds to power-law emission with $\Gamma \sim 0.8$. The hard signal implies there is a significant population of X-ray absorbed (obscured) AGN within this subsample. The remaining 13 galaxies (effectively SFGs) produce a stacked signal that was only detected in the soft band which was best approximated by a power-law $\Gamma \sim 1.7$. This is consistent with the X-ray emission expected from pure star formation (Persic and Rephaeli, 2002).

**Table 5.9:** Results of stacking optically selected galaxies with all emission lines detected at SN$>3$ that have been subjected to MEx analysis that do not have an X-ray counterpart. All stacked fluxes are calculated assuming the emission has an unobscured power-law profile with $\Gamma = 1.4$. Column (1): subsample name; column (2): number of X-ray undetected galaxies that have been stacked; column (3): SN of the soft band (0.5-2.0 keV) stacked emission; column (4): SN of the hard band (2.0-7.0 keV) stacked emission; column (5): SN of the full band (0.5-7.0 keV) stacked emission; column (6): average flux per galaxy for the 0.5-2.0 keV derived from soft band stacked emission, units $10^{-17}$ erg s$^{-1}$ cm$^{-2}$; column (7): average flux per galaxy for the 2.0-10.0 keV derived from hard band stacked emission, units $10^{-17}$ erg s$^{-1}$ cm$^{-2}$; column (8): average flux per galaxy for the 0.5-10.0 keV derived from the full band stacked emission, units $10^{-17}$ erg s$^{-1}$ cm$^{-2}$; column (9): hardness ratio of stacked emission, HR=(H-S)/(H+S) where H and S are the hard- (2.0-7.0 keV) and soft-band (0.5-2.0 keV) stacked emission count rates respectively; column (10): median 0.5-2.0 keV luminosity for stacked sources, units $10^{39}$ erg s$^{-1}$; column (11): median 2.0-10.0 keV luminosity for stacked sources, units $10^{39}$ erg s$^{-1}$.

| | | Signal-to-Noise Ratio | | | Stacked Flux | | | | | |
|---|---|---|---|---|---|---|---|---|---|---|
| Class<br>(1) | $N_{stack}$<br>(2) | $SN_{soft}$<br>(3) | $SN_{hard}$<br>(4) | $SN_{full}$<br>(5) | $F_{soft}$<br>(6) | $F_{hard}$<br>(7) | $F_{full}$<br>(8) | HR<br>(9) | $L_{0.5-2keV}$<br>(10) | $L_{2-10keV}$<br>(11) |
| MEx AGN | 37 | 18.72 | 9.89 | 20.79 | 14.04±0.75 | 28.12±2.82 | 48.88±2.34 | -0.49±0.05 | 50.92±0.27 | 86.66±0.87 |
| MEx trans | 33 | 4.31 | 1.07 | 3.63 | 1.48±0.34 | ... | 4.78±1.32 | ... | 19.94±0.46 | ... |
| MEx SFG | 87 | 5.52 | 3.17 | 5.76 | 1.07±0.20 | 4.02±1.26 | 4.63±0.81 | -0.22±0.17 | 4.43±0.08 | 31.48±0.99 |

The results of repeating the stacking analysis of Section 5.5.3 using the more conservative emission-line galaxy sample are presented in Table 5.9. Contrary to the results of the stacking analysis of Juneau et al. (2011), stacking the X-ray undetected MEx AGN and MEx transition galaxies produces a soft signal consistent with low luminosity unobscured AGN emission as opposed to obscured AGN activity. The stacked signal of the MEx SFGs is consistent with the stacked signal of P(AGN)<30% of Juneau et al. (2011). The reasons for this discrepancy between the P(AGN)>30% stacked signal of Juneau et al. (2011) and the stacked signal of X-ray undetected MEx AGN presented in this work remains unclear. It could simply be a reflection of the difference in the depth of the X-ray data used to create the stacked signals in the two studies. For example, the deeper GOODS-N 2Ms X-ray data used by Juneau et al. (2011) might be resolving and omitting soft X-ray sources that have been included in the shallower EGS 800ks data used in this work. Stacking the same data in surveys of differing X-ray depth can lead to dramatic variations in the stacked emission, e.g. the stacking analysis of BzK galaxies in Chapter 3. To comprehensively test this hypothesis would require X-ray data in the EGS of equivalent depth to that in the CDFN (ie of order 2Ms).

## 5.7 Discussion

### 5.7.1 Summary of results

The purpose of this work was to investigate and compare the X-ray properties of galaxies classified as AGN using the CEx (Yan et al., 2011) and MEx (Juneau et al., 2011) classification techniques. The optical sample consists of 1367 galaxies with $0.3 \leq z \leq 0.8$ that lie in the EGS 800ks footprint. Optical spectroscopy for these galaxies was compiled as part of the DEEP2 survey (Davis et al., 2003). Subsamples of AGN, SFGs and Transition galaxies were generated from the optical sample using the CEx and MEx techniques, while optically "dull" sources were classified as QGs (412 sources). The EGS 800ks X-ray point source catalogue was created using the Imperial College X-ray reduction pipeline (Nandra et al. prep) and contains 937 sources. Likelihood ratio matching of the X-ray catalogue to the optical sample produces 71 matches which are subjected to spectral fitting analysis. The X-ray detected fraction of optical sources presented in this work is slightly higher than that of Yan et al. (2011), but this is expected given the X-ray observations used in this work are deeper. A control sample of 133 X-ray sources with $0.3 \leq z \leq 0.8$ is subjected to the same spectral analysis for comparison.

The CEx analysis identifies 147 AGN and 808 SFGs. The CEx AGN have a higher X-ray detection rate than the CEx SFGs ($> 5\sigma$ significance) and QGs which is a strong indicator of elevated AGN activity within this sample. Spectral analysis of the X-ray detected sources reveals the X-ray detected CEx AGN possess a higher obscured AGN fraction (80%) and higher absorption corrected X-ray luminosities than the X-ray detected CEx SFGs and QGs. This is consistent with emission from type 2 AGN. The absorption corrected X-ray luminosities of the X-ray detected CEx SFG imply they are in fact AGN-SF composites (see Figure 5.5). The X-ray properties of the X-ray detected CEx SFG subsample are remarkably similar to the control sample. AGN have been known to contaminate the SED of their host galaxies, making them appear bluer than they actually are (Nandra et al., 2007a). Therefore correcting $(U-B)_0$ of the AGN-SF composite galaxies in the CEx SFG region for AGN contamination might drive them into the CEx AGN region. Stacking the emission of X-ray undetected CEx AGN produces a hard signal consistent with a high fraction of these galaxies harbouring obscured AGN. The average X-ray luminosity of these sources also exceeds the X-ray luminosity predicted from their average SFR (using the relations of Ranalli et al. 2003; Equations 4.3 and 4.4), further evidence that there are contributions from X-ray undetected AGN. The X-ray undetected CEx SFG exhibit much softer stacked emission and the stacked X-ray luminosity is consistent with the X-ray luminosity predicted from their average SFR. In conclusion, X-ray analysis of CEx classified galaxies suggests this technique is successfully separating type 2 AGN from SFGs with a high degree of accuracy.

The MEx analysis identifies 348 AGN, 211 Transition galaxies and 307 SFGs. The MEx AGN have a higher X-ray detected fraction than the MEx transition galaxies and MEx SFGs. In fact almost all X-ray detected galaxies with at least an [OIII] or H$\beta$ detection (ie not a QG or in the control sample) are classified as MEx AGN by the MEx analysis (48/52; 92.3±3.7%). The MEx AGN selection technique has a much higher completeness, in terms of X-ray detected AGN selection, than the CEx AGN selection. However, plotting BPT classified AGN on the MEx diagram suggests this portion of the MEx AGN selection region may be fallible to contamination from transition galaxies (see Figure 5.4). Spectral analysis of the MEx AGN reveals that they possess a higher obscured fraction than either the QGs or the control sample. On the other had, the distribution of their absorption corrected X-ray luminosities is quite similar to that of the QGs and control sample galaxies. If the X-ray detected MEx AGN were all type 2 AGN one would expect the obscured fraction to be considerably higher ($> 80\%$; Kirhakos and Steiner 1990). Instead it appears that the MEx AGN criterion includes numerous unobscured low luminosity AGN as well. In fact the X-ray properties of the MEx AGN are almost identical to those of galaxies in the control sample.

The X-ray undetected MEx AGN population is much larger than the X-ray undetected CEx AGN population. The average stacked X-ray luminosity of the X-ray undetected MEx AGN is higher than the X-ray luminosity predicted from their average SFRs. This strongly suggests that there are additional contributors to the stacked X-ray emission as opposed to just star formation activity. The HR of the stacked emission, however, is much softer than that of the X-ray undetected CEx AGN. In fact it is identical to that of the full optical sample, which suggests that, unlike the CEx AGN, there are very few obscured and Compton thick AGN present in this sample. Therefore the most abundant X-ray emitting sources among the X-ray undetected MEx AGN are probably unobscured low luminosity AGN. The 3 X-ray detected MEx Transition galaxies and 1 X-ray detected MEx SFG are unobscured low luminosity AGN. These characteristics are not atypical of the expected X-ray properties of galaxies in these subsamples, but the X-ray detected fractions are considerably lower than those observed by Juneau et al. (2011). The X-ray undetected MEx transition galaxies and MEx SFGs both produce soft stacked emission and neither possess a statistically significant signal in the hard band. The stacked luminosities of both these subsamples are consistent with the X-ray luminosity predicted from the average SFRs. There is no evidence to support the notion that the X-ray undetected MEx transition galaxies feature co-eval SMBH and star formation activity, as was suggested by Juneau et al. (2011).

The X-ray detected QG (XBONG) population has very similar X-ray properties to the control sample, and there is no evidence to suggest they are in fact a unique sample of X-ray sources. This is consistent with the observations of Yan et al. (2011). Rigby et al. (2006) find evidence that XBONGs are optically "dull" because dust from the host galaxy is obscuring optical emission lines produced by the AGN. While this assertion cannot be tested directly through the X-ray analysis presented in this work, none of the XBONGs containing obscured AGN are best fit by the dust torus obscuration model (model C). Therefore, it is possible that the majority of the observed column density is created by obscuring material distributed over a galactic scale as opposed to a localised torus. This sample, however, is too small to draw a more statistically robust conclusion.

The CEx and MEx classification techniques are both variants/approximations of the classic BPT classification technique of Baldwin et al. (1981) that have been designed to explore more distant redshifts ($z \leq 0.8$). Both have been shown to replicate the results of BPT classification with a reasonable degree of accuracy at lower redshifts ($0.2 \leq z \leq 0.4$; see Section 5.4) and show good agreement with one another. Through this analysis it has been demonstrated that at higher redshifts the properties of the AGN populations identified by the CEx and MEx classifications are different. The X-ray analysis presented in this chapter suggests that the CEx AGN classification is more conservative than the MEx AGN classification. While the CEx AGN selection region does not identify as large a fraction of the X-ray detected sample, it appears to target obscured AGN more accurately than the MEx AGN technique.

### 5.7.2 CEx versus MEx selection

The initial motivation of both CEx and MEx AGN selection techniques was to target type 2 AGN at higher redshifts than the original BPT technique. The results of this analysis suggest the CEx classification technique performs well in this regard. The obscured fraction of the X-ray detected CEx AGN is consistent with the obscured fraction of local type 2 AGN (e.g. Kirhakos and Steiner 1990). Yan et al. (2011) observe that the detected fraction of CEx AGN is consistent with the X-ray detected fraction predicted for a sample of type 2 AGN at $0.3 \leq z \leq 0.8$. Given that the X-ray detected fraction of CEx AGN found in this work is consistent with that of Yan et al. (2011), it stands to reason that this prediction should still hold true. The observed Compton-thick AGN fraction among the X-ray detected CEx AGN alone falls well short of local observations, but many of the Compton thick AGN are likely to remain undetected in the 800ks observations. Stacking the X-ray undetected AGN reveals a hard signal, likely generated by obscured and Compton thick AGN emission. Therefore the "missing" Compton thick AGN are probably in the X-ray undetected CEx AGN sample. Yan et al. (2011) acknowledge that in some cases the AGN emission lines may be drowned out by emission from star-formation. The X-ray detected CEx SFG in this analysis are a prime example of this exact issue, with their absorption corrected X-ray luminosities exceeding those predicted from their optical SFRs. This issue appears to be confined to the X-ray detected CEx SFG ($2.6 \pm 0.6\%$ of the CEx SFGs) because the stacked emission of X-ray undetected CEx SFG does not exhibit any sign of AGN activity.

The MEx AGN selection does not appear to be identifying type 2 (obscured AGN) with the same accuracy as the CEx AGN selection, at least for the optical sample presented in this work. The MEx AGN selection identifies nearly all the X-ray detected AGN that do not reside in QGs. This implies that the MEx diagnostic is fairly complete, ie it is efficient at selecting AGN as identified by their X-ray emission (except for the XBONGs). On the other hand the efficiency of MEx for selecting obscured sources is less clear. X-ray spectral fitting analysis demonstrates that there is little evidence for excess obscuration among the X-ray detected MEx AGN. Additionally stacking X-ray undetected MEx AGN reveals there is very little evidence to support a significant population of X-ray undetected heavily obscured and/or Compton thick AGN. A large population of low luminosity unobscured AGN appears to be present in the stacked emission of the X-ray undetected MEx AGN instead. Imposing the stricter optical emission line requirements (SN>3) used by Juneau et al. (2011) does not improve the accuracy with which the MEx AGN selection identifies obscured/type 2 AGN. Juneau et al. (2011) argue that the MEx technique has the potential to identify heavily reddened, obscured AGN more effectively than the CEx technique. On the basis of the X-ray analysis presented in this work, however, there appears to be little evidence to support this.

The CEx AGN selection identifies obscured AGN in this sample with greater accuracy than the MEx AGN selection (see Tables 5.5 and 5.7). The lingering question is why is this the case? It is most likely because the CEx technique is dependant upon optical colour $(U\text{-}B)_0$. The threshold [OIII]/H$\beta$ ratio of the CEx technique falls as the U-V colour gets redder. An unobscured AGN, however, is likely to contribute significantly to the blue end of the spectrum (optical and UV). This means galaxies hosting unobscured AGN are likely be driven beyond the AGN parameter space defined by the CEx technique (unless their [OIII]/H$\beta$ ratio is high). This culls the majority of the unobscured AGN population from the CEx selection. The observations of Nandra et al. (2007a) are consistent with this picture, with galaxies on the "red-sequence" of the colour-magnitude diagram tending to

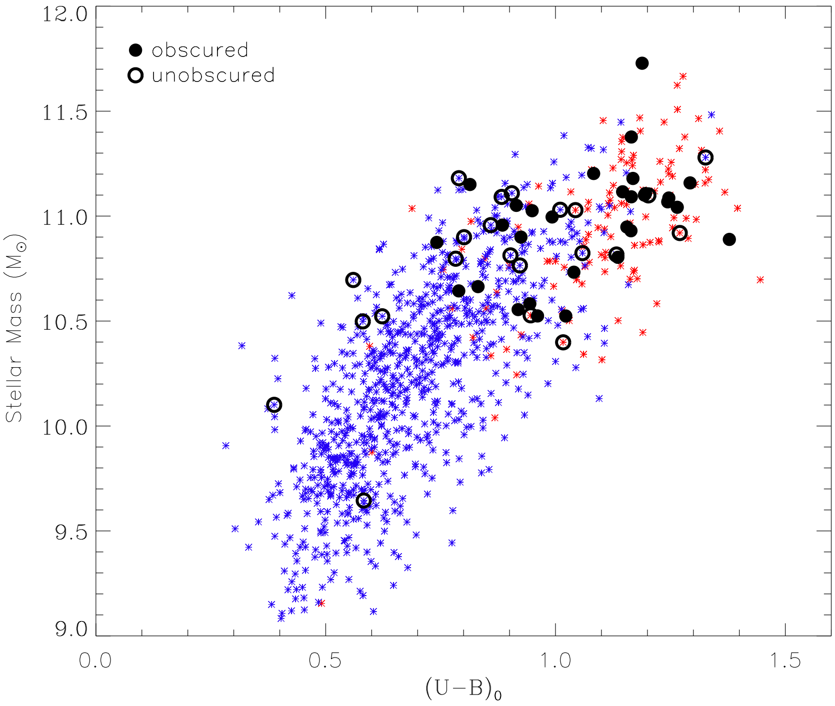

**Figure 5.14:** Plot of (U-B)$_0$ colour versus galaxy stellar mass with galaxies classified using the CEx diagnostic. Red crosses represent emission line AGN and blue crosses are SFGs. Obscured and unobscured X-ray sources has also been overlaid onto the plot.

exhibit hard X-ray emission while galaxies in the "blue cloud" tending to exhibit soft X-ray emission. A similar effect is not observed in the MEx selection because the galaxy mass estimation is independent of the galaxy colour. Therefore the MEx selection identifies nearly all unobscured and obscured AGN.

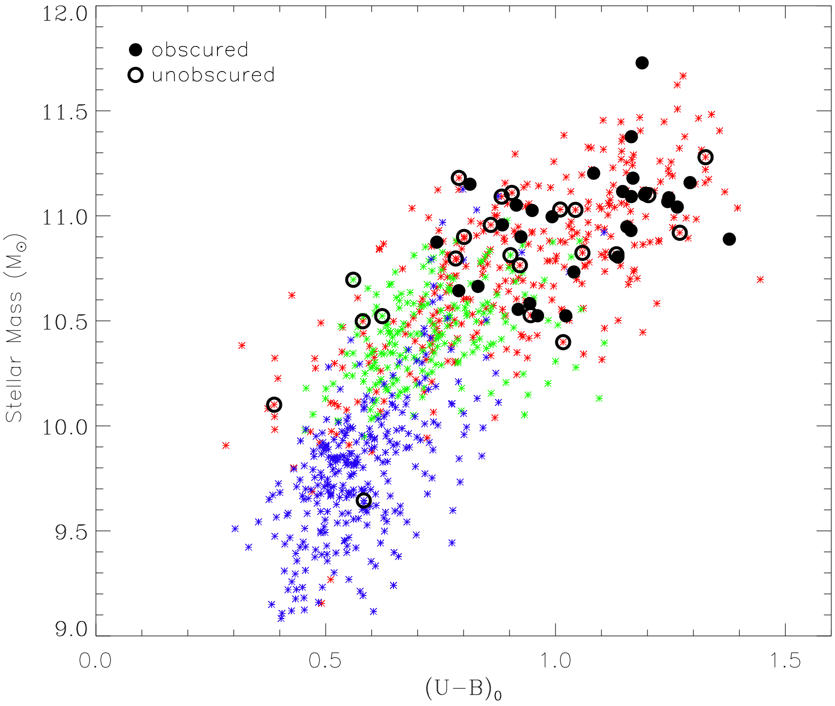

**Figure 5.15:** Plot of $(U\text{-}B)_0$ colour versus galaxy stellar mass with galaxies classified using the MEx diagnostic. Red crosses represent emission line AGN, green crosses are AGN-SF transition galaxies and blue crosses are SFGs. Obscured and unobscured X-ray sources has also been overlaid onto the plot.

**Table 5.10:** Obscured and Compton thick fractions for subsamples of X-ray undetected galaxies binned by stellar mass, $(U\text{-}B)_0$ and $L_{[OIII]}$. Galaxies lacking [OIII] and H$\beta$ emission (ie QGs) have been omitted from this analysis. Column (1): emission line diagnostic classification; column (2): number of optical sources; column (3): number of optical sources LR matched to X-ray counterparts; column (4): percentage of optical sources with X-ray counterparts; column (5): number of X-ray detected galaxies with signatures of obscured emission; column (6): percentage of X-ray detected galaxies with obscured emission (ie best fit by models C, D or E), with binomial error; column (7): number of X-ray detected galaxies exhibiting Compton thick emission; column (8): percentage of X-ray detected galaxies exhibiting Compton thick emission.

| Type<br>(1) | $N_{src}$<br>(2) | $N_X$<br>(3) | $F_X$<br>(4) | $N_{obs}$<br>(5) | $F_{obs}$<br>(6) | $N_{CT}$<br>(7) | $F_{CT}$<br>(8) |
|---|---|---|---|---|---|---|---|
| $M_* < 10^{10.0}$ | 285 | 1 | 0.3±0.3 | 0 | ... | 0 | ... |
| $10^1 0.0 \leq M_* < 10^{10.5}$ | 300 | 3 | 1.0±0.6 | 0 | ... | 0 | ... |
| $10^1 0.5 \leq M_* < 10^{11.0}$ | 266 | 26 | 9.8±1.8 | 11 | 42.3±9.7 | 4 | 15.4±7.1 |
| $M_* \geq 10^{11.0}$ | 104 | 22 | 21.2±4.0 | 13 | 59.1±10.5 | 1 | .4.5±4.4. |
| $(U\text{-}B)_0 < 0.6$ | 275 | 4 | 1.5±0.7 | 0 | ... | 0 | ... |
| $0.6 \leq (U\text{-}B)_0 < 0.8$ | 342 | 5 | 1.5±0.6 | 0 | ... | 0 | ... |
| $0.8 \leq (U\text{-}B)_0 < 1.1$ | 235 | 24 | 10.2±2.0 | 11 | 45.8±10.2 | 2 | 8.3±5.6 |
| $(U\text{-}B)_0 \geq 1.1$ | 103 | 19 | 18.4±3.8 | 13 | 68.4±10.7 | 3 | 15.8±8.4 |
| $L_{[0III]} < 10^{40.0}$ | 155 | 6 | 3.9±1.5 | 0 | ... | 0 | ... |
| $10^{40.0} \leq L_{[0III]} < 10^{40.5}$ | 310 | 9 | 2.9±1.0 | 3 | 33.3±15.7 | 0 | ... |
| $10^{40.5} \leq L_{[0III]} < 10^{41.0}$ | 312 | 15 | 4.8±1.2 | 9 | 60.0±12.6 | 1 | 6.7±6.4 |
| $L_{[0III]} \geq 10^{41.0}$ | 178 | 22 | 12.4±2.5 | 12 | 54.5± 10.6 | 4 | 18.2±8.2 |

To gain further insight into the relative merits of using galaxy colour and galaxy mass as tracers of AGN activity, the CEx and MEx identifications have been overlaid onto plots of $(U\text{-}B)_0$ versus galaxy mass (Figures 5.14 and 5.15). The QG subsample has been omitted from these plots for the purpose of this analysis as they are essentially independent of the CEx and MEx classified galaxies. There is a clear positive correlation between stellar mass and $(U\text{-}B)_0$ of a galaxy, with the most massive galaxies possessing the reddest $(U\text{-}B)_0$ colours. A similar correlation between galaxy mass and colour was observed by Weiner et al. (2009; Figure 10) out to $z \sim 1.4$. As a result the X-ray detected fractions of galaxies binned by $(U\text{-}B)_0$ and galaxy mass (see Table 5.10) are both positively correlated. The X-ray detected fraction increases as galaxy stellar mass increases because more massive galaxies tend to contain more massive black holes (Magorrian et al., 1998; McLure et al., 2006) which are in turn more luminous and thus more likely to be detected. A similar increase is thus observed in the X-ray detected fraction as the $(U\text{-}B)_0$ colour becomes redder. There is also a strong increase in the obscured fraction of X-ray detected obscured AGN as stellar mass and $(U\text{-}B)_0$ increase.

There is a fairly clean separation of CEx AGN and SFGs in Figure 5.14; the majority of the CEx AGN can be isolated within a region $M_* > 10^{10.8}$ $M_\odot$ and $(U\text{-}B)_0 > 1.0$, with minimal contamination from CEx SFG. Compare this to Figure 5.15 which is far more chaotic, with the various MEx subsamples contaminating one another to a substantial extent. The most severe contamination occurs between the MEx AGN and the MEx Transition galaxy subsamples. There is no way to disentangle these populations using the $(U\text{-}B)_0$ colour or the stellar mass of the galaxy either in concert or isolation. If the MEx Transition galaxies were predominantly SF-AGN composites, as observed by Juneau et al. (2011), then this cross-contamination would be understandable. There is, however, no evidence to support significant AGN activity within the MEx Transition galaxy subsample used in this work. Evidently, $(U\text{-}B)_0$ is providing a cleaner separation for CEx classified galaxies than stellar mass does for MEx classified galaxies. This makes the MEx selection technique far more sensitive to the calibration of its own AGN and Transition galaxy boundaries than the CEx technique, thus increasing the risk of false identifications if these are calibrated incorrectly.

It might be possible to target obscured AGN in the MEx plot by redefining the MEx AGN cutoff region. Figure 5.16 is a reproduction of the CEx diagnostic plot for this sample with obscured and unobscured X-ray detected sources overlaid. This plot clearly demonstrates the CEx AGN selection targeting obscured AGN. Superimposing the CEx classifications onto a MEx diagnostic plot (see Figure 5.17), the MEx AGN region is seen to select all the CEx AGN, but it also suffers from heavy contamination by CEx SFGs. The majority of the CEx SFGs, as well as most of the unobscured low luminosity X-ray sources, lie close to the MEx AGN boundary. This suggests that the [OIII]/H$\beta$ requirement imposed on MEx AGN is generally lower than that imposed on CEx AGN. While this allows the detection of lower luminosity AGN, the majority of these sources

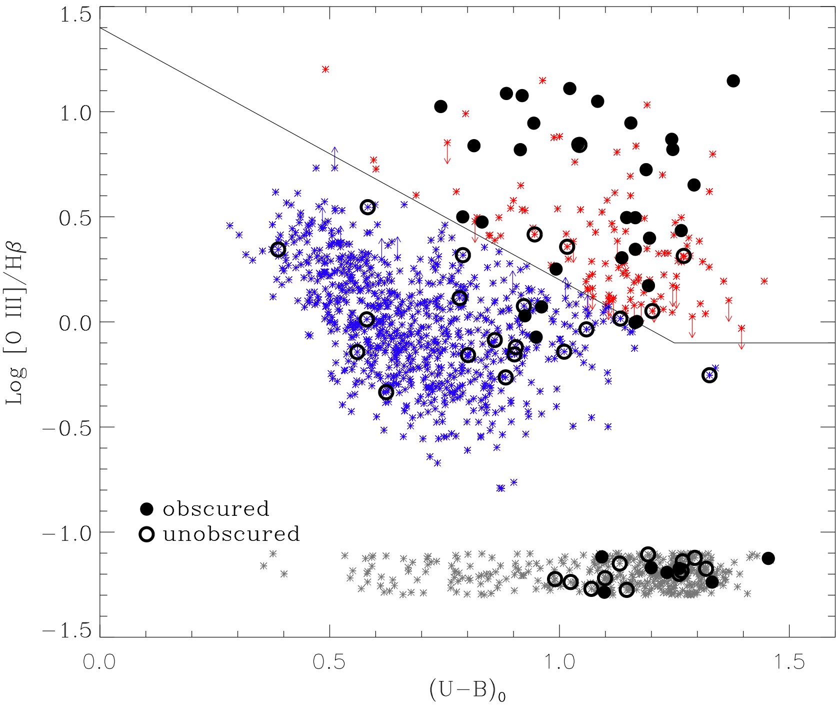

**Figure 5.16:** CEx diagnostic plot of optical emission line galaxies ($0.3 \leq z \leq 0.8$) with obscured and unobscured X-ray sources identified. Red crosses represent emission line AGN, blue crosses are SFGs and the grey crosses are QGs with no optical emission lines. An upwards arrow highlights sources for which $\log_{10}$ [OIII]/H$\beta$ is a lower limit (ie no [OIII] detected) whereas a downwards arrow is used when $\log_{10}$ [OIII]/H$\beta$ is an upper limit (ie no H$\beta$ detection).

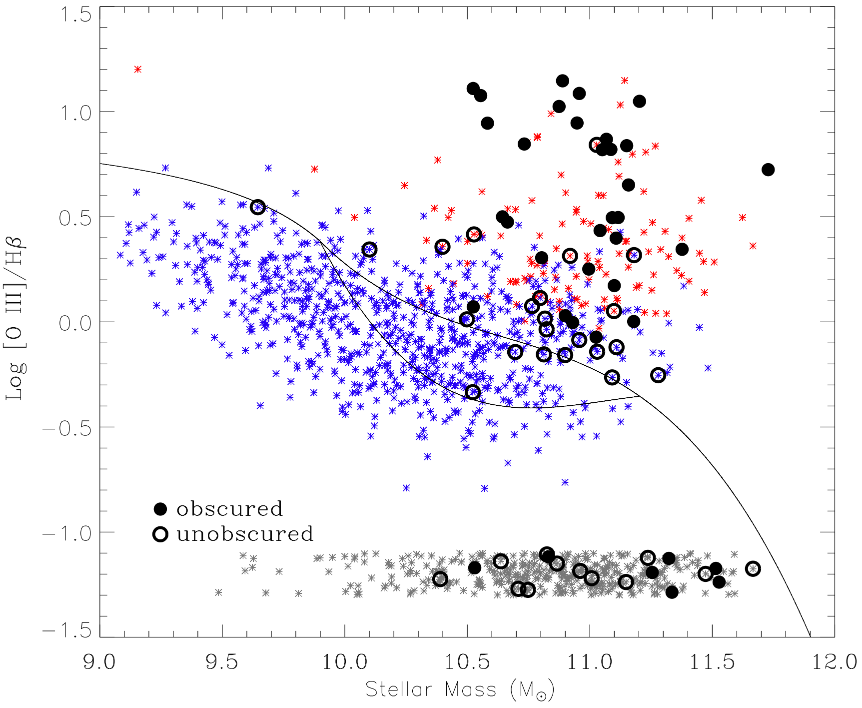

**Figure 5.17:** MEx diagnostic plot of optical emission line galaxies ($0.3 \leq z \leq 0.8$) which have been classified using the CEx diagnostic. Red crosses represent emission line AGN, blue crosses are SFGs and the grey crosses are QGs with no optical emission lines. An upwards arrow highlights sources for which $\log_{10}$ [OIII]/H$\beta$ is a lower limit (ie no [OIII] detected) whereas a downwards arrow is used when $\log_{10}$ [OIII]/H$\beta$ is an upper limit (ie no H$\beta$ detection). Obscured and unobscured X-ray sources have also been overlaid.

appear to be unobscured. Lowering the [OIII]/H$\beta$ also leaves the MEx AGN selection more vulnerable to contamination from SFGs. Revising the MEx AGN boundary upwards would greatly improve the agreement between the CEx and MEx AGN selections and hopefully increase the accuracy with which obscured AGN are identified.

**Table 5.11:** Results of stacking optically selected galaxies that do not have an X-ray counterpart binned according to stellar mass, $(U\text{-}B)_0$ colour and $L_{[OIII]}$. Galaxies lacking [OIII] and H$\beta$ emission (ie QGs) have been omitted from this analysis. All stacked fluxes are calculated assuming the emission has an unobscured power-law profile with $\Gamma = 1.4$. Column (1): subsample name; column (2): number of X-ray undetected galaxies that have been stacked; column (3): SN of the soft band (0.5-2.0 keV) stacked emission; column (4): SN of the hard band (2.0-7.0 keV) stacked emission; column (5): SN of the full band (0.5-7.0 keV) stacked emission; column (6): average flux per galaxy for the 0.5-2.0 keV derived from soft band stacked emission, units $10^{-17}$ erg s$^{-1}$ cm$^{-2}$; column (7): average flux per galaxy for the 2.0-10.0 keV derived from hard band stacked emission, units $10^{-17}$ erg s$^{-1}$ cm$^{-2}$; column (8): average flux per galaxy for the 0.5-10.0 keV derived from the full band stacked emission, units $10^{-17}$ erg s$^{-1}$ cm$^{-2}$; column (9): hardness ratio of stacked emission, HR=(H-S)/(H+S) where H and S are the hard- (2.0-7.0 keV) and soft-band (0.5-2.0 keV) stacked emission count rates respectively; column (10): median 0.5-2.0 keV luminosity for stacked sources, units $10^{39}$ erg s$^{-1}$; column (11): median 2.0-10.0 keV luminosity for stacked sources, units $10^{39}$ erg s$^{-1}$.

| | | Signal-to-Noise Ratio | | | Stacked Flux | | | | | |
|---|---|---|---|---|---|---|---|---|---|---|
| Class (1) | $N_{stack}$ (2) | $SN_{soft}$ (3) | $SN_{hard}$ (4) | $SN_{full}$ (5) | $F_{soft}$ (6) | $F_{hard}$ (7) | $F_{full}$ (8) | HR (9) | $L_{0.5-2keV}$ (10) | $L_{2-10keV}$ (11) |
| $M_* < 10^{10.0}$ | 121 | 5.92 | 2.16 | 5.63 | 0.95±0.16 | ... | 3.80±0.68 | ... | 4.45±0.75 | ... |
| $10^{10.0} \leq M_* < 10^{10.5}$ | 122 | 7.62 | 2.78 | 6.98 | 1.31±0.17 | ... | 4.72±0.68 | ... | 8.60±1.12 | ... |
| $10^{10.5} \leq M_* < 10^{11.0}$ | 90 | 8.40 | 4.52 | 8.87 | 1.86±0.22 | 5.90±1.29 | 7.64±0.86 | -0.30±0.11 | 14.43±1.71 | 26.99±5.90 |
| $M_* \geq 10^{11.0}$ | 33 | 17.78 | 9.44 | 19.78 | 13.85±0.78 | 27.96±2.94 | 48.34±2.43 | -0.49±0.06 | 33.23±1.87 | 110.52±11.62 |
| $(U\text{-}B)_0 < 0.6$ | 112 | 7.40 | 2.77 | 6.79 | 1.37±0.19 | ... | 4.92±0.73 | ... | 9.87±1.37 | ... |
| $0.6 \leq (U\text{-}B)_0 < 0.8$ | 138 | 7.85 | 2.49 | 6.81 | 1.28±0.16 | ... | 4.32±0.64 | ... | 5.65±0.71 | ... |
| $0.8 \leq (U\text{-}B)_0 < 1.1$ | 83 | 17.30 | 8.06 | 18.17 | 5.93±0.34 | 12.38±1.51 | 20.96±1.14 | -0.48±0.06 | 11.64±0.67 | 33.48±4.08 |
| $(U\text{-}B)_0 \geq 1.1$ | 33 | 6.40 | 5.59 | 8.30 | 2.58±0.40 | 13.79±2.46 | 13.35±1.60 | -0.05±0.12 | 17.32±2.69 | 77.38±13.80 |
| $L_{[0III]} < 10^{40.0}$ | 61 | 3.36 | 2.87 | 4.20 | 0.74±0.22 | ... | 4.00±0.95 | ... | 1.86±0.55 | ... |
| $10^{40.0} \leq L_{[0III]} < 10^{40.5}$ | 130 | 6.95 | 2.62 | 6.36 | 1.12±0.16 | ... | 4.09±0.65 | ... | 5.79±0.83 | ... |
| $10^{40.5} \leq L_{[0III]} < 10^{41.0}$ | 120 | 18.46 | 8.05 | 18.82 | 4.89±0.26 | 9.81±1.21 | 16.99±0.90 | -0.49±0.06 | 23.70±1.26 | 41.35±5.10 |
| $L_{[0III]} \geq 10^{41.0}$ | 55 | 7.79 | 4.11 | 8.21 | 2.42±0.31 | 7.05±1.72 | 9.58±1.17 | -0.34±0.12 | 25.27±3.24 | 75.08±18.32 |

Stacking the optical samples in bins of $(\mathrm{U}\text{-}\mathrm{B})_0$ and stellar mass provides additional insight into how the X-ray undetected AGN content might vary relative to these host galaxy properties (see Table 5.11). From this it is possible to infer the impact these relations have upon the CEx and MEx subsamples. Once again the QGs have been omitted from the optical sample for the purpose of this analysis. The bin sizes were calibrated such that they maximise the resolution across the $(\mathrm{U}\text{-}\mathrm{B})_0$ and galaxy mass distributions but still produced statistically robust stacking analyses. As demonstrated in Figures 5.14, the CEx subsamples occupy fairly distinct parameter spaces in $(\mathrm{U}\text{-}\mathrm{B})_0$ and, to a lesser extent, stellar mass. Therefore these results are discussed in the context of CEx classifications where possible. A similar discussion regarding the MEx classified galaxy composition is not possible because of the cross-contamination demonstrated in Figure 5.15.

The two lowest bins of $(\mathrm{U}\text{-}\mathrm{B})_0$ and stellar mass produce soft signals which lack statistically robust stacked emission in the hard band. The average $L_{0.5-2keV}$ of the stacked emission observed in all these bins are consistent, within errors, with the X-ray luminosities predicted from their average optical SFR estimates. There is no evidence to suggest AGN are contributing to the stacked X-ray emission of galaxies in these bins. This is consistent with the low X-ray detected fractions and the complete absence of obscured AGN activity among X-ray detected galaxies in these bins (see Table 5.10). The obvious conclusion is that the stacked X-ray emission of these galaxies is generated by star formation activity, which is consistent with their almost ubiquitous classification as CEx SFGs (see Figure 5.15).

Galaxies with $10^{10.5}\mathrm{M}_\odot \leq \mathrm{M}_* < 10^{11.0}\mathrm{M}_\odot$ produce the hardest stacked emission of all the mass binned subsamples, with a corresponding $\Gamma = 1.6^{+0.2}_{-0.2}$. The average X-ray luminosity of the stacked galaxies, however, is consistent with the X-ray luminosity predicted from the average optical SFR. Therefore, although the hard signal suggests that there are some X-ray undetected obscured AGN, they are vastly outnumbered by purely star forming galaxies. If not, the stacked emission would exhibit an excess in $L_{2-10keV}$ relative to star formation. The stacked emission of $\mathrm{M}_* \geq 10^{11.0}\mathrm{M}_\odot$ is softer than that of the $10^{10.5}\mathrm{M}_\odot \leq \mathrm{M}_* < 10^{11.0}\mathrm{M}_\odot$ galaxies, with $\Gamma = 2.0^{+0.1}_{-0.1}$ (consistent with CEx SFGs). The average stacked $L_{2-10keV}$ exceeds that of some of the X-ray detected galaxies in this sample. Note that this does not mean that the source detection is flawed. Instead this is because these galaxies are either at higher redshift or higher OAA than the lowest luminosity sources in the X-ray detected sample, pushing them below the detection limit of the survey. While there is definitive evidence for strong X-ray undetected AGN activity in this subsample it is consistent with primarily low luminosity unobscured AGN activity ($\Gamma \sim 1.9$).

Similar to the mass binned galaxies, the average fluxes and stacked luminosities of $(\mathrm{U}\text{-}\mathrm{B})_0$ binned galaxies are positively correlated to the $(\mathrm{U}\text{-}\mathrm{B})_0$ colour (ie. they increase as galaxies get redder). This rate of increase is not as striking as what has been observed when galaxies are binned by stellar mass. In all likelihood, the correlation between red galaxies and increased X-ray activity is in fact a byproduct of the close relation between galaxy mass and the (U-B)$_0$ colour (see Figures 5.14 and 5.15). The stacked emission of $0.8 \leq$ (U-B)$_0$ $< 1.1$ galaxies produces a soft signal with a predicted $\Gamma$ that is consistent with that of CEx SFG, the primary constituent of this bin. The average $L_{2-10keV}$ of the stacked sources exceed those predicted from their average optical SFR estimate. Therefore there must be some additional contribution to the stacked emission from AGN. The soft signal indicates these are most likely unobscured low luminosity AGN. The stacked emission of (U-B)$_0$ $\geq 1.1$ produces the hardest signal of any subsample subjected to broad band stacking analysis in this work. The predicted $\Gamma = 1.1^{+0.2}_{-0.2}$ is consistent (within errors) with that of CEx AGN, the dominant class of object in this (U-B)$_0$ colour range. The average X-ray luminosity of the stacked sources greatly exceeds the X-ray luminosity predicted from the average of the SFRs. Considered in conjunction with the hard stacked signal, this is clear evidence of a large population of X-ray undetected obscured and/or Compton thick AGN contributing to the stacked X-ray emission.

### 5.7.3 [OIII] luminosity as an indicator of intrinsic AGN luminosity

The luminosity of the high-excitation [OIII] emission line has long been used as an indicator of the intrinsic luminosity of AGN, proving effective in identifying obscured and Compton thick AGN (e.g. Bassani et al. 1999). X-ray detected sources demonstrate a clear positive correlation between their [OIII] luminosities and their absorption corrected X-ray luminosities (Figure 5.18). This is especially for obscured X-ray sources. Some unobscured low X-ray luminosity sources deviate from this trend. These galaxies are primarily identified as SFGs by the CEx classification technique.

In Figure 5.19 the ratio of the absorbed $L_{2-10keV}$ and $L_{[OIII]}$ (the so-called T-ratio) is plotted against the column density of the X-ray detected sources. The QG do not exhibit any apparent correlation between the T-ratio and column density. This is expected as by definition they lack [OIII] detections and thus invariably possess low $L_{[OIII]}$ values. The obscured CEx AGN exhibit a roughly negative correlation between the T-ratio and column density. Most importantly, the CEx AGN with the lowest T-ratios are all classified as Compton thick AGN. The obscured CEx SFGs also exhibit a similar trend but this observation is less statistically robust because of the small sample size. The T-ratio fails for CEx SFG when unobscured sources are included. The unobscured CEx SFGs with low T-ratio values are the same as those that were deviating from the $L_X - L_{[OIII]}$ trend in Figure 5.18. This suggests that strong star formation activity can produce significant [OIII] emission giving the appearance of an intrinsically luminous AGN. Therefore a population of obscured AGN candidates selected using the T-ratio would be contaminated by SFGs containing unobscured low luminosity AGN unless the [OIII] contribution due to star formation had been accounted for.

Figures 5.18 and 5.19 indicate that that $L_{[OIII]}$ is a suitable tracer of the intrinsic AGN luminosity as long as there is only limited star formation. Therefore by plotting the

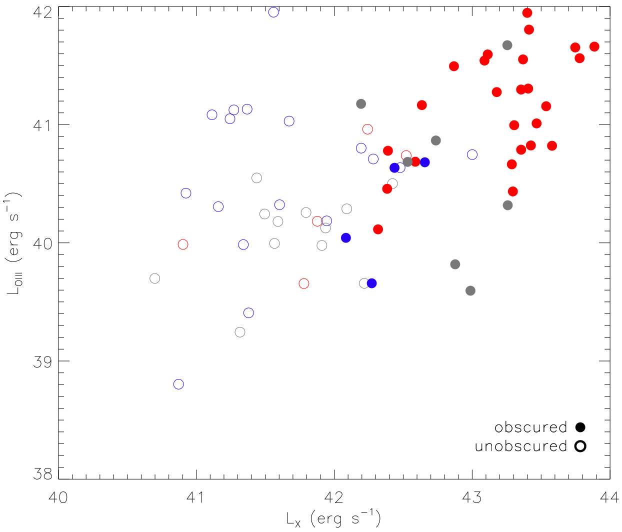

**Figure 5.18:** Plot of X-ray luminosity versus $L_{[OIII]}$ for X-ray detected optical emission line galaxies ($0.3 \leq z \leq 0.8$) which have been classified using the CEx diagnostic. Red circles represent emission line AGN, blue circles are SFGs and grey circles are QGs. Open circles represent galaxies which are unobscured while filled circles are obscured galaxies.

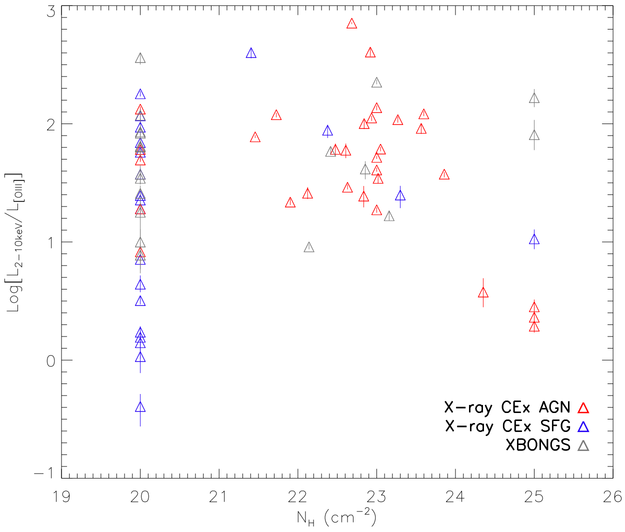

**Figure 5.19:** Plot of the T-ratio (Bassani et al., 1999) versus column density of best fitting X-ray model spectrum for CEx classified galaxies. Red triangles represent emission line AGN, blue triangles are SFGs and grey triangles are QGs.

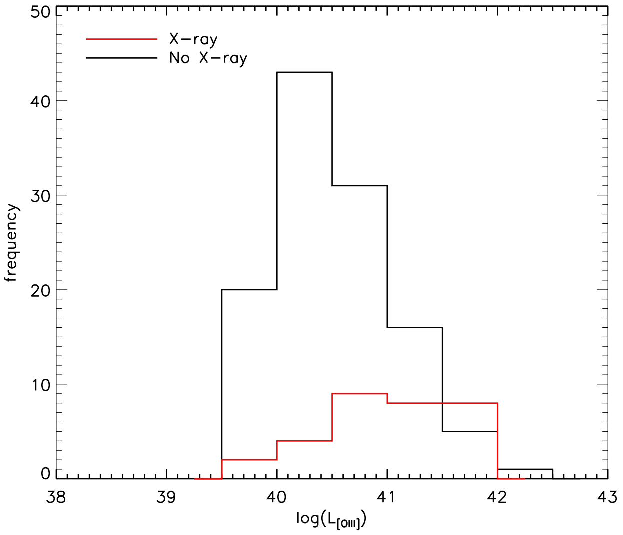

**Figure 5.20:** Histogram of $L_{[OIII]}$ for X-ray detected and X-ray undetected CEx AGN in the optical emission line galaxy sample ($0.3 \leq z \leq 0.8$). The red histogram represents X-ray detected CEx AGN while the black histogram represents the X-ray undetected CEx AGN.

$L_{[OIII]}$ distributions of CEx and MEx AGN it is possible to determine whether the X-ray detected sources are detected simply because their AGN are more intrinsically luminous. Figures 5.20 and 5.21 suggest the X-ray detected CEx and MEx AGN possess slightly higher $L_{[OIII]}$ on average than X-ray undetected CEx and MEx AGN. Therefore it could be that CEx and MEx AGN are detected in X-rays simply because they are more intrinsically luminous than the majority of X-ray undetected CEx and MEx AGN. However, there are still a significant number of [OIII] luminous sources among the X-ray undetected CEx and MEx AGN. These sources are strong heavily obscured AGN candidates, and produce hard emission when stacked. Therefore it is likely the levels of obscuration in X-ray undetected CEx and MEx AGN are the same, or possibly slightly higher, than those observed in the X-ray detected CEx and MEx AGN. This is consistent with the observations of Yan et al. (2011).

The X-ray detected and obscured AGN fractions do not appear to be strongly positively correlated to $L_{[OIII]}$ (see Table 5.10). This is due to [OIII] luminous blue SFGs diluting the AGN fraction in higher $L_{[OIII]}$ bins. Stacking the X-ray undetected galaxies binned by $L_{[OIII]}$ yields analogous results (5.11). The two lowest $L_{[OIII]}$ bins have soft stacked signals and fail to produce statistically significant stacked emission in the hard band and their average stacked luminosities are consistent with pure star formation. Stacking $10^{40.5}$erg s$^{-1}$ $\leq L_{[OIII]} < 10^{41.0}$erg s$^{-1}$ galaxies produces a soft signal with average X-ray luminosity that is consistent with the X-ray luminosity predicted from the average of their SFRs. Therefore there is no evidence of additional contributions from X-ray undetected AGN to the stacked signal. Stacking the $L_{[OIII]} \geq 10^{41.0}$erg s$^{-1}$ galaxies

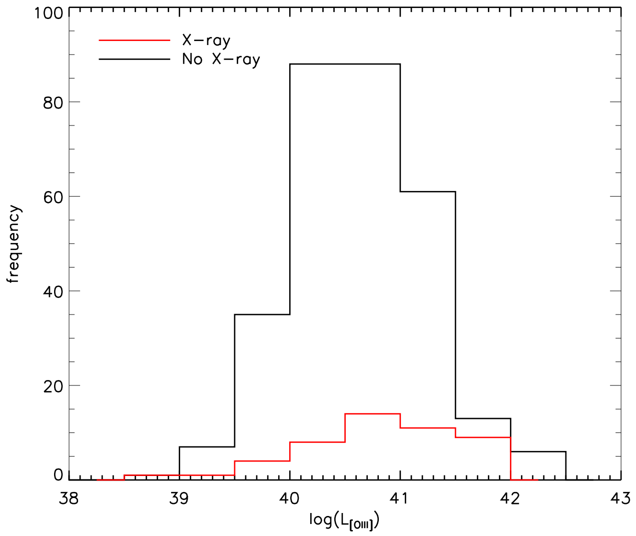

**Figure 5.21:** Histogram of $L_{[OIII]}$ for X-ray detected and X-ray undetected MEx AGN in the optical emission line galaxy sample ($0.3 \leq z \leq 0.8$). The red histogram represents X-ray detected MEx AGN while the black histogram represents the X-ray undetected MEx AGN.

produces a slightly harder stacked signal $\Gamma = 1.7^{+0.3}_{-0.3}$ and the average $L_{2-10keV}$ luminosity exceeds that predicted from the average SFR. Therefore it appears that there is an additional contribution to the hard X-ray emission from AGN, but the number of obscured AGN contributing to the stacked emission must be relatively small. As with the X-ray detected galaxies, it would appear that in order to better isolate AGN activity using the [OIII] luminosity, galaxies exhibiting strong star formation would need to be omitted to reduce contamination. In conclusion $L_{OIII}$ is only an effective measure of intrinsic AGN luminosity if the contamination due to star formation activity is properly accounted for.

## 5.8 Summary

In this chapter, the efficacy of the CEx and MEx optical emission line diagnostic techniques has been investigated using a sample of 1367 galaxies at $0.3 \leq z \leq 0.8$. Both techniques are modified versions of the BPT selection technique, which is limited to $z < 0.4$ when using optical spectroscopy. By combining X-ray spectral fitting and X-ray stacking analyses it has been possible to determine the accuracy with which the two techniques identify type 2 AGN. The main results are as follow:

(i) The CEx AGN subsample has the highest X-ray detected fraction of all the optical emission line galaxy subsamples ($21.1 \pm 3.4\%$). The X-ray detected fraction of the MEx AGN subsample possesses the second highest X-ray detected fraction ($13.8 \pm 1.9\%$) and is significantly elevated relative to all non-AGN subsamples. This is strong evidence for elevated AGN activity among the AGN subsamples. There are, however, very few X-ray detected MEx transition galaxies ($1.4 \pm 0.8\%$) which is peculiar given that this subsample is expected to isolate AGN-SF composite galaxies. This is because the MEx AGN subsample identifies practically all X-ray galaxies that are not identified as QGs (48/52).

(ii) Spectral fitting of the CEx AGN subsample reveals a high fraction of obscured AGN activity among the X-ray detected AGN, consistent with observations of type 2 AGN in the local universe (e.g. Kirhakos and Steiner 1990). There are not as many toroidally obscured AGN, however, as expected. The X-ray detected CEx SFGs are predominantly best fit by unobscured spectra and their obscured fraction is significantly lower than that of the control sample. The absorption corrected X-ray luminosities of CEx SFGs are lower than those of the CEx AGN but are still in excess of the X-ray luminosities expected from pure star formation. Therefore it would appear that the X-ray detected CEx SFGs are actually AGN-SF composite galaxies.

(iii) The MEx AGN have a lower obscured fraction ($62.5 \pm 7.0\%$) than the CEx AGN which is consistent with the obscured fraction control sample ($53.4 \pm 4.3\%$) at the $< 2\sigma$ level and lower than expected for type 2 AGN. This suggests the MEx AGN selection is not purely selecting type 2 AGN. The absorption corrected X-ray luminosities of all X-ray detected galaxies subjected to MEx analysis exceed those predicted from star formation which suggests that there are AGN residing in all these galaxies.

(iv) The X-ray detected QGs (XBONGs) exhibit similar obscuration properties to the control sample, consistent with the findings of Yan et al. (2011).

(v) All CEx AGN are classified as MEx AGN, but there are many CEx SFGs that are also classified as MEx AGN. The MEx transition galaxy subsample also entirely consists of CEx SFGs. In conclusion the CEx AGN diagnostic selects type 2 AGN more accurately than the MEx AGN diagnostic. Recalibrating the MEx AGN boundary could make it as effective as the CEx AGN selection. Generally, however, it appears that the MEx diagnostic is more sensitive to incorrect calibration because mass does not separate AGN and SFGs as effectively as $(U\text{-}B)_0$.

(vi) The uncanny ability of the CEx technique to identify and isolate obscured AGN may be related to its preferential selection of red galaxies. Emission from unobscured AGN causes their host galaxies to appear bluer, which biases the CEx selection technique against them. The MEx selection technique is independent of colour therefore is unbiased with respect to AGN obscuration.

(vii) Stacking X-ray undetected CEx AGN reveals a hard signal with effective $\Gamma = 1.1^{+0.3}_{-0.2}$. Additionally their average stacked X-ray luminosity exceeds that predicted from the average SFR of the stacked sources, which suggests a significant contribution from actively accreting AGN. This is indicative that a high concentration of obscured and Compton thick AGN, consistent with type 2 AGN, resides within the X-ray undetected CEx AGN subsample. The stacked signal of X-ray undetected CEx SFGs is much softer and their average stacked X-ray luminosities are consistent with their star formation activity (within errors).

(viii) Stacking X-ray undetected MEx AGN produces a soft stacked signal but the average stacked $L_{2-10keV}$ of these galaxies exceeds that predicted from their average SFRs. Therefore, while there appears to be actively accreting AGN in the MEx AGN subsample, the accuracy with which type 2 AGN are selected is severely diminished relative to the CEx AGN selection. The MEx transition galaxy and MEx SFG subsamples lack statistically significant stacked hard band emission and their stacked X-ray luminosities are lower than expected from their SFRs. Thus their is no evidence supporting a significant population actively accreting AGN within these subsamples.

(ix) The [OIII] luminosity is an effective tracer of the intrinsic luminosity of AGN subsamples and it appears that the T-ratio of galaxies identified as containing AGN (e.g. CEx AGN) could be used to identify which are heavily obscured. However, star formation also appears to contribute to [OIII] emission and therefore [OIII] luminosity is not an effective tracer of intrinsic AGN luminosity in SFGs unless star formation is corrected for.

# Chapter 6

# Summary

The aim of the work undertaken in this thesis was to improve our understanding of obscured AGN activity at high redshifts primarily using X-ray data from *Chandra*. Only with this information is it possible to investigate the extent to which obscured AGN activity affects the evolution of their host galaxies, if at all. Three separate studies have been attempted in order to accomplish this. The first was a study of the X-ray properties of mid-IR excess galaxies using deep X-ray surveys in the CDFS and CDFN (4Ms and 2Ms exposures respectively) in order to determine whether they represented strong obscured AGN candidates. The second study focused on the characteristics of AGN hosted within compact and extended massive galaxies at $z \sim 2$, the former of which having no direct analogue in the local universe. The third and final study investigated the efficiency with which optical emission line diagnostics, derived from the BPT technique, identify obscured AGN at $0.3 \leq z \leq 0.8$.

Chapter 3 presents the results of a reinvestigation of the X-ray properties of mid-IR excess sBzK galaxies at $z \sim 2$ that had previously been identified as strong obscured AGN candidates by Daddi et al. (2007). The key results of this investigation are as follows:

- Direct X-ray detections along with broad and narrow band stacking analyses reveal the obscured fraction of mid-IR excess sBzK galaxies to be very similar to that of the mid-IR non-excess sBzK galaxies.
- The X-ray detected fraction of the sample is found to be strongly correlated to the $L_{IR}$ estimate. Binning by $L_{IR}$ reveals that the elevated fraction of X-ray detected AGN among the mid-IR excess sBzKs is a consequence of their higher $L_{IR}$ relative to mid-IR non-excess sBzKs. Obscured X-ray detected AGN are distributed evenly between the mid IR excess and mid IR non-excess samples.
- The X-ray undetected IR excess and IR non-excess sBzKs produce composite spectra when stacked in narrow bands which are indicative of contributions from a mixture of obscured and unobscured AGN and star formation activity to the stacked emission. While it is not possible to disentangle the relative contributions of each process, there

is no evidence to indicate a strong concentration of Compton thick AGN among the IR excess sBzKs as predicted by Daddi et al. (2007).

- Broad band stacking analysis of X-ray undetected IR excess sBzKs using 4Ms CDFS produces a softer signal than was found by Daddi et al. (2007) using 1Ms CDFS observations. This is because there are a handful of hard sources that lie below the 1Ms CDFS detection limit and were thus included in the stacking of X-ray undetected sources, skewing the stacked emission to give the impression of significant obscured AGN activity. Consequently the stack became significantly softer when these galaxies were detected in the 4Ms CDFS and excluded from the broad band stacking.
- These results indicate that the discrepancy between SFRs derived from MIPS $24\mu m$ and UV observations is not due to AGN activity enhancing the mid-IR emission of the host galaxy. Instead it appears that at high values of $L_{IR}$, the SFR derived from MIPS $24\mu m$ emission is systematically overestimated, while dust corrected UV tends to underestimate the SFR in these galaxies.
- Passive BzKs have a higher X-ray detected fraction than star forming BzKs, thus there is no strong evidence of co-eval star formation and obscured AGN activity in sBzKs.

The research presented in Chapter 4 investigates the properties of AGN within massive galaxies at $z \sim 2$, in particular the relation to the galaxies' compactness. Evidence for two accretion modes is found within the massive galaxy population, with the nature of AGN accretion seemingly determined by galaxy compactness. More specifically:

- AGN in compact galaxies tend to be heavily obscured and highly X-ray luminous which suggests they are rapidly accreting material in dense gas rich environments. These AGN appear to be in a "transformative mode" of accretion (similar to the "quasar mode" outlined in Hopkins et al. 2005), in which violent AGN feedback rapidly quenches star formation activity in the host galaxy.
- AGN in extended galaxies tend to be unobscured and have lower X-ray luminosities than AGN in compact galaxies ($> 99\%$ confidence) which suggests they reside in low density, gas poor environments. These AGN appear to be in a "maintenance mode" (similar to the "radio-mode" outlined in Croton et al. 2006) in which the further star formation in the host galaxy is suppressed by gentle low luminosity AGN feedback.
- The merger rates at high redshifts appear to be too low to explain the strong size evolution observed in massive galaxies at $z \sim 2$. The violent feedback of "transformative mode" AGN could drive size evolution within the host compact galaxies, converting them into extended galaxies. The high fraction of AGN within the extended QG

sample suggests they would be the ultimate destination of AGN driven size evolution. Assuming this is the case, the AGN wind feedback mechanism proposed by Fan et al. (2008) would appear to produce galaxies with similar characteristics to extended QGs.

- Broad band stacking reveals additional obscured AGN activity within the X-ray undetected compact SFG sample as well as low luminosity AGN activity in the X-ray undetected extended SFG sample. The stacked emission of X-ray QGs is much weaker than that of X-ray undetected SFGs, but remains consistent with limited low luminosity AGN activity.

Chapter 5 presents a comparison of two optical emission line diagnostic techniques designed to target Type 2 AGN out to $z \sim 1$; colour-excitation (CEx) of Yan et al. (2011) and mass-excitation (MEx) of Juneau et al. (2011). On the basis of X-ray spectral fitting and X-ray stacking analyses it appears that the CEx selection technique selects Type 2 AGN more cleanly than the MEx technique. The current boundaries for the MEx AGN region allow for too much contamination from SFGs. The main results of this study are as follows:

- The CEx AGN selection identifies a high fraction of X-ray detected galaxies, nearly all of which are obscured. The MEx AGN selection also identifies many X-ray detected AGN, but a much larger fraction of these are unobscured.

- Stacking X-ray undetected CEx AGN produces a hard signal that is sufficiently X-ray luminous to suggest a large fraction of obscured, and possibly Compton thick, AGN. The X-ray undetected MEx AGN produce stacked emission that is more X-ray luminous than star formation predicts. The signal is much softer, however, than that of X-ray undetected CEx AGN, probably because of a lower concentration of obscured AGN. As such it appears the Type 2 AGN sample, generated by MEx selection contains many unobscured AGN and, possibly, is contaminated by SFGs.

- The X-ray detected CEx SFGs appear to be AGN-SF composite galaxies but the X-ray undetected CEx SFGs appear to be normal star forming galaxies. It is possible that some of the X-ray detected CEx SFGs would be reclassified as CEx AGN if their $(U\text{-}B)_0$ were corrected for contamination by AGN light. There are very few X-ray detected MEx transition galaxies and the X-ray undetected MEx transition galaxies do not exhibit stacked emission associated with substantial AGN activity.

- The $(U\text{-}B)_0$ colour proves to be an effective way to separate obscured (ie Type 2) AGN (red host galaxies) from unobscured AGN (blue host galaxies). This trend is consistent with observations of Nandra et al. (2007a). The stellar mass, however, does not provide the same level of separation between Type 2 AGN and transition galaxies/SFGs which makes the MEx selection more sensitive to the calibration of the

AGN selection boundary/cutoff. Empirical recalibration of the MEx AGN boundary for this galaxy sample could produce a more robust Type 2 AGN selection.

- The [O III] luminosity distributions of X-ray undetected CEx AGN and MEx AGN suggest that their obscured AGN fractions are similar to those of X-ray detected CEx AGN and MEx AGN respectively. While the [O III] luminosity can be an effective tracer of intrinsic AGN luminosity, it is vulnerable to contamination from star formation in SFGs. This can cause low luminosity AGN in SFGs to be confused with heavily obscured sources when using [O III] luminosity diagnostics (ie T-ratio Bassani et al. 1999) unless the [O III] emission contribution from star formation is corrected for.

## 6.1 Future work

There is wide scope for further studies that build upon the research presented in this thesis. For example, one of the key findings regarding mid-IR excess galaxies is the fallibility of $L_{IR}$ estimates made with a single photometric band (ie $24\mu m$). Applying a more rigorous model fitting procedure utilising longer wavelength IR emission from the PACS and SPIRE instruments aboard *Herschel* would greatly improve the accuracy of these measurements. Additional IR measurements could also be used to assess the contribution of an AGN dust torus component (e.g. Rowan-Robinson et al. 2005).

While there appear to be two distinct accretion modes for massive galaxies at $z \sim 2$, the sample size is small. Reproducing a similar analysis to Chapter 4 in other fields with deep X-ray data (e.g. 2Ms CDFN and 800ks EGS) would swell the number, producing a more statistically robust sample. This would allow better characterisation of the evolution of the compactness parameter as galaxies transition between “transformative mode” and “maintenance mode” accretion. It would also be worthwhile to examine the buildup of extended QGs relative to the decline of compact QGs and SFGs at $z < 1.4$ to search for further evidence of AGN feedback driving galaxy size evolution.

The results presented in Chapter 5 suggest that the MEx AGN selection is less effective at selecting obscured AGN than the CEx AGN selection. Using the CEx AGN distribution on the MEx diagnostic plot as a guide, a revised MEx AGN selection region could be devised to target obscured AGN with greater accuracy. Repeating the analysis in fields with deeper X-ray data has the potential to uncover further low luminosity AGN and obscured AGN activity implied by the hard stacked signal produced by X-ray undetected CEx AGN. The CEx and MEx plots probe a redshift range where XRB modelling (e.g. Gilli et al. 2007) suggest an as yet undetected population of obscured and Compton thick AGN may reside (due to the observed hard X-ray deficit). It is likely that the obscured AGN in the X-ray undetected CEx AGN sample are responsible for some of the X-ray background deficit. Therefore another study (similar to Worsley et al. 2005) could be carried out with the X-ray undetected CEx AGN included in the analysis to assess the fraction of the X-ray hard background deficit these galaxies resolve.

# References

Abraham, R. G., Nair, P., McCarthy, P. J., Glazebrook, K., Mentuch, E., Yan, H., Savaglio, S., Crampton, D., Murowinski, R., Juneau, S., Le Borgne, D., Carlberg, R. G., Jørgensen, I., Roth, K., Chen, H.-W., and Marzke, R. O.: 2007, ApJ **669**, 184

Adelberger, K. L., Steidel, C. C., Shapley, A. E., Hunt, M. P., Erb, D. K., Reddy, N. A., and Pettini, M.: 2004, ApJ **607**, 226

Aird, J., Coil, A. L., Moustakas, J., Blanton, M. R., Burles, S. M., Cool, R. J., Eisenstein, D. J., Smith, M. S. M., Wong, K. C., and Zhu, G.: 2012, ApJ **746**, 90

Aird, J., Nandra, K., Laird, E. S., Georgakakis, A., Ashby, M. L. N., Barmby, P., Coil, A. L., Huang, J.-S., Koekemoer, A. M., Steidel, C. C., and Willmer, C. N. A.: 2010, MNRAS **401**, 2531

Alexander, D. M., Bauer, F. E., Brandt, W. N., Daddi, E., Hickox, R. C., Lehmer, B. D., Luo, B., Xue, Y. Q., Young, M., Comastri, A., Del Moro, A., Fabian, A. C., Gilli, R., Goulding, A. D., Mainieri, V., Mullaney, J. R., Paolillo, M., Rafferty, D. A., Schneider, D. P., Shemmer, O., and Vignali, C.: 2011, ApJ **738**, 44

Alonso-Herrero, A., Pérez-González, P. G., Alexander, D. M., Rieke, G. H., Rigopoulou, D., Le Floc'h, E., Barmby, P., Papovich, C., Rigby, J. R., Bauer, F. E., Brandt, W. N., Egami, E., Willner, S. P., Dole, H., and Huang, J.-S.: 2006, ApJ **640**, 167

Alonso-Herrero, A., Quillen, A. C., Simpson, C., Efstathiou, A., and Ward, M. J.: 2001, AJ **121**, 1369

Antonucci, R.: 1993, ARA&A **31**, 473

Antonucci, R. R. J. and Miller, J. S.: 1985, ApJ **297**, 621

Arnaud, K. A.: 1996, in G. H. Jacoby and J. Barnes (eds.), *Astronomical Data Analysis Software and Systems V*, Vol. 101 of *Astronomical Society of the Pacific Conference Series*, p. 17

Arnaud, K. A., Branduardi-Raymont, G., Culhane, J. L., Fabian, A. C., Hazard, C., McGlynn, T. A., Shafer, R. A., Tennant, A. F., and Ward, M. J.: 1985, MNRAS **217**, 105

Arnouts, S., Walcher, C. J., Le Fèvre, O., Zamorani, G., Ilbert, O., Le Brun, V., Pozzetti, L., Bardelli, S., Tresse, L., Zucca, E., Charlot, S., Lamareille, F., McCracken, H. J., Bolzonella, M., Iovino, A., Lonsdale, C., Polletta, M., Surace, J., Bottini, D., Garilli, B., Maccagni, D., Picat, J. P., Scaramella, R., Scodeggio, M., Vettolani, G., Zanichelli, A., Adami, C., Cappi, A., Ciliegi, P., Contini, T., de la Torre, S., Foucaud, S., Franzetti, P., Gavignaud, I., Guzzo, L., Marano, B., Marinoni, C., Mazure, A., Meneux, B., Merighi, R., Paltani, S., Pellò, R., Pollo, A., Radovich, M., Temporin, S., and Vergani, D.: 2007, A&A **476**, 137

Aschenbach, B.: 1985, *Reports on Progress in Physics* **48**, 579

Awaki, H., Koyama, K., Inoue, H., and Halpern, J. P.: 1991, PASJ **43**, 195

Baldwin, J. A., Phillips, M. M., and Terlevich, R.: 1981, **93**, 5

Balogh, M. L., Morris, S. L., Yee, H. K. C., Carlberg, R. G., and Ellingson, E.: 1999, ApJ **527**, 54

Banerji, M., McMahon, R. G., Hewett, P. C., Alaghband-Zadeh, S., Gonzalez-Solares, E., Venemans, B. P., and Hawthorn, M. J.: 2012, MNRAS **427**, 2275

Barcons, X., Barret, D., Decourchelle, A., den Herder, J.-W., Dotani, T., Fabian, A. C., Fraga-Encinas, R., Kunieda, H., Lumb, D., Matt, G., Nandra, K., Piro, L., Rando, N., Sciortino, S., Smith, R. K., Strüder, L., Watson, M. G., White, N. E., and Willingale, R.: 2012, *ArXiv e-prints*

Barro, G., Faber, S. M., Pérez-González, P. G., Koo, D. C., Williams, C. C., Kocevski, D. D., Trump, J. R., Mozena, M., McGrath, E., van der Wel, A., Wuyts, S., Bell, E. F., Croton, D. J., Ceverino, D., Dekel, A., Ashby, M. L. N., Cheung, E., Ferguson, H. C., Fontana, A., Fang, J., Giavalisco, M., Grogin, N. A., Guo, Y., Hathi, N. P., Hopkins, P. F., Huang, K.-H., Koekemoer, A. M., Kartaltepe, J. S., Lee, K.-S., Newman, J. A., Porter, L. A., Primack, J. R., Ryan, R. E., Rosario, D., Somerville, R. S., Salvato, M., and Hsu, L.-T.: 2013, ApJ **765**, 104

Bassani, L., Dadina, M., Maiolino, R., Salvati, M., Risaliti, G., della Ceca, R., Matt, G., and Zamorani, G.: 1999, ApJS **121**, 473

Bauer, A. E., Conselice, C. J., Pérez-González, P. G., Grützbauch, R., Bluck, A. F. L., Buitrago, F., and Mortlock, A.: 2011, MNRAS **417**, 289

Bauer, F. E., Alexander, D. M., Brandt, W. N., Hornschemeier, A. E., Vignali, C., Garmire, G. P., and Schneider, D. P.: 2002, AJ **124**, 2351

Bell, E. F., McIntosh, D. H., Katz, N., and Weinberg, M. D.: 2003, ApJS **149**, 289

Bell, E. F., Naab, T., McIntosh, D. H., Somerville, R. S., Caldwell, J. A. R., Barden, M., Wolf, C., Rix, H.-W., Beckwith, S. V., Borch, A., Häussler, B., Heymans, C., Jahnke, K., Jogee, S., Koposov, S., Meisenheimer, K., Peng, C. Y., Sanchez, S. F., and Wisotzki, L.: 2006, ApJ **640**, 241

Bell, E. F., Papovich, C., Wolf, C., Le Floc'h, E., Caldwell, J. A. R., Barden, M., Egami, E., McIntosh, D. H., Meisenheimer, K., Pérez-González, P. G., Rieke, G. H., Rieke, M. J., Rigby, J. R., and Rix, H.-W.: 2005, ApJ **625**, 23

Bell, E. F., Wolf, C., Meisenheimer, K., Rix, H.-W., Borch, A., Dye, S., Kleinheinrich, M., Wisotzki, L., and McIntosh, D. H.: 2004, ApJ **608**, 752

Blanton, M. R.: 2006, ApJ **648**, 268

Blanton, M. R. and Roweis, S.: 2007, AJ **133**, 734

Bluck, A. F. L., Conselice, C. J., Bouwens, R. J., Daddi, E., Dickinson, M., Papovich, C., and Yan, H.: 2009, MNRAS **394**, L51

Bongiorno, A., Merloni, A., Brusa, M., Magnelli, B., Salvato, M., Mignoli, M., Zamorani, G., Fiore, F., Rosario, D., Mainieri, V., Hao, H., Comastri, A., Vignali, C., Balestra, I., Bardelli, S., Berta, S., Civano, F., Kampczyk, P., Le Floc'h, E., Lusso, E., Lutz, D., Pozzetti, L., Pozzi, F., Riguccini, L., Shankar, F., and Silverman, J.: 2012, MNRAS **427**, 3103

Bower, R. G., Benson, A. J., Malbon, R., Helly, J. C., Frenk, C. S., Baugh, C. M., Cole, S., and Lacey, C. G.: 2006, MNRAS **370**, 645

Boyle, B. J., Griffiths, R. E., Shanks, T., Stewart, G. C., and Georgantopoulos, I.: 1993, MNRAS **260**, 49

Boyle, B. J. and Terlevich, R. J.: 1998, MNRAS **293**, L49

Brammer, G. B., van Dokkum, P. G., and Coppi, P.: 2008, ApJ **686**, 1503

Brandt, W. N., Alexander, D. M., Hornschemeier, A. E., Garmire, G. P., Schneider, D. P., Barger, A. J., Bauer, F. E., Broos, P. S., Cowie, L. L., Townsley, L. K., Burrows, D. N., Chartas, G., Feigelson, E. D., Griffiths, R. E., Nousek, J. A., and Sargent, W. L. W.: 2001, AJ **122**, 2810

Brightman, M. and Nandra, K.: 2011a, MNRAS **413**, 1206

Brightman, M. and Nandra, K.: 2011b, MNRAS **414**, 3084

Brightman, M. and Nandra, K.: 2012, MNRAS **422**, 1166

Brightman, M. and Ueda, Y.: 2012, MNRAS **423**, 702

Brinkman, A. C., Kaastra, J. S., van der Meer, R. L. J., Kinkhabwala, A., Behar, E., Kahn, S. M., Paerels, F. B. S., and Sako, M.: 2002, A&A **396**, 761

Broos, P. S., Townsley, L. K., Feigelson, E. D., Getman, K. V., Bauer, F. E., and Garmire, G. P.: 2010, ApJ **714**, 1582

Brown, M. J. I., Dey, A., Jannuzi, B. T., Brand, K., Benson, A. J., Brodwin, M., Croton, D. J., and Eisenhardt, P. R.: 2007, ApJ **654**, 858

Brusa, M., Fiore, F., Santini, P., Grazian, A., Comastri, A., Zamorani, G., Hasinger, G., Merloni, A., Civano, F., Fontana, A., and Mainieri, V.: 2009, A&A **507**, 1277

Brusa, M., Gilli, R., and Comastri, A.: 2005, ApJL **621**, L5

Brusa, M., Zamorani, G., Comastri, A., Hasinger, G., Cappelluti, N., Civano, F., Finoguenov, A., Mainieri, V., Salvato, M., Vignali, C., Elvis, M., Fiore, F., Gilli, R., Impey, C. D., Lilly, S. J., Mignoli, M., Silverman, J., Trump, J., Urry, C. M., Bender, R., Capak, P., Huchra, J. P., Kneib, J. P., Koekemoer, A., Leauthaud, A., Lehmann, I., Massey, R., Matute, I., McCarthy, P. J., McCracken, H. J., Rhodes, J., Scoville, N. Z., Taniguchi, Y., and Thompson, D.: 2007, ApJS **172**, 353

Bruzual, G. and Charlot, S.: 2003, MNRAS **344**, 1000

Buitrago, F., Trujillo, I., Conselice, C. J., Bouwens, R. J., Dickinson, M., and Yan, H.: 2008, ApJL **687**, L61

Bundy, K., Ellis, R. S., Conselice, C. J., Taylor, J. E., Cooper, M. C., Willmer, C. N. A., Weiner, B. J., Coil, A. L., Noeske, K. G., and Eisenhardt, P. R. M.: 2006, ApJ **651**, 120

Bundy, K., Georgakakis, A., Nandra, K., Ellis, R. S., Conselice, C. J., Laird, E., Coil, A., Cooper, M. C., Faber, S. M., Newman, J. A., Pierce, C. M., Primack, J. R., and Yan, R.: 2008, ApJ **681**, 931

Busko, I. C. and Steiner, J. E.: 1988, MNRAS **232**, 525

Cagnoni, I., della Ceca, R., and Maccacaro, T.: 1998, ApJ **493**, 54

Calzetti, D., Armus, L., Bohlin, R. C., Kinney, A. L., Koornneef, J., and Storchi-Bergmann, T.: 2000, ApJ **533**, 682

Capak, P., Cowie, L. L., Hu, E. M., Barger, A. J., Dickinson, M., Fernandez, E., Giavalisco, M., Komiyama, Y., Kretchmer, C., McNally, C., Miyazaki, S., Okamura, S., and Stern, D.: 2004, AJ **127**, 180

Cardamone, C. N., van Dokkum, P. G., Urry, C. M., Taniguchi, Y., Gawiser, E., Brammer, G., Taylor, E., Damen, M., Treister, E., Cobb, B. E., Bond, N., Schawinski, K., Lira, P., Murayama, T., Saito, T., and Sumikawa, K.: 2010, ApJS **189**, 270

Cash, W.: 1979, ApJ **228**, 939

Cassata, P., Giavalisco, M., Guo, Y., Renzini, A., Ferguson, H., Koekemoer, A. M., Salimbeni, S., Scarlata, C., Grogin, N. A., Conselice, C. J., Dahlen, T., Lotz, J. M., Dickinson, M., and Lin, L.: 2011, ApJ **743**, 96

Cassata, P., Giavalisco, M., Williams, C. C., Guo, Y., Lee, B., Renzini, A., Ferguson, H., Faber, S. F., Barro, G., McIntosh, D. H., Lu, Y., Bell, E. F., Koo, D. C., Papovich, C. J., Ryan, R. E., Conselice, C. J., Grogin, N., Koekemoer, A., and Hathi, N. P.: 2013, *ArXiv e-prints*

Castellano, M., Salimbeni, S., Trevese, D., Grazian, A., Pentericci, L., Fiore, F., Fontana, A., Giallongo, E., Santini, P., Cristiani, S., Nonino, M., and Vanzella, E.: 2007, ApJ **671**, 1497

Chary, R. and Elbaz, D.: 2001, ApJ **556**, 562

Ciliegi, P., Zamorani, G., Hasinger, G., Lehmann, I., Szokoly, G., and Wilson, G.: 2003, A&A **398**, 901

Cimatti, A., Daddi, E., and Renzini, A.: 2006, A&A **453**, L29

Ciotti, L. and van Albada, T. S.: 2001, ApJL **552**, L13

Civano, F., Elvis, M., Brusa, M., Comastri, A., Salvato, M., Zamorani, G., Aldcroft, T., Bongiorno, A., Capak, P., Cappelluti, N., Cisternas, M., Fiore, F., Fruscione, A., Hao, H., Kartaltepe, J., Koekemoer, A., Gilli, R., Impey, C. D., Lanzuisi, G., Lusso, E., Mainieri, V., Miyaji, T., Lilly, S., Masters, D., Puccetti, S., Schawinski, K., Scoville, N. Z., Silverman, J., Trump, J., Urry, M., Vignali, C., and Wright, N. J.: 2012, ApJS **201**, 30

Coil, A. L., Newman, J. A., Kaiser, N., Davis, M., Ma, C.-P., Kocevski, D. D., and Koo, D. C.: 2004, ApJ **617**, 765

Comastri, A.: 2004, in A. J. Barger (ed.), *Supermassive Black Holes in the Distant Universe*, Vol. 308 of *Astrophysics and Space Science Library*, p. 245

Comastri, A., Gilli, R., and Hasinger, G.: 2005, *Experimental Astronomy* **20**, 41

Comastri, A., Ranalli, P., Iwasawa, K., Vignali, C., Gilli, R., Georgantopoulos, I., Barcons, X., Brandt, W. N., Brunner, H., Brusa, M., Cappelluti, N., Carrera, F. J., Civano, F., Fiore, F., Hasinger, G., Mainieri, V., Merloni, A., Nicastro, F., Paolillo, M., Puccetti, S., Rosati, P., Silverman, J. D., Tozzi, P., Zamorani, G., Balestra, I., Bauer, F. E., Luo, B., and Xue, Y. Q.: 2011, A&A **526**, L9

Comastri, A., Setti, G., Zamorani, G., and Hasinger, G.: 1995, A&A **296**, 1

Conselice, C. J.: 2006, ApJ **638**, 686

Cooper, M. C., Griffith, R. L., Newman, J. A., Coil, A. L., Davis, M., Dutton, A. A., Faber, S. M., Guhathakurta, P., Koo, D. C., Lotz, J. M., Weiner, B. J., Willmer, C. N. A., and Yan, R.: 2012, MNRAS **419**, 3018

Cooper, M. C., Newman, J. A., Weiner, B. J., Yan, R., Willmer, C. N. A., Bundy, K., Coil, A. L., Conselice, C. J., Davis, M., Faber, S. M., Gerke, B. F., Guhathakurta, P., Koo, D. C., and Noeske, K. G.: 2008, MNRAS **383**, 1058

Cox, T. J., Dutta, S. N., Di Matteo, T., Hernquist, L., Hopkins, P. F., Robertson, B., and Springel, V.: 2006, ApJ **650**, 791

Croton, D. J., Springel, V., White, S. D. M., De Lucia, G., Frenk, C. S., Gao, L., Jenkins, A., Kauffmann, G., Navarro, J. F., and Yoshida, N.: 2006, MNRAS **365**, 11

Crummy, J., Fabian, A. C., Gallo, L., and Ross, R. R.: 2006, MNRAS **365**, 1067

Daddi, E., Alexander, D. M., Dickinson, M., Gilli, R., Renzini, A., Elbaz, D., Cimatti, A., Chary, R., Frayer, D., Bauer, F. E., Brandt, W. N., Giavalisco, M., Grogin, N. A., Huynh, M., Kurk, J., Mignoli, M., Morrison, G., Pope, A., and Ravindranath, S.: 2007, ApJ **670**, 173

Daddi, E., Cimatti, A., Renzini, A., Fontana, A., Mignoli, M., Pozzetti, L., Tozzi, P., and Zamorani, G.: 2004, ApJ **617**, 746

Daddi, E., Dickinson, M., Chary, R., Pope, A., Morrison, G., Alexander, D. M., Bauer, F. E., Brandt, W. N., Giavalisco, M., Ferguson, H., Lee, K.-S., Lehmer, B. D., Papovich, C., and Renzini, A.: 2005, ApJL **631**, L13

Dale, D. A., Bendo, G. J., Engelbracht, C. W., Gordon, K. D., Regan, M. W., Armus, L., Cannon, J. M., Calzetti, D., Draine, B. T., Helou, G., Joseph, R. D., Kennicutt, R. C., Li, A., Murphy, E. J., Roussel, H., Walter, F., Hanson, H. M., Hollenbach, D. J., Jarrett, T. H., Kewley, L. J., Lamanna, C. A., Leitherer, C., Meyer, M. J., Rieke, G. H., Rieke, M. J., Sheth, K., Smith, J. D. T., and Thornley, M. D.: 2005, ApJ **633**, 857

Dale, D. A. and Helou, G.: 2002, ApJ **576**, 159

Damjanov, I., McCarthy, P. J., Abraham, R. G., Glazebrook, K., Yan, H., Mentuch, E., Le Borgne, D., Savaglio, S., Crampton, D., Murowinski, R., Juneau, S., Carlberg, R. G., Jørgensen, I., Roth, K., Chen, H.-W., and Marzke, R. O.: 2009, ApJ **695**, 101

D'Ammando, F., Bianchi, S., Jiménez-Bailón, E., and Matt, G.: 2008, A&A **482**, 499

Davis, M., Faber, S. M., Newman, J., Phillips, A. C., Ellis, R. S., Steidel, C. C., Conselice, C., Coil, A. L., Finkbeiner, D. P., Koo, D. C., Guhathakurta, P., Weiner, B., Schiavon, R., Willmer, C., Kaiser, N., Luppino, G. A., Wirth, G., Connolly, A., Eisenhardt, P., Cooper, M., and Gerke, B.: 2003, in P. Guhathakurta (ed.), *Society of Photo-Optical Instrumentation Engineers (SPIE) Conference Series*, Vol. 4834 of *Society of Photo-Optical Instrumentation Engineers (SPIE) Conference Series*, pp 161–172

de Santis, C., Grazian, A., Fontana, A., and Santini, P.: 2007, **12**, 271

Dickey, J. M. and Lockman, F. J.: 1990, ARA&A **28**, 215

Donley, J. L., Rieke, G. H., Pérez-González, P. G., and Barro, G.: 2008, ApJ **687**, 111

Donley, J. L., Rieke, G. H., Rigby, J. R., and Pérez-González, P. G.: 2005, ApJ **634**, 169

Eddington, Sir, A. S.: 1940, MNRAS **100**, 354

Efstathiou, A. and Rowan-Robinson, M.: 1995, MNRAS **273**, 649

Elbaz, D., Dickinson, M., Hwang, H. S., Díaz-Santos, T., Magdis, G., Magnelli, B., Le Borgne, D., Galliano, F., Pannella, M., Chanial, P., Armus, L., Charmandaris, V., Daddi, E., Aussel, H., Popesso, P., Kartaltepe, J., Altieri, B., Valtchanov, I., Coia, D., Dannerbauer, H., Dasyra, K., Leiton, R., Mazzarella, J., Alexander, D. M., Buat, V., Burgarella, D., Chary, R.-R., Gilli, R., Ivison, R. J., Juneau, S., Le Floc'h, E., Lutz, D., Morrison, G. E., Mullaney, J. R., Murphy, E., Pope, A., Scott, D., Brodwin, M., Calzetti, D., Cesarsky, C., Charlot, S., Dole, H., Eisenhardt, P., Ferguson, H. C., Förster Schreiber, N., Frayer, D., Giavalisco, M., Huynh, M., Koekemoer, A. M., Papovich, C., Reddy, N., Surace, C., Teplitz, H., Yun, M. S., and Wilson, G.: 2011, A&A **533**, A119

Elvis, M.: 2000, ApJ **545**, 63

Elvis, M., Wilkes, B. J., McDowell, J. C., Green, R. F., Bechtold, J., Willner, S. P., Oey, M. S., Polomski, E., and Cutri, R.: 1994, ApJS **95**, 1

Erb, D. K., Shapley, A. E., Steidel, C. C., Pettini, M., Adelberger, K. L., Hunt, M. P., Moorwood, A. F. M., and Cuby, J.-G.: 2003, ApJ **591**, 101

Faber, S. M., Tremaine, S., Ajhar, E. A., Byun, Y.-I., Dressler, A., Gebhardt, K., Grillmair, C., Kormendy, J., Lauer, T. R., and Richstone, D.: 1997, AJ **114**, 1771

Faber, S. M., Willmer, C. N. A., Wolf, C., Koo, D. C., Weiner, B. J., Newman, J. A., Im, M., Coil, A. L., Conroy, C., Cooper, M. C., Davis, M., Finkbeiner, D. P., Gerke, B. F., Gebhardt, K., Groth, E. J., Guhathakurta, P., Harker, J., Kaiser, N., Kassin, S., Kleinheinrich, M., Konidaris, N. P., Kron, R. G., Lin, L., Luppino, G., Madgwick, D. S., Meisenheimer, K., Noeske, K. G., Phillips, A. C., Sarajedini, V. L., Schiavon, R. P., Simard, L., Szalay, A. S., Vogt, N. P., and Yan, R.: 2007, ApJ **665**, 265

Fabian, A. C.: 2012, ARA&A **50**, 455

Fan, L., Lapi, A., Bressan, A., Bernardi, M., De Zotti, G., and Danese, L.: 2010, ApJ **718**, 1460

Fan, L., Lapi, A., De Zotti, G., and Danese, L.: 2008, ApJL **689**, L101

Ferrarese, L. and Merritt, D.: 2000, ApJL **539**, L9

Feruglio, C., Daddi, E., Fiore, F., Alexander, D. M., Piconcelli, E., and Malacaria, C.: 2011, ApJL **729**, L4

Feulner, G., Gabasch, A., Salvato, M., Drory, N., Hopp, U., and Bender, R.: 2005, ApJL **633**, L9

Fiore, F., Grazian, A., Santini, P., Puccetti, S., Brusa, M., Feruglio, C., Fontana, A., Giallongo, E., Comastri, A., Gruppioni, C., Pozzi, F., Zamorani, G., and Vignali, C.: 2008, ApJ **672**, 94

Fontana, A., Pozzetti, L., Donnarumma, I., Renzini, A., Cimatti, A., Zamorani, G., Menci, N., Daddi, E., Giallongo, E., Mignoli, M., Perna, C., Salimbeni, S., Saracco, P., Broadhurst, T., Cristiani, S., D'Odorico, S., and Gilmozzi, R.: 2004, A&A **424**, 23

Forman, W., Jones, C., and Tucker, W.: 1985, ApJ **293**, 102

Franx, M., Labbé, I., Rudnick, G., van Dokkum, P. G., Daddi, E., Förster Schreiber, N. M., Moorwood, A., Rix, H.-W., Röttgering, H., van der Wel, A., van der Werf, P., and van Starkenburg, L.: 2003, ApJL **587**, L79

Garmire, G. P., Bautz, M. W., Ford, P. G., Nousek, J. A., and Ricker, Jr., G. R.: 2003, in J. E. Truemper and H. D. Tananbaum (eds.), *Society of Photo-Optical Instrumentation Engineers (SPIE) Conference Series*, Vol. 4851 of *Society of Photo-Optical Instrumentation Engineers (SPIE) Conference Series*, pp 28–44

Gawiser, E., van Dokkum, P. G., Herrera, D., Maza, J., Castander, F. J., Infante, L., Lira, P., Quadri, R., Toner, R., Treister, E., Urry, C. M., Altmann, M., Assef, R., Christlein, D., Coppi, P. S., Durán, M. F., Franx, M., Galaz, G., Huerta, L., Liu, C., López, S., Méndez, R., Moore, D. C., Rubio, M., Ruiz, M. T., Toft, S., and Yi, S. K.: 2006, ApJS **162**, 1

Gebhardt, K., Bender, R., Bower, G., Dressler, A., Faber, S. M., Filippenko, A. V., Green, R., Grillmair, C., Ho, L. C., Kormendy, J., Lauer, T. R., Magorrian, J., Pinkney, J., Richstone, D., and Tremaine, S.: 2000, ApJL **539**, L13

Gehrels, N.: 1986, ApJ **303**, 336

Genzel, R., Thatte, N., Krabbe, A., Kroker, H., and Tacconi-Garman, L. E.: 1996, ApJ **472**, 153

Georgakakis, A., Nandra, K., Laird, E. S., Aird, J., and Trichas, M.: 2008, MNRAS **388**, 1205

Georgakakis, A., Rowan-Robinson, M., Nandra, K., Digby-North, J., Pérez-González, P. G., and Barro, G.: 2010, MNRAS **406**, 420

Georgantopoulos, I., Akylas, A., Georgakakis, A., and Rowan-Robinson, M.: 2009, A&A **507**, 747

Georgantopoulos, I., Georgakakis, A., Rowan-Robinson, M., and Rovilos, E.: 2008, A&A **484**, 671

Georgantopoulos, I., Stewart, G. C., Blair, A. J., Shanks, T., Griffiths, R. E., Boyle, B. J., Almaini, O., and Roche, N.: 1997, MNRAS **291**, 203

George, I. M. and Fabian, A. C.: 1991, MNRAS **249**, 352

Giacconi, R., Gursky, H., Paolini, F. R., and Rossi, B. B.: 1962, *Physical Review Letters* **9**, 439

Giacconi, R., Kellogg, E., Gorenstein, P., Gursky, H., and Tananbaum, H.: 1971, ApJL **165**, L27

Gierliński, M. and Done, C.: 2004, MNRAS **349**, L7

Gilli, R., Comastri, A., and Hasinger, G.: 2007, A&A **463**, 79

Gilli, R., Su, J., Norman, C., Vignali, C., Comastri, A., Tozzi, P., Rosati, P., Stiavelli, M., Brandt, W. N., Xue, Y. Q., Luo, B., Castellano, M., Fontana, A., Fiore, F., Mainieri, V., and Ptak, A.: 2011, ApJL **730**, L28

Glazebrook, K., Abraham, R. G., McCarthy, P. J., Savaglio, S., Chen, H.-W., Crampton, D., Murowinski, R., Jørgensen, I., Roth, K., Hook, I., Marzke, R. O., and Carlberg, R. G.: 2004, Nature **430**, 181

Goldader, J. D., Meurer, G., Heckman, T. M., Seibert, M., Sanders, D. B., Calzetti, D., and Steidel, C. C.: 2002, ApJ **568**, 651

Graessle, D. E., Blake, R. L., Burek, A. J., Dyson, S. E., Fitch, J. J., Schwartz, D. A., and Soufli, R.: 1998, in R. B. Hoover and A. B. Walker (eds.), *Society of Photo-Optical Instrumentation Engineers (SPIE) Conference Series*, Vol. 3444 of *Society of Photo-Optical Instrumentation Engineers (SPIE) Conference Series*, pp 140–159

Graessle, D. E., Soufli, R., Aquila, A. L., Gullikson, E. M., Blake, R. L., and Burek, A. J.: 2004, in K. A. Flanagan and O. H. W. Siegmund (eds.), *Society of Photo-Optical Instrumentation Engineers (SPIE) Conference Series*, Vol. 5165 of *Society of Photo-Optical Instrumentation Engineers (SPIE) Conference Series*, pp 469–481

Grazian, A., Fontana, A., de Santis, C., Nonino, M., Salimbeni, S., Giallongo, E., Cristiani, S., Gallozzi, S., and Vanzella, E.: 2006, A&A **449**, 951

Grogin, N. A., Kocevski, D. D., Faber, S. M., Ferguson, H. C., Koekemoer, A. M., Riess, A. G., Acquaviva, V., Alexander, D. M., Almaini, O., Ashby, M. L. N., Barden, M., Bell, E. F., Bournaud, F., Brown, T. M., Caputi, K. I., Casertano, S., Cassata, P., Castellano, M., Challis, P., Chary, R.-R., Cheung, E., Cirasuolo, M., Conselice, C. J., Roshan Cooray, A., Croton, D. J., Daddi, E., Dahlen, T., Davé, R., de Mello, D. F., Dekel, A., Dickinson, M., Dolch, T., Donley, J. L., Dunlop, J. S., Dutton, A. A., Elbaz, D., Fazio, G. G., Filippenko, A. V., Finkelstein, S. L., Fontana, A., Gardner, J. P., Garnavich, P. M., Gawiser, E., Giavalisco, M., Grazian, A., Guo, Y., Hathi, N. P., Häussler, B., Hopkins, P. F., Huang, J.-S., Huang, K.-H., Jha, S. W., Kartaltepe, J. S., Kirshner, R. P., Koo, D. C., Lai, K., Lee, K.-S., Li, W., Lotz, J. M., Lucas, R. A., Madau, P., McCarthy, P. J., McGrath, E. J., McIntosh, D. H., McLure, R. J., Mobasher, B., Moustakas, L. A., Mozena, M., Nandra, K., Newman, J. A., Niemi, S.-M., Noeske, K. G., Papovich, C. J., Pentericci, L., Pope, A., Primack, J. R., Rajan, A., Ravindranath, S., Reddy, N. A., Renzini, A., Rix, H.-W., Robaina, A. R., Rodney, S. A., Rosario, D. J., Rosati, P., Salimbeni, S., Scarlata, C., Siana, B., Simard, L., Smidt, J., Somerville, R. S., Spinrad, H., Straughn, A. N., Strolger, L.-G., Telford, O., Teplitz, H. I., Trump, J. R., van der Wel, A., Villforth, C., Wechsler, R. H., Weiner, B. J., Wiklind, T., Wild, V., Wilson, G., Wuyts, S., Yan, H.-J., and Yun, M. S.: 2011, ApJS **197**, 35

Guainazzi, M., Matt, G., and Perola, G. C.: 2005, A&A **444**, 119

Guo, Y., Ferguson, H. C., Giavalisco, M., Barro, G., Willner, S. P., Ashby, M. L. N., Dahlen, T., Donley, J. L., Faber, S. M., Fontana, A., Galametz, A., Grazian, A., Huang, K.-H., Kocevski, D. D., Koekemoer, A. M., Koo, D. C., McGrath, E. J., Peth, M., Salvato, M., Wuyts, S., Castellano, M., Cooray, A. R., Dickinson, M. E., Dunlop, J. S., Fazio, G. G., Gardner, J. P., Gawiser, E., Grogin, N. A., Hathi, N. P., Hsu, L.-T., Lee, K.-S., Lucas, R. A., Mobasher, B., Nandra, K., Newman, J. A., and van der Wel, A.: 2013, ApJS **207**, 24

Guo, Y., Giavalisco, M., Cassata, P., Ferguson, H. C., Dickinson, M., Renzini, A., Koekemoer, A., Grogin, N. A., Papovich, C., Tundo, E., Fontana, A., Lotz, J. M., and Salimbeni, S.: 2011, ApJ **735**, 18

Haardt, F. and Maraschi, L.: 1993, ApJ **413**, 507

Häring, N. and Rix, H.-W.: 2004, ApJL **604**, L89

Hasinger, G.: 1998, *Astronomische Nachrichten* **319**, 37

Hasinger, G., Miyaji, T., and Schmidt, M.: 2005, A&A **441**, 417

Hatziminaoglou, E., Omont, A., Stevens, J. A., Amblard, A., Arumugam, V., Auld, R., Aussel, H., Babbedge, T., Blain, A., Bock, J., Boselli, A., Buat, V., Burgarella, D., Castro-Rodríguez, N., Cava, A., Chanial, P., Clements, D. L., Conley, A., Conversi, L., Cooray, A., Dowell, C. D., Dwek, E., Dye, S., Eales, S., Elbaz, D., Farrah, D., Fox, M., Franceschini, A., Gear, W., Glenn, J., González Solares, E. A., Griffin, M., Halpern, M., Ibar, E., Isaak, K., Ivison, R. J., Lagache, G., Levenson, L., Lu, N., Madden, S., Maffei, B., Mainetti, G., Marchetti, L., Mortier, A. M. J., Nguyen, H. T., O'Halloran, B., Oliver, S. J., Page, M. J., Panuzzo, P., Papageorgiou, A., Pearson, C. P., Pérez-Fournon, I., Pohlen, M., Rawlings, J. I., Rigopoulou, D., Rizzo, D., Roseboom, I. G., Rowan-Robinson, M., Sanchez Portal, M., Schulz, B., Scott, D., Seymour, N., Shupe, D. L., Smith, A. J., Symeonidis, M., Trichas, M., Tugwell, K. E., Vaccari, M., Valtchanov, I., Vigroux, L., Wang, L., Ward, R., Wright, G., Xu, C. K., and Zemcov, M.: 2010, A&A **518**, L33

Heavens, A., Panter, B., Jimenez, R., and Dunlop, J.: 2004, Nature **428**, 625

Hogg, D. W., Baldry, I. K., Blanton, M. R., and Eisenstein, D. J.: 2002, *ArXiv Astrophysics e-prints*

Hopkins, P. F., Bundy, K., Murray, N., Quataert, E., Lauer, T. R., and Ma, C.-P.: 2009, MNRAS **398**, 898

Hopkins, P. F., Hernquist, L., Cox, T. J., Di Matteo, T., Martini, P., Robertson, B., and Springel, V.: 2005, ApJ **630**, 705

Hopkins, P. F., Hernquist, L., Cox, T. J., Di Matteo, T., Robertson, B., and Springel, V.: 2006, ApJS **163**, 1

Ilbert, O., Arnouts, S., McCracken, H. J., Bolzonella, M., Bertin, E., Le Fèvre, O., Mellier, Y., Zamorani, G., Pellò, R., Iovino, A., Tresse, L., Le Brun, V., Bottini, D., Garilli, B., Maccagni, D., Picat, J. P., Scaramella, R., Scodeggio, M., Vettolani, G., Zanichelli, A., Adami, C., Bardelli, S., Cappi, A., Charlot, S., Ciliegi, P., Contini, T., Cucciati, O., Foucaud, S., Franzetti, P., Gavignaud, I., Guzzo, L., Marano, B., Marinoni, C., Mazure, A., Meneux, B., Merighi, R., Paltani, S., Pollo, A., Pozzetti, L., Radovich, M., Zucca, E., Bondi, M., Bongiorno, A., Busarello, G., de La Torre, S., Gregorini, L., Lamareille, F., Mathez, G., Merluzzi, P., Ripepi, V., Rizzo, D., and Vergani, D.: 2006, A&A **457**, 841

Ilbert, O., Capak, P., Salvato, M., Aussel, H., McCracken, H. J., Sanders, D. B., Scoville, N., Kartaltepe, J., Arnouts, S., Le Floc'h, E., Mobasher, B., Taniguchi, Y., Lamareille, F., Leauthaud, A., Sasaki, S., Thompson, D., Zamojski, M., Zamorani, G., Bardelli, S., Bolzonella, M., Bongiorno, A., Brusa, M., Caputi, K. I., Carollo, C. M., Contini, T., Cook, R., Coppa, G., Cucciati, O., de la Torre, S., de Ravel, L., Franzetti, P., Garilli, B., Hasinger, G., Iovino, A., Kampczyk, P., Kneib, J.-P., Knobel, C., Kovac, K., Le Borgne, J. F., Le Brun, V., Fèvre, O. L., Lilly, S., Looper, D., Maier, C., Mainieri, V., Mellier, Y., Mignoli, M., Murayama, T., Pellò, R., Peng, Y., Pérez-Montero, E., Renzini, A., Ricciardelli, E., Schiminovich, D., Scodeggio, M., Shioya, Y., Silverman, J., Surace, J., Tanaka, M., Tasca, L., Tresse, L., Vergani, D., and Zucca, E.: 2009, ApJ **690**, 1236

Ishibashi, W., Fabian, A. C., and Canning, R. E. A.: 2013, MNRAS **431**, 2350

Ishisaki, Y., Ueda, Y., Yamashita, A., Ohashi, T., Lehmann, I., and Hasinger, G.: 2001, PASJ **53**, 445

Iwasawa, K. and Comastri, A.: 1998, MNRAS **297**, 1219

Juneau, S., Dickinson, M., Alexander, D. M., and Salim, S.: 2011, ApJ **736**, 104

Juneau, S., Dickinson, M., Bournaud, F., Alexander, D. M., Daddi, E., Mullaney, J. R., Magnelli, B., Kartaltepe, J. S., Hwang, H. S., Willner, S. P., Coil, A. L., Rosario, D. J., Trump, J. R., Weiner, B. J., Willmer, C. N. A., Cooper, M. C., Elbaz, D., Faber, S. M., Frayer, D. T., Kocevski, D. D., Laird, E. S., Monkiewicz, J. A., Nandra, K., Newman, J. A., Salim, S., and Symeonidis, M.: 2013, ApJ **764**, 176

Kajisawa, M., Ichikawa, T., Tanaka, I., Yamada, T., Akiyama, M., Suzuki, R., Tokoku, C., Katsuno Uchimoto, Y., Konishi, M., Yoshikawa, T., Nishimura, T., Omata, K., Ouchi, M., Iwata, I., Hamana, T., and Onodera, M.: 2011, PASJ **63**, 379

Kauffmann, G., Heckman, T. M., Tremonti, C., Brinchmann, J., Charlot, S., White, S. D. M., Ridgway, S. E., Brinkmann, J., Fukugita, M., Hall, P. B., Ivezić, Ž., Richards, G. T., and Schneider, D. P.: 2003, MNRAS **346**, 1055

Kaviraj, S., Cohen, S., Ellis, R. S., Peirani, S., Windhorst, R. A., O'Connell, R. W., Silk, J., Whitmore, B. C., Hathi, N. P., Ryan, R. E., Dopita, M. A., Frogel, J. A., and Dekel, A.: 2013a, MNRAS **428**, 925

Kaviraj, S., Cohen, S., Windhorst, R. A., Silk, J., O'Connell, R. W., Dopita, M. A., Dekel, A., Hathi, N. P., Straughn, A., and Rutkowski, M.: 2013b, MNRAS **429**, L40

Kaviraj, S., Tan, K.-M., Ellis, R. S., and Silk, J.: 2011, MNRAS **411**, 2148

Kennicutt, Jr., R. C.: 1998, ARA&A **36**, 189

Kereš, D., Katz, N., Weinberg, D. H., and Davé, R.: 2005, MNRAS **363**, 2

Kewley, L. J., Dopita, M. A., Sutherland, R. S., Heisler, C. A., and Trevena, J.: 2001, ApJ **556**, 121

Kewley, L. J. and Ellison, S. L.: 2008, ApJ **681**, 1183

Kewley, L. J., Groves, B., Kauffmann, G., and Heckman, T.: 2006, MNRAS **372**, 961

Khachikian, E. Y. and Weedman, D. W.: 1974, ApJ **192**, 581

Khochfar, S. and Silk, J.: 2006a, ApJL **648**, L21

Khochfar, S. and Silk, J.: 2006b, MNRAS **370**, 902

King, A.: 2003, ApJL **596**, L27

Kinkhabwala, A., Sako, M., Behar, E., Kahn, S. M., Paerels, F., Brinkman, A. C., Kaastra, J. S., Gu, M. F., and Liedahl, D. A.: 2002, ApJ **575**, 732

Kinney, A. L., Calzetti, D., Bohlin, R. C., McQuade, K., Storchi-Bergmann, T., and Schmitt, H. R.: 1996, ApJ **467**, 38

Kirhakos, S. D. and Steiner, J. E.: 1990, AJ **99**, 1722

Kocevski, D. D., Faber, S. M., Mozena, M., Koekemoer, A. M., Nandra, K., Rangel, C., Laird, E. S., Brusa, M., Wuyts, S., Trump, J. R., Koo, D. C., Somerville, R. S., Bell, E. F., Lotz, J. M., Alexander, D. M., Bournaud, F., Conselice, C. J., Dahlen, T., Dekel, A., Donley, J. L., Dunlop, J. S., Finoguenov, A., Georgakakis, A., Giavalisco, M., Guo, Y., Grogin, N. A., Hathi, N. P., Juneau, S., Kartaltepe, J. S., Lucas, R. A., McGrath, E. J., McIntosh, D. H., Mobasher, B., Robaina, A. R., Rosario, D., Straughn, A. N., van der Wel, A., and Villforth, C.: 2012, ApJ **744**, 148

Koekemoer, A. M., Faber, S. M., Ferguson, H. C., Grogin, N. A., Kocevski, D. D., Koo, D. C., Lai, K., Lotz, J. M., Lucas, R. A., McGrath, E. J., Ogaz, S., Rajan, A., Riess, A. G., Rodney, S. A., Strolger, L., Casertano, S., Castellano, M., Dahlen, T., Dickinson, M., Dolch, T., Fontana, A., Giavalisco, M., Grazian, A., Guo, Y., Hathi, N. P., Huang, K.-H., van der Wel, A., Yan, H.-J., Acquaviva, V., Alexander, D. M., Almaini, O., Ashby, M. L. N., Barden, M., Bell, E. F., Bournaud, F., Brown, T. M., Caputi, K. I., Cassata, P., Challis, P. J., Chary, R.-R., Cheung, E., Cirasuolo, M., Conselice, C. J., Roshan Cooray, A., Croton, D. J., Daddi, E., Davé, R., de Mello, D. F., de Ravel, L., Dekel, A., Donley, J. L., Dunlop, J. S., Dutton, A. A., Elbaz, D., Fazio, G. G., Filippenko, A. V., Finkelstein, S. L., Frazer, C., Gardner, J. P., Garnavich, P. M., Gawiser, E., Gruetzbauch, R., Hartley, W. G., Häussler, B., Herrington, J., Hopkins, P. F., Huang, J.-S., Jha, S. W., Johnson, A., Kartaltepe, J. S., Khostovan, A. A., Kirshner, R. P., Lani, C., Lee, K.-S., Li, W., Madau, P., McCarthy, P. J., McIntosh, D. H., McLure, R. J., McPartland, C., Mobasher, B., Moreira, H., Mortlock, A., Moustakas, L. A., Mozena, M., Nandra, K., Newman, J. A., Nielsen, J. L., Niemi, S., Noeske, K. G., Papovich, C. J., Pentericci, L., Pope, A., Primack, J. R., Ravindranath, S., Reddy, N. A., Renzini, A., Rix, H.-W., Robaina, A. R., Rosario, D. J., Rosati, P., Salimbeni, S., Scarlata, C., Siana, B., Simard, L., Smidt, J., Snyder, D., Somerville, R. S., Spinrad, H., Straughn, A. N., Telford, O., Teplitz, H. I., Trump, J. R., Vargas, C., Villforth, C., Wagner, C. R., Wandro, P., Wechsler, R. H., Weiner, B. J., Wiklind, T., Wild, V., Wilson, G., Wuyts, S., and Yun, M. S.: 2011, ApJS **197**, 36

Kormendy, J. and Gebhardt, K.: 2001, in J. C. Wheeler and H. Martel (eds.), *20th Texas Symposium on relativistic astrophysics*, Vol. 586 of *American Institute of Physics Conference Series*, pp 363–381

Kormendy, J. and Richstone, D.: 1995, ARA&A **33**, 581

Kriek, M., van der Wel, A., van Dokkum, P. G., Franx, M., and Illingworth, G. D.: 2008, ApJ **682**, 896

Kriek, M., van Dokkum, P. G., Franx, M., Illingworth, G. D., and Magee, D. K.: 2009, ApJL **705**, L71

Krolik, J. H. and Kallman, T. R.: 1987, ApJL **320**, L5

Lacy, M., Storrie-Lombardi, L. J., Sajina, A., Appleton, P. N., Armus, L., Chapman, S. C., Choi, P. I., Fadda, D., Fang, F., Frayer, D. T., Heinrichsen, I., Helou, G., Im, M., Marleau, F. R., Masci, F., Shupe, D. L., Soifer, B. T., Surace, J., Teplitz, H. I., Wilson, G., and Yan, L.: 2004, ApJS **154**, 166

Lagache, G., Dole, H., and Puget, J.-L.: 2003, MNRAS **338**, 555

Laidler, V. G., Papovich, C., Grogin, N. A., Idzi, R., Dickinson, M., Ferguson, H. C., Hilbert, B., Clubb, K., and Ravindranath, S.: 2007, **119**, 1325

Laird, E. S., Nandra, K., Adelberger, K. L., Steidel, C. C., and Reddy, N. A.: 2005, MNRAS **359**, 47

Laird, E. S., Nandra, K., Georgakakis, A., Aird, J. A., Barmby, P., Conselice, C. J., Coil, A. L., Davis, M., Faber, S. M., Fazio, G. G., Guhathakurta, P., Koo, D. C., Sarajedini, V., and Willmer, C. N. A.: 2009, ApJS **180**, 102

Lawrence, A.: 1991, MNRAS **252**, 586

Lawrence, A. and Elvis, M.: 1982, ApJ **256**, 410

Lightman, A. P. and White, T. R.: 1988, ApJ **335**, 57

Lilly, S. J., Le Fevre, O., Hammer, F., and Crampton, D.: 1996, ApJL **460**, L1

Lin, L., Koo, D. C., Weiner, B. J., Chiueh, T., Coil, A. L., Lotz, J., Conselice, C. J., Willner, S. P., Smith, H. A., Guhathakurta, P., Huang, J.-S., Le Floc'h, E., Noeske, K. G., Willmer, C. N. A., Cooper, M. C., and Phillips, A. C.: 2007, ApJL **660**, L51

Longhetti, M., Saracco, P., Severgnini, P., Della Ceca, R., Mannucci, F., Bender, R., Drory, N., Feulner, G., and Hopp, U.: 2007, MNRAS **374**, 614

Luo, B., Brandt, W. N., Xue, Y. Q., Alexander, D. M., Brusa, M., Bauer, F. E., Comastri, A., Fabian, A. C., Gilli, R., Lehmer, B. D., Rafferty, D. A., Schneider, D. P., and Vignali, C.: 2011, ApJ **740**, 37

Maccacaro, T., della Ceca, R., Gioia, I. M., Morris, S. L., Stocke, J. T., and Wolter, A.: 1991, ApJ **374**, 117

Madau, P., Ferguson, H. C., Dickinson, M. E., Giavalisco, M., Steidel, C. C., and Fruchter, A.: 1996, MNRAS **283**, 1388

Magdziarz, P. and Zdziarski, A. A.: 1995, MNRAS **273**, 837

Magnelli, B., Elbaz, D., Chary, R. R., Dickinson, M., Le Borgne, D., Frayer, D. T., and Willmer, C. N. A.: 2009, A&A **496**, 57

Magorrian, J., Tremaine, S., Richstone, D., Bender, R., Bower, G., Dressler, A., Faber, S. M., Gebhardt, K., Green, R., Grillmair, C., Kormendy, J., and Lauer, T.: 1998, AJ **115**, 2285

Mainieri, V., Bongiorno, A., Merloni, A., Aller, M., Carollo, M., Iwasawa, K., Koekemoer, A. M., Mignoli, M., Silverman, J. D., Bolzonella, M., Brusa, M., Comastri, A., Gilli, R., Halliday, C., Ilbert, O., Lusso, E., Salvato, M., Vignali, C., Zamorani, G., Contini, T., Kneib, J.-P., Le Fèvre, O., Lilly, S., Renzini, A., Scodeggio, M., Balestra, I., Bardelli, S., Caputi, K., Coppa, G., Cucciati, O., de la Torre, S., de Ravel, L., Franzetti, P., Garilli, B., Iovino, A., Kampczyk, P., Knobel, C., Kovač, K., Lamareille, F., Le Borgne, J.-F., Le Brun, V., Maier, C., Nair, P., Pello, R., Peng, Y., Perez Montero, E., Pozzetti, L., Ricciardelli, E., Tanaka, M., Tasca, L., Tresse, L., Vergani, D., Zucca, E., Aussel, H., Capak, P., Cappelluti, N., Elvis, M., Fiore, F., Hasinger, G., Impey, C., Le Floc'h, E., Scoville, N., Taniguchi, Y., and Trump, J.: 2011, A&A **535**, A80

Maiolino, R. and Rieke, G. H.: 1995, ApJ **454**, 95

Maiolino, R., Salvati, M., Bassani, L., Dadina, M., della Ceca, R., Matt, G., Risaliti, G., and Zamorani, G.: 1998, A&A **338**, 781

Malkan, M. A., Gorjian, V., and Tam, R.: 1998, ApJS **117**, 25

Man, A. W. S., Toft, S., Zirm, A. W., Wuyts, S., and van der Wel, A.: 2012, ApJ **744**, 85

Mancini, C., Daddi, E., Renzini, A., Salmi, F., McCracken, H. J., Cimatti, A., Onodera, M., Salvato, M., Koekemoer, A. M., Aussel, H., Le Floc'h, E., Willott, C., and Capak, P.: 2010, MNRAS **401**, 933

Marconi, A. and Hunt, L. K.: 2003, ApJL **589**, L21

Marshall, F. E., Boldt, E. A., Holt, S. S., Miller, R. B., Mushotzky, R. F., Rose, L. A., Rothschild, R. E., and Serlemitsos, P. J.: 1980, ApJ **235**, 4

Matt, G., Brandt, W. N., and Fabian, A. C.: 1996, MNRAS **280**, 823

Matt, G., Guainazzi, M., Frontera, F., Bassani, L., Brandt, W. N., Fabian, A. C., Fiore, F., Haardt, F., Iwasawa, K., Maiolino, R., Malaguti, G., Marconi, A., Matteuzzi, A., Molendi, S., Perola, G. C., Piraino, S., and Piro, L.: 1997, A&A **325**, L13

McCarthy, P. J.: 2004, ARA&A **42**, 477

McLure, R. J., Jarvis, M. J., Targett, T. A., Dunlop, J. S., and Best, P. N.: 2006, MNRAS **368**, 1395

Miller, J. S. and Antonucci, R. R. J.: 1983, ApJL **271**, L7

Miyaji, T., Hasinger, G., and Schmidt, M.: 2000, A&A **353**, 25

Mortlock, D. J., Warren, S. J., Venemans, B. P., Patel, M., Hewett, P. C., McMahon, R. G., Simpson, C., Theuns, T., Gonzáles-Solares, E. A., Adamson, A., Dye, S., Hambly, N. C., Hirst, P., Irwin, M. J., Kuiper, E., Lawrence, A., and Röttgering, H. J. A.: 2011, Nature **474**, 616

Moustakas, J., Kennicutt, Jr., R. C., and Tremonti, C. A.: 2006, ApJ **642**, 775

Mushotzky, R. F., Cowie, L. L., Barger, A. J., and Arnaud, K. A.: 2000, Nature **404**, 459

Naab, T., Johansson, P. H., and Ostriker, J. P.: 2009, ApJL **699**, L178

Naab, T. and Ostriker, J. P.: 2009, ApJ **690**, 1452

Nandra, K., Georgakakis, A., Willmer, C. N. A., Cooper, M. C., Croton, D. J., Davis, M., Faber, S. M., Koo, D. C., Laird, E. S., and Newman, J. A.: 2007a, ApJL **660**, L11

Nandra, K., George, I. M., Mushotzky, R. F., Turner, T. J., and Yaqoob, T.: 1997, ApJ **477**, 602

Nandra, K., Laird, E. S., Adelberger, K., Gardner, J. P., Mushotzky, R. F., Rhodes, J., Steidel, C. C., Teplitz, H. I., and Arnaud, K. A.: 2005, MNRAS **356**, 568

Nandra, K., Mushotzky, R. F., Arnaud, K., Steidel, C. C., Adelberger, K. L., Gardner, J. P., Teplitz, H. I., and Windhorst, R. A.: 2002, ApJ **576**, 625

Nandra, K., O'Neill, P. M., George, I. M., and Reeves, J. N.: 2007b, MNRAS **382**, 194

Nandra, K. and Pounds, K. A.: 1994, MNRAS **268**, 405

Newman, A. B., Ellis, R. S., Bundy, K., and Treu, T.: 2012, ApJ **746**, 162

Nipoti, C., Londrillo, P., and Ciotti, L.: 2003, MNRAS **342**, 501

Nordon, R., Lutz, D., Genzel, R., Berta, S., Wuyts, S., Magnelli, B., Altieri, B., Andreani, P., Aussel, H., Bongiovanni, A., Cepa, J., Cimatti, A., Daddi, E., Fadda, D., Förster Schreiber, N. M., Lagache, G., Maiolino, R., Pérez García, A. M., Poglitsch, A., Popesso, P., Pozzi, F., Rodighiero, G., Rosario, D., Saintonge, A., Sanchez-Portal, M., Santini, P., Sturm, E., Tacconi, L. J., Valtchanov, I., and Yan, L.: 2012, ApJ **745**, 182

Olsen, K. P., Rasmussen, J., Toft, S., and Zirm, A. W.: 2013, ApJ **764**, 4

Osmer, P. S., Porter, A. C., and Green, R. F.: 1994, ApJ **436**, 678

Peng, C. Y., Ho, L. C., Impey, C. D., and Rix, H.-W.: 2002, AJ **124**, 266

Penston, M. V. and Perez, E.: 1984, MNRAS **211**, 33P

Persic, M. and Rephaeli, Y.: 2002, A&A **382**, 843

Pier, E. A. and Krolik, J. H.: 1992, ApJ **401**, 99

Pier, E. A. and Krolik, J. H.: 1993, ApJ **418**, 673

Pimbblet, K. A. and Jensen, P. C.: 2012, MNRAS **426**, 1632

Pogge, R. W.: 1988, ApJ **328**, 519

Polletta, M., Weedman, D., Hönig, S., Lonsdale, C. J., Smith, H. E., and Houck, J.: 2008, ApJ **675**, 960

Pounds, K. A., Nandra, K., Stewart, G. C., George, I. M., and Fabian, A. C.: 1990, Nature **344**, 132

Ranalli, P., Comastri, A., and Setti, G.: 2003, A&A **399**, 39

Rangel, C., Nandra, K., Laird, E. S., and Orange, P.: 2013, MNRAS **428**, 3089

Reddy, N. A., Erb, D. K., Steidel, C. C., Shapley, A. E., Adelberger, K. L., and Pettini, M.: 2005, ApJ **633**, 748

Rees, M. J.: 1984, ARA&A **22**, 471

Reynolds, C. S., Fabian, A. C., Makishima, K., Fukazawa, Y., and Tamura, T.: 1994, MNRAS **268**, L55

Rigby, J. R., Rieke, G. H., Donley, J. L., Alonso-Herrero, A., and Pérez-González, P. G.: 2006, ApJ **645**, 115

Risaliti, G., Gilli, R., Maiolino, R., and Salvati, M.: 2000, A&A **357**, 13

Risaliti, G., Maiolino, R., and Salvati, M.: 1999, ApJ **522**, 157

Rosario, D. J., Mozena, M., Wuyts, S., Nandra, K., Koekemoer, A., McGrath, E., Hathi, N. P., Dekel, A., Donley, J., Dunlop, J. S., Faber, S. M., Ferguson, H., Giavalisco, M., Grogin, N., Guo, Y., Kocevski, D. D., Koo, D. C., Laird, E., Newman, J., Rangel, C., and Somerville, R.: 2013a, ApJ **763**, 59

Rosario, D. J., Santini, P., Lutz, D., Netzer, H., Bauer, F. E., Berta, S., Magnelli, B., Popesso, P., Alexander, D. M., Brandt, W. N., Genzel, R., Maiolino, R., Mullaney, J. R., Nordon, R., Saintonge, A., Tacconi, L., and Wuyts, S.: 2013b, ApJ **771**, 63

Rowan-Robinson, M.: 1977, ApJ **213**, 635

Rowan-Robinson, M., Babbedge, T., Surace, J., Shupe, D., Fang, F., Lonsdale, C., Smith, G., Polletta, M., Siana, B., Gonzalez-Solares, E., Xu, K., Owen, F., Davoodi, P., Dole, H., Domingue, D., Efstathiou, A., Farrah, D., Fox, M., Franceschini, A., Frayer, D., Hatziminaoglou, E., Masci, F., Morrison, G., Nandra, K., Oliver, S., Onyett, N., Padgett, D., Perez-Fournon, I., Serjeant, S., Stacey, G., and Vaccari, M.: 2005, AJ **129**, 1183

Salvato, M., Hasinger, G., Ilbert, O., Zamorani, G., Brusa, M., Scoville, N. Z., Rau, A., Capak, P., Arnouts, S., Aussel, H., Bolzonella, M., Buongiorno, A., Cappelluti, N., Caputi, K., Civano, F., Cook, R., Elvis, M., Gilli, R., Jahnke, K., Kartaltepe, J. S., Impey, C. D., Lamareille, F., Le Floc'h, E., Lilly, S., Mainieri, V., McCarthy, P., McCracken, H., Mignoli, M., Mobasher, B., Murayama, T., Sasaki, S., Sanders, D. B., Schiminovich, D., Shioya, Y., Shopbell, P., Silverman, J., Smolčić, V., Surace, J., Taniguchi, Y., Thompson, D., Trump, J. R., Urry, M., and Zamojski, M.: 2009, ApJ **690**, 1250

Salvato, M., Ilbert, O., Hasinger, G., Rau, A., Civano, F., Zamorani, G., Brusa, M., Elvis, M., Vignali, C., Aussel, H., Comastri, A., Fiore, F., Le Floc'h, E., Mainieri, V., Bardelli, S., Bolzonella, M., Bongiorno, A., Capak, P., Caputi, K., Cappelluti, N., Carollo, C. M., Contini, T., Garilli, B., Iovino, A., Fotopoulou, S., Fruscione, A., Gilli, R., Halliday, C., Kneib, J.-P., Kakazu, Y., Kartaltepe, J. S., Koekemoer, A. M., Kovac, K., Ideue, Y., Ikeda, H., Impey, C. D., Le Fevre, O., Lamareille, F., Lanzuisi, G., Le Borgne, J.-F., Le Brun, V., Lilly, S., Maier, C., Manohar, S., Masters, D., McCracken, H., Messias, H., Mignoli, M., Mobasher, B., Nagao, T., Pello, R., Puccetti, S., Perez-Montero, E., Renzini, A., Sargent, M., Sanders, D. B., Scodeggio, M., Scoville, N., Shopbell, P., Silvermann, J., Taniguchi, Y., Tasca, L., Tresse, L., Trump, J. R., and Zucca, E.: 2011, ApJ **742**, 61

Sandage, A.: 1965, ApJ **141**, 1560

Sanders, D. B. and Mirabel, I. F.: 1996, ARA&A **34**, 749

Sanders, D. B., Phinney, E. S., Neugebauer, G., Soifer, B. T., and Matthews, K.: 1989, ApJ **347**, 29

Santini, P., Fontana, A., Grazian, A., Salimbeni, S., Fiore, F., Fontanot, F., Boutsia, K., Castellano, M., Cristiani, S., de Santis, C., Gallozzi, S., Giallongo, E., Menci, N., Nonino, M., Paris, D., Pentericci, L., and Vanzella, E.: 2009, A&A **504**, 751

Santini, P., Rosario, D. J., Shao, L., Lutz, D., Maiolino, R., Alexander, D. M., Altieri, B., Andreani, P., Aussel, H., Bauer, F. E., Berta, S., Bongiovanni, A., Brandt, W. N., Brusa, M., Cepa, J., Cimatti, A., Daddi, E., Elbaz, D., Fontana, A., Förster Schreiber, N. M., Genzel, R., Grazian, A., Le Floc'h, E., Magnelli, B., Mainieri, V., Nordon, R., Pérez Garcia, A. M., Poglitsch, A., Popesso, P., Pozzi, F., Riguccini, L., Rodighiero, G., Salvato, M., Sanchez-Portal, M., Sturm, E., Tacconi, L. J., Valtchanov, I., and Wuyts, S.: 2012, A&A **540**, A109

Sarazin, C. L.: 1997, in M. Arnaboldi, G. S. Da Costa, and P. Saha (eds.), *The Nature of Elliptical Galaxies; 2nd Stromlo Symposium*, Vol. 116 of *Astronomical Society of the Pacific Conference Series*, p. 375

Savaglio, S., Glazebrook, K., Le Borgne, D., Juneau, S., Abraham, R. G., Chen, H.-W., Crampton, D., McCarthy, P. J., Carlberg, R. G., Marzke, R. O., Roth, K., Jørgensen, I., and Murowinski, R.: 2005, ApJ **635**, 260

Scarlata, C., Carollo, C. M., Lilly, S. J., Feldmann, R., Kampczyk, P., Renzini, A., Cimatti, A., Halliday, C., Daddi, E., Sargent, M. T., Koekemoer, A., Scoville, N., Kneib, J.-P., Leauthaud, A., Massey, R., Rhodes, J., Tasca, L., Capak, P., McCracken, H. J., Mobasher, B., Taniguchi, Y., Thompson, D., Ajiki, M., Aussel, H., Murayama, T., Sanders, D. B., Sasaki, S., Shioya, Y., and Takahashi, M.: 2007, ApJS **172**, 494

Schawinski, K., Simmons, B. D., Urry, C. M., Treister, E., and Glikman, E.: 2012, MNRAS **425**, L61

Schmidt, M.: 1963, Nature **197**, 1040

Schramm, M. and Silverman, J. D.: 2013, ApJ **767**, 13

Setti, G. and Woltjer, L.: 1973, in H. Bradt and R. Giacconi (eds.), *X- and Gamma-Ray Astronomy*, Vol. 55 of *IAU Symposium*, p. 208

Setti, G. and Woltjer, L.: 1989, A&A **224**, L21

Seyfert, C. K.: 1943, ApJ **97**, 28

Shapley, A. E., Steidel, C. C., Erb, D. K., Reddy, N. A., Adelberger, K. L., Pettini, M., Barmby, P., and Huang, J.: 2005, ApJ **626**, 698

Shen, S., Mo, H. J., White, S. D. M., Blanton, M. R., Kauffmann, G., Voges, W., Brinkmann, J., and Csabai, I.: 2003, MNRAS **343**, 978

Silk, J. and Rees, M. J.: 1998, A&A **331**, L1

Silverman, J. D., Green, P. J., Barkhouse, W. A., Kim, D.-W., Kim, M., Wilkes, B. J., Cameron, R. A., Hasinger, G., Jannuzi, B. T., Smith, M. G., Smith, P. S., and Tananbaum, H.: 2008, ApJ **679**, 118

Simpson, C.: 2005, MNRAS **360**, 565

Smith, D. A. and Done, C.: 1996, MNRAS **280**, 355

Springel, V. and Hernquist, L.: 2005, ApJL **622**, L9

Stern, D., Eisenhardt, P., Gorjian, V., Kochanek, C. S., Caldwell, N., Eisenstein, D., Brodwin, M., Brown, M. J. I., Cool, R., Dey, A., Green, P., Jannuzi, B. T., Murray, S. S., Pahre, M. A., and Willner, S. P.: 2005, ApJ **631**, 163

Sunyaev, R. A. and Titarchuk, L. G.: 1980, A&A **86**, 121

Sutherland, W. and Saunders, W.: 1992, MNRAS **259**, 413

Szomoru, D., Franx, M., van Dokkum, P. G., Trenti, M., Illingworth, G. D., Labbé, I., Bouwens, R. J., Oesch, P. A., and Carollo, C. M.: 2010, ApJL **714**, L244

Tadhunter, C. and Tsvetanov, Z.: 1989, Nature **341**, 422

Tanaka, Y., Nandra, K., Fabian, A. C., Inoue, H., Otani, C., Dotani, T., Hayashida, K., Iwasawa, K., Kii, T., Kunieda, H., Makino, F., and Matsuoka, M.: 1995, Nature **375**, 659

Tananbaum, H., Avni, Y., Branduardi, G., Elvis, M., Fabbiano, G., Feigelson, E., Giacconi, R., Henry, J. P., Pye, J. P., Soltan, A., and Zamorani, G.: 1979, ApJL **234**, L9

Thomas, D., Maraston, C., Bender, R., and Mendes de Oliveira, C.: 2005, ApJ **621**, 673

Thompson, D., Beckwith, S. V. W., Fockenbrock, R., Fried, J., Hippelein, H., Huang, J.-S., von Kuhlmann, B., Leinert, C., Meisenheimer, K., Phleps, S., Röser, H.-J., Thommes, E., and Wolf, C.: 1999, ApJ **523**, 100

Toft, S., van Dokkum, P., Franx, M., Labbe, I., Förster Schreiber, N. M., Wuyts, S., Webb, T., Rudnick, G., Zirm, A., Kriek, M., van der Werf, P., Blakeslee, J. P., Illingworth, G., Rix, H.-W., Papovich, C., and Moorwood, A.: 2007, ApJ **671**, 285

Toomre, A.: 1977, in B. M. Tinsley and R. B. G. Larson, D. Campbell (eds.), *Evolution of Galaxies and Stellar Populations*, p. 401

Townsley, L. K., Broos, P. S., Garmire, G. P., and Nousek, J. A.: 2000, ApJL **534**, L139

Tozzi, P., Gilli, R., Mainieri, V., Norman, C., Risaliti, G., Rosati, P., Bergeron, J., Borgani, S., Giacconi, R., Hasinger, G., Nonino, M., Streblyanska, A., Szokoly, G., Wang, J. X., and Zheng, W.: 2006, A&A **451**, 457

Treister, E., Schawinski, K., Volonteri, M., Natarajan, P., and Gawiser, E.: 2011, Nature **474**, 356

Tremonti, C. A., Heckman, T. M., Kauffmann, G., Brinchmann, J., Charlot, S., White, S. D. M., Seibert, M., Peng, E. W., Schlegel, D. J., Uomoto, A., Fukugita, M., and Brinkmann, J.: 2004, ApJ **613**, 898

Trujillo, I., Conselice, C. J., Bundy, K., Cooper, M. C., Eisenhardt, P., and Ellis, R. S.: 2007, MNRAS **382**, 109

Trujillo, I., Ferreras, I., and de La Rosa, I. G.: 2011, MNRAS **415**, 3903

Trujillo, I., Feulner, G., Goranova, Y., Hopp, U., Longhetti, M., Saracco, P., Bender, R., Braito, V., Della Ceca, R., Drory, N., Mannucci, F., and Severgnini, P.: 2006, MNRAS **373**, L36

Trump, J. R., Konidaris, N. P., Barro, G., Koo, D. C., Kocevski, D. D., Juneau, S., Weiner, B. J., Faber, S. M., McLean, I. S., Yan, R., Pérez-González, P. G., and Villar, V.: 2013, ApJL **763**, L6

Trump, J. R., Weiner, B. J., Scarlata, C., Kocevski, D. D., Bell, E. F., McGrath, E. J., Koo, D. C., Faber, S. M., Laird, E. S., Mozena, M., Rangel, C., Yan, R., Yesuf, H., Atek, H., Dickinson, M., Donley, J. L., Dunlop, J. S., Ferguson, H. C., Finkelstein, S. L., Grogin, N. A., Hathi, N. P., Juneau, S., Kartaltepe, J. S., Koekemoer, A. M., Nandra, K., Newman, J. A., Rodney, S. A., Straughn, A. N., and Teplitz, H. I.: 2011, ApJ **743**, 144

Turner, T. J., George, I. M., Nandra, K., and Mushotzky, R. F.: 1997, ApJS **113**, 23

Ueda, Y., Akiyama, M., Ohta, K., and Miyaji, T.: 2003, ApJ **598**, 886

Ueda, Y., Takahashi, T., Inoue, H., Tsuru, T., Sakano, M., Ishisaki, Y., Ogasaka, Y., Makishima, K., Yamada, T., Ohta, K., and Akiyama, M.: 1998, Nature **391**, 866

Urry, C. M. and Padovani, P.: 1995, **107**, 803

Uttley, P., McHardy, I. M., Papadakis, I. E., Guainazzi, M., and Fruscione, A.: 1999, MNRAS **307**, L6 van der Wel, A., Bell, E. F., Häussler, B., McGrath, E. J., Chang, Y.-Y., Guo, Y., McIntosh, D. H., Rix, H.-W., Barden, M., Cheung, E., Faber, S. M., Ferguson, H. C., Galametz, A., Grogin, N. A., Hartley, W., Kartaltepe, J. S., Kocevski, D. D., Koekemoer, A. M., Lotz, J., Mozena, M., Peth, M. A., and Peng, C. Y.: 2012, ApJS **203**, 24

van Dokkum, P. G.: 2005, AJ **130**, 2647

Veilleux, S. and Osterbrock, D. E.: 1987, ApJS **63**, 295

Weiner, B. J., Coil, A. L., Prochaska, J. X., Newman, J. A., Cooper, M. C., Bundy, K., Conselice, C. J., Dutton, A. A., Faber, S. M., Koo, D. C., Lotz, J. M., Rieke, G. H., and Rubin, K. H. R.: 2009, ApJ **692**, 187

Weiner, B. J., Papovich, C., Bundy, K., Conselice, C. J., Cooper, M. C., Ellis, R. S., Ivison, R. J., Noeske, K. G., Phillips, A. C., and Yan, R.: 2007, ApJL **660**, L39

Weiner, B. J., Phillips, A. C., Faber, S. M., Willmer, C. N. A., Vogt, N. P., Simard, L., Gebhardt, K., Im, M., Koo, D. C., Sarajedini, V. L., Wu, K. L., Forbes, D. A., Gronwall, C., Groth, E. J., Illingworth, G. D., Kron, R. G., Rhodes, J., Szalay, A. S., and Takamiya, M.: 2005, ApJ **620**, 595

Weisskopf, M. C., Brinkman, B., Canizares, C., Garmire, G., Murray, S., and Van Speybroeck, L. P.: 2002, **114**, 1

White, S. D. M. and Frenk, C. S.: 1991, ApJ **379**, 52

Willmer, C. N. A., Faber, S. M., Koo, D. C., Weiner, B. J., Newman, J. A., Coil, A. L., Connolly, A. J., Conroy, C., Cooper, M. C., Davis, M., Finkbeiner, D. P., Gerke, B. F., Guhathakurta, P., Harker, J., Kaiser, N., Kassin, S., Konidaris, N. P., Lin, L., Luppino, G., Madgwick, D. S., Noeske, K. G., Phillips, A. C., and Yan, R.: 2006, ApJ **647**, 853

Willott, C. J.: 2011, ApJL **742**, L8

Winkler, H.: 1992, MNRAS **257**, 677

Worsley, M. A., Fabian, A. C., Bauer, F. E., Alexander, D. M., Hasinger, G., Mateos, S., Brunner, H., Brandt, W. N., and Schneider, D. P.: 2005, MNRAS **357**, 1281

Wuyts, S., Förster Schreiber, N. M., Lutz, D., Nordon, R., Berta, S., Altieri, B., Andreani, P., Aussel, H., Bongiovanni, A., Cepa, J., Cimatti, A., Daddi, E., Elbaz, D., Genzel, R., Koekemoer, A. M., Magnelli, B., Maiolino, R., McGrath, E. J., Pérez García, A., Poglitsch, A., Popesso, P., Pozzi, F., Sanchez-Portal, M., Sturm, E., Tacconi, L., and Valtchanov, I.: 2011, ApJ **738**, 106

Wuyts, S., Labbé, I., Schreiber, N. M. F., Franx, M., Rudnick, G., Brammer, G. B., and van Dokkum, P. G.: 2008, ApJ **682**, 985

Xue, Y. Q., Brandt, W. N., Luo, B., Rafferty, D. A., Alexander, D. M., Bauer, F. E., Lehmer, B. D., Schneider, D. P., and Silverman, J. D.: 2010, ApJ **720**, 368

Xue, Y. Q., Luo, B., Brandt, W. N., Bauer, F. E., Lehmer, B. D., Broos, P. S., Schneider, D. P., Alexander, D. M., Brusa, M., Comastri, A., Fabian, A. C., Gilli, R., Hasinger, G., Hornschemeier, A. E., Koekemoer, A., Liu, T., Mainieri, V., Paolillo, M., Rafferty, D. A., Rosati, P., Shemmer, O., Silverman, J. D., Smail, I., Tozzi, P., and Vignali, C.: 2011, ApJS **195**, 10

Yamada, T., Kodama, T., Akiyama, M., Furusawa, H., Iwata, I., Kajisawa, M., Iye, M., Ouchi, M., Sekiguchi, K., Shimasaku, K., Simpson, C., Tanaka, I., and Yoshida, M.: 2005, ApJ **634**, 861

Yan, R., Ho, L. C., Newman, J. A., Coil, A. L., Willmer, C. N. A., Laird, E. S., Georgakakis, A., Aird, J., Barmby, P., Bundy, K., Cooper, M. C., Davis, M., Faber, S. M., Fang, T., Griffith, R. L., Koekemoer, A. M., Koo, D. C., Nandra, K., Park, S. Q., Sarajedini, V. L., Weiner, B. J., and Willner, S. P.: 2011, ApJ **728**, 38

Yan, R., Newman, J. A., Faber, S. M., Coil, A. L., Cooper, M. C., Davis, M., Weiner, B. J., Gerke, B. F., and Koo, D. C.: 2009, MNRAS **398**, 735

Yan, R., Newman, J. A., Faber, S. M., Konidaris, N., Koo, D., and Davis, M.: 2006, ApJ **648**, 281

Zezas, A. L., Georgantopoulos, I., and Ward, M. J.: 1998, MNRAS **301**, 915

Zirm, A. W., van der Wel, A., Franx, M., Labbé, I., Trujillo, I., van Dokkum, P., Toft, S., Daddi, E., Rudnick, G., Rix, H.-W., Röttgering, H. J. A., and van der Werf, P.: 2007, ApJ **656**, 66